Bettina Olshausen

Shining bright:

Fluorescent tools for drug discovery, development and delivery

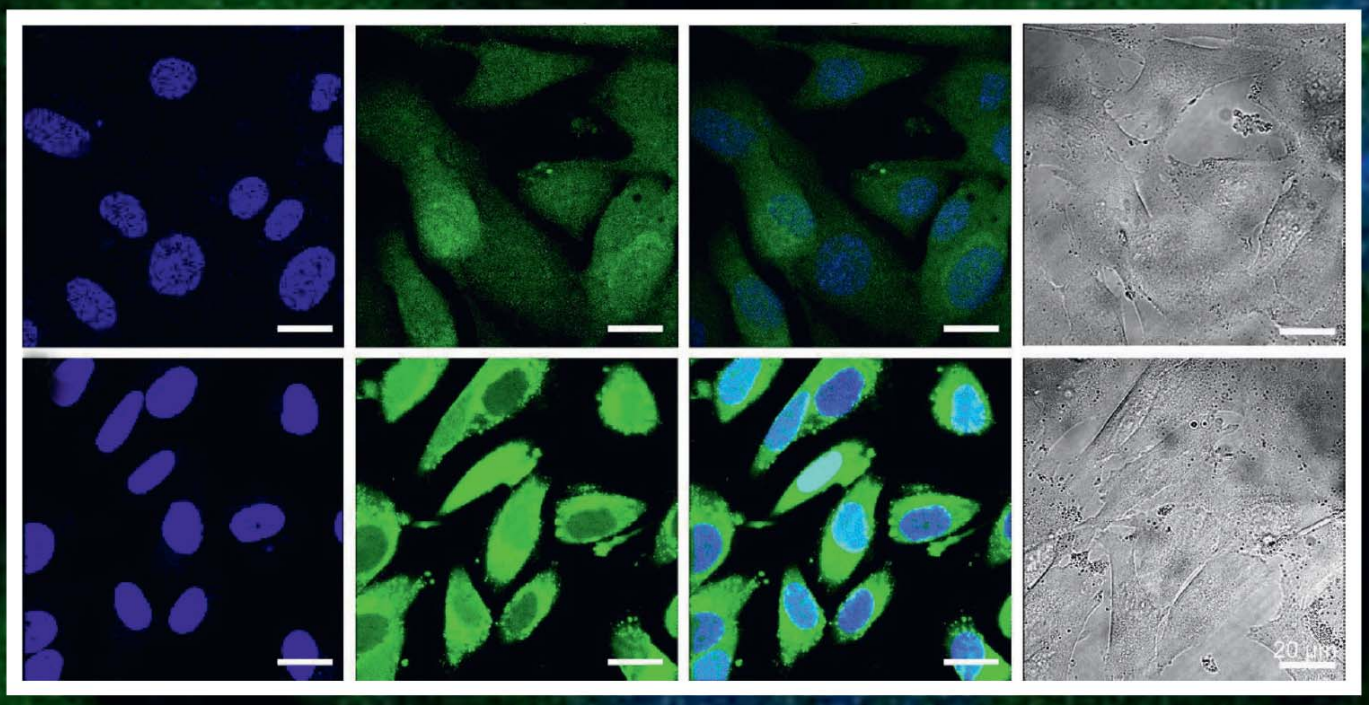

Cuvillier Verlag Göttingen
Internationaler wissenschaftlicher Fachverlag

Shining bright: Fluorescent tools for drug discovery, development and delivery

Shining bright: Fluorescent tools for drug discovery, development and delivery

Zur Erlangung des akademischen Grades eines
DOKTORS DER NATURWISSENSCHAFTEN
(Dr. rer. nat.)

der KIT-Fakultät für Chemie und Biowissenschaften
des Karlsruher Instituts für Technologie (KIT)

genehmigte
DISSERTATION

von
M.Sc. Bettina Olshausen
aus Bühl

Karlsruhe, 2017

1. Referentin: Prof. Dr. Ute Schepers
2. Referent: Prof. Dr. Hans-Achim Wagenknecht

Tag der mündlichen Prüfung: 12.12.2017

Bibliografische Information der Deutschen Nationalbibliothek
Die Deutsche Nationalbibliothek verzeichnet diese Publikation in der Deutschen Nationalbibliografie; detaillierte bibliographische Daten sind im Internet über http://dnb.d-nb.de abrufbar.
1. Aufl. - Göttingen: Cuvillier, 2018
Zugl.: Karlsruhe (KIT) , Univ., Diss., 2017

Nonnenstieg 8, 37075 Göttingen
Telefon: 0551-54724-0
Telefax: 0551-54724-21
www.cuvillier.de

1. Auflage, 2018
Gedruckt auf umweltfreundlichem, säurefreiem Papier aus nachhaltiger Forstwirtschaft.

ISBN 978-3-7369-9816-2
eISBN 978-3-7369-8816-3

There are two ways of spreading light: To be the candle or the mirror that reflects it.

- Edith Wharton

Meiner Familie

Statement

Die vorliegende Arbeit wurde in der Zeit von November 2014 bis Dezember 2017 am Institut für Toxikologie und Genetik (ITG), sowie am Institut für Organische Chemie (IOC) des Karlsruher Institut für Technologie (KIT) und am Massachusetts General Hospital (MGH), Boston unter Anleitung von Prof. Dr. Ute Schepers durchgeführt. Während des Zeitraumes vom 23. Januar 2017 bis 21. Juli 2017 lag die wissenschaftliche Betreuung bei Prof. Dr. Ralph Mazitschek (MGH, Harvard Medical School). Die Arbeit wurde gefördert durch ein Promotionsstipendium der Landesgraduiertenförderung Baden-Württemberg, sowie ein Reisestipendium des Karlsruhe House of Young Scientists (KHYS).

This work was developed between November 2014 and December 2017 at the Institute for Toxicology and Genetics (ITG), as well as at the Institute for Organic Chemistry (IOC) at the Karlsruhe Institute of Technology (KIT) and Massachusetts General Hospitel, Boston under supervision of Prof. Dr. Ute Schepers. Between January 23rd 2017 and July 21st 2017 the work was cosupervised by Prof. Dr. Ralph Mazitschek (MGH, Harvard Medical School). This thesis was financially supported by a graduate scholarship granted by the state of Baden-Württemberg as well as a travel scholarship from the Karlsruhe House of Young Scientists (KHYS).

Hiermit erkläre ich, die vorliegende Arbeit selbstständig verfasst und keine anderen als die angegebenen Quellen und Hilfsmittel verwendet zu haben. Die Dissertation wurde bisher an keiner anderen Hochschule oder Universität eingereicht.

Bettina Olshausen

Karlsruhe, 6.November 2017

Acknowledgements

Over the last 3 years, many people accompanied me on this journey and contributed to its success. I am grateful for all the support I experienced and that enabled this work.

First of all, I would like to express my gratitude to my supervisor Prof. Dr. Ute Schepers for her guidance, scientific support, and the freedom in shaping this PhD project, as well as Prof. Dr. Stefan Bräse for hosting me in his lab, his help and support, and Prof. Dr. Ralph Mazitschek for his hospitality and supervision during my work in Boston.

For productive cooperation, I would like to thank my collaboration partners Dr. Heidi-Kristin Walter and Jeannine Steinmeyer, as well as Matthias Eing for the friendship, our joint work, the invaluable discussions and all the beer-drinking-science-talking meetings.

I am grateful for all my fellow lab members in the Schepers group at ITG, the Bräse group at IOC and the Mazitschek group at MGH. I could always count on their support and assistance. A special thank goes to Vanessa Kappings, who was climbing all the hills and valleys on this journey side by side with me.

I would also like to thank all the students who were contributing to this work, Maximilian Benz, Andreas Klinkusch and Yannik Matt.

For the revisions of this work, I would like to thank Dr. John Burkhardt, Matthias Eing, Jeannine Steinmeyer, Dr. Sofia Santos, and Alena Kalyakina.

I offer my appreciation to the Research Training Group 2039 as well as the BioInterfaces International Graduate School (BIF-IGS) for expanding my knowledge beyond the scientific context.

For their financial support I would like to thank the Landesgraduiertenförderung Baden-Württemberg and the Karlsruhe House of Young Scientists (KHYS) for granting me a travel scholarship that enabled the unique experience of living and working in Boston.

None of this would have been possible without friends and family. Andrea, Caro, and Franzi: What would I have done without your friendship, the girls' nights out and this unforgettable trip to NYC? Thilo, Vio, Rebekka, Ruben, Manni, Steven, Eva, Anne, Paddy, Jessi and all the other fellow ChemBios: It was a pleasure to spend the last 8 years with you. John, thank you for your love, strength, and constant emotional support over the last 6 months. You have been my rock. Finally, I am grateful for the unconditional love and support of my family. My mum and my siblings who always believed in me and my dad who would have been immoderately proud seeing me graduate.

Publications and Communications

Papers and patents:

Walter, H. K., **Olshausen, B.**, Schepers, U. & Wagenknecht, H. A., A postsynthetically 2'-"clickable" uridine with arabino configuration and its application for fluorescent labeling and imaging of DNA. *Beilstein J Org Chem* 13, 127-137, doi:10.3762/bjoc.13.16 (2017).

Olshausen, B., Bräse, S. & Schepers, U. Fluorescent compounds for the detection of malignant melanoma (patent pending). E. P. Office.

Eing, M., **Olshausen, B.**, Fairfull-Smith, K., Schepers, U., Barner-Kowollik, C., Blinco, J.P., Reporting pH-sensitive Drug Release via Unpaired Spin Fluorescence Silencing. *Polym. Chem.*, 9, 499-505 (2018).

Steinmeyer, J., H. K. Walter, M. A. Bichelberger, V. Schneider, T. Kubar, F. Ronicke, **B. Olshausen**, K. Nienhaus, G. U. Nienhaus, U. Schepers, M. Elstner and H. A. Wagenknecht, "siRNA traffic lights": arabino-configured 2'-anchors for fluorescent dyes are key for dual color readout in cell imaging." *Org Biomol Chem*. (2018).

Olshausen, B., Bräse, S., Schepers, U., A melanocyte specific fluorescent compound and its potential application in melanoma early detection, *in preparation*

Oral communications in conferences

Olshausen, B., Bräse, S., Schepers, U., Fluorescent Melanocyte markers with possible application in the early detection of melanoma, Symposium o Molecular Architectures for Fluorescent Imaging of Cells, KIT, Karlsruhe, 2017

Posters in conferences

Olshausen, B., Schepers, U.: Novel fluorescent compounds for the early detection of melanoma, Gordon Research Conference High Throughput Chemistry & Chemical Biology, Proctor Academy, Andover, NH, USA, 2017

Olshausen, B., Schepers, U.: Novel fluorescent compounds for the early detection of melanoma, The Society for Melanoma Research Congress, Boston, MA, USA, 2016

Abstract

We believe what we see. While perhaps not uniformly applicable, this adage still has a kernel of truth. The visualization of processes and reactions facilitates their understanding and therefore is of invaluable advantage in science. In chemical biology, the fluorescent labeling of molecules and usage of fluorescence-based imaging techniques for visualizing molecular interactions at a subcellular level is a key feature and contributes significantly to the elucidation of disease mechanisms. Furthermore, potential drug target sites can be identified, drugs acting on such sites can be developed, and by their labeling, the interactions of drugs and targets can be uncovered. In this work, innovative approaches for the fluorescent labeling of proteins, nucleic acids, and drugs are presented. A novel methodology for the facile synthesis of a versatile, functionalized, water-soluble, tunable fluorescent probe has been developed. The resulting small, uncharged BODIPY dye with favorable physico-chemical properties avoids the common drawbacks of cell membrane interactions and unspecific staining of membrane structures caused by a high lipophilicity of this class of molecules, as well as the introduction of large substituents or charged moieties that are often introduced to improve hydrophilicity. It was successfully synthesized in only three steps, applied in a HaloTag labeling system, and evaluated in a biological setting. The new dye exhibits great potential in various labeling approaches of biologically active molecules. Within the class of these active compounds, oligonucleotides, such as siRNA constructs, are promising novel drug candidates. However, the visualization of these double stranded molecules is challenging and established methods often suffer from the limitations of single color readouts. The development of a dual-color readout DNA/RNA “Traffic Lights” concept, based on the energy transfer of two dyes in interstrand positions of double stranded oligonucleotides, is a way to overcome these obstacles in the reliable tracking of cellular delivery, target binding, and structural integrity of nucleic acids. Several new dye combinations as energy transfer pairs, as well as the influence of the dye orientation within the helical structure of DNA and RNA double strands, have been examined for efficient energy transfer, integrity, toxicity, and function in a cellular environment. For many diseases, especially those of cancerous nature, not only is the development of new drug candidates and their visualization crucial, but the healing chances are decisively influenced by an efficient early detection. The synthesis of a melanocyte-specific fluorescent compound reveals a promising new approach to the early detection of melanoma via non-invasive fluorescence microscopy after topical administration. A lead structure has been found, and could be optimized and evaluated in tailored screening settings, utilizing novel tissue engineering strategies. If a cancerous disease with a solid tumor is detected, the efficient transport of a drug to the tumor site and local accumulation is of meaningful impact, thus increasing the drug efficacy while decreasing systemic side effects. A polymeric nanocarrier system for targeted tumor transport and triggered drug release has been developed, following an approach of not only tracking a successful tumor site transport. A direct visualization of the drug release from the carrier system could also be achieved in a process of fluorescence silencing and recovery in an analytical as well as biological settings. The four different projects presented in this work reflect all the stages in the visualization process of biologically active molecules, from the

synthesis of a fluorescent probe to the labeling of proteins, nucleic acids, drugs, and drug carrier systems.

Zusammenfassung

Wir glauben nur, was wir auch sehen können. Obwohl diese Aussage weder vollständig wahr, noch allgemeingültig anwendbar ist, besitzt sie doch einen wahren Kern. Die Sichtbarmachung von Prozessen und Reaktionen vereinfacht deren Verständnis für uns und ist daher von unschätzbarem Wert in den Naturwissenschaften. Die fluoreszente Markierung von molekularen Strukturen und ihre Visualisierung durch Fluoreszenz-basierte bildgebende Verfahren ist daher ein zentraler Bestandteil der Forschung in der Chemischen Biologie und trägt maßgeblich zur Aufklärung von Krankheits-auslösenden Mechanismen bei. Neue therapeutische Ansatzpunkte können identifiziert und entsprechende Wirkstoffe entwickelt werden. Durch ihre fluoreszente Markierung kann dabei das Zusammenspiel zwischen einem Wirkstoff und dessen Zielstruktur aufgedeckt werden. In dieser Arbeit werden innovative Ansätze zur fluoreszenten Markierung von Proteinen, Nukleinsäuren und Medikamenten vorgestellt. Es wurde eine neue Methodologie zur einfachen Synthese von vielseitig einsetzbaren, funktionalisierten, wasserlöslichen Fluorezenzfarbstoffen mit abstimmbarem Wellenlängen-Bereich entwickelt. Der dabei entstandene kleine und ungeladene BODIPY Fluorophor mit erstrebenswerten physikalisch-chemischen Eigenschaften, vermeidet die weit verbreiteten Schwierigkeiten von unspezifischen Hintergrundfärbungen zellulärer Membranstrukturen durch Lipophilie-bedingte Membran-Wechselwirkungen unter Umgehung der üblichen Einführung großer oder geladener Substituenten zur Verbesserung der Hydrophilie. Die erfolgreiche Synthese des Fluorophors konnte in nur drei Stufen realisiert werden und die Verbindung in einem HaloTag Markierungssystem zur Anwendung gebracht, sowie in einem biologischen System evaluiert werden. Dabei zeigt der neue Fluorophor ein großes Potential für vielfältige Ansätze zur Markierung biologisch aktiver Moleküle. Innerhalb dieser Molekül-Klasse stellen Oligonukleotide, wie beispielsweise siRNA Konstrukte, vielversprechende neue Wirkstoff-Kandidaten dar. Deren Visualisierung ist jedoch schwierig und etablierte Methoden sind häufig eingeschränkt durch die Ausgabe eines einzigen Farbsignals für doppelsträngige Strukturen. Die Entwicklung eines zweifarbigen DNA/RNA “Traffic Lights“ Konzepts, basierend auf dem Energietransfer zwischen zwei Fluorophoren, die in Interstrang-Orientierung auf einem Oligonukleotid-Doppelstrang installiert sind, verspricht diese Hürden in der zuverlässigen Verfolgung von zellulärem Transport, Bindung an die Zielstruktur und struktureller Integrität zu überwinden. Verschiedene neue Fluorophor-Kombinationen, sowie der Einfluss ihrer räumlichen Orientierung innerhalb der helikalen Struktur von DNA- oder RNA-Doppelsträngen, wurden auf ihre Energietransfer-Effizienz, strukturelle Integrität, Toxizität und Funktion in zellulärer Umgebung hin untersucht. Für viele (speziell für krebsartige) Erkrankungen sind allerdings nicht nur die Entwicklung neuer Wirkstoffe und deren Visualisierung in einem zellulärem Kontext von Bedeutung, sondern vor allem eine effiziente Früherkennung bestimmt die Prognose maßgeblich. Die hier vorgestellte Synthese einer Melanozyten-spezifischen fluoreszenten Verbindung verspricht einen neuen Ansatz zur Detektion von malignen Melanomen via nicht-invasiver Fluoreszenz-Mikroskopie nach lokalem Aufbringen des Moleküls auf die Haut. Eine Leistruktur für eine solche Verbindung wurde gefunden und konnte optimiert werden. Die Evaluation der Aufnahme erfolgte in speziell designten Test-

Systemen unter Zuhilfenahme moderner *Tissue Engineering* Strategien. Wenn eine Krebserkrankung mit Ausbildung eines soliden Tumors detektiert wird, ist ein effizienter Wirkstoff-Transport zur Tumor-Region bedeutend, da auf diese Weise die Wirkung des Medikaments verstärkt und systemische Nebenwirkungen reduziert werden können. In diesem Zusammenhang wurde eine Polymer-basierte Transporter-Plattform für den zielgerichteten Tumor-Transport und Stimulus-abhängige Wirkstoff-Freigabe entwickelt, die nicht nur die Verfolgung des erfolgreichen Tumor-Transports der Plattform ermöglicht, sondern auch, durch einen Mechanismus von Fluoreszenzlöschung und –Erholung, die erfolgreiche Wirkstoff-Freigabe am Zielort visualisiert. Die vier unterschiedlichen Projekte, die in dieser Arbeit vorgestellt werden, spiegeln alle Stadien in der Visualisierung von biologisch aktiven Molekülen wider, von der Synthese eines Fluorophors über die Markierung von Porteinen, Nukleinsäuren und Wirkstoffen bis hin zu Wirkstoff-Transportsystemen.

Table of Contents

µM	micromolar
4-MU	4-methylumbelliferone
5-ALA	5-aminolevulinic acid
A	absorption
a.u.	absorption unit
abs.	absolute
ACN	Acetonitrile
AcOH	acetic acid
$AlCl_3$	aluminum chloride
ALI	air-liquid interface
ALM	acral lentiginous melanoma
AO	antisense oligonucleotide
ATR	attenuated total refelection
BCC	basal cell carcinoma
bHMA	*tert*-butyloxycarbonyl-hydrazidomethacrylate
Boc	*tert*-butyloxycarbonyl
BODIPY	boron-dipyrromethene
B-PER	bacterial protein extraction reagent
BuLi	n-butyllithium
C	emission color contrast
CCD	charge-coupled device
CDK	cyclin-dependent kinase
CDKIN2A	cyclin-dependent kinase inhibitor 2A
CH	cyclohexanes
$CHCl_3$	chloroform
CLSM	confocal laser scanning microscopy
CMA	core monoalkoxy
CO_2	carbon dioxide
CPP	cell penetrating peptides
CPPo	cell penetrating peptoid
d	day(s)
DCM	dichloromethane
DDS	drug delivery system
DEL	DNA-encoded libraries
DEPT	distortionless enhancement by polarisation transfer
DIC	diisopropylcarbodiimide
DIPEA	*N,N*-diisopropylethylamine
DMF	dimethylformamide
DMSO	dimethyl sulfoxide
DNA	deoxyribonucleic acid
DOX	doxorubicin
ds	double strand
dSTORM	direct stochastic optical reconstruction
ECM	extracellular matrix
EDCI	1-ethyl-3-(3-dimethylaminopropyl)carbodiimide
EDTA	ethylenediaminetetraacetic acid
EE	ethyl acetate
ELISA	enzyme-linked immunosorbent assay

em	emission
EPR effect	enhanced permeability and retention effect
EPR spectroscopy	electron paramagnetic resonance spectroscopy
equiv.	equivalents
ER	endoplasmatic reticulum
ET	energy transfer
Et_2O	diethylether
EtOAc	ethyl acetate
EtOH	ethanol
exc	excitation
F	fluorescence
FA	formic acid
FAD	flavin adenine dinucleotide
FISH	fluorescence in situ hybridization
FLIM	fluorescence lifetime imaging
FMN	flavin mononucleotide
Fmoc	fluorenylmethoxycarbonyl
FRAP	fluorescence recovery after photobleaching
FRET	Förster/fluorescence resonance energy transfer
FT	full thickness
g	gram
GelMA	gelatin methycryloyl
GFP	green fluorescent protein
GPC	gel permeation chromatography
GPCR	G-protein coupled receptors
h	hours
H_2O_2	hydrogen peroxide
H_2SO_4	sulfuric acid
HCl	hydrochloric acid
HGP	Human Genome Project
HMA	hydrazidomethacrylate
HOBt	hydroxybenzotriazole
HPLC	high performance liquid chromatography
HTS	high throughput screening
IC	internal conversion
iPrOH	isopropanol
IPTG	isopropyl β-D-1-thiogalactopyranoside
IR	infrared spectroscopy
ISC	intersystem crossing
kD	kilo Dalton
KHMDS	potassium bis(trimethylsilyl)amide
LAP	lithium-phenyl-(2,4,6-trimethylbenzoyl)phosphine
LC/MS	liquid chromatography mass spectrometry
LDA	lithium diisopropylamide
LiOH	lithium hydroxide
LMM	lentigo maligna melanoma
M	molar
MALDI	matrix-assisted laser desorption/ionization
mCPBA	meta-chloroperoxybenzoic acid
MeOH	methanol

min	minute(s)
miRNA	micro RNA
mM	millimolar
mmol	milli mol
MRI	magnetic resonance imaging
MS	molecular sieves
MSF	multispectral imaging in the frequency domain
MSS	multispectral imaging in the spatial domain
N_3	azide
Na	sodium
Na_2SO_4	sodium sulfate
NaCl	sodium chloride
NADH	nicotinamide adenine dinucleotide
NaH	sodium hydride
$NAHCO_3$	sodium bicarbonate
NEt_3	triethylamine
NHDF	normal human dermal fibroblasts
NHEK	normal human epidermal keratinocytes
NHEM	normal human epidermal melanocytes
NHS	*N*-hydroxysuccinimide
NIR	near-infrared
NM	nodular melanoma
nm	nanometer
NMSC	non-melanoma skin cancer
NP	nanoparticle
ns	nanosecond(s)
OCT	optical coherence tomography
OD	optical density
P	phosphorescence
PAGE	polyacrylamide gel electrophoresis
PALM	photoactivation localization microscopy
PBS	phosphate buffered saline
PCR	polymerase chain reaction
PEG	polyethylene glycol
PFA	paraformaldehyde
PMT	photomultiplier voltage
PpIX	protoporphyrin IX
ppm	parts per million
PPTTC	pentyl-(cyanoisopropyl)-trithiocarbonate PPTTC
PyBOP	benzotriazolyloxy-tris[pyrrolidino]-phosphonium hexafluorophosphate
RAFT	reversible addition-fragmentation chain-transfer
RET	resonance energy transfer
RFP	red fluorescent protein
RHE	reconstructed human epidermis
RNA	ribonucleic acid
RNAi	RNA interference
ROS	reactive oxygen species
rt	room temperature
s	second(s)
SBDD	structure-based drug design

SCC	squamous cell carcinoma
shRNA	short-hairpin RNA
SIM	structured illumination microscopy
SMLM	single molecule localization microscopy
SPAAC	strain-promoted azide-alkyne cycloaddition
SSM	superficial spreading melanoma
STED	stimulated emission depletion
STORM	stochastic optical reconstruction microscopy
TAMRA	carboxytetramethylrhodamine
TBAF	tetrabutylammoniumfluoride
TCM	chloroforme
TEGMA	triethylene glycol methacrylate
TEMPO	2,2,6,6-tetramethylpipridine-1-oxyl
TFA	trifluoroacetic acid
THF	tetrahydrofuran
THz	tetrahertz
TIRF	on total internal reflection fluorescence
TLC	thin layer chromatography
TMIO	tetramethylisoindoline
TMPMA	tetramethyl-piperidyl-methacrylate
TMSOTf	trimethylsilyl trifluoromethanesulfonate
TO	thiazole orange
TOF	time-of-flight
Tol	toluene
TR	thiazole red
UV	ultraviolet (radiation)
V	Volt
VR	vibrational relaxation
λ	wavelength
Φ_F	fluorescence quantum yield

Introduction

1 Introduction

The discovery and development of new drugs is a key process in the fight against diseases. However, it is a time- and cost-intensive cycle. From the identification of a lead structure to the clinical trials, 14 years and about 800 million US dollars are estimated to be consumed.[1] Hence, every step of the process is subject to optimization and fluorescence-based imaging techniques are useful instruments in their optimization by visualization. Typically, the different steps are defined as target identification, target validation, lead identification, lead optimization, preclinical stage, and finally clinical trials.[2] The ideal drug target is a macromolecule, closely linked to the tackled disease that binds a small molecule.[3] Proteins and especially enzymes are therefore often chosen as valuable targets but also nucleic acids with a defined secondary structure have been successfully employed as drug targets.[4-7] Furthermore, G-protein coupled receptors (GPCRs) are popular target structures.[8-10] The aim of the interaction with the target is often the alteration of pathological protein functions, or in case of drugs targeting pathogens, the elimination of a unique target that leads to cell death. Especially in cancer, the identification of a valid target can be challenging since the physiological counterparts of dysfunctional proteins present in degenerated cells, often fulfill crucial functions in healthy tissue. Therefore, careful target validation is of tremendous significance to decrease the risk of interference with physiological functions or other pathways, the occurrence of side effects, and down-stream cost incurrence.[11,12] Besides biological and genetic approaches, the verification of a target in an *in vivo* disease model is a central step, often employing highly sophisticated fluorescence-based imaging techniques.[13] After successful identification and validation of a valuable drug target, small molecules interacting with the target are identified as potential leads. In the discovery of lead structures, two general strategies are applied: the high throughput screening (HTS) of large compound libraries or a structure-based drug design (SBDD). A broad variety of HTS has been developed over the last years, enabling the screening of up to 100,000 compounds per day in micro-titer scale assays based on fluorescence, radiometric, or colorimetric methods in a fully automated manner.[14-17] The recent development of DNA-encoded libraries (DELs) enables the investigation of thousands of different molecules with a target in a one-pot approach providing even more cost-efficiency in screenings. A whole library of molecules, each of them labeled with a specific DNA sequence, can be incubated within a protein binding assay for example, with a target protein and upon binding of one of the molecules, the lead can be identified using the DNA tag (**Figure 1.1**).[18-20]

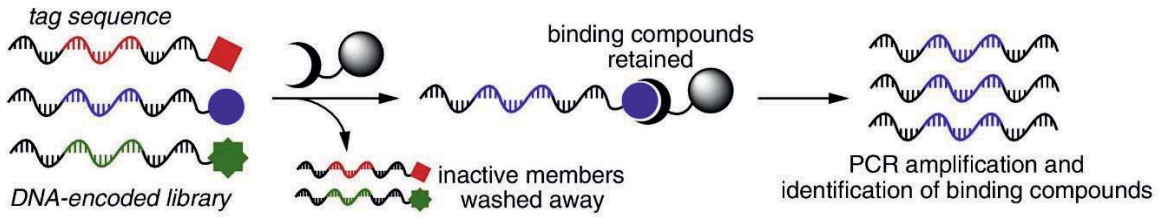

Figure 1.1: Simple example of a DNA encoded library assay with a target on solid phase.[18] [i]

The quality of large compound libraries has been significantly improved with defining the chemical space in which a potential lead is most likely situated. Lipinski proposed in 1996, after scanning and analyzing various libraries and positive lead hits, that poor permeation and absorption, which are critical characteristics for potential leads, are more likely if a compound exhibits a) more than 5 H-bond donors (expressed as the sum of OHs and NHs), b) a molecular weight greater than 500 g/mol, c) a log P (as a measure for hydrophilicity/lipophilicity) over 5, d) more than 10 H-bond acceptors (expressed as the sum of Ns and Os). Compound classes that are substrates for biological transporters have been defined as an exception to that rule.[21,22] By limiting compound libraries according to criteria like Lipinski's rule of 5 or the supposed ADME (absorption, distribution, metabolism and excretion) criteria, an increased efficiency in drug screenings has been achieved. A great advantage of HTS is that the binding site of the target does not have to be known *a priori*. However, if the binding site is known, often by resolving the protein crystal structures, a more rational approach to lead identification can be taken by the structure based drug design. Computational methods such as DOCK, aiming at finding the correct conformation of a ligand and its receptor, often in combination with molecular dynamic simulations, can result in exact lead predictions.[23,24] Iterative cycles and evaluations of these processes, together with the identification of structure-function relationships, are providing lead optimization. In the following preclinical phase, a synthetic strategy is usually developed that allows to synthesize the optimized lead efficiently in large scales and high purity. Additionally, a formulation is developed as a way to administer the drug (pill, spray, ointment etc.). Toxicity studies in animals are the basis of the permission process with regulatory authorities before entering the clinical phase and administering the potential drug to humans.[25] The final clinical development consists of four different phases: in phase 0, minimal concentrations of the investigated drug, significantly smaller than the therapeutic range, are administered to a small group of healthy individuals to gather preliminary ADME data in humans. In phase I, safety, tolerability, pharmacokinetic properties, and pharmacological effects are tested in a group of 20-100, usually healthy, volunteers. In phase II, the effectiveness of the potential drug is tested in a group of a few hundred patients while monitoring side effects and in case of success, the test group is increased to several thousand patients in phase III.[26]

[i] Reprinted from Current Opinion in Chemical Biology, Vol 26, Alix I Chan,Lynn M McGregor,David R Liu, Novel selection methods for DNA-encoded chemical libraries, 55-61, Copyright (2015), with permission from Elsevier

1.1 Targeted drug delivery systems

Whenever a drug is administered to a body, if systemically, locally or orally, there are various obstacles a drug has to face before it reaches its target. In general, the degradation of drugs by different enzymes is a major problem, as well as occurring side effects, or the provocation of an undesired immune response. When systemically applied, renal or hepatic clearance, vascular heterogeneity, and the access to the targeted tissue or cells is an issue. Local administration is limited by anatomical barriers, additional risks are material-induced tissue damage or an uncontrolled (burst) release combined with then occurring toxicity. The success of oral drug uptake is highly depending on variations in pH values and enzymes in the gastrointestinal tract, as well as on mucosal or epithelial barriers. Additionally, the residence time of the drug in the body is usually shorter than 30 h, the time the passage from intake to excretion takes in average (**Figure 1.2**).[27]

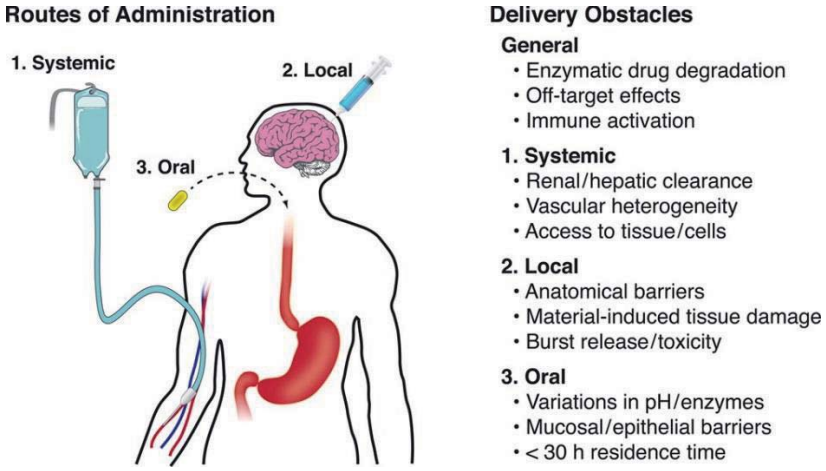

Figure 1.2: Different routes of drug administration and the various hurdles of drug delivery.[ii 27]

With the development of various drug delivery systems (DDSs), scientists have tried to overcome these obstacles in recent years. The aim of those systems is either the transport of a small molecule to a specific tissue with a targeted release to reduce undesired systemic effects, as well as to increase local drug concentration, and therefore drug efficacy. Or the aim is a controlled release in a specific tissue over time to avoid peaks and valleys in drug concentration, such as in implants or drug-covered stents.[28,29] For the former, either classic carrier molecules are utilized with a transport depending on the molecular structure, or by applying modern nanocarrier techniques, with effects mostly relying on the particle size.[30] Among the conventional carrier molecules are naturally occurring biomolecules, including lipid-based carriers and cell penetrating peptides (CPPs).[31-34] Both show the ability of transporting a cargo into a

[ii] Reprinted with permission from Tibbitt, M. W., Dahlman, J. E. & Langer, R. Emerging frontiers in drug delivery. *Journal of the American Chemical Society* **138**, 704-717. Copyright (2016) American Chemical Society.

target cell by interacting with cell membranes. While lipids can easily pass membranes due to their hydrophobicity, the mechanism is not completely clear for CPPs. However, it is proposed that they strongly interact with negative charges on cell surfaces due to their polycationic character.[35] Unfortunately, the half-life of CPPs in biological systems is limited by their high sensitivity towards various enzymes and peptidases. The development of peptidomimetics, such as cell penetrating peptoids (CPPos) that display a shift of peptide side chains from the peptide bond α-carbon to the nitrogen atom, significantly increases their stability.[35-37] In nanocarrier systems, biodegradable and biocompatible polymeric materials, various nanoparticles, dendrimers, self-assembling micelles, or polymer-biomolecule hybrids are popular approaches towards drug delivery. Depending on the particle size, many of these systems are applied in cancer therapy. Solid tumors are highly vascularized and interestingly, the blood vessels in a tumor environment show an enhanced permeability for large molecules up to 300 nm in diameter, due to a fenestration with gaps between endothelial cells and a discontinuous or absent basement membrane.[38] If a drug is connected to a nanocarrier transporter in the desired size, it will show a prolonged circulation time in the blood stream after systemic injection since the large molecular systems are not able to pass the barrier of a healthy endothelial layer. When arriving at the tumor site, however, the molecules are able to leave the blood vessels and therefore, a targeted tumor transport is achieved. This effect is widely known as the enhanced permeation and retention (EPR) effect (**Figure 1.3**).[39,40]

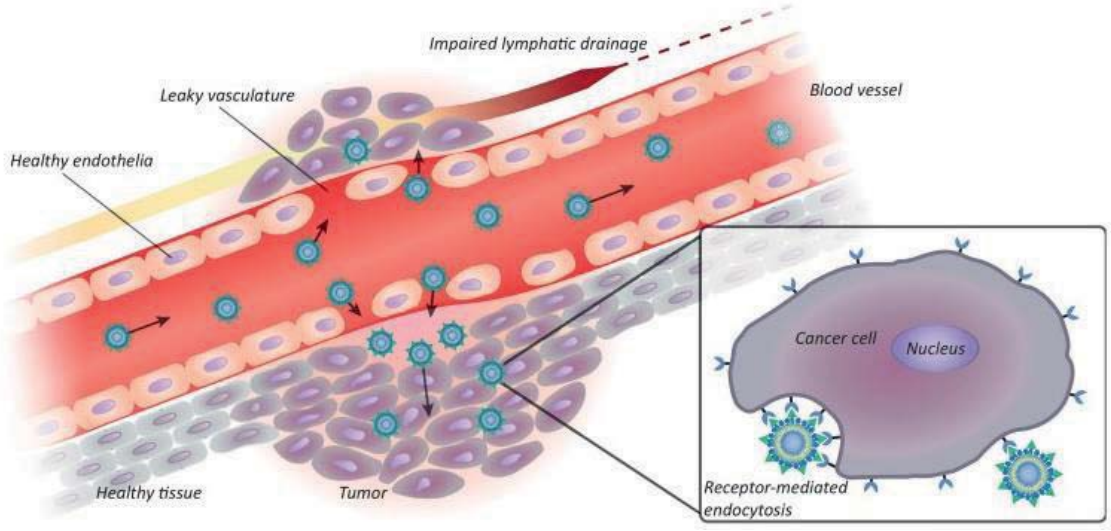

Figure 1.3: Passive tumor targeted drug delivery utilizing the EPR (enhanced permeation and retention) effect. Uptake of nanocarrier molecules through the damaged endothelial layer of blood vessels in tumor environments.[iii] [41]

A triggered release of the cargo from the nanocarrier can be achieved via different external stimuli such as the reduced pH value of tumor tissue.[29] With the application of

[iii] Reprinted from Trends in Biotechnology, Vol 32, Issue 1, Gavin T. Noble, Jared F. Stefanick, Jonathan D. Ashley, Tanyel Kiziltepe, Basar Bilgicer, igand-targeted liposome design: challenges and fundamental considerations, 32-45, Copyright (2014), with permission from Elsevier

fluorescence-labeling and imaging techniques, a convenient tracking of successful delivery to the target site is possible.

1.2 Fluorescence-based imaging techniques

Along with the development of fluorescent labeling techniques, also the techniques of fluorescence imaging evolved since the first fluorescence-based microscopes were built in the early 1900s. In the basic set-up, the wide field fluorescence microscopy that is still a common tool in modern biology, a sample containing intrinsic or (most often) extrinsic fluorophores is excited as a whole specimen by a parallel beam of light combined with a filter set, allowing for specific fluorophore excitation. The simplicity of the instrumental set-up, together with the possibility of fast image acquisition when observing the whole sample at once, are of great advantage. However, due to diffraction and the projection of out-of-focus light, spatial resolution and contrast are often limited and the technique is only suited for thin specimen.[42] A possibility to improve the resolution of fluorescence microscopy came with the development of confocal laser scanning microscopy (CLSM). By using laser scanning excitation, the light is not directed to the whole specimen but to single points in the sample, and images are created by scanning the specimen point by point and subsequent computational reconstruction.[43] As in the wide-field method, the confocal set-up includes a dichroic mirror that directs the exciting light of a specific wavelength to the sample and the emitted light from the sample to a photomultiplier detector. However, by installing a pinhole between the mirror and the detector, the emitted light is bundled and out-of-focus light is widely excluded.[44] It is possible to detect specific layers within a thicker specimen in high resolution in a live-cell imaging approach. By shifting the focus level in z-direction and taking images of different layers, the single images can be combined afterwards to 3-dimensional structures. In extension of the single pinhole in CLSM, the spinning-disk confocal microscopy, often also referred to as Nipkow systems, was developed. Here, multiple pinholes are installed on a fast spinning disk, scanning multiple points within the specimen simultaneously and instead of a photomultiplier, a charge-coupled device (CCD) camera serves as a detector.[45] This method is especially valuable in the observation of dynamic processes such as fluorescence resonance energy transfer (FRET) between two different fluorophores, fluorescence recovery after photobleaching (FRAP) and fluorescence lifetime imaging (FLIM). While FRAP is used to measure molecular dynamics within cells and cell surfaces, FLIM provides information from an ensemble of fluorophores about their local environment.[46] Despite all that progress, fluorescence-based imaging techniques were for a long time limited to the resolution borders Ernst Abbe stated already in 1873. According to his law, lateral resolution is limited to roughly half the wavelength of the illumination light.[47] Just recently, novel techniques in super-resolution microscopy have succeeded to overcome these limitations. The long-known resolution limit of about 200 nm could be decreased to about 10 nm, thus resolving structures on a subcellular level.[48] Different methods belong to this sophisticated class of imaging that can be

broadly divided into those patterning the illumination light and those detecting and localizing single molecules. Structured illumination microscopy (SIM) and stimulated emission depletion microscopy (STED) belong to the former category, stochastic optical reconstruction microscopy (STORM) and photoactivation localization microscopy (PALM) belongs to the latter.[49] The structured illumination microscopy is taking advantage of an effect known as the moiré effect. If two patterns are superposed, a specific beat pattern, the moiré fringes, will appear in their product. In case of SIM, one pattern is the unknown structure of the fluorescent signal that is supposed to be resolved, and the other pattern is the structured illumination. By the known illumination pattern and detecting the resulting moiré fringes, conclusions about the unknown pattern are possible (**Figure 1.4**).[50] Advantages of the technique are the requirement of relatively low illumination power and the easy accessibility of multicolor imaging.[51]

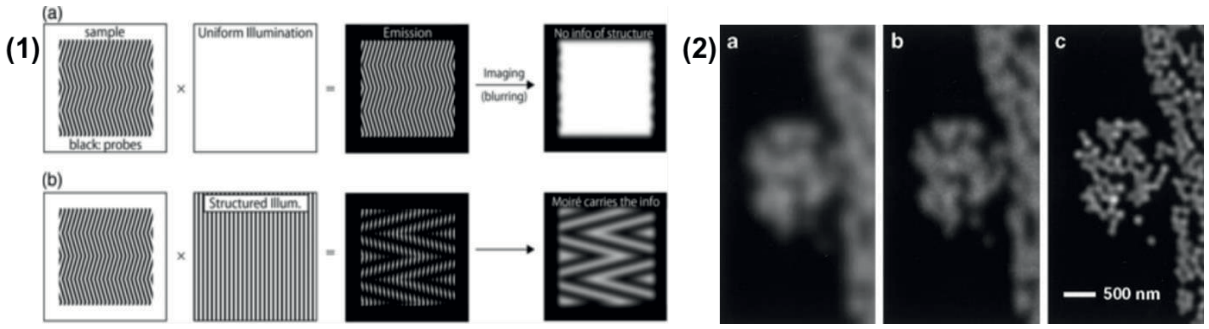

Figure 1.4: (1) Comparison of the image formation in a) conventional wide-field and b) structured illumination microscopy, producing moiré fringes.[iv] **(2)** Fluorescent microspheres, imaged a) as conventional wide-field, b) confocal and c) structured illumination microscopy.[v]

In 1994, Stefan Hell first proposed the principle of STED microscopy before he received the Nobel prize for his discovery in 2014.[52] As in confocal microscopy, the sample is illuminated by a point laser. However, besides the confocal laser that excites the fluorophores in the illuminated spot, a second, antagonistic STED laser is employed for specific de-excitation of every fluorescent signal except in the very center of the laser beam by stimulated emission at the long wavelength end of the spontaneous emission spectrum.[53] Since the STED system is very similar to confocal microscopy in the basic set-up, it exhibits several of the advantages present in confocal microscopy, such as the possibility of optical sectioning of thicker samples and the broad applicability for various organic dyes and fluorescent proteins. Furthermore, high imaging rates are achievable and, by tuning the STED laser, the tuning of resolution is possible.[54] In contrast to STED, the single molecule localization microscopy (SMLM) methods STORM and PALM are not relying on confocal microscopy as the technical basis of illumination but are similar to total internal reflection fluorescence (TIRF) microscopy in their set-up.[55] Here, the illumination is based on an evanescent field

[iv] Reprinted from: Yamanaka, Masahito; Smith, Nicholas I., Introduction to super-resolution microscopy, Microscopy, 2014, pp. 177-192, by permission of Oxford University press

[v] Reprinted with permission from M.G.L. Gustaffson, Surpassing the lateral resolution limit by a factor of two using structured illumination microscopy, Journal of Microscopy, 2000, Vol. 198, Pt 2, pp. 82-87.

produced by total internal reflection of light on a cover glass/substrate interface. Deeper tissue penetration and therefore out-of-plane light is avoided.[56] Both techniques are based on switching fluorescent molecules on and off, detecting the single distant signals, taking thousands of pictures and afterwards recombining them to a whole image. While PALM is applying fluorophores with direct control of their emitting stage such as fluorescent proteins, STORM is based on stochastically switching organic dyes by adapting buffer and illumination conditions.[57] In comparison to STED, SMLM techniques achieve a higher spatial resolution but require longer acquisition times.[58]

All the described methods, conventional as well as super resolution techniques, rely on the principle of exciting and detecting one fluorophore with one photon at a time. They are ideally suited to provide sophisticated images from a comparatively thin specimen. However, in the field of *in vivo* imaging, another advancement is of great significance: the development of 2-photon or multiphoton microscopy. In contrast to the before mentioned techniques, this method relies on the simultaneous absorption of two photons of a long wavelength in one fluorophore caused by the high photon density in a pulsed laser beam.[59] Typically, an excitation wavelength in the near infrared (NIR) range of about 700-1100 nm is applied, providing deep tissue penetration while causing minimum tissue damage.[60] Remarkably, the wavelength of the emitted photon is shorter. The simultaneous absorption of two (or more) red/NIR photons under addition of their energy can cause the emission of a green wavelength photon thus providing a great opportunity in imaging living animals with broad applications in biological and medical research as well as in the various stages of drug development.[61-64]

1.3 Fluorescence and related energy transfer mechanisms

The phenomenon of fluorescence was first described by Sir Frederik William Herschel in 1845, when he stated an “extremely vivid and beautiful celestial blue color” in a quinine solution in sunlight, an effect that could not be explained with the knowledge of that time.[65] The general effect of light emission after absorption of a photon, called luminescence, can be divided into the two categories fluorescence and phosphorescence and is explained in the Jablonski diagram (**Figure 1.5**).[66] When a (typically) aromatic molecule absorbs a photon, an electron is excited from the S_0 singlet ground state to the first or second excited singlet state (S_1 or S_2). For every singlet state there are several vibrational states (0, 1, 2, 3 etc.). Electrons are usually excited to a higher vibrational state and relax very fast (typically 10^{-12} s or less) via vibrational relaxation (VR) and internal conversion (IC) to the lowest vibrational state of the S_1 level. The electron in the excited state orbital is paired to an electron in the ground-state orbital by opposite spin and therefore return to the ground state by emission of a photon (called fluorescence) is a spin-allowed process and occurs rapidly. The average fluorescence lifetime is in the range of 10 ns. Since the return to the ground state usually occurs to a higher vibrational level with subsequent relaxation

to the lowest level, emission spectra show a vibrational structure similar to absorption spectra. Alternatively, electrons in the first excited state can migrate to an excited triplet state (T_1) under spin conversion via intersystem crossing (ISC). In the T_1 state, electron spins have the same orientation as in the ground state and transition from there to the ground state via photon emission (called phosphorescence) is a spin-forbidden process. The emission rates are slow and the average phosphorescence lifetime is with milliseconds to seconds several magnitudes higher than the one of fluorescence. Due to many potential deactivation processes like non-radiative decay and quenching, phosphorescence occurs less frequently than fluorescence.[67,68] Quenching processes such as collisional quenching, do not only influence the frequency of phosphorescence occurrence but also the occurrence and intensity of fluorescence. Molecules with electrons in excited states can interact with other molecules in solution in various electron exchange interactions and form non-fluorescent complexes with quenchers.[69,70] Besides these non-fluorescent interactions, two fluorescent molecules can interact in a resonance energy transfer (RET), if the emission spectrum of a donor molecule overlaps with the absorption spectrum of an acceptor molecule. This spectral overlap is described as the Förster distance. Since the efficiency of these interactions is depending on the Förster distance and the distance between the donor and acceptor molecule, the measurement of energy transfer efficiency between a known donor-acceptor pair is widely used to measure distances of molecules, for example in biological macromolecules.[71,72]

The emission of a photon via fluorescence (or phosphorescence) inhibits lower energy than the absorption and it is usually related to longer wavelengths, a phenomenon discovered by Stokes in 1852. Hence, the difference in wavelengths between absorption and emission is called the Stokes Shift, one of the most important characteristics of fluorescent molecules.[73] Other important factors in the description of fluorescent molecules are the quantum yield, described as the rate between absorbed and emitted photons and a measure of fluorescence brightness, and the fluorescence lifetime, described as the time frame in which the electrons in excited states relax to the ground state.

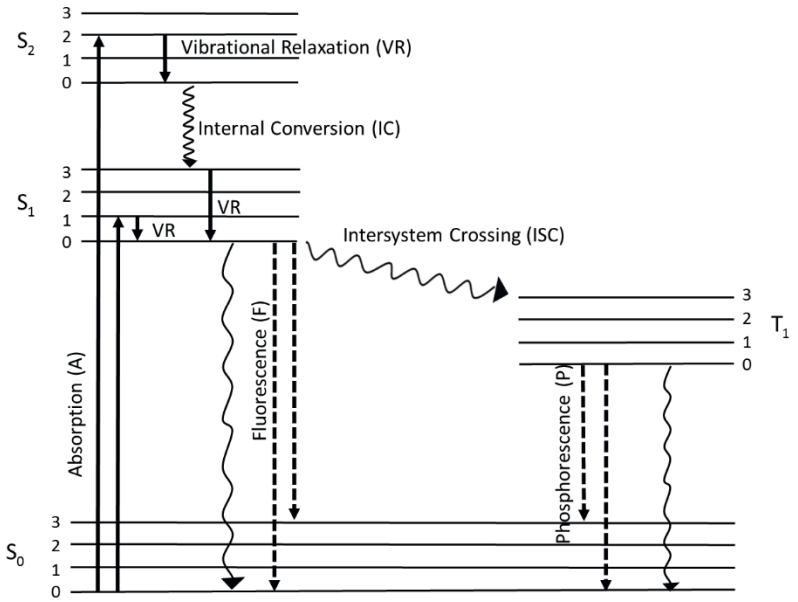

Figure 1.5: One form of a Jablonski diagram, depicting the processes of electron excitation by absorption (A) of a photon and relaxation into ground state by various processes, including vibrational relaxation (VR), internal conversion (IC), intersystem crossing (ISC), fluorescence (F) and phosphorescence (P).

1.4 Fluorophore classes

In general, fluorescent molecules can be divided into the categories of intrinsic or extrinsic fluorophores. While intrinsic fluorescence occurs naturally, extrinsic fluorescence is caused by the addition of a fluorescent molecule to a sample.[67] Important representatives of intrinsic fluorophores are the aromatic amino acids tryptophan[74], tyrosine[75], and phenylalanine[76], the fluorescent enzyme cofactors nicotinamide adenine dinucleotide (NADH)[77], pyridoxyl phosphate[78], riboflavin, flavin mononucleotide (FMN), and flavin adenine dinucleotide (FAD)[79-81] or chlorophyll.[82,83] Since these naturally occurring fluorescent molecules are absorbing and emitting mostly in the UV to blue light range and therefore are limited in their potential application in imaging, the synthesis of small molecule dyes is crucial to cover the area of higher absorption/emission wavelengths. Representatives of the various existing fluorophore classes are depicted in **Figure 1.6** with the archetypic quinine fluorophore indicated as number **1**. Starting in the range of UV-excited fluorophores, polycyclic aromatic compounds such as naphthalene, pyrene or anthracene derivatives are popular fluorophores and widely used scaffolds of commercially available dyes (i.e., “Lucifer yellow”, numbers **8** and **9**).[84-87] Their spectral properties are depending on the size of the aromatic system, as well as on electron density influencing substitutions. Besides this class, in many natural products and pharmaceuticals, the coumarin motif is a central building block and, upon substitution, exhibits fluorescence with a large

Stokes shift in the UV-range (i.e., 4-methylumbelliferone (4-MU), , number **10**). A facile synthesis route, usually a Pechmann condensation from a phenol and a β-carbonyl ester, as well as flexible chemistry belong to the benefits of this still developing fluorophore class.[88] Indole and imidazole compounds, such as DAPI (number **12**) or Hoechst 33342 (number **13**) are widely used as DNA- intercalating dyes.[89,90] In the green to yellow wavelength range, fluorescein (number **17**) is one of the oldest fluorophore scaffolds (first synthesized by Baeyer in 1871) and until today, a widely used and extremely versatile dye.[91] It can be prepared from phthalic anhydride and resorcinol in the presence of zinc chloride and exists in two different forms: a closed, non-fluorescent lactone and an open, fluorescent quinoid form.[92]

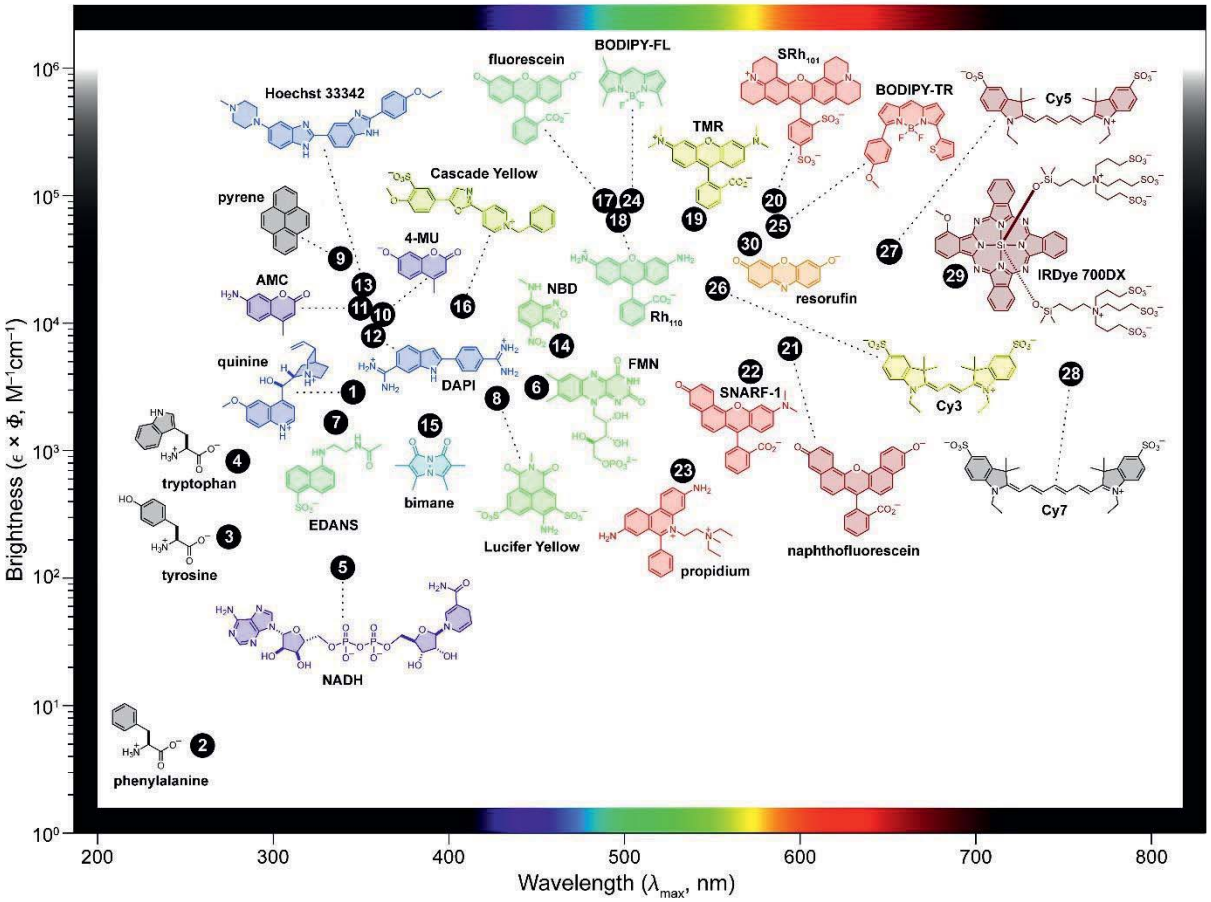

Figure 1.6: Common fluorophore classes plotted as brightness against maximum absorption wavelength. Reprinted with permission from Lavis et al.[93] Copyright © 2008, American Chemical Society.

Since the closed form can be locked by substituting the phenolic oxygens, which efficiently masks the fluorescein fluorescence, this equilibrium has been used to create photo- or enzyme-sensitive switchable dyes.[94,95] Additionally, fluorescein shows a fluorescence sensitivity towards surrounding pH values and therefore has been employed in the development of intracellular pH sensors.[96,97] An alteration and red-shift of the emission wavelength range of fluoresceins can be achieved by condensations of further phenyl units in Friedel-Crafts type reactions and results in naphthofluorescein or seminaphthofluorescein derivatives (number **22** and **21**).

Another popular representative in the same excitation range as fluorescein is its amino analogue rhodamine (number **18**). Almost as old as fluorescein (patented in 1887), rhodamine displays many properties similar to fluorescein.[98] Substitutions of the phenyl nitrogens lock rhodamine in a non-fluorescent lactone form and make it an excellent profluorescent compound.[99] However, rhodamine shows a higher photostability, lower pH sensitivity and tunable spectral properties, enabling a bathochromic shift.[100] The first synthesis relied on the acid-catalyzed condensation of an aminophenol with a benzaldehyde, followed by an oxidation with iron(III) chloride. A more common route uses a condensation of phthalic anhydride and 3-aminophenol, or alternatively, rhodamines are generated directly from fluoresceins triflates using a Buchwald-Hartwig cross coupling.[88] Due to the similar excitation and emission wavelengths, and therefore efficient energy transfer properties, fluorescein and rhodamine labels are an extensively used dye pair in RET experiments.[101,102] Also very similar in the spectral properties to fluorescein and rhodamine in its unsubstituted form is the boron-dipyrromethene (BODIPY) scaffold (number **24**). With its insensitivity to environmental influences, small Stokes shift, neutral charge and overall lipophilicity it displays often superior properties for fluorescent labeling approaches compared to fluorescein or rhodamine.[103] The original synthesis was performed as a condensation of 2-formyl-3,5-dimethylpyrrole and 3,5-dimethylpyrrole followed by treatment with boron trifluoride.[88] More shifted to the red wavelength area and up to the NIR range, the highly tunable class of cyanine dyes is located. These dyes are characterized by a polymethine chain between two nitrogens, resembling the retinaldimine visual pigment of rhodopsin. Their most common representatives are the CyDye fluorophores, based on a sulfoindocyanine structure and defined by the number of carbon atoms between the dihydroindole units (Cy3, Cy5 and Cy7, numbers **26**, **27** and **28**).[93]

Extrinsic fluorophores find application in the labeling of various biologically active molecules such as proteins and nucleic acids, small molecule drugs, as well as in the labeling of macromolecular drug carrier systems (**Figure 1.7**).

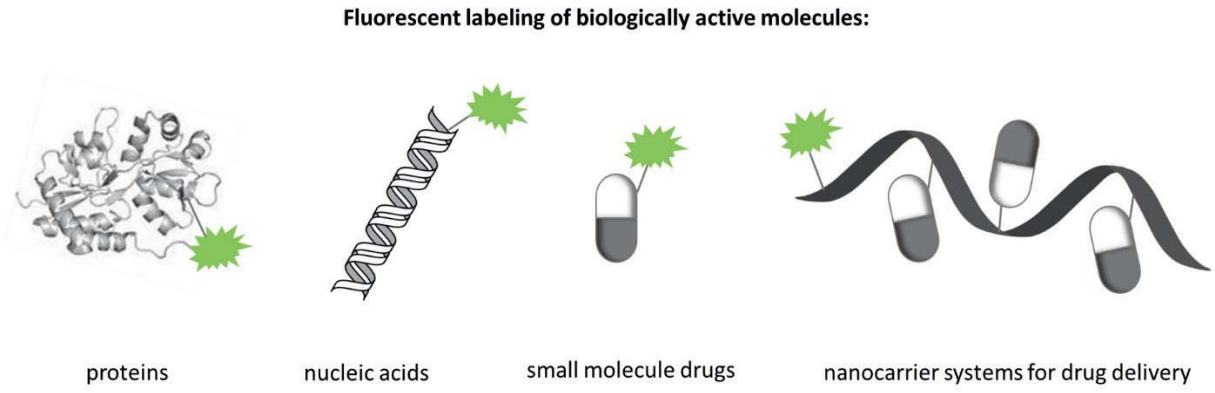

Figure 1.7: Fluorescent labeling of biologically active molecules.

Results

2 Fluorescent labeling of proteins

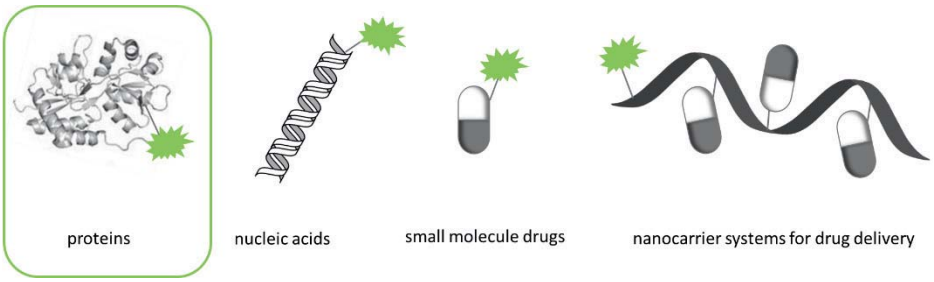

Over the last two decades, optical imaging and fluorescence-based techniques have gained increasing significance in the lengthy and expensive process of drug discovery and development, replacing more and more the classic radio-label methods.[104] Major advantages of this approach include a high spatiotemporal resolution and detection levels close to the single molecule level that enable the investigation of receptor targets at a single-cell stage without perturbing the investigated biological system.[105-107] Being a versatile tool, fluorescence based and other molecular imaging techniques find application in every step of the 5-phase drug development process: Target identification and validation, lead finding and optimization, compound profiling in animal disease models, safety evaluation, and eventually clinical evaluation.[108] In the identification and validation of a promising new target, one method is the *in vivo* imaging of transgenic animals using fluorescent dyes.[109-112] Furthermore, specific drug-target interactions at a subcellular resolution in the validation process can be visualized and measured by advanced multiphoton fluorescence anisotropy microscopy live cell imaging.[113] Once a valid drug target is identified, the finding of a lead structure for a potential drug and its optimization is the next step. High-throughput screenings (HTS) in biochemical and two- or even three-dimensional cellular assays provide crucial information such as cell permeability and cytotoxicity of the tested compounds, and also detect subpopulations resistant to or sensitive to the drug treatment.[114] After successful screenings, the optimized lead structure is usually transferred from the *in vitro* cell culture based assays to *in vivo* or *ex vivo* animal studies and disease models to generate information on drug efficacy, absorption, distribution, and metabolism.[115] Multiphoton microscopy and fluorescent dyes in the far-red or near-infrared region allow the detection of fluorescently labeled compounds even in deeper tissue layers.[116-120] During the later phases of the drug development process the use of imaging techniques is less common; nevertheless, there are examples of *in vivo* and *ex vivo* animal imaging during safety evaluation and *in vivo* imaging in clinical studies.[108] Depending on the disease, imaging can be beneficial by increasing the diagnostic capacity and allowing for shorter studies with fewer patients, thus resulting in a faster time-to-market and remarkable financial savings.[121]

Especially during the phase of compound profiling in animal disease models, synthetic small molecule fluorescent dyes are of tremendous significance since they allow for the specific labeling of early stage drug candidates and direct observation of their behavior on a cellular level or in a complete organism system. While there are other

forms of fluorescent labeling available, including the widely used fluorescent proteins[122-124], quantum dots[125,126] or lanthanide ions[127,128], small molecule fluorescent dyes are still state of the art for many imaging applications. Being small in size and therefore less likely to disturb the observed system, the simplicity in the introduction of modifications to adapt to a specific experimental setting and bioorthogonal properties are great advantages.[129] Common classes of small molecule fluorescent dyes employ polycyclic aromatics, fluorescein, rhodamine, quinoline, cyanine, and boron dipyrromethene (BODIPY) backbones. Favorable photophysical properties like a high photostability, sharp absorption and emission spectra, and high quantum yields combined with a neutral charge and insensitivity to the polarity and pH of their environment make the fluorescent dyes of the BODIPY family popular tools in drug discovery and biomedical imaging.[130,131] First described by Treibs and Kreuzer in 1968, BODIPY dyes were investigated as laser dyes from the early 1990s on.[132-137] A rapidly-growing number of publications in recent years illustrates the impact of this fluorophore class on modern applications in imaging or in photodynamic therapy.[138] While the absorption and emission wavelengths of the BODIPY core are around 490 and 505 nm, these dyes can be tuned relatively easy by various substitutions to absorption maxima of 650-900 nm, thereby creating near-infrared (NIR) dyes.[139-143] This wavelength range is particularly preferred in *in vivo* applications, providing not only deeper tissue penetration but also minimal photo-damage to the surrounding tissue, as well as minimal auto-absorption and auto-fluorescence, resulting in low background noise and high signal-to-noise ratios.[140] However, the distribution and localization of the fluorophores in biological samples is often problematic. Their high lipophilicity enables them to easily penetrate membranes but also causes an accumulation in organelle membranes such as the endoplasmic reticulum (ER), lysosomes, mitochondria, and Golgi apparatus, thus altering the observed localization of a fluorescence-tagged bioactive molecule or drug and creating background through unspecific staining.[144] Only few examples of BODIPY dyes that are soluble in water or biological media have been reported so far and most of them focus on the substitution of the BODIPY core with phosphonate[145], sulfonate[146,147], or oligo ethylene glycol groups.[148,149] These dyes show high hydrophilicity and good photophysical properties, but bearing charged phosphonate or sulfonate moieties alters their membrane permeability. Substitution with oligo ethylene glycol chains results in a tremendous increase of molecular weight and often exceeds the size of the unsubstituted parent compound many times over. Therefore, the current need for a small, uncharged, and water-soluble BODIPY dye with potential for further modifications is still unmet.

The aim of this project was to synthesize a water-soluble boron dipyrromethene (BODIPY) dye that is functionalized for potential drug- or drug-linker couplings. A synthetic methodology developed in the group of Prof. Dr. Ralph Mazitschek (Massachusetts General Hospital, Boston, MA) was applied in order to achieve this goal.[vi] Previous work conducted in this group has shown that one of the two fluorines contained in the canonical BF_2-dipyrromethene core present in this fluorophore class

[vi] All work described in this chapter was performed in the group and under supervision of Prof. Dr. Ralph Mazitschek at Massachusetts General Hospital (MGH) in Boston, MA.

can be selectively activated by trimethylsilyl trifluoromethanesulfonate (TMSOTf) (**Scheme 2.1**). A subsequent exchange with ^{18}F not only allows for fluorescence detection of the probe but also for its use as a hybrid optical and Positron Emission Tomography (PET) reporter. [150]

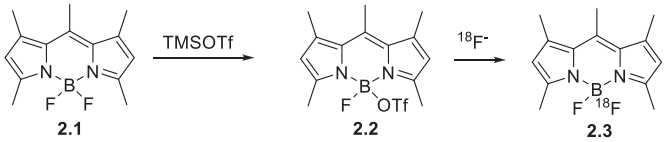

Scheme 2.1: Trimethylsilyl trifluoromethanesulfonate activated selective ^{18}F exchange on the BF_2-dipyrromethene core (adapted from Hendricks et al. 2012[150]).

Further investigations of the TMSOTf activation showed that this convenient one pot-two step synthesis approach can be used to also selectively exchange one of the core fluorides with an alcohol in order to generate core monoalkoxy (CMA) BODIPYs with improved physicochemical properties (**Scheme 2.2**).[151] Due to the lipophilic and poor water soluble properties of the unsubstituted BODIPY core **2.1**, these dyes are often incorporated in lipophilic cell compartments such as ER and Golgi membranes when used in imaging applications, resulting in strong unspecific background staining.[139,152,153]

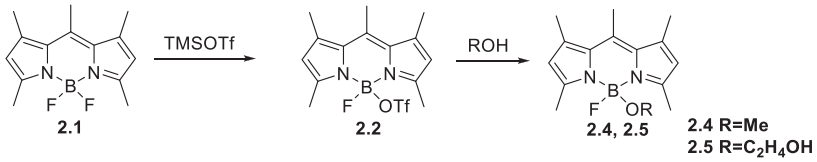

Scheme 2.2: Trimethylsilyl trifluoromethanesulfonate activated selective alcohol exchange on the BF_2-dipyrromethene core (adapted from Courtis et al. 2014[151]).

Introduction of a core alkoxy group increases water-solubility of the dye without the cost of increased molecule size or charged moieties that could influence membrane interactions, as it is widely prevalent in common methods of enhancing hydrophilicity such as introduction of oligo ethylene glycol, sulfonate, or phosphonate groups.[145,154] Additionally, the alkoxy group is expected to interrupt the planarity of the BODIPY core and thus reduce the π-π stacking of the fluorophore in membranes. Next, the Mazitschek group developed a method using molecular sieves to catalyze the exchange of the core alkoxy group with a second hydroxyl functionalized small molecule under mild conditions, taking advantage of the fast kinetics in the exchange of the monomethoxy BODIPY **2.4** with a hydroxyl group compared to the unsubstituted pentamethyl BODIPY scaffold **2.1**.[155] This second exchange would allow for the introduction of a broad variety of hydroxyl-functionalized small molecules such as drugs or drug-linker constructs for their fluorescent labeling. Furthermore, previous

studies for this purpose[vii] have shown that the introduction of 3-hydroxyoxetane in the second exchange step displays favorable physico-chemical properties.[155] Accordingly, the synthesis of an asymmetrically substituted BODIPY dye containing an oxetane alkoxy group as well as a moiety with an open functional group for various coupling approaches was designed, using the previously-developed methodology as the next step towards a small, uncharged, water-soluble, versatile tool for cellular imaging.

2.1 Strategy in the chemical synthesis

The synthetic strategy was developed using the commercially available 1,3,5,7,8-pentamethyl BODIPY **2.1** as a starting point (**Scheme 2.3**). The previously-established TMSOTf activation enables the substitution of one of the core fluorines with methanol to generate the monomethoxy BODIPY **2.4**. This precursor displays faster kinetics in the second reaction step compared to the parent difluoro-BODIPY **2.1**. In an alkoxy exchange and a subsequent second fluorine/alkoxy exchange the methoxy group as well as the second core fluorine are substituted symmetrically with 1-Fmoc-3-hydroxyazetidine **2.6**. In a consecutive boronic acid transesterification one of the Fmoc-protected azetidine substituents is replaced by 3-hydroxyoxetane **2.7** to provide ideal physico-chemical properties. Deprotection of the azetidine **2.8** finally creates a free secondary amine as a versatile functional group for the coupling of small molecules.

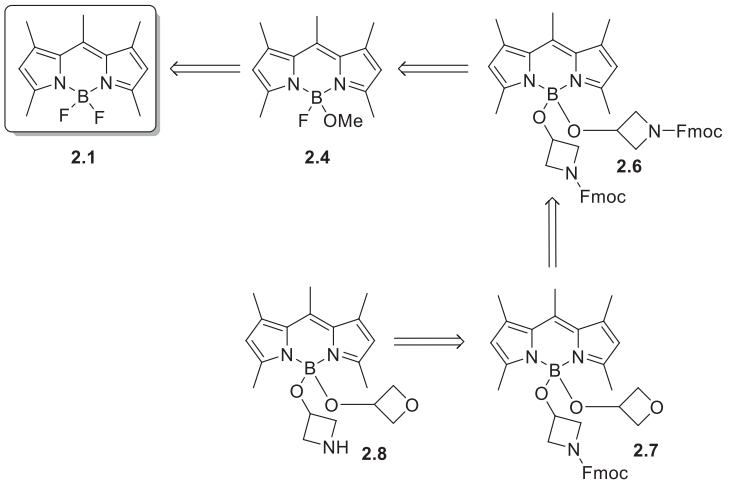

Scheme 2.3: Retrosynthetic strategy in the synthesis of an asymmetrically substituted functionalized alkoxy BODIPY.

[vii] Conducted by Dr. S. Santos, Mazitschek group, Massachusetts General Hospital (MGH) in Boston, MA

2.1.1 Synthesis of an Oxetane-azetidine BODIPY

The first step in the synthesis of the desired asymmetrically-substituted oxetane-azetidine BODIPY **2.8** was the formation of the monomethoxy BODIPY **2.4** via a previously established TMSOTf activation.[151] Since the BODIPY-OTf intermediate **2.2** was not stable at temperatures above 0 °C nor stable for prolonged times under the required reaction conditions, the reaction is performed on an ice bath and under dry conditions with close follow-up of reaction kinetics via LC/MS. The addition of TMSOTf to the parent difluoro-BODIPY **2.1** was followed quickly by the addition of methanol (MeOH) as a suitable alcohol in the fluorine/alkoxy exchange and simultaneous addition of *N,N*-diisopropylethylamine (DIPEA, Hünig's base) (**Scheme 2.4**). As a mild and non-nucleophilic base, DIPEA buffers the acidity of the basic reaction without acting as a competitor with the MeOH in the nucleophilic substitution. Following this procedure BODIPY **2.4** could be generated in a moderate yield of 46%.

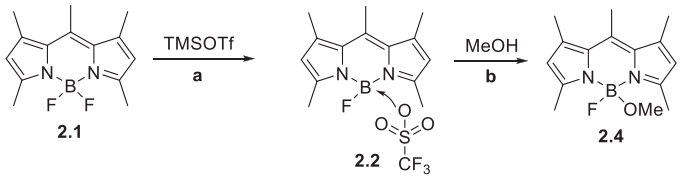

Scheme 2.4: Synthesis of monomethoxy BODIPY. a) DCM, TMSOTf, TCM, 0 °C, 2.5 min. b) MeOH, DIPEA, 0 °C, 60 min.

In the second step of the synthesis strategy both the methoxy and the fluorine group of **2.4** on the central boron atom were substituted with 1-Fmoc-3-hydroxyazetidine moieties in a previously-developed procedure. In previous studies, using the monomethoxy BODIPY as a precursor instead of direct substitution of both fluorine atoms in compound **2.1** showed faster kinetics. The reaction of **2.4** and a slight excess of 1-Fmoc-3-hydroxyazetidine in toluene when heated overnight at 60 °C, resulted in the formation of bis-Fmoc-azetidine BODIPY **2.6** in good yields of up to 80% (**Scheme 2.5**). Adding 5A molecular sieves (50 mg/mg fluorophore) to catalyze the alkoxy exchange reaction was found to be crucial since the sieves will trap the forming methanol and push the reaction equilibrium towards the azetidine substitution.

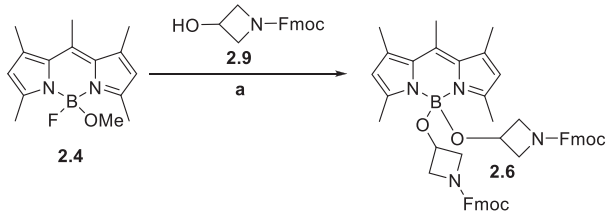

Scheme 2.5: Synthesis of bis-Fmoc-azetidine BODIPY. a) Molecular sieves 5A, Toluene, 60 °C, o.n.

While the formation to the bissubstituted azetidine product was completed after 14-16 hours, the optimal time frame for a monosubstitution was found to be 2 hours. Interestingly, these findings cannot be directly transferred to the next reaction step, namely the boronic acid transesterification with 3-Hydroxyoxetane (**Scheme 2.6**). In previous work the reaction showed comparatively fast kinetics favoring the bissubstituted oxetane BODIPY **2.11** with only 8% yield of the monosubstituted oxetane **2.7** after 1 h reaction time and a full conversion to the bissubstituted side product **2.11** after 8 h at 60 °C.[155] Therefore, the optimization of this reaction was a key step in further synthesis.

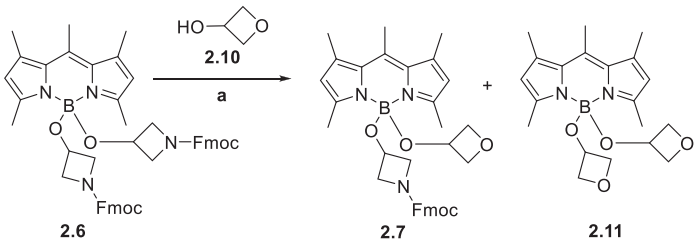

Scheme 2.6: Boronic acid transesterification with 3-Hydroxyoxetane. a) Molecular Sieves 5A, Toluene, 60°C, 1-8 h.

A close follow-up of the reaction via liquid chromatography/mass spectrometry (LC/MS) showed a maximum of the desired mono-product after 30 min reaction at 50 °C with a reduced amount of 3-hydroxyoxetane compared to previous studies. Hence, in the first optimization step the amount of alcohol used was optimized (**Table 2.1**).

Entry	Alcohol 2.10 (equiv.)	Solvent	Temp. [°C]	Time [min]	2.7	2.11	2.6
1	2.5	Toluene	50	30	15%	-	63%
2	3.5	Toluene	50	30	20%	-	64%
3	4.5	Toluene	50	30	27%	-	20%
4	5.5	Toluene	50	30	28%	7%	23%
5	6.5	Toluene	50	30	28%	10%	12%
6	7.5	Toluene	50	30	26%	12%	9%
7	10.0	Toluene	50	30	19%	18%	6%
8	12.5	Toluene	50	30	14%	19%	6%
9	15.0	Toluene	50	30	13%	20%	6%

Table 2.1: First optimization step of the boronic acid transesterification. Structures of molecules **2.6**, **2.7**, **2.10**, **2.11** given in **Scheme 2.6**.

Screening of different quantities of 3-oxetanol under the same reaction conditions showed the highest ratio of the desired product **2.7** compared to side product **2.11** while consuming most of the starting material **2.6** when adding 6.5 equivalents of alcohol (**Table 2.2**, entry 5). Subsequently, optimization of temperature and time conditions for the given amount of alcohol resulted in an overnight reaction time of 16h at room temperature as the best results (**Table 2.2**, entry 7).

Entry	Alcohol 2.10 (equiv.)	Solvent	Temp. [°C]	Time [min]	2.7	2.11	2.6
1	6.5	Toluene	50	30	28%	10%	12%
2	6.5	Toluene	90	12	24%	7%	13%
3	6.5	Toluene	90	20	23%	4%	14%
4	6.5	Toluene	90	30	19%	-	15%
5	6.5	Toluene	rt	30	17%	13%	32%
6	6.5	Toluene	rt	75	25%	16%	13%
7	6.5	Toluene	rt	16h	32%	9%	15%

Table 2.2: Second optimization step of the boronic acid transesterification. Structures of molecules **2.6**, **2.7**, **2.10**, **2.11** given in **Scheme 2.6**.

Using anhydrous solvent stored over molecular sieves was found to be beneficial, while alternative approaches in the reaction like the slow addition of 3-hydroxyoxetane over

3 h via syringe pump or the start from the bissubstituted oxetane BODIPY **2.11** with subsequent back substitution to the asymmetric product **2.7** with 1-Fmoc-3-hydroxyazetidine did not result in higher yields.

The cleavage of the Fmoc group in order to deprotect the secondary amine and generate a versatile functional group for drug or linker couplings was the next step following the successful synthesis of the asymmetrically substituted Fmoc-azetidine-oxetane BODIPY **2.7** (**Scheme 2.7**).

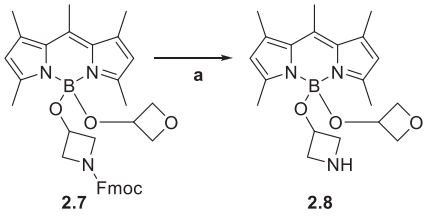

Scheme 2.7: Fmoc deprotection. a) Piperidine 20%, DMF, rt, 2 min.

To identify the most efficient and mild deprotection method, three different reagents were investigated under several conditions as depicted in **Table 2.3**. Among all tested methods, namely different quantities of piperidine in DMF, TBAF in THF[156], and a mild removal method with NaN_3 in DMF[157], only the cleavage using 20% piperidine in DMF showed a complete deprotection of **2.7** by LC/MS while avoiding degradation products (**Table 2.3**, entry 5).

Entry	Reagent	Quantity	Solvent	Temp.	Time [min]
1	TBAF	0.1 M	THF	rt	5
2	NaN_3	1.2 equiv.	DMF	50 °C	60
3	Piperidine	1%	DMF	rt	20
4	Piperidine	10%	DMF	rt	5
5	Piperidine	20%	DMF	rt	2

Table 2.3: Reagents and conditions in the screening of different Fmoc deprotection methods.

However, it was not possible to isolate the desired deprotected product **2.8** due to its poor overall stability. Especially under the influence of increased temperatures, degradation products could be observed within minutes. The free amine in the azetidine and/or residual piperidine molecules seemed to attack the BODIPY core in an unclear (intramolecular) mechanism. To prove this theory the bissubstituted oxetane BODIPY **2.11** was stirred with different quantities of piperidine in DMF at different temperatures and monitored via LC/MS. While the fluorescent compound was

relatively stable when stirred with 20-100% Piperidine over night at room temperature, a fast increase in degradation products could be observed when the temperature was elevated to 50-60 °C. After 4 h at 50 °C with >40% piperidine the BODIPY signal had entirely disappeared. These observations supported the theory of a low stability of our desired asymmetrically-substituted azetidine-oxetane BODIPY **2.8** due to an attack of the free amine. In a subsequent reprotection attempt the Fmoc-azetidine BODIPY was deprotected with 20% piperidine in DMF for 2 min at room temperature (rt), purified via reversed phase column chromatography and directly coupled with *N*-acetoxy-succinimide to generate the acetyl-protected BODIPY **2.13** (**Scheme 2.8**). A shift in retention times (+0.3 min) and the correct corresponding mass by LC/MS indicated the successful reprotection. Yet the product could not be isolated in sufficient purity.

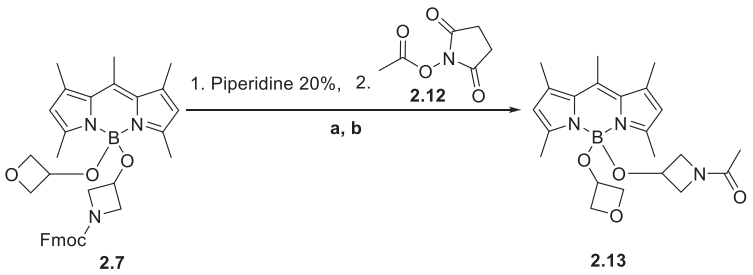

Scheme 2.8: Fmoc deprotection and subsequent reprotection with *N*-acetoxy-succinimide. a) DMF, rt, 2 min b) DMF, rt, on.

Since it was the aim of this project to develop an asymmetrically substituted BODIPY dye as a versatile tool for cellular imaging and the azetidine-oxetane BODIPY **2.8** did not show the required capacity in stability due to its free secondary amine, we developed a new strategy using a carboxylic acid as an alternative functional group.

2.1.2 Synthesis of a 3-hydroxycyclobutanecarboxylic acid substituted BODIPY

Similar to the previous synthesis strategy applied in chapter 2.1.1, we used the commercially available 1,3,5,7,8-pentamethyl BODIPY (**2.1**) as a starting material and converted it into the monomethoxy BODIPY **2.4** to benefit from its faster kinetics in the alkoxy exchange reactions. The monomethoxy BODIPY **2.4** is either converted to the bissubstituted oxetane BODIPY **2.11** and in the following step monosubstituted with 3-hydroxycyclobutanecarboxylic acid to provide the desired carboxylic acid and still retains the oxetane moiety for optimized physico-chemical properties in BODIPY **2.14**, or the methoxy group of **2.4** undergoes a direct substitution with 3-hydroxycyclobutanecarboxylic acid to obtain the monosubstituted cyclobutanecarboxylic acid BODIPY **2.15** (**Scheme 2.9**).

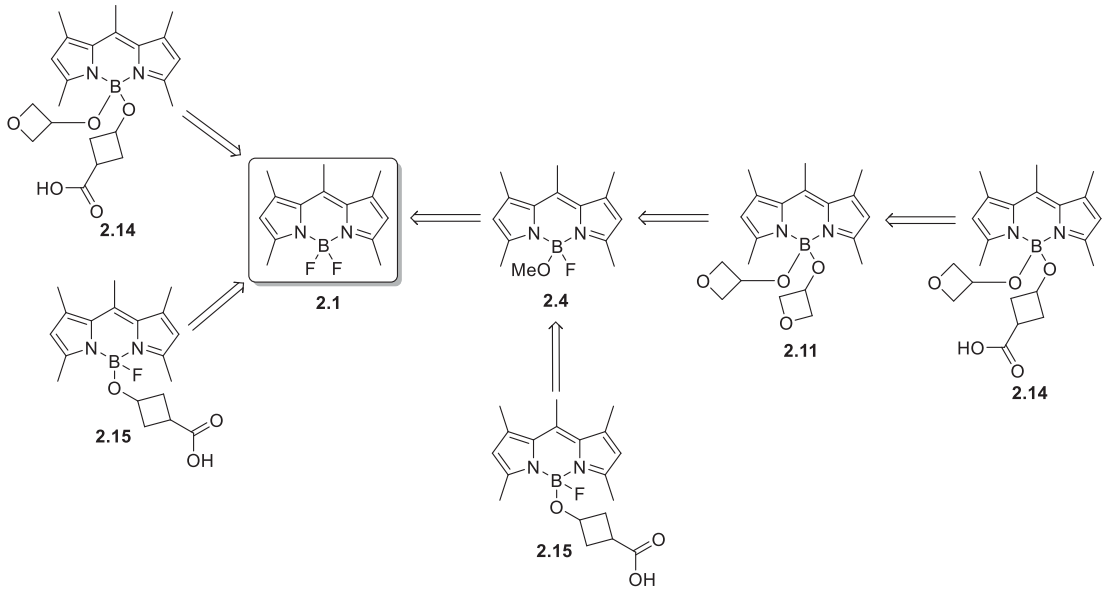

Scheme 2.9: Retrosynthetic strategy in the synthesis of a 3-hydroxycyclobutanecarboxylic acid substituted BODIPY.

In the direct alkoxy exchange of the methoxy group from BODIPY **2.4** with 3-hydroxycyclobutanecarboxylic acid (**Scheme 2.10**) several reaction conditions were screened as listed in **Table 2.4** to obtain the best ratio between the desired product **2.15** and an undesired side product. Since not only the hydroxyl group but also the carboxylic acid group of **2.16** shows some tendency to participate in the alkoxy exchange, the formation of the bridged BODIPY **2.17** could be observed.

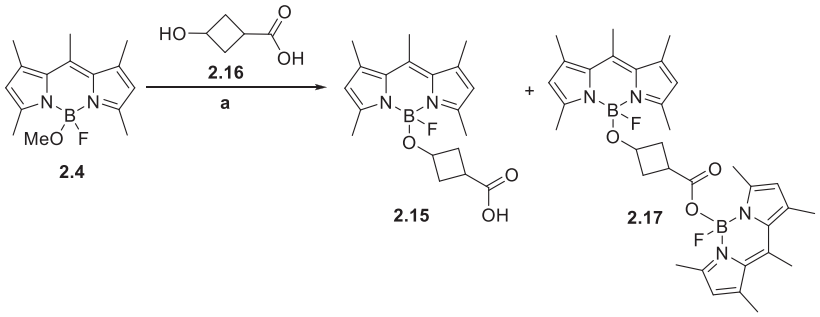

Scheme 2.10: Alkoxy exchange with 3-hydroxycyclobutanehydroxylic acid. a) Toluene, 60 °C, 5 min.

Entry	Alcohol 2.16 (equiv.)	5A MS [mg/mg]	Solvent	Temp. [°C]	Time [min]	2.15	2.17	2.4
1	1.25	50	Toluene	60	15	4%	38%	18%
2	2.5	50	Toluene	rt	60	31%	19%	45%
3	**2.5**	**50**	**Toluene**	**60**	**5**	**62%**	**9%**	**5%**
4	2.5	50	Toluene	60	10	57%	10%	15%
5	2.5	50	Toluene	60	15	53%	10%	-
6	5.0	50	Toluene	rt	60	37%	17%	42%
7	5.0	50	Toluene	60	15	63%	-	28%
8	7.50	50	Toluene	rt	60	39%	19%	38%
9	10.0	50	Toluene	rt	60	42%	15%	39%
10	5.0	-	Toluene	rt	24h	-	-	95%
11	5.0	5	Toluene	rt	3h	6%	5%	76%
12	5.0	5	Toluene	rt	5h	38%	11%	25%
13	5.0	5	Toluene	rt	24h	14%	26%	14%

Table 2.4: Optimization of the alkoxy exchange with 3-hydroxycyclobutanehydroxylic acid. Structures of molecules **2.4**, **2.15**, **2.16** and **2.17** given in **Scheme 2.10**, amount of 5A MS is given in mg/mg fluorophore.

After optimizing the reaction conditions such as the amount of alcohol, the amount of molecular sieves used, temperature, and time, the desired monosubstituted cyclobutanecarboxylic acid BODIPY **2.15** could be generated in a 5 min reaction at 60 °C using 50mg/mg fluorophore 5A MS. After purification the product could be isolated in a moderate yield of 30%.

In the alternative approach to synthesize the asymmetrically substituted BODIPY **2.14**, the first step was the targeted conversion from monomethoxy BODIPY **2.4** to the bissubstituted oxetane BODIPY **2.11** (**Scheme 2.11**).

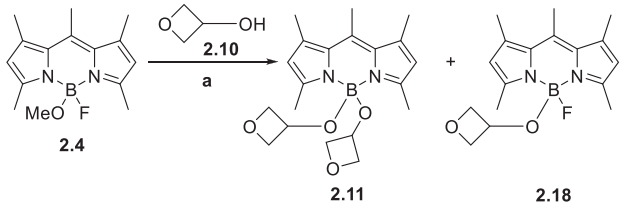

Scheme 2.11: Synthesis of bisoxetane BODIPY. a) Molecular sieves 5A, toluene, rt-80°C, o.n.-7d.

While its formation as a side product in the boronic acid transesterification (**Scheme 2.6**) was found to be comparably fast, the direct conversion from BODIPY **2.4** showed significantly slower kinetics. After 48 h with 5.0 equiv. 3-hydroxyoxetane at room temperature, only 35% product conversion was observed while 56% remained monosubstituted. After the addition of another 2.5 equiv. of alcohol **2.10** and heating of the reaction to 50 °C for additional 96 h, still more than 50% of the monosubstituted side product **2.18** remained monosubstituted. Adding another 5.0 equiv. of 3-hydroxyoxetane and heating of the reaction overnight at 80 °C resulted in full conversion to the bissubstituted product. Subsequent purification allowed for the isolation of the desired product **2.11** in a low yield of 12%.

The transesterification of the 3-hydroxycyclobutanecarboxylic acid to the cyclobutanecarboxylic acid-oxetane BODIPY **2.14** was performed using 2.5 equiv. of 3-hydroxycyclobutanecarboxylic acid **2.16** at room temperature for 24 h (**Scheme 2.12**). The formation of a bridged side product due to the participation of the carboxy group in the reaction was again observed. Unfortunately, the resulting amount of isolated product after purification was too small to determine the yield.

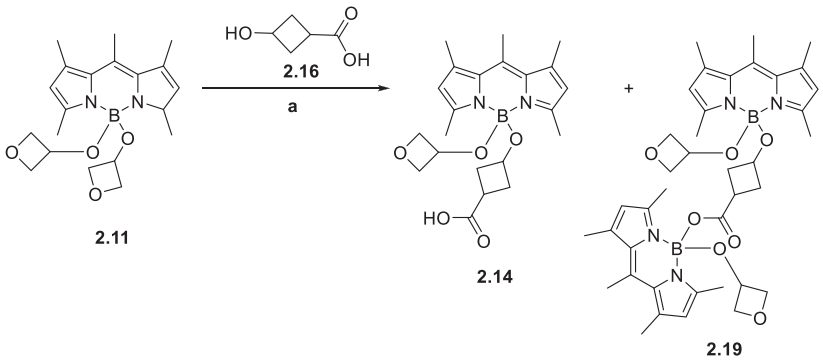

Scheme 2.12: Boronic acid transesterification with 3-hydroxycyclobutanehydroxylic acid. a) Molecular sieves 5A, toluene, rt, 24 h.

Further optimization of the synthesis of BODIPY **2.14** is required. The monosubstituted cyclobutanecarboxylic acid BODIPY **2.15** was further used in a HaloTag protein fusion system for imaging purposes.

2.1.3 Synthesis of a BODIPY dye Halo linker construct

In fluorescent protein labeling, several different techniques are available. Besides the widely-used fusion with fluorescent proteins such as the green fluorescent protein GFP[158,159], modular protein tagging systems like SNAP-tag[160], CLIP-tag[161], and HaloTag[162] have been developed during the last decade. In the HaloTag system, a modified haloalkane dehalogenase bacterial protein, is fused to the protein of interest and binds covalently to a chloroalkane ligand with high specificity and efficiency. This ligand can be synthetically coupled to different target molecules for various purposes such as exogenous fluorophores for imaging and cellular localization or solid support for protein immobilization.[163,164] The cyclobutanecarboxylic acid BODIPY **2.15** is then coupled to the chloroalkane Halo ligand and used in the HaloTag labeling system as an exogenous fluorophore (**Scheme 2.13**).

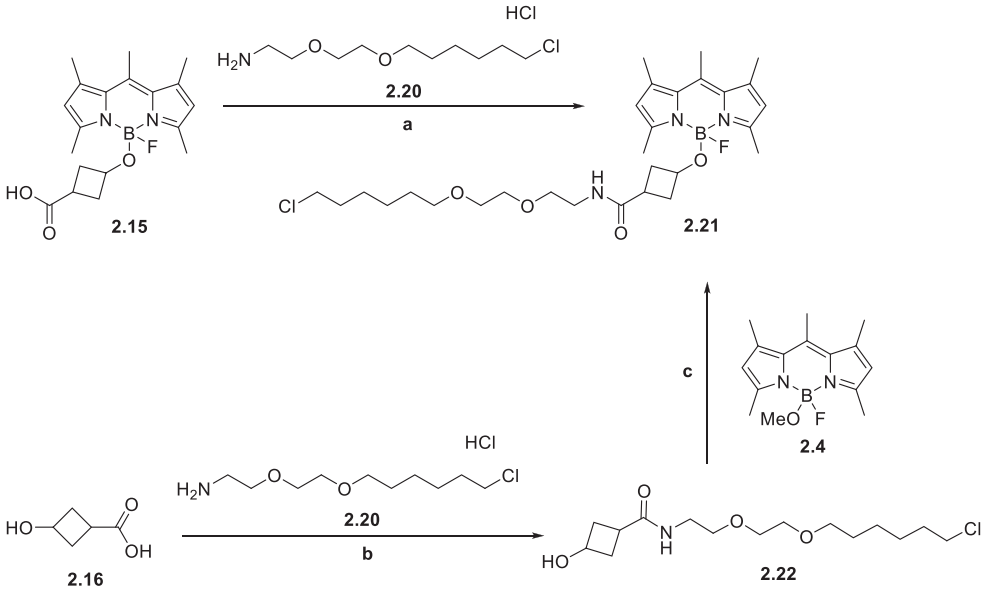

Scheme 2.13: Synthesis of a Halo ligand BODIPY. a) DIPEA, PyBOP, DMF, rt, 10 min, b) DIPEA, PyBOP, DMF, rt, 1 h, c) Molecular sieves 5A, toluene, rt, o.n.

The Halo ligand **2.20**[viii] was either directly bound to the carboxylic acid functional group of **2.15** via standard peptide coupling conditions using PyBOP[165] as a coupling reagent

[viii] Synthesized by Dr. A. Nibbs, Mazitschek group, Massachusetts General Hospital (MGH) in Boston, MA

to generate the Halo ligand BODIPY **2.21**. Alternatively, it was synthesized in a two-step approach, coupling the Halo ligand **2.20** under similar conditions to 3-hydroxycyclobutanecarboxylic acid **2.16** before an alkoxy exchange with monomethoxy BODIPY **2.4** was performed. The previously-described new methodology was applied in this step. While the yield in the favored one-step approach was too small to be determined (>1 mg alkoxy), the Halo ligand BODIPY **2.21** could be isolated after the two-step approach in a satisfying overall yield of 14%.

2.2 Protein labeling of the functionalized alkoxy BODIPY in the Halo/HaloSNAP Tag labeling system

To evaluate the applicability of the cyclobutanecarboxylic acid BODIPY in the Halo Tag labeling system, the Halo-BODIPY ligand **2.21** was incubated with an isolated HaloSNAP protein, and the binding of protein and ligand was verified via polyacrylamide gel electrophoresis (PAGE). In a subsequent extension of this experiment, the Halo-BODIPY ligand was incubated with *E. coli* cells expressing the HaloSNAP protein and fluorescent labeling was observed via fluorescence microscopy.[ix]

2.2.1 Labeling of isolated HaloSNAP fusion protein

The HaloSNAP fusion protein was expressed in BL21(DE3) competent *E. coli* cells and isolated following standard protocols, before being incubated with 0.1 mM of Halo-BODIPY ligand **2.21** and, as a control, with 0.1 mM of a Halo-TAMRA (carboxytetramethylrhodamine) ligand[x]. The successful binding of protein and ligand was evaluated via SDS-PAGE. As an additional control, a competition assay was performed. The isolated protein was incubated first with 0.1 mM of a Halo H3 ac peptide, before Halo-BODIPY ligand **2.21** and Halo-TAMRA ligand were added in the same concentration.

[ix] All biochemical and *in vitro* binding assays performed by Dr. S. Santos, Mazitschek group, Massachusetts General Hospital (MGH) in Boston, MA

[x] Synthesized by Dr. A. Nibbs, Mazitschek group, Massachusetts General Hospital (MGH) in Boston, MA

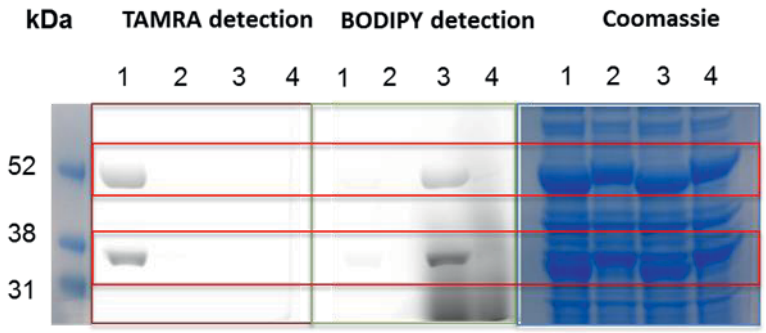

Figure 2.1: SDS-PAGE labeling assay of the isolated HaloSNAP protein with **1)** 0.1 mM Halo-TAMRA ligand, **2)** 0.1 mM Halo H3 ac peptide + 0.1 mM Halo-TAMRA ligand, **3)** 0.1 mM Halo-BODIPY ligand and **4)** 0.1 mM Halo H3 ac peptide + 0.1 mM Halo-BODIPY ligand. The upper red box refers to HaloSNAP fusion protein (55 kDa), the lower red box to Halo Tag (34 kDa). Different detection methods from left to right: TAMRA detection as Cy3- setting and BODIPY detection as Cy2 setting (400 PMT (photomultiplier voltage)) at a Typhoon Phosphorimager, SimplyBlue™ Coomassie staining.

The SDS-PAGE (**Figure 2.1**) shows a successful binding of Halo-BODIPY ligand **2.21** (BODIPY detection, column 3) and Halo-TAMRA ligand (TAMRA detection, column 1) to the protein with detectable bands in the regions of the 34 kDa Halo Tag protein and the 55 kDa HaloSNAP. The Coomassie stain also shows the strongest bands in the observed mass regions in columns 1 and 3, and additionally reveals the expected shift to higher molecular weight related bands for the competition assays in column 2 and 4, that refer to the binding with the Halo H3 ac peptide.

2.2.1.1 In vitro labeling of the HaloSNAP protein

E. coli cells BL21(DE3) expressing HaloSNAP protein were incubated overnight with 10 µM and 100 µM of Halo-BODIPY ligand **2.21** after inducing protein expression with 0.5 mM IPTG. Imaging of the cells via fluorescence microscopy (**Figure 2.2**) shows an efficient labeling at a concentration of 10 µM of Halo-BODIPY ligand **2.21**. Control samples included: induced protein expression without Halo-BODIPY ligand which did not show a fluorescent signal (**a**), and incubation with 10 µM (**b**) or 100 µM (**c**) of **2.21** without induction of protein expression which show a moderate level of fluorescent labeling. A distinct fluorescent signal was observed as a white coloration of the bacteria cells and therefore efficient protein labeling after inducing protein expression and incubating with 10 µM (**d**) or 100 µM (**e**) of Halo-BODIPY ligand **2.21**. The similar level of fluorescence signal in the images **d** and **e** indicates a saturation of protein labeling at a concentration of 10 µM Halo-BODIPY ligand **2.21** or smaller.

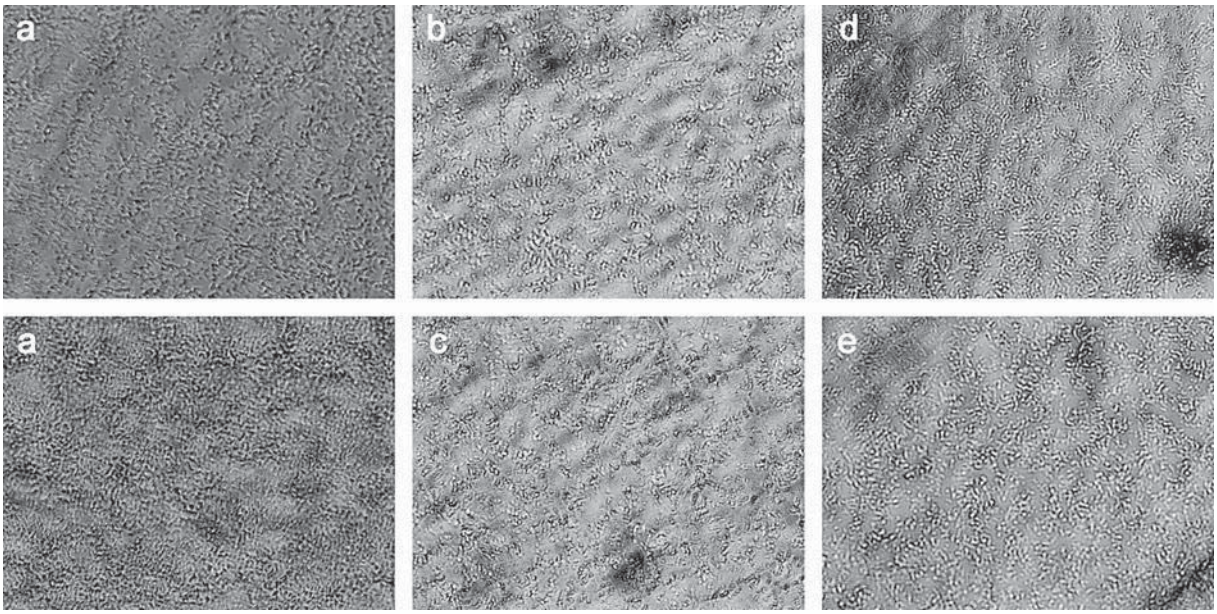

Figure 2.2: *In vitro* labeling of bacteria expressing HaloSNAP protein (strain: pGWHaloSNAP in BL21(DE3)) with Halo-BODIPY ligand **2.21**. Protein expression was induced using 0.5 mM IPTG. **a)** Control: induced protein expression, no treatment with **2.21**, **b)** protein expression not induced, 10 µM **2.21**, **c)** protein expression not induced, 100 µM **2.21**, **d)** induced protein expression, 10 µM **2.21**, **e)** induced protein expression, 100 µM **2.21**. The visualization was performed using a Zeiss Axiovert 100M inverted epifluorescence microscope with a 40x objective.

2.3 Conclusion

Fluorescence imaging is a key player in drug discovery methodologies, finding application in almost all of the steps in the drug development process.[108] Visualization of drug-target interactions, uptake, biodistribution, and metabolization of biologically active compounds is an important asset, especially in target identification and validation as well as during the compound profiling in animal disease models. Small molecule dyes offer a simple and highly tunable way to fluorescently tag a molecule of interest, and among the different classes of dyes, the BODIPY family shows favorable properties.[130,131] Excellent photophysical characteristics, neutral charge, insensitivity to polarity and pH of their environment, and particularly the possibility of creating far-red and near-infrared dyes by relatively simple substitutions are responsible for the popularity of BODIPY dyes in imaging in recent years. However, the high lipophilicity and low water-solubility of these compounds lead to accumulation of the dyes in lipophilic cell compartments such as ER and Golgi apparatus.[144] Efforts to increase the hydrophilicity of BODIPY dyes have been made and focus mainly on the substitution of charged functional groups such as sulfonate or phosphonate moieties or on the incorporation of oligo ethylene glycol chains.[145-149] While the former alters the charge of the molecule and potentially impairs membrane permeability, the latter increases the overall molecule size significantly. Based on the selective activation of one of the fluorine atoms in the canonical BF_2-dipyrromethene core with TMSOTf, a one-pot-two-step synthesis of a core monoalkoxy BODIPY (CMA) with improved water-solubility and, in a next step, a new methodology using molecular sieves to catalyze an exchange of the core alkoxy group with another hydroxyl functionalized small molecule has been developed.[151] In the first alkoxy exchange studies, the introduction of an oxetane alkoxy group was found to result in favorable physico-chemical properties.[155] In this study we present the synthesis of an alkoxy BODIPY dye carrying a carboxy functional group for various drug or linker couplings. In a first attempt, the aim of our synthesis was an asymmetrically-substituted BODIPY with an oxetane alkoxy group for improved solubility and an azetidine alkoxy group with a free secondary amine for drug or linker couplings. Despite various optimization attempts, the desired compound could not be successfully isolated due to its low stability. While the exchange reactions were successful and the dye was stable as the protected Fmoc-azetidine oxetane BODIPY, the free secondary amine after deprotection seemed to attack the core molecule, especially at increased temperatures during the purification process. Since chemical robustness is one of the necessary properties of a versatile labeling dye, we searched for a more stable alternative target molecule. The introduction of a carboxylic acid instead of a free amine as a functional group for couplings was a promising direction to explore. We synthesized in a parallel approach a monosubstituted cyclobutanecarboxylic acid BODIPY and again an asymmetrically substituted cyclobutanecarboxylic acid oxetane BODIPY. The exchange reactions on the route to the asymmetrically-substituted cyclobutanecarboxylic acid oxetane BODIPY were of poor efficiency and required for further optimization. The monosubstituted cyclobutanecarboxylic acid BODIPY on the contrary could be successfully synthesized, purified, and isolated in sufficient yields. Less elaborate in its appearance, this fluorescent dye can be synthesized from the parent pentamethyl

BODIPY in three easy steps using the one-pot-two-step synthesis to create a monomethoxy BODIPY and subsequently exchanging the methoxy group with 3-hydroxycyclobutanecarboxylic acid applying the molecular sieves catalyzed methodology. This new functionalized dye could be successfully coupled to a chloroalkane ligand and used with the HaloTag system to explore its labeling capacities in a biological application. Incubation of the dye-ligand construct with an isolated HaloSNAP protein showed a successful ligand binding and fluorescence detection in a gel electrophoresis. The incubation overnight of HaloSNAP protein expressing bacteria with the dye-ligand construct and evaluation using fluorescence microscopy showed a successful fluorescent labeling of the bacteria.

To conclude, the application of the newly developed molecular sieves catalyzed alkoxy exchange methodology in the synthesis of a functionalized alkoxy BODIPY in only three reaction steps and its coupling to a target molecule in a biological experimental setting for effective fluorescent labeling was successfully showed. The photophysical and physico-chemical properties of the monosubstituted cyclobutanecarboxylic acid BODIPY like absorption-emission spectra, quantum yields, solubility, and long-term stability still need to be determined, but it is expected that this small, uncharged, easily accessible dye exhibits the potential of becoming a versatile tool for various labeling and imaging approaches. Since the only present substituent is on the central boron atom, many other positions for further substitutions to tune absorption/emission wavelengths remain free. A bandwidth of functionalized BODIPY dyes with wavelengths in the whole range from UV/Vis to near-infrared is conceivable.

3 Fluorescent labeling of nucleic acids

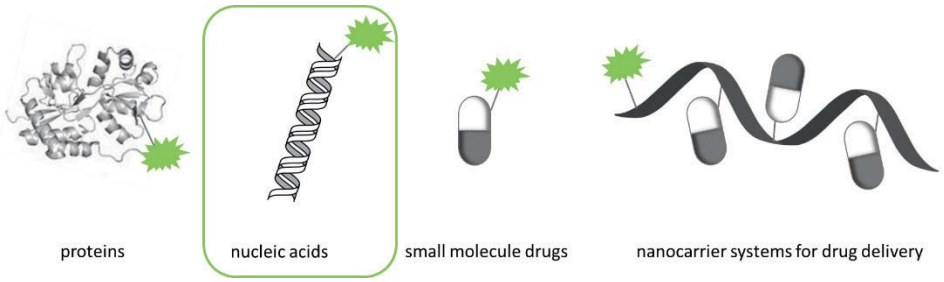

In order to better understand biological processes, the visualization of biomolecules in their natural environment has become an essential tool over the past decade. Since most cellular functions are based on protein interactions, it is obvious that most effort and therefore the most progress has been made in the field of protein labeling and imaging.[166] The development of the green fluorescent protein GFP and its multicolor analogues by Shimomura, Chalfie, and Tsien, who were awarded with the 2008 Nobel Prize in Chemistry for their work, represents a milestone in the history of molecular imaging in proteins.[167] Nevertheless, the function of non-proteinaceous biomolecules such as nucleic acids is of tremendous significance in the understanding of molecular processes, and their alterations hold great potential in therapeutic applications. As nucleic acid aptamers, but most frequently as micro RNAs (micro ribonucleic acid, miRNA), small interfering RNA strands (siRNA), and short-hairpin RNAs (shRNAs), nucleic acid oligomers have gained increasing attention as novel therapeutics via RNA interference (RNAi) mediated gene silencing.[168,169] Especially since the completion of the Human Genome Project (HGP) a novel technology tool box combating diseases by knocking down the expression of disease-related proteins has been generated. Virtually every gene in the human genome has become targetable for gene silencing and thus regulation by using siRNAs.[170] The synthetic small interfering RNA double strands are either brought into the cells directly via standard transfection methods or vector-based (plasmid or lentiviral vectors) as longer shRNAs with subsequent cleavage by the enzyme Dicer into the shorter corresponding siRNA fragments. One of the strands of these fragments, complementary to the targeted mRNA sequence, is thereafter incorporated into the RNA-induced silencing complex (RISC) and guides the complex to the target mRNA through hybridization. Subsequently Argonaute, the catalytic component of RISC, cleaves the targeted mRNA and thus inhibits the translation into the protein of interest (**Figure 3.1**)[171,172]

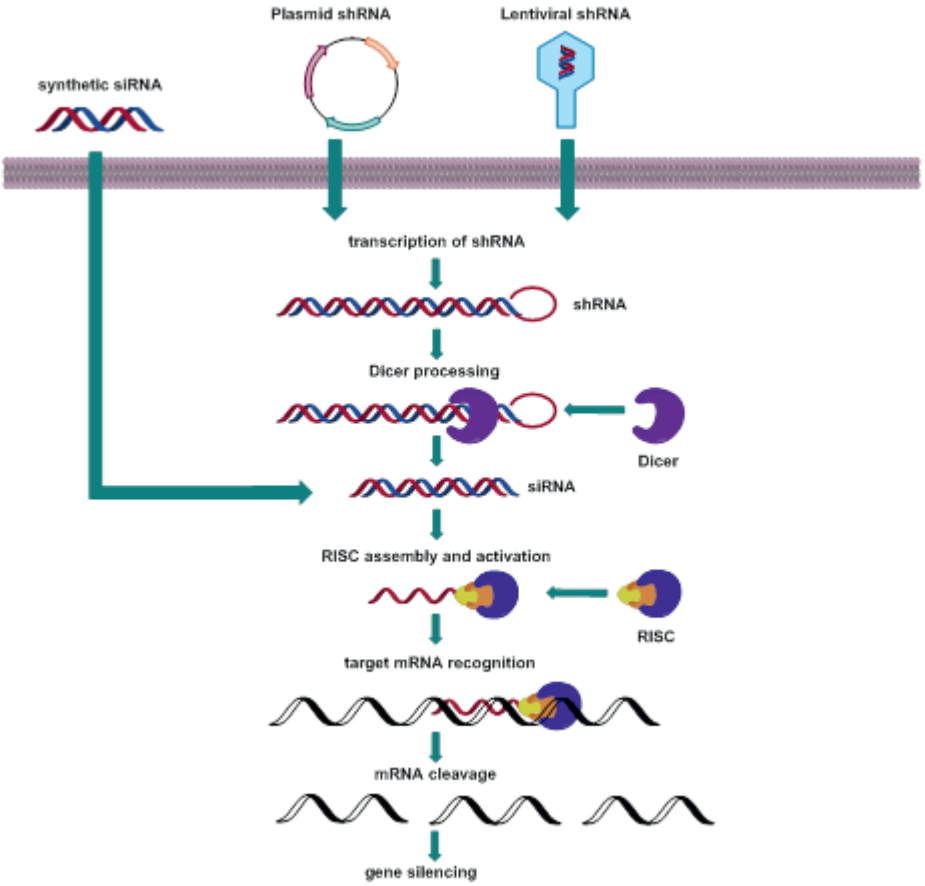

Figure 3.1: siRNA and shRNA mediated gene silencing via RNA interference. Figure adapted with permission from Iyer et al. 2014[168]. Copyright (2017) American Chemical Society.

Despite some drawbacks concerning targeted cellular delivery and long-term stability of the oligonucleotide constructs, until today approximately 20 different miRNA and siRNA based therapeutics have been introduced in clinical trials.[173] As for all drug candidates, the visualization of target binding via fluorescence microscopy methods is especially valuable. Fluorescent labeling of DNA (deoxyribonucleic acid) or RNA strands can be achieved by applying various strategies. Fluorophores can be attached at the 3'- or 5'-end of oligonucleotide strands, at the backbone or to internal bases, directly or via the installation of anchors for postsynthetic modifications such as "click chemistry" type reactions.[174] However, the introduction of only one fluorescent label and a one-color readout bears the risk of false-positive or false-negative results due to quenching properties of different cellular components, autofluorescence effects, and/or lacking integrity of the nucleic acid probe.[175] Wavelength-shifting probes that provide a dual-color readout by excimer formation of two identical fluorophores or energy transfer between two different dyes (Förster resonance energy transfer (FRET) pairs) are a convenient method to overcome these drawbacks.[176] When the dyes are in close proximity to each other, after exciting the fluorophore with the smaller excitation wavelength (donor dye), an energy transfer to the FRET partner with the larger excitation and emission wavelength (acceptor dye) takes place, and therefore the larger emission wavelength of the FRET partner can be detected instead of the smaller emission wavelength of the excited fluorophore. Hence a color change indicates proximity of the dyes. DNA and RNA "Traffic Lights" are an example of an interstrand

FRET pair with an application in molecular beacons, or in the imaging of siRNA mediated gene silencing.[177] In the molecular beacon format, a hairpin structure is used to bring the dyes into spatial proximity, and by using a FRET pair an energy transfer is observable, i.e., exciting a donor dye that is usually emitting at 400-550 nm and detecting a higher emission in the wavelength range 600-750 nm from the FRET acceptor (**Figure 3.2**).

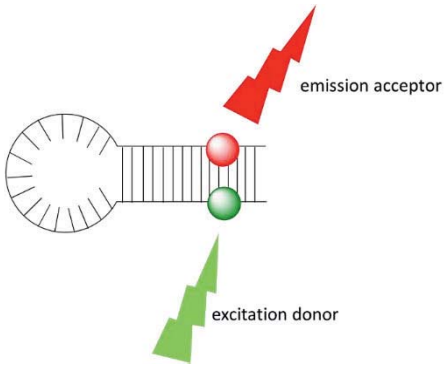

Figure 3.2: Molecular beacon hairpin structure with FRET donor and acceptor in close proximity. The donor dye is excited and the emission of the acceptor dye is detected.

By hybridization to the target nucleic acid, the hairpin structure is opened, the energy transfer is prevented, and a color change from the red FRET emission to the initial green emission of the excited dye is visible.[178] The principle is similar for using an RNA "Traffic Light" consisting of thiazole orange (TO) as FRET donor and thiazole red (TR) as FRET acceptor, to visualize and track siRNA mediated gene silencing. When the double stranded siRNA fragment, with the FRET donor on one strand and the acceptor on the complementary strand, is transfected into cells, the red fluorescence emission of TR is detected. A color change from red to green indicates a dissociation of the siRNA, either by hybridization to the target mRNA or due to low stability of the construct in a cellular environment. Additional information is provided by using a GFP expressing target mRNA sequence in order to indicate successful hybridization and gene silencing by the GFP knockdown. This combination of fluorophores allows for seamless tracking of siRNA integrity and RNA interference.[179] However, new generations of fluorophores exceed the brightness, photostability, and fluorescence intensity of the TO-TR FRET pair in the presence of nucleic acids and require further investigation.

Based on the aforementioned DNA/RNA "Traffic Lights" that use FRET pairs of fluorophores to enable a dual-color readout of nucleic acid binding and integrity, it was the aim of this project to improve the photophysical properties of these fluorescently labeled oligo nucleotides and evaluate their *in vitro* behavior via confocal microscopy as well as their cytotoxicity. To achieve enhanced optical properties, and especially an improved photostability, different approaches were taken. The traditional FRET pair of thiazole orange and thiazole red was substituted by novel dyes of a cyanine-styryl class, with improved brightness and photostability in the presence of nucleic acids.[180] Additionally, the position of the fluorophores within the DNA or RNA duplex structure was altered. While in the traditional configuration of the DNA strands, the fluorophores

point to the minor groove of the double stranded helical structure of nucleic acids, a look at the 3-dimensional structure of these oligomers reveals that an easy alteration in the configuration of the anchor bases would result in a pointing of the fluorophores to the major groove instead, which is suspected to further enhance their photostability as well as their emission color contrast, main parameters in energy transfer experiments.[181]

3.1 Synthesis of cyanine styryl dyes in DNA double strands and evaluation of the influence of dye orientation within the helical structure

In general, there are two different ways fluorescent labels can be incorporated into oligonucleotides. Either the building blocks that are used to build up the oligomers via phosphoramidite chemistry are modified with a label beforehand. Or a linker molecule is incorporated that can be addressed with a postsynthetic coupling to the fluorescent label.[182] The latter inhibits a greater flexibility in the implementation of different labels. Huisgen and subsequently Sharpless and Meldal developed the copper-catalyzed 3+2 cycloaddition of an azide and an alkyne that is nowadays known as “click reaction”. It exhibits, among many other applications, a great potential in the postsynthetic modification of oligonucleotides.[183-186] In the work presented here, a 2’-propargyl modified uridine analog was used to form an attachment site for azide functionalized cyanine-styryl dyes.[xi] To investigate the influence of orientation of the fluorophores within the helical oligonucleotide structure, not only the “natural” ribo configured 2’-propargylated uridine analog **3.1** was synthesized, but also its arabino configured equivalent **3.2** that alters the orientation of the attached fluorophore from pointing into the minor groove of the double helix into pointing towards the major groove (**Scheme 3.1**).

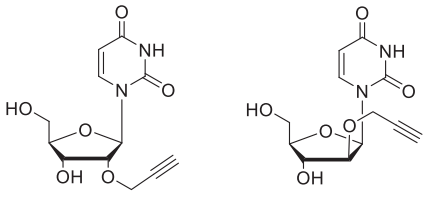

3.1 **3.2**

Scheme 3.1: 2’-propargylated uridine analog in ribo (**3.1**) and arabino (**3.2**) configuration.

[xi] All chemical syntheses of oligonucleotides, dyes and their combinations as well as photophysical measurements described in this chapter were performed by Dr. H.-K. Walter, J. Steinmeyer, and Dr. P. Bohländer of the Wagenknecht group, Karlsruhe Institute of Technology (KIT).

Both components were incorporated in DNA sequences first, before the (especially in terms of transfection and *in vitro* behavior) more challenging RNA sequences were synthesized and investigated. The resulting two DNA strands **3.3** and **3.4**, that are identical except for the configuration of the uridine analog, were coupled via a copper(I)-catalyzed azide-alkyne cycloaddition (CuAAC) to four different azide modified donor dyes **3.5**-**3.8**. Afterwards, two complementary DNA strands **3.9** and **3.10,** with a propargylic fluorophore attachment site in ribo and arabino configuration in a diagonal interstrand position, were synthesized and coupled to five different acceptor dyes **3.11**-**3.15** (**Scheme 3.2**). Each of the resulting eight DNA strands with donor dyes were hybridized with each of the resulting ten DNA strands with acceptor dyes, and then screened for their emission color contrast $C=I_{AC}/I_{D0}$ (fluorescence intensity near maximum of acceptor divided by fluorescence intensity near maximum of donor) and for their fluorescence quantum yield Φ_F (**Table 3.1**). The only exception to the screening permutations were the combinations from donor dyes **3.6**-**3.8** with the acceptor dyes **3.11** and **3.12**. Since the fluorescence spectra of donors and absorption spectra of acceptors for these dye combinations show a broad overlap, a specific excitation is not possible. The screening revealed that in general, the dye combinations with both nucleotides in arabino configuration pointing towards the major groove do not show an improvement in emission color contrast compared to both dyes in ribo configuration pointing towards the minor groove. Yet there are few exceptions. The dye combination **3.8** and **3.14** showed a slightly enhanced quantum yield and emission color contrast in both arabino configuration compared to both ribo configuration, and the dye combination **3.6** and **3.14** showed an enhanced quantum yield in both arabino, as well as ribo-arabino, and vice versa combinations, while in the both ribo configuration the fluorescence is quenched due to excitonic interactions in the ground state[181]. Remarkably, among all the dye combinations there are several examples of enhanced emission color contrasts with one dye in ribo and the other one in arabino configuration, suggesting that a slightly bigger distance between the fluorophores and their position in different grooves has a stabilizing effect and improves their photophysical properties.

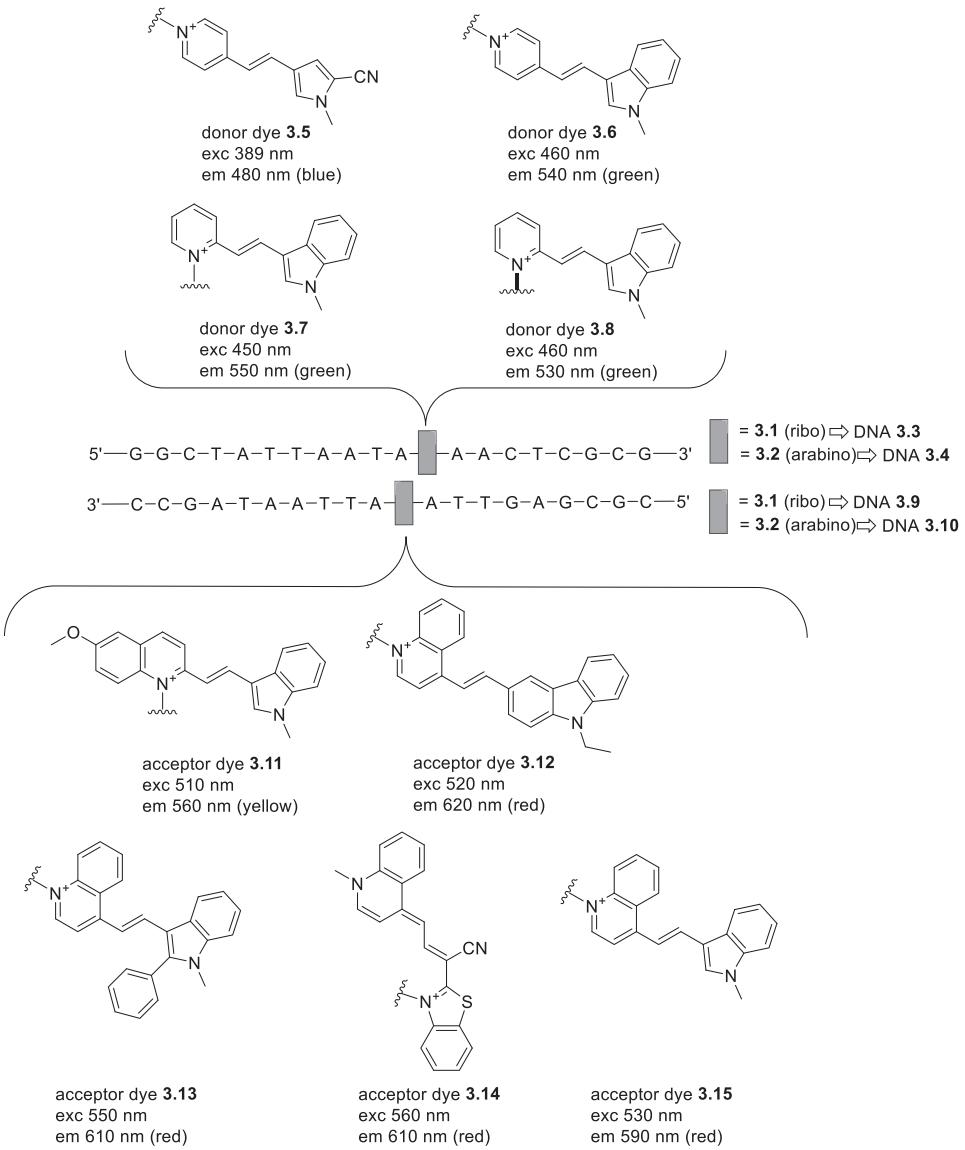

Scheme 3.2: Synthesized DNA double strands with propargylic uridine component in ribo and arabino configuration and the coupled donor and acceptor dyes. Structure of uridine analogs 3.1 and 3.2 given in Scheme 3.1.

		DNA 3.3 and 3.4							
Donor dyes →		**dye 3.5**		**dye 3.6**		**dye 3.7**		**dye 3.8**	
acceptor dyes ↓		**C**	**Φ_F**	**C**	**Φ_F**	**C**	**Φ_F**	**C**	**Φ_F**
DNA 3.9 and 3.10									
dye **3.11**	a-a	35	0.146[a]	-	-	-	-	-	-
	a-r	198	0.606	-	-	-	-	-	-
	r-a	129	0.224	-	-	-	-	-	-
	r-r	70	0.217	-	-	-	-	-	-
dye **3.12**	a-a	15	0.148[b]	-	-	-	-	-	-
	a-r	48	0.227	-	-	-	-	-	-
	r-a	11	0.127	-	-	-	-	-	-
	r-r	40	0.206	-	-	-	-	-	-
dye **3.13**	a-a	44	0.273[c]	20	0.237[d]	41	0.198[d]	69	0.212[d]
	a-r	85	0.357	36	0.245	177	0.319	39	0.214
	r-a	46	0.213	10	0.210	82	0.218	108	0.168
	r-r	93	0.340	60	0.312	136	0.218	153	0.229
dye **3.14**	a-a	109	0.606[c]	20	0.466[e]	41	0.528[f]	83	0.672[e]
	a-r	80	0.576	12	0.427	43	0.564	48	0.592
	r-a	215	0.719	15	0.378	77	0.549	86	0.534
	r-r	87	0.545	3	0.078	40	0.388	45	0.366
dye **3.15**	a-a	60	0.307[g]	11	0.222[h]	9	0.148[h]	28	0.220[h]
	a-r	58	0.306	23	0.245	62	0.285	27	0.258
	r-a	215	0.240	7	0.132	30	0.237	34	0.184
	r-r	69	0.245	25	0.226	59	0.244	38	0.206

Table 3.1: Measured emission color contrasts and quantum yields for all hybridized DNA and dye combinations in ribo (r) and arabino (a) configurations. a) λ_{exc}= 389 nm, λ_{em}= 515-800 nm; b) λ_{exc}= 389 nm, λ_{em}= 525-800 nm; c) λ_{exc}= 389 nm, λ_{em}= 550-800 nm; d) λ_{exc}= 435 nm, λ_{em}= 550-800 nm; e) λ_{exc}= 430 nm, λ_{em}= 550-800 nm; f) λ_{exc}= 430 nm, λ_{em}= 540-800 nm; g) λ_{exc}= 389 nm, λ_{em}= 530-800 nm; h) λ_{exc}= 423 nm, λ_{em}= 550-800 nm.[181]

3.2 Synthesis of siRNA strands with a cyanine styryl energy transfer pair in different orientations

Since DNA and RNA double strand (ds) duplexes form very different 3-dimensional structures, the insights gained in chapter 3.1, on the influence of spatial orientation on efficient energy transfer, cannot be directly transferred to RNA double strands. While dsDNA preferably forms B-type helices in solution, dsRNA forms primarily A-type helices. Both are right-handed helix-types, but with 11-12 nucleosides per winding in A-type helices and 10 nucleosides per winding in B-type helices, the structure looks more dense and twisted for dsRNA, thus resulting in a different geometry for the minor and major groove.[187-189] In the B-type DNA helices both grooves are deep (depth minor: 7.5 Å, depth major: 8.5 Å) and vary mostly in width (width minor: 5.7 Å, width major: 11.7 Å), whereas in A-type RNA helices the minor groove is much more shallow and wide (depth: 2.8 Å, width: 11.0 Å) compared to a deep and tight major groove (depth: 13.5 Å, width: 2.7 Å).[190] In order to investigate the influence of dye orientation on the energy transfer and to create an improved siRNA "Traffic Light" probe, siRNA double strands with the same FRET pair in different orientations were synthesized. Compound **3.6** was chosen as a green emitting donor dye and compound **3.13** as a red emitting acceptor dye (**Scheme 3.3**).

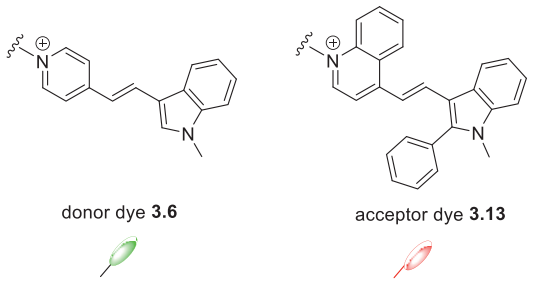

Scheme 3.3: Donor and acceptor dye combination for energy transfer in RNA strands.

As for the different siRNA strands, in the first combination **3.16** the dye pair was directly incorporated as building blocks via phosphoramidite chemistry, whereas in the second combination the dye incorporation in **3.17** was achieved via a "click reaction" with an acyclic *(S)*-2-Amino-1,3-propane diol linker. The combinations **3.18** and **3.19** used the before mentioned 2'-propargylated uridine analog in ribo and arabino configuration as an attachment site for the dye "click reaction" (see chapter 3.1). In the siRNA double strand **3.20** the connecting point was also the 2'-propargylated uridine analog in arabino configuration, but the position in the base sequence was altered. While for the strands **3.16**-**3.19** the dyes were in a directly-diagonal-to-each-other interstrand position, in strand **3.20** they were arranged with one base pair distance to allow for more movement and flexibility, and to reduce potential π-stacking between the dyes (**Scheme 3.4**). Measurements of fluorescence and absorption spectra of the synthesized siRNA-dye constructs showed a significant quenching in the fluorescence for the dyes in both ribo-configuration in siRNA **3.18**, compared to the arabino analog

anchored siRNA **3.19**.[191] The ribo configured uridine anchor directs the dyes in the minor groove of the RNA A-type helix, which is shallow and wide, resulting in a less perfect fit in the groove with enhanced excitonic dye-dye interactions and therefore less energy transfer. This theory is also supported by a 2 °C increase in melting temperature of **3.18** (84.5°C) compared to **3.19** (82.5°C).[191] The Amino-1,3-propane diol linker construct **3.17** showed a medium melting temperature (83.6°C) and fluorescence intensity between the ribo and arabino strands. Increasing the distance between the dyes and reducing π-stacking as intended in the synthesis of **3.20** resulted in an increase in fluorescence intensity of 60% and a decrease in melting temperature of 1 °C. These results substantiate the idea of a more efficient energy transfer by allowing more molecular movements and increasing freedom.[191]

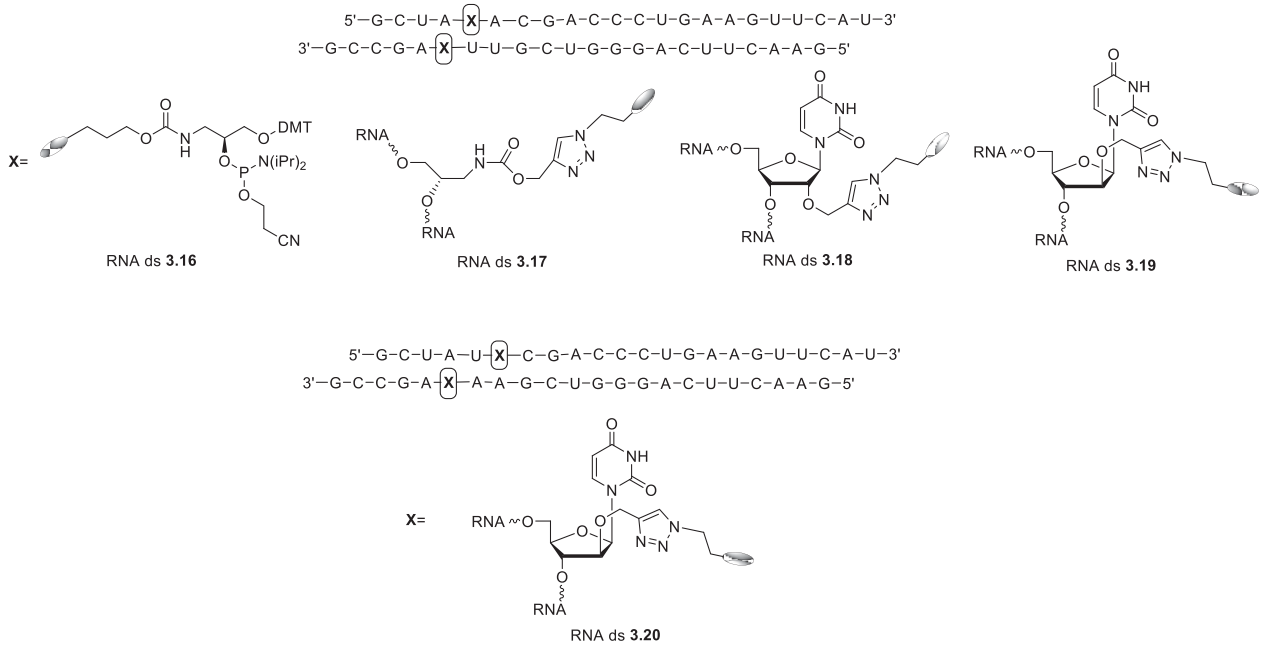

Scheme 3.4: Synthesized siRNA double strands (ds) with direct dye incorporation as phosphoramidite building blocks (RNA ds **3.16**)[192], dyes "clicked" using an acyclic *(S)*-2-Amino-1,3-propane diol linker (siRNA ds **3.17**), dyes "clicked" using the 2'-propargylated uridine analog in ribo configuration **3.1** as a linker (siRNA ds **3.18**), and dyes "clicked" using the 2'-propargylated uridine analog in arabino configuration **3.2** as a linker (siRNA ds **3.19**) in a directly-diagonal-to-each-other interstrand position as well as an siRNA double strand using the 2'-propargylated uridine analog in arabino configuration **3.2** as a linker in a diagonal interstrand position with a one base pair increased distance (siRNA ds **3.20**). Structures of the donor and acceptor dyes are given in **Scheme 3.3**.

3.3 In vitro studies of the cyanine-styryl dye-DNA and –RNA constructs

3.3.1 Cytotoxicity of fluorophores used in FRET pairs

The fluorescent dyes that were used in the synthesis of the previously described DNA duplexes (chapter 3.1) were examined for their influence on cell viability using a standard MTT (3-(4,5-dimethylthiazole-2-yl)-2,5-diphenyltetrazoliumbromide) cytotoxicity test. This assay is based on the intracellular reduction of a yellow tetrazolium salt (MTT) into a violet formazan product by mitochondrial dehydrogenases. This process only takes place in metabolically active cells. Therefore, the amount of the generated formazan which can be determined by absorbance measurements at 595 nm is directly linked to cell viability. Normalization of the measured absorbance values to those of untreated positive control (living) cells as well as with Triton X-100 (Serva) treated negative control (dead) cells reveals the percentage of viable cells. HeLa cells were treated with different concentrations (0.0375 µM - 0.3 µM) of the dyes **3.5**, **3.6**, **3.8**, **3.11**, and **3.14** for 72 h (details are given in chapter 6.2.4.6). The LD_{50} value, which describes the concentration of a sample that leads to 50% cell viability, was found to be >0.3 µM (**Figure 3.3**). Therefore, no obvious cytotoxic effects caused by the fluorophores were expected for subsequent imaging experiments with DNA double strands containing dyes corresponding to a concentration of 0.075 µM.

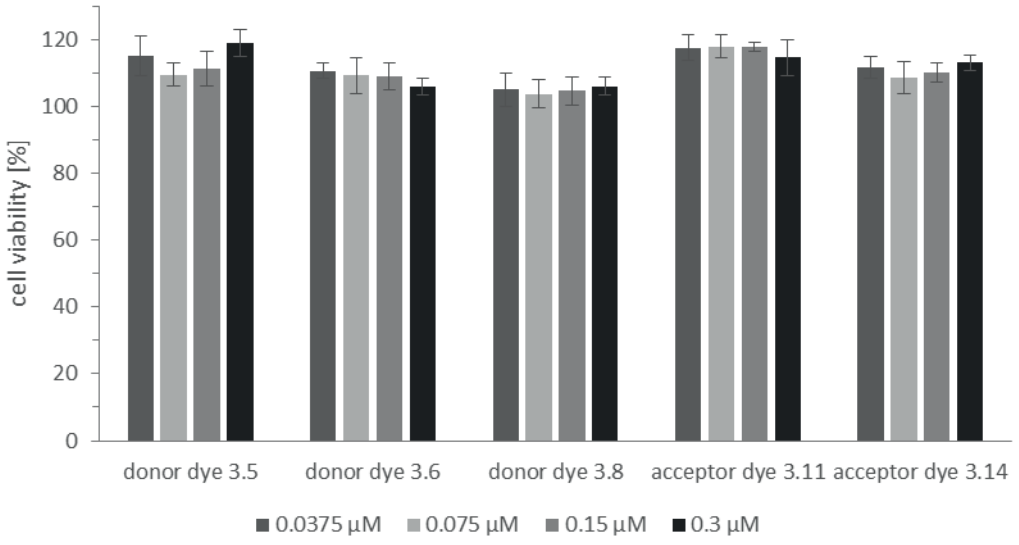

Figure 3.3: Cytotoxicity assay of the dyes **3.5**, **3.6**, **3.8**, **3.11**, and **3.14** after 72 h incubation of HeLa cells in the concentration range 0.0375 – 0.3 µM. Statistical error bars were calculated as standard deviations from a quadruplicate of *n*=4 experiments.

3.3.2 Confocal microscopy of selected dye-DNA constructs

In order to investigate the DNA double strands with incorporated cyanine-styryl dyes (in different combinations of ribo and arabino configurations as described in chapter 3.1) for their stability in a cellular environment, four selected representatives were transiently transfected into HeLa cells and investigated after 24 h via confocal laser scanning microscopy (CLSM, **Figure 3.4**). 15 pmol of the oligonucleotides were transfected per investigated cell culture well, correlating to a dye concentration of 0.075 µM (for transfection details see chapter 6.2.4.1). The duplexes DNA**3.4**dye**3.5**(donor)- DNA**3.9**dye**3.11**(acceptor) (a-r), DNA**3.3**dye**3.5**(donor)- DNA**3.10**dye**3.14**(acceptor) (r-a), DNA**3.4**dye**3.6**(donor)- DNA**3.10**dye**3.14**(acceptor) (a-a) and DNA**3.3**dye**3.8**(donor)- DNA**3.10**dye**3.14**(acceptor) (r-a) were imaged using the excitation wavelength of the energy donor (dye **3.5** λ_{exc}= 405 nm, dyes **3.6** and **3.8** λ_{exc}= 488 nm). The efficiency of the energy transfer was observed by detecting the fluorescence of the donor dye (**Figure 3.4**, left column) as well as the fluorescence of the acceptor dye (**Figure 3.4**, second column from the left). In all cells a perinuclear staining and accumulation of the dyes in endosomes and vesicles is visible, indicating an endocytic uptake. Detectable fluorescence for all acceptor dye wavelengths showed a sufficient energy transfer between the FRET pairs and therefore at least partially intact duplex constructs after transfection into cells with donor and acceptor dyes in close proximity. Due to a partial dissociation of the double strands and incomplete energy transfer processes, also the donor fluorescence is still detectable.

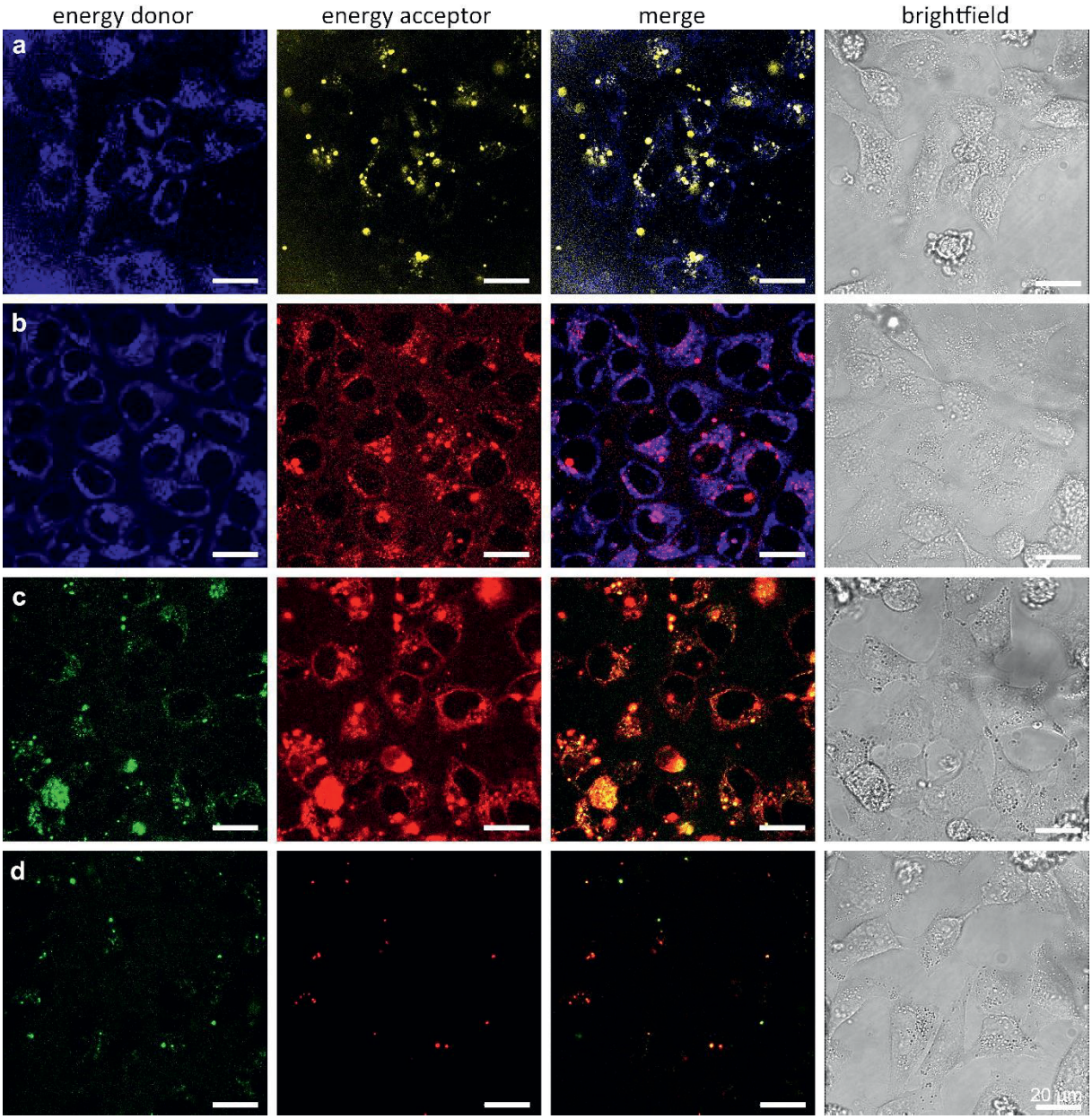

Figure 3.4: Confocal laser scanning microscopy of HeLa cells after transient transfection with **a**) DNA**3.4**dye**3.5**(donor)- DNA**3.9**dye**3.11**(acceptor) (a-r), **b**) DNA**3.3**dye**3.5**(donor)- DNA**3.10**dye**3.14**(acceptor) (r-a), **c**) DNA**3.4**dye**3.6**(donor)- DNA**3.10**dye**3.14**(acceptor) (a-a) and **d**) DNA**3.3**dye**3.8**(donor)- DNA**3.10**dye**3.14**(acceptor) (r-a). $4x10^4$ HeLa cells were seeded in an 8-well chamber slide 24 h prior to transfection. 15 pmol of DNA duplexes were then transiently transfected into cells for 24 h. The visualization was performed using a Leica TCS-SPE (DMi8) inverted microscope with an ACS APO 63x/1.30 oil objective. Fluorophores were excited using an UV laser (λ_{exc}= 405 nm) for duplexes DNA**3.4**dye**3.5**(donor)-DNA**3.9**dye**3.11**(acceptor) and DNA**3.3**dye**3.5**(donor)- DNA**3.10**dye**3.14**(acceptor)and an argon ion laser (λ_{exc}= 488 nm) for duplexes DNA**3.4**dye**3.6**(donor)- DNA**3.10**dye**3.14**(acceptor) and DNA**3.3**dye**3.8**(donor)- DNA**3.10**dye**3.14**(acceptor). The emission detection bandwidths were at λ_{em}= 435-470 nm (blue) and λ_{em}= 575-750 nm (yellow) for **a**) DNA**3.4**dye**3.5**(donor)-DNA**3.9**dye**3.11**(acceptor), λ_{em}= 415-550 nm (blue) and λ_{em}= 575-750 nm (red) for **b**) DNA**3.3**dye**3.5**(donor)- DNA**3.10**dye**3.14**(acceptor), λ_{em}= 490-550 nm (green) and λ_{em}= 550-675 nm (red) for **c**) DNA**3.4**dye**3.6**(donor)- DNA**3.10**dye**3.14**(acceptor), λ_{em}= 490-550 nm (green) and λ_{em}= 675-800 nm (red) for **d**) DNA**3.3**dye**3.8**(donor)-DNA**3.10**dye**3.14**(acceptor). Using the acquisition software Leica Application Suite (LAS) X 2.0.1.14392, the picture ratio was adjusted to 1024 × 1024 pixels 8 bit depth. Scale bar: 20 µm.

3.3.3 Cytotoxicity of RNA double strands

The siRNA duplexes that were previously described in chapter 3.2 were examined for their influence on cell viability using a standard MTT cytotoxicity test (for assay information see chapter 3.3.1). HeLa cells cultured to a confluent layer were treated with different concentration of the siRNA strands **3.16**, **3.17**, **3.19** and **3.20** (0.0375 µM - 0.15 µM) and their respective concentrations of transfection reagent (ScreenFect®A) for 72 h (for details see chapter 6.2.4.7). The siRNA concentration intended to be used in subsequent transfection and imaging approaches corresponded to 0.075 µM (**Figure 3.5**). As controls, an unmodified dsRNA was also added to the samples, as well as an unmodified dsRNA, that were exposed to the same "click reaction" conditions as the strands **3.17-3.20** to reveal a potential influence of Cu(I) catalysis residues on the cell viability. The negative control cells (living) were exposed to a concentration of transfection reagent corresponding to the highest sample concentration (0.15 µM). The LD_{50} value for the examined RNA double strands was found to be >0.15 µM. Cells treated with this dsRNA concentration still showed a cell viability of 80-100% and therefore comparable rates to the negative control (living) cells. The significantly higher cell viability rates of the samples in lower concentrations of dsRNA and transfection reagent (up to 200% for 0.0375 µM) indicate a cytotoxic effect caused by the transfection regent itself. The unmodified dsRNA as well as the unmodified dsRNA that was exposed to copper "click" conditions showed no significant difference in viability rates compared to the dye-labeled strands **3.16-3.20**, suggesting no cytotoxic effects caused by the dye coupling and/or the use of Cu(I) to catalyze the coupling reaction.

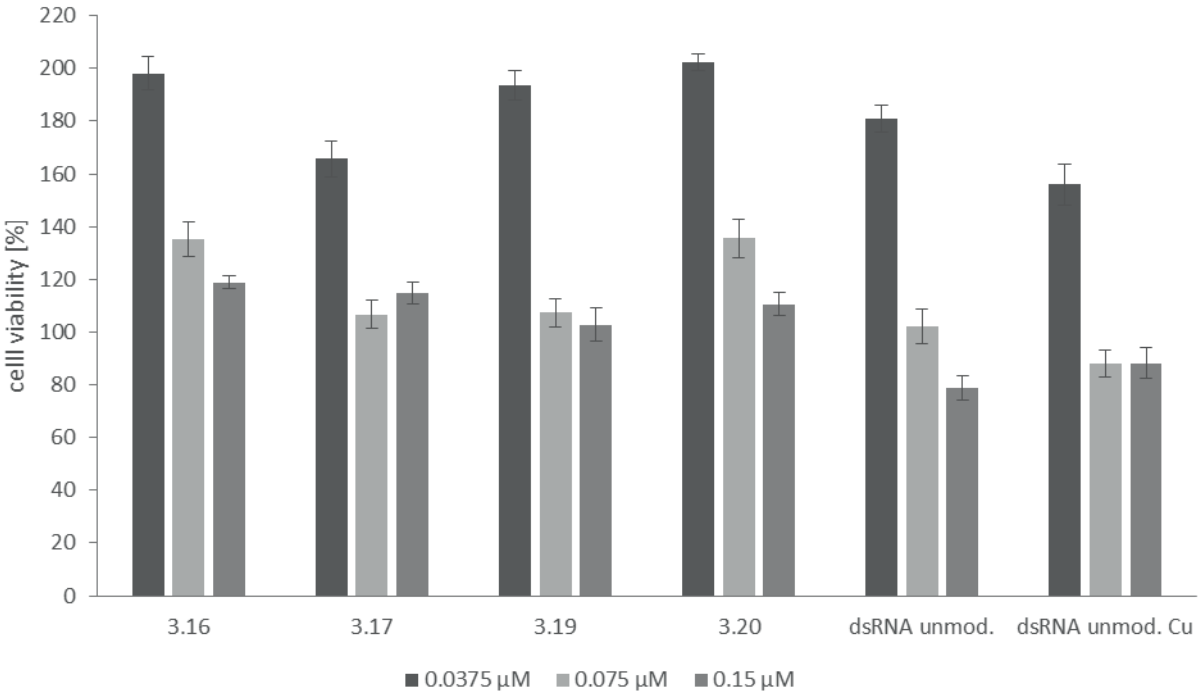

Figure 3.5: Cytotoxicity assay of the siRNAs **3.16**, **3.17**, **3.19**, **3.20**, an unmodified control RNA strand, and an unmodified control RNA strand exposed to Cu(I) "click" conditions, after 72 h incubation of HeLa cells in the concentration range 0.0375 – 0.15 µM. Statistical error bars were calculated as standard deviations from a sextuplicate of *n*=6 experiments.

3.3.4 Confocal microscopy of selected siRNA double strands

After examining the cytotoxic effects and choosing suitable conditions for transfection, the siRNA double strands **3.16**, **3.17**, **3.19,** and **3.20** were investigated for their energy transfer efficiency and stability in a cellular environment via confocal laser scanning microscopy (CLSM, **Figure 3.6**). HeLa cells were cultured to confluency and transfected with 15 pmol of the RNA complexes for 24 h (for details see chapter 6.2.4.2). Since the siRNA **3.18** showed a quenching behavior in fluorescence measurements, it was not suitable for *in vitro* experiments and therefore excluded. The RNA duplexes were imaged using the excitation wavelength of the energy donor **3.6** λ_{exc}= 488 nm. The efficiency of the energy transfer was observed by detecting the fluorescence of the donor dye (**Figure 3.6**, left column) as well as the fluorescence of the acceptor dye **3.13** (**Figure 3.6**, second column from the left). Sufficient fluorescence signals for both dyes could be detected for the siRNA strands **3.16** and **3.19** (**Figure 3.6**, row 1 + 3), while only a very weak signal for the acceptor dye could be detected for the siRNAs **3.17** and **3.20** (**Figure 3.6**, row 2 + 4). Since there was no detectable donor fluorescence for **3.17** and **3.20**, the lack of fluorescence signal is most likely not due to an insufficient energy transfer or degradation of the siRNA probe, but to an insufficient transfection efficiency. siRNAs **3.16** and **3.19** were successfully transfected into the HeLa cells and showed a signal in the perinuclear region for the donor as well as for the acceptor dye, indicating an energy transfer and thus at least partially intact duplex constructs with donor and acceptor dyes in close proximity.

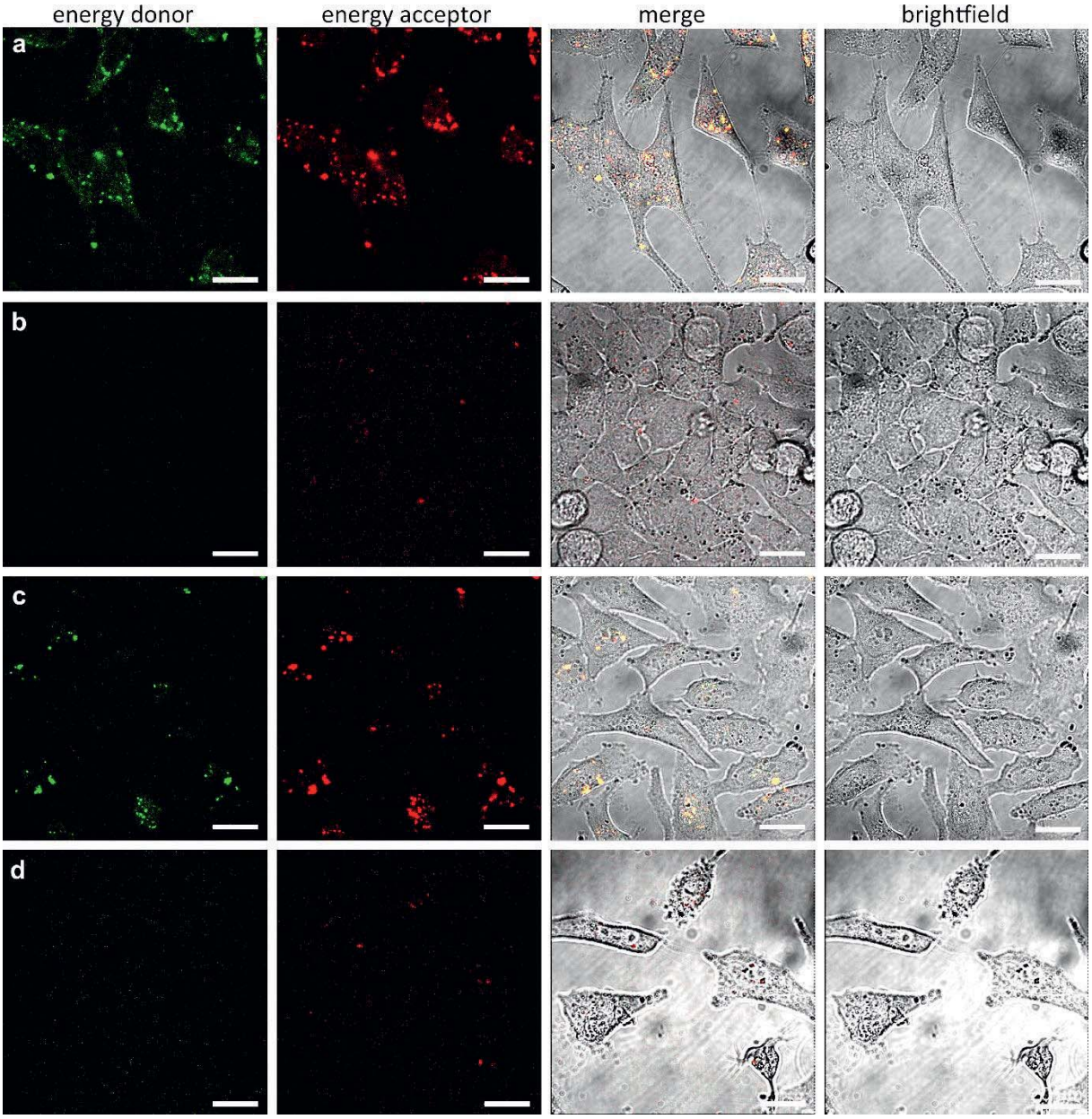

Figure 3.6: Confocal laser scanning microscopy of HeLa cells after transient transfection with **a)** dsRNA **3.16**, **b**) dsRNA **3.17**, **c**) dsRNA **3.19** and **d**) dsRNA **3.20**. $4x10^4$ HeLa cells were seeded in an 8-well chamber slide 48 h prior to transfection. 15 pmol of RNA duplexes were then transiently transfected into cells for 24 h. The visualization was performed using a Leica TCS-SPE (DMi8) inverted microscope with an ACS APO 63x/1.30 oil objective. Fluorophores were excited using an argon ion laser (λ_{exc}= 488 nm). The emission detection bandwidths were at λ_{em}= 490-515 nm (green) and λ_{em}= 675-800 nm (red). Using the acquisition software Leica Application Suite (LAS) X 2.0.1.14392, the picture ratio was adjusted to 1024 × 1024 pixels 8 bit depth. Scale bar: 20 µm.

3.3.5 GFP knockdown

The RNA sequence that was used to synthesize the siRNA strands described in chapter 3.2 is complimentary to parts of the GFP mRNA. When transfected into GFP expressing cells, not only the integrity of the siRNA double strands should be observable by detection of the acceptor fluorescence of the FRET pair, but also the successful binding to the target mRNA and gene silencing via RNAi should be detectable by a knockdown of the GFP fluorescence. 15 pmol of the siRNA double strands **3.16**, **3.17**, **3.19,** and **3.20** (for structures see **Scheme 3.4**), as well as a commercially available control siRNA strand (Dharmacon® GFP Duplex I), were transiently transfected into HeLa GFP cells and investigated after 24 h via confocal laser scanning microscopy (CLSM, **Figure 3.7**) in comparison to untreated HeLa GFP cells. Again, the siRNA **3.18** was excluded from imaging experiments due to insufficient energy transfer and therefore low acceptor fluorescence. The RNA duplexes were imaged using the excitation wavelength of the energy donor **3.6** λ_{exc}= 488 nm that is also suitable for the excitation of GFP. All synthesized siRNA duplexes (**Figure 3.7**, rows **c**-**f**) showed a fluorescent signal of the acceptor dye (2nd column), indicating the integrity of the double strands and, compared to the untreated HeLa GFP cells in row **a**, a slight knockdown of GFP expression (especially in row **f** for siRNA **3.20**, magnification of knockdown area given in **Figure 3.8**). Remarkably, the commercially-available control siRNA strand that is supposed to provide an efficient GFP knockdown, also did not show a better knockdown of the GFP fluorescence than our synthesized strands **3.16**-**3.20**, indicating an insufficiency rather in the transfection rate than in RNA hybridization.[193]

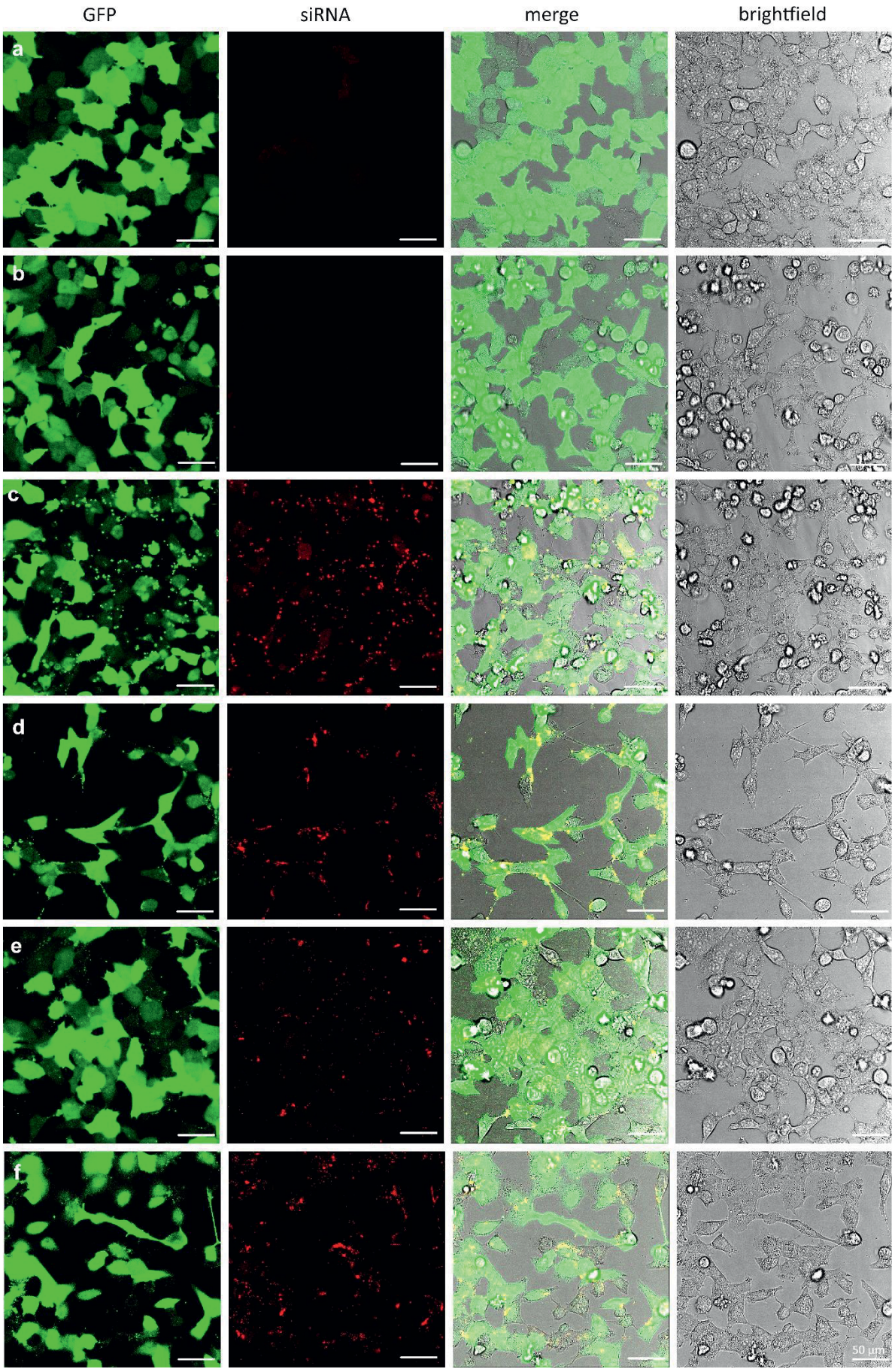

Figure 3.7: Confocal laser scanning microscopy of **a)** untreated HeLa GFP cells and after transient transfection with **b)** positive control siRNA (Dharmacon™ GFP Duplex I), **c)** siRNA **3.16**, **d**) siRNA **3.17**, **e**) siRNA **3.19,** and **f**) siRNA **3.20**. 7x10^4 HeLa cells were seeded in an 8-well chamber slide 4 h prior to transfection. 15 pmol of siRNA duplexes were then transiently transfected into cells for 24 h. The visualization was performed using a Leica TCS-SP8 inverted microscope with an HCPL APO CS2 40x/1.10 water objective. Fluorophores were excited using an argon ion laser (λ_{exc}= 488 nm). The emission detection bandwidths were at λ_{em}= 535-567 nm (GFP, green) and λ_{em}= 675-800 nm (siRNA, red). Using the acquisition software Leica Application Suite (LAS) X 1.1.0.12420, the picture ratio was adjusted to 1024 × 1024 pixels 8 bit depth. Scale bar: 50 µm.

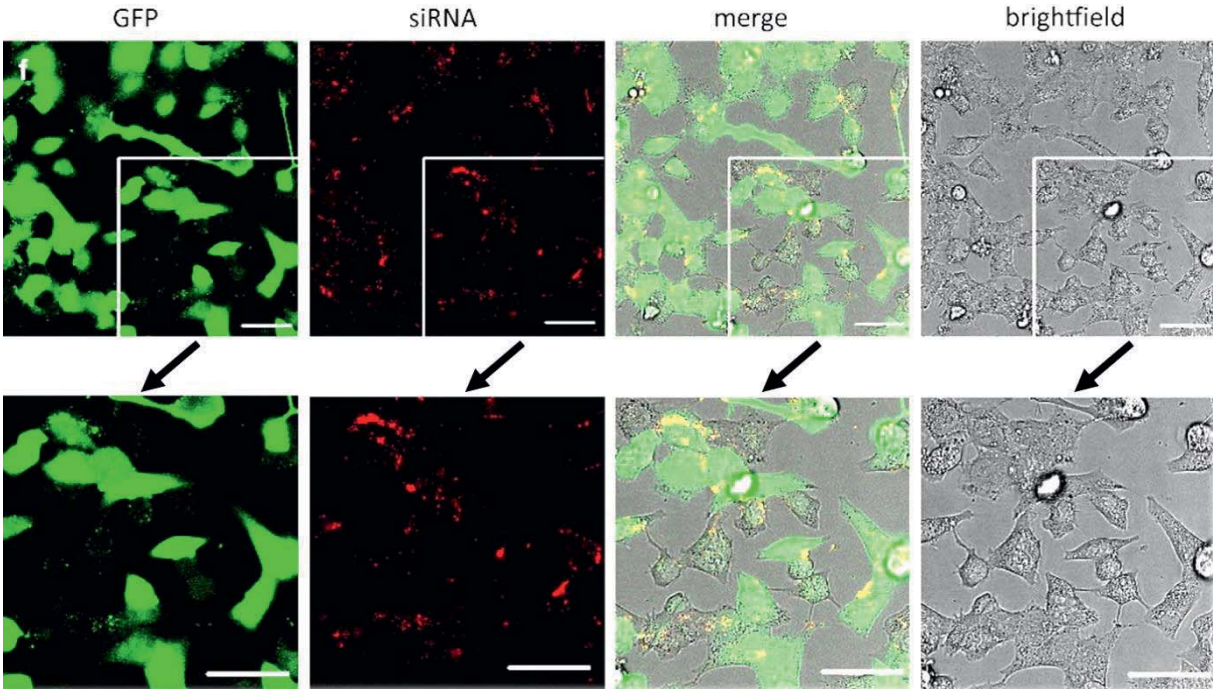

Figure 3.8: Confocal laser scanning microscopy of HeLa GFP cells after transient transfection with siRNA **3.20** and magnification of GFP knockdown area. For imaging parameters see description **Figure 3.7**.

3.4 Conclusion

With the increasing insight in genomic information, particularly since the completion of the Human Genome Project (HGP) in 2003, scientist have identified numerous genetic causes and factors for the development of diseases like Parkinson's, Alzheimer's, and cancer, and the potential in addressing these causes via new oligonucleotide-based treatments takes us one step further towards the great goal of personalized medicine.[194-197] Besides micro RNAs (miRNAs), aptamers, and antisense oligonucleotides (AOs), small interfering RNAs (siRNAs) in particular provide promising candidates for targeted gene silencing and gene therapy.[198] Since the visualization of drug delivery and target binding is crucial for the understanding of underlying mechanisms, various imaging techniques have become important tools in drug development.[199] Several methods are available in the fluorescent labeling and imaging of oligonucleotides, from the well-established fluorescence in situ hybridization (FISH) in fixed cells to live-imaging via fluorescently labeled aptamers, cell permeable intercalating dyes such as Hoechst 33342 and Draq5, histones fused to fluorescent proteins, or more sophisticated approaches like CRISPR-Cas imaging.[200-202] Super-resolution microscopy techniques like stimulated emission depletion (STED) and direct stochastic optical reconstruction (dSTORM) provide detailed structural information about the fluorescently labeled oligonucleotides.[203] Yet, despite this sophistication, all of these methods have one drawback in common. They are all based on a single-color readout and bear the risk of false positive or false negative signals, mostly due to quenching effects of cellular components.[175] The development of a dual-color readout DNA/RNA "Traffic Lights" concept, based on the energy transfer of two dyes in interstrand positions of double stranded oligonucleotides, is a promising new method for reliable tracking of cellular delivery, target binding, and structural integrity of nucleic acid probes.[177,179] In the work presented here, several new dye combinations as energy transfer (ET) pairs, as well as the influence of the dye orientation within the helical structure of DNA and RNA double strands, were examined for efficient energy transfer, integrity, toxicity, and function in a cellular environment. In a first step, various combinations of ET pairs out of four different cyanine styryl donor and five different acceptor dyes were incorporated into a DNA double strand by using a 2'-propargylated uridine analog in two different configurations (ribo and arabino) as a linker for postsynthetic modification via copper catalyzed "click chemistry." While the linker directs the fluorophores to pointing towards the minor groove of the DNA double helix in the natural ribo configuration, it directs them into the major groove in arabino configuration. Photophysical measurements of the DNA constructs revealed the best ET efficiencies and color contrasts for combinations with one ribo configured fluorophore anchor on one strand and an arabino configured dye anchor on the complimentary strand, and therefore increased distance between the fluorophores, pointing into different grooves. Interactions of each dye with diverse nucleotides could decrease π-stackings and other undesired dye-dye interactions with ground state energy transfers, thus quenching fluorescence energy transfers. Subsequent transfection of selected DNA constructs into HeLa cells showed the strong desired fluorescence signals for the acceptor dye in perinuclear vesicles, indicating intact double strands even in a cellular environment, as well as a fluorescence signal for the

donor dye in the same compartment, due to a partial dissociation of the double strands and incomplete energy transfer processes. A cytotoxicity assay of the cyanine styryl dyes used in the imaged DNA constructs showed no inherent cytotoxicity of these molecules. In a second step, one of the ET pairs with suitable photophysical properties was incorporated into a siRNA double strand using different linker with different orientations. Besides the before-mentioned 2'-propargylated uridine analog in ribo and arabino configuration, an acyclic *(S)*-2-amino-1,3-propane diol linker and a direct incorporation via phosphoramidite building blocks were chosen. Additionally, a similar siRNA double strand was synthesized with arabino oriented propargylic uridine analogs in more distant positions (one base pair difference compared to other siRNA constructs). In contrast to the former small DNA library, within one double strand, only identical linkers were used (i.e. only ribo-ribo and arabino-arabino instead of ribo-arabino and vice versa). Photophysical measurements showed significant fluorescence quenching events with both ribo configured dye anchors directing the fluorophores into the RNA minor groove, and the highest fluorescence for the both arabino configured dye anchors with an enlarged distance. Since the RNA minor groove is wide but very shallow[190], it is suggested that the fluorophores do not "fit" into the groove and due to less nucleotide interactions, they show increased interaction behavior between each other leading to more ground state energy exchange and reduced fluorescence energy transfer. The theory is supported by melting temperature measurements. A higher melting temperature indicates more dye-dye interactions and the quenched fluorescence configuration shows a 3 °C higher melting temperature compared to the distant arabino pair. Transfection of the RNA duplexes into HeLa cells showed partially intact double helices comparable to the previously-tested DNA strands for some samples, but also a lack of overall transfection efficiency. Subsequent transfection into GFP-expressing HeLa cells, to show not only the fluorescence signal of the intact transfected siRNA strands but also siRNA binding to the target mRNA and RNAi mediated gene silencing by knocking down the GFP fluorescence, revealed weak acceptor fluorescence signals and only a slight GFP knockdown for the synthesized samples, as well as for a commercially available GFP knockdown duplex, indicating again a low transfection efficiency. These findings are congruent with the major drawbacks in RNAi therapy, the fragility of siRNAs and their delivery.[204] A cytotoxicity assay of the synthesized siRNAs, an unmodified RNA double strand, and an unmodified strand exposed to Cu(I)-"click" conditions revealed no inherent toxicity of the siRNAs or remaining copper, but a toxicity of the transfection reagent.

In conclusion, important insights into the influence of structural modifications within oligonucleotide duplexes on successful energy transfer between two suitable dyes could be gained. A higher flexibility of the dyes with more distance to each other, combined with a position promoting nucleotide interactions and therefore avoiding dye-dye interactions, leads to improved fluorescence energy transfer. These findings can be applied in cellular systems, retaining partial integrity over the course of 24 h. Incorporation of these improved "Traffic Light" systems into siRNA drug candidates could be of significant value in the imaging and drug development process.

4 Fluorescent labeling of drugs

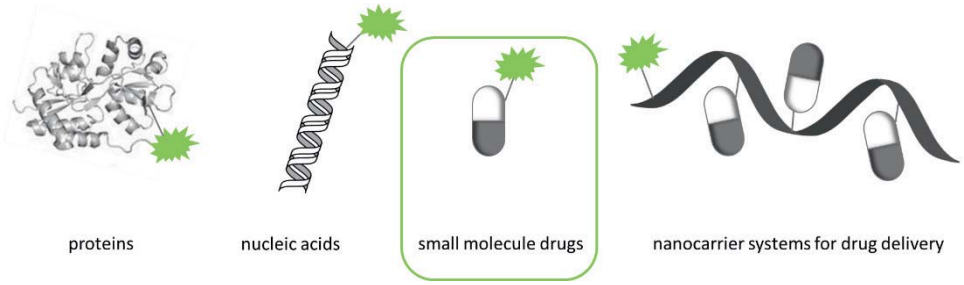

For diagnostic purposes, the fluorescent labeling of small molecules is often crucial to achieve a staining of specific cell types or molecular substructures within certain cell types. This specific labeling of cells is an important tool in the detection of diseases, in understanding the underlying mechanisms of disease development, and therefore crucial for successful drug design.[205] Several well-established methods exist for the fluorescent labeling of cellular substructures, ranging from DNA intercalating dyes such as 4,6-diamidino-2-phenylindole (DAPI) or Hoechst 33342 for the visualization of cell nuclei to reliable commercially available staining kits for cytoplasm, mitochondria, lysosomes, endoplasmatic reticulum (ER), and Golgi.[206,207] These methods label specific organelles in mammalian cells, independent from the type of cell or the tissue they are derived from, and are especially useful as a multicolor readout for determining the location of an investigated labeled biomolecule within a cell.[208] However, for many purposes such as investigations of disease development, diagnostic methods, or observation of treatments, a specific labeling of certain cell types (i.e., cancer cells) is required. The targeting of cell-specific biomarkers, molecules that are expressed or overexpressed in specific cell types, by various fluorescence- and non-fluorescence-based methods, like immunohistochemistry, enzyme-linked immunosorbent assay (ELISA), polymerase chain reaction (PCR), and fluorescence in situ hybridization (FISH) to name only a few, is one possibility to differentiate cell types and is often used in diagnostics.[209-213] An interesting and often-used example in detecting diseases, such as acute inflammation, various types of tumors, and cardiovascular diseases, are proteins of the S 100 family. Being involved in aspects of proliferation regulation, differentiation, apoptosis, inflammation, migration/invasion, and many more, they show cell-specific expression patterns that can vary between physiological and pathological conditions.[214] However, these methods are limited to *in vitro* applications and biochemical assays. When disease development or treatment success needs to be monitored, as for example via observation of tumor growth or shrinkage, or cell migration related to metastases, *in vivo* fluorescence-based live cell tracking is required.[215,216] In general, a direct labeling of specific cell types via injection of fluorescently labeled antibodies or antibody fragments is one available technique; another one is the *ex vivo* isolation and labeling of cells with fluorescent cell tracers and subsequent transfer into recipient organisms, or the use of animal models expressing fluorescent proteins in specific cell populations.[217,218] For example, in order to track the migration of immune cells into tumor regions, T cells have been labeled

with near infrared (NIR) dyes prior to injection and their movements were observed *in vivo*, resulting in a better understanding in the formation of premetastatic niches.[219,220] In another early study, red fluorescent protein (RFP) expressing tumors have been genetically engineered and implanted into green fluorescent protein (GFP) expressing transgenic mice to reveal detailed insights into tumor-stroma interactions, angiogenesis, and other tumor-environment related mechanisms.[221,222] Besides these traditional versatile techniques, different ways of direct labeling and imaging of tumors *in vivo* have been reported lately. Cyclooxygenase-2 (COX-2) is an inducible enzyme, which is expressed in response to inflammation and proliferation stimuli, and therefore is often highly overexpressed in tumor cells. Several fluorescently-labeled compounds such as COX-2 inhibitors (COXIBs), carboxylic acid-containing nonsteroidal anti-inflammatory drugs (NSAIDs), and indomethacin conjugates, can target and bind COX-2 specifically after i.v. injection and therefore provide an excellent opportunity for imaging various types of cancers in all states of development (**Figure 4.1**).[223,224]

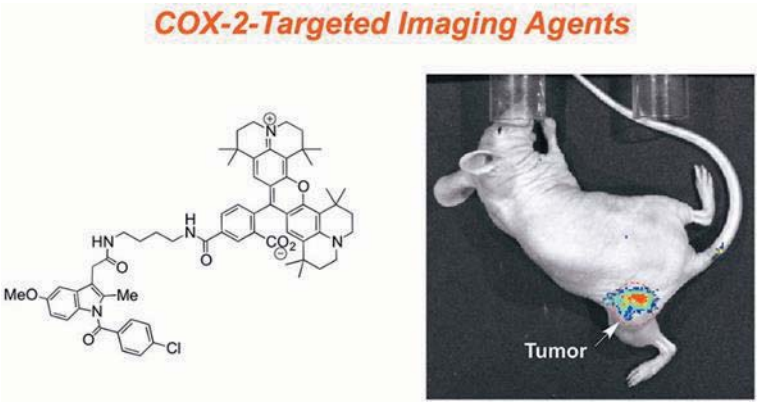

Figure 4.1: Cyclooxygenase-2 (COX-2) targeted fluorescent labeling and *in vivo* tumor imaging. Reprinted from Uddin et al.[224] Copyright (2013) American Chemical Society.[xii]

Keeping the example of cancerous diseases, by applying all these techniques, an almost seamless visualization of the formation, growth, environment interactions, and maturation until metastasis is possible, offering invaluable information to derive potential diagnostic and treatment targets. Since the prognosis for patients with cancerous diseases is highly depending on the state in which a solid tumor is diagnosed, an efficient early detection as well as extensive screening and awareness strategies are a key factor in combating widespread types of cancer such as melanoma.

[xii] Further permissions related to the material excerpted should be directed to the ACS. http://pubs.acs.org/doi/abs/10.1021/bc300693w

4.1 Melanoma – a widespread disease and its challenges

Melanoma, a malignancy of melanocytes, is the cancer with the fastest growing incidence among all other preventable cancers in the United States.[225] Between 1950 and 2007, the incidence rates rose 17-fold in men and 9-fold in women in the US, with comparable rates in Western Europe and Australia.[226-228] With an overall global incidence of 15-25 per 100,000 individuals, melanoma contributes only to 5% of all skin cancer cases but to 75% of all deaths.[229,230] While most of the melanoma are diagnosed at an operable state, in up to 20% of the diagnoses, metastases have already developed and among those, 44% are brain metastases with a median overall survival of only 4 months.[231]

Melanocytes, which are derived from the neural crest, a group of highly migratory embryonic cells, are dendritic cells located amongst the basal layer of epidermis, hair bulbs, eyes, ears, and meninges.[232-235] These important melanin-producing cells can be distinguished from another type of dendritic cell present in the epidermis, the Langerhans' cells, by their localization. Langerhans' cells are antigen-processing cells and mostly found in the suprabasal layer of the epidermis.[236] While melanocytes and Langerhans' cells fulfill important functions in the top layer of the human skin, they make up only about 10% of the cells. 90% of the epidermis cells are keratinocytes that proliferate on the basal layer and then migrate slowly to the surface, where they form a protective barrier against external influences, the stratum corneum.[237] During the approximately 30 day journey, the keratinocytes differentiate to flattened cells without nuclei, filled with keratin.[238] Each melanocyte is connected to approximately 36 keratinocytes and delivers to them the pigment melanin, which is formed in specific lysosome-like organelles, the melanosomes, and forms a cap on the top of nuclei of mitotically active basal cells (similar to an umbrella) to protect the nucleus from ultraviolet injuries.[239] The fourth cell type in the epidermis are Merkel cells, which are probably derived from keratinocytes and act as mechanosensory receptors in the skin.[240] Beneath the epidermis, the dermis forms the largest portion of the skin. It consists mainly of collagen and elastic fibers, contains hair follicles, sweat glands, lymph vessels and nerve ends, and is important in thermoregulation, wound healing, and sense of touch. The subcutaneous layer underneath it contains blood vessels and fatty tissue (**Figure 4.2**)

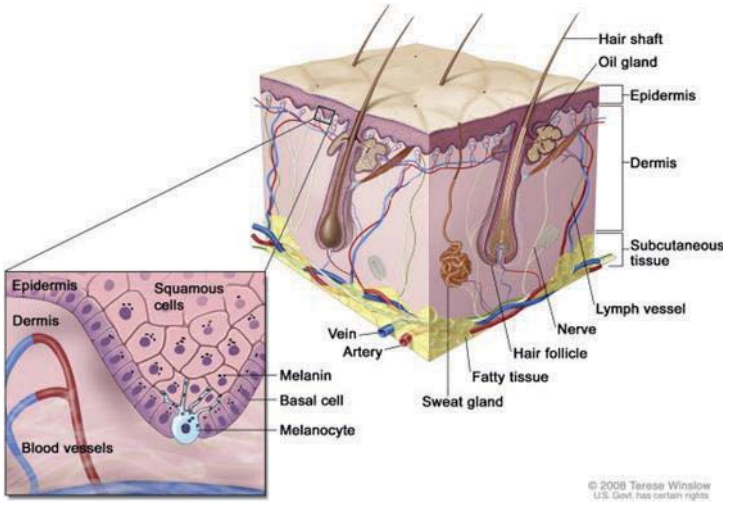

Figure 4.2: Anatomy of the skin. Reprinted from Korotkov et al. [241] Copyright (2012), with permission from Elsevier[xiii]

Most skin cancers do not derive from melanocytes as pigmented cells but are non-pigmented lesions such as basal cell carcinoma (BCC, 80% of non-melanoma skin cancers (NMSCs)) and squamous cell carcinoma (SCC, 20% of NMSCs).[242-244] Furthermore, only a mere fraction of pigmented skin lesions (PSLs) are melanoma. Among the most common benign PSLs are common nevi, blue nevi, atypical or dysplastic nevi, congenital nevi, and pigmented Spitz nevi.[245] Melanoma can develop *de novo* or from these benign lesions; hence a close observation of benign lesions is crucial in melanoma early detection. The different types of melanoma are classified as superficial spreading melanoma (SSM, 50-75%), nodular melanoma (NM, 15-35%), lentigo maligna melanoma (LMM, 5-15%), acral lentiginous melanoma (ALM, 5-10%), desmoplastic melanoma (uncommon), and a miscellaneous group (rare).[239] Besides their type, they are also characterized according to their growth phase. Primary melanoma progress in general through three different growth phases: the *in situ* radial growth phase (RGP), the invasive RGP, and the vertical growth phase (VGP) of tumorigenic melanoma (**Figure 4.3**).[246,247]

[xiii] Reprinted from „Computerized analysis of pigmented skin lesions: A review“, Volume 56, Issue 2, K. Korotkov, R. Garcia, Artificial Intelligence in Medicine, Pages 69-90, Copyright (2012), with permission from Elsevier.

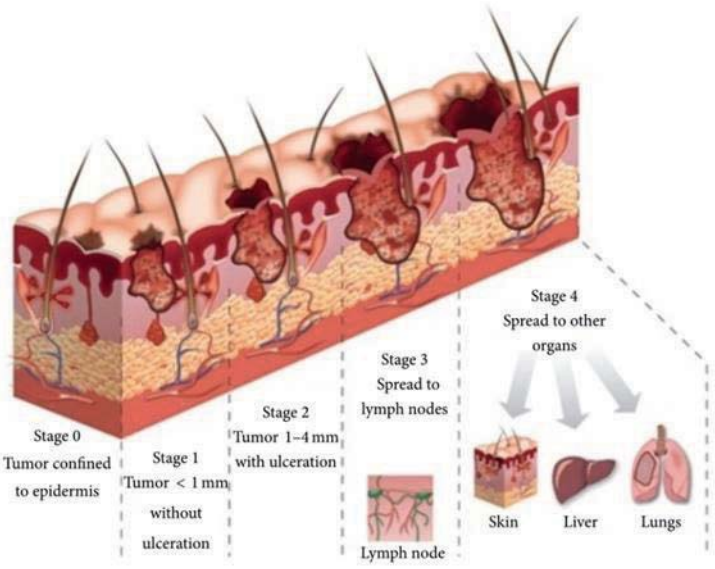

Figure 4.3: Stages in the evolution of melanoma. Radial growth phase (stage 0) and different manifestations of vertical growth phase (stages 1-4). Adapted from Jaworek-Korjakowska et al.[248]

Various exogenic as well as endogenic factors are considered to be risk factors in developing melanoma. Most importantly, exposure to sunlight and a history of sunburns, especially in childhood, as an environmental factor contributes significantly; other sources of UV radiation such as fluorescent light, sunlamps, and tanning beds have also been suggested.[249-253] Weaker factors are considered to be occupation (i.e., pilots or professions exposed to certain chemicals)[254], reproductive factors and oral contraceptive use (levels of estrogen and progesterone)[255,256], as well as obesity, together with other lifestyle factors.[257] Additional host factors are the type, size, number, and location of melanocytic nevi[258], immunosuppression[259,260] and a family history of melanoma[261], suggesting a genetic predisposition. About 8% of all melanoma patients have a familial predisposition and 40% of those carry a germline mutation of the cyclin-dependent kinase inhibitor 2A (CDKN2A) locus, which encodes for the distinct tumor suppressors $p16^{INK4A}$ and $p14^{ARF}$.[262,263] Both control the cell cycle via different ways, $p16^{INK4A}$ by inhibiting cyclin-dependent kinase 4 (CDK4) or CDK6 related phosphorylation and inactivation of the retinoblastoma-associated protein (RB); $p14^{ARF}$ prevents ubiquitylation and degradation of cellular tumor antigen p53, and therefore CDK2A mutations cause uncontrolled proliferation behavior by loss of the cell cycle regulators RB and p53.[264,265] Besides germline mutations, sporadic mutations and UV-induced loss-of-function mutations also play an important role in the $p16^{INK4A}$-CDK4/CDK6-RB pathway and together, they occur in about 90% of all melanoma cases.[266,267] Hence, inhibition of CDK4/CDK6 is a promising target in melanoma drug development.[268] A second important pathway in melanoma development, which is not UV-dependent, is the mitogen-activated protein kinase (MAPK) cascade. Among the most common mutations are $BRAF^{V600E}$ (in about 50% of all melanoma cases), NRAS mutations (approximately 15-20%, i.e. $NRAS^{Q61L/R}$), KIT, and GNAQ/GNA11 mutations.[265]

Since the healing chances for melanoma are very good when detected at an early stage, before the tumor penetrates the epidermis (>99% 5-year survival rate), and decrease significantly for later detections (about 15% 5-year survival rate), the early detection is of particular significance.[269,270] The manifestation of the vast majority of melanoma in visible areas, on the surface of the skin, makes improved screenings and detection methods the most promising levers in the fight against this disease.[271,272] The gold standard in melanoma early detection remains the visual examinations by a physician. However, since the presentation during early stages is very diverse, with different morphologies and histopathologic variants described as spindle cell, small cell, clear cell, myxoid, desmoplastic, or rhabdoid, as well as Schwannian, fibroblastic, smooth muscle, rhabdomyoblastic, or ganglionic differentiations, their detection can be challenging.[273] Even physicians that are trained in visual skin examinations and melanoma detection achieve not more than a sensitivity of about 80% and a specificity of approximately 65%, resulting in false positive or false negative diagnoses in almost one out of 3.[274-277] The visual assessment of pigmented skin lesions relies on classical methods like the ABCDE rule, observing the features asymmetry, border irregularity, color variation, diameter (>6mm), and evolving (or changing), or the 7 points checklist.[278] The latter considers atypical pigment network, blue-whitish veil, atypical vascular pattern, irregular streaks, irregular pigmentation, irregular dots/globules, and regression structures (**Figure 4.4**).[279]

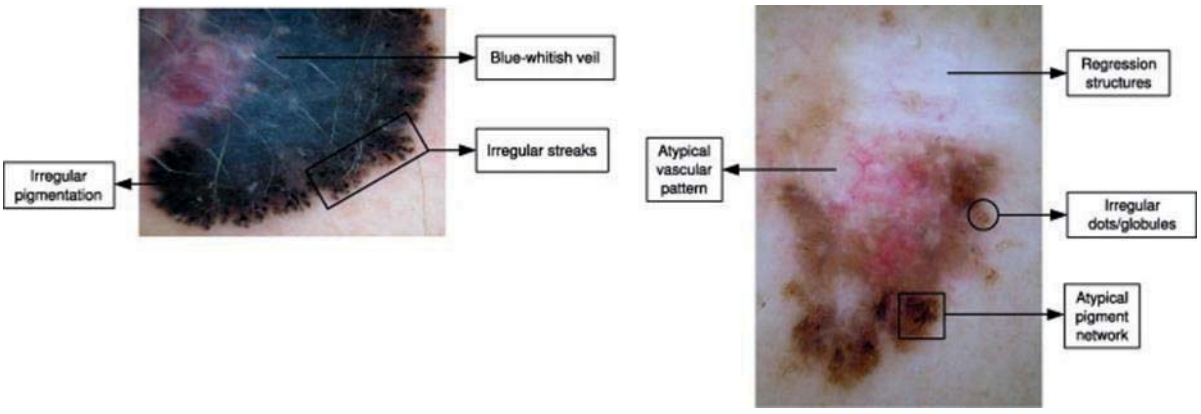

Figure 4.4: Dermoscopic structures with examples for patterns used in the 7 points checklist for melanoma assessment. Reprinted from Capdehourat et al. [280] Copyright (2011), with permission from Elsevier.[xiv]

Efforts have been made in the last two decades in improving the process and the methods of melanoma detection. The former still relies on the same criteria as in the visual examinations, but using machine learning approaches or other combined tools in establishing decision support systems for dermatologists on the basis of digital photography and image analysis.[280,281] Besides increasing accuracy by using digital photography to compare full-body images or single lesion patterns over a course of time, dermoscopy was developed as a relatively simple tool to increase the sensitivity

[xiv] Reprinted from „Toward a combined tool to assist dermatologists in melanoma detection from dermoscopic images of pigmented skin lesions“, Volume 32, G. Capdehourat, A. Corez, A. Bazzano, R. Alonso, P. Musé, Pattern Recognition Letters, Pages 2187-2196, Copyright (2011), with permission from Elsevier.

in diagnosis. A handheld microscope and polarized light enable the imaging of deeper structures of skin lesions and have been reported to increase the accuracy in melanoma diagnosis by 5-30%, depending on the user's experience.[269] But far more sophisticated detection methods have also been developed: Multispectral imaging in the spatial domain (MSS, radiation measurement at a particular point or region) like the MelaFind® technology by Mela Sciences[282-284], as well as in the frequency domain (MSF, radiation measurement as function of wavelength) like IR and Raman spectroscopy, Tetrahertz (THz) imaging, infrared (IR) in the spatial domain, high frequency ultrasound, confocal laser scanning microscopy (CLSM, fluorescence or reflectance) to reveal cellular and nuclear details *in vivo,* and optical coherence tomography (OCT) deliver high-resolution 3D images of biological tissue.[269,285] Still, despite these major improvements in diagnosis sensitivity and specificity, all of the sophisticated methods have their shortcomings, especially in competing in price and ease of use with visual detection and can only act supportively after a physician's decision as to which one of hundreds of lesions needs to be investigated further.

A former project in our group with the aim of fluorescent labeling of cell surface glycans via strain-promoted azide-alkyne cycloaddition (SPAAC) for the investigation of topology differences in various cell lines, resulted in a promising finding to fulfill this need. We found by chance that the fluorescent compound we were using for our labeling studies showed an uptake in murine and human melanoma cells. A broad variety of cell lines from different tissues, including HeLa (human cervix adenocarcinoma), HCT 116 (human colorectal carcinoma), Hep G2 (human hepatocellular carcinoma), HEK-293 (human embryonic kidney), H4 (human neuroglioma), A549 (human epithelial lung carcinoma), SH-SY5Y (human bone marrow neuroblastoma), U-2 OS (human osteosarcoma), U-251 MG (human glioblastoma astrocytoma), HUVEC (human umbilical vein/vascular endothelium) and MCF7 (human mammary gland adenocarcinoma), were incubated with an azide-modified mannose.[286] This sugar is integrated by the glycan biosynthetic machinery into various glycoconjugates, thus presenting azide functional groups for bioorthogonal labeling on the surface.[287,288] A subsequent incubation of the cells with a fluorescently labeled cyclooctyne compound results in a strain-promoted [3+2] azide-alkyne cycloaddition and therefore a fluorescent labeling of the cell membranes (

Figure 4.5).[289] In all the investigated cell lines a fluorescent labeling of the cell membranes was achieved, and without sugar incubation though, no fluorescent signal was detectable, since the fluorescent cyclooctyne compound showed no membrane permeation properties. This picture changed dramatically when we used murine or human melanoma cell lines (MEB4 or SK-Mel 28). When the melanoma cells were incubated with the fluorescent compound, in the presence or absence of azide modified sugars, an intensive staining of the complete cytoplasm was observed. Based on this observation, we developed the idea of using the uptake in melanoma cells and therefore their fluorescent staining as a detection method in the early diagnosing of melanoma.[290] A melanoma-specific uptake after application of a fluorescent compound on the skin as ointment or spray, incubating on and subsequently washing off the treated skin areas, would allow for the identification of melanoma cells on the skin surface by excitation of the fluorophore and detection of a fluorescent signal. Depending on the signal intensity and equipment sensitivity, a detection of a

melanoma-associated lesion would be possible already at a very early stage with only few degenerated cells, therefore facilitating a new time- and cost-efficient diagnostic method. Based on this hypothesis, it was the aim of this study to synthesize a combinatorial library of derivatives of the fluorescein-labeled cyclooctyne lead structure as potential melanoma markers and microscopically screen the compounds for their cellular uptake in melanoma cells to identify structure-function relationships. Additionally, we sought to create an extension of the 2D cell culture and screening experiments featuring novel 3D cell culture models.

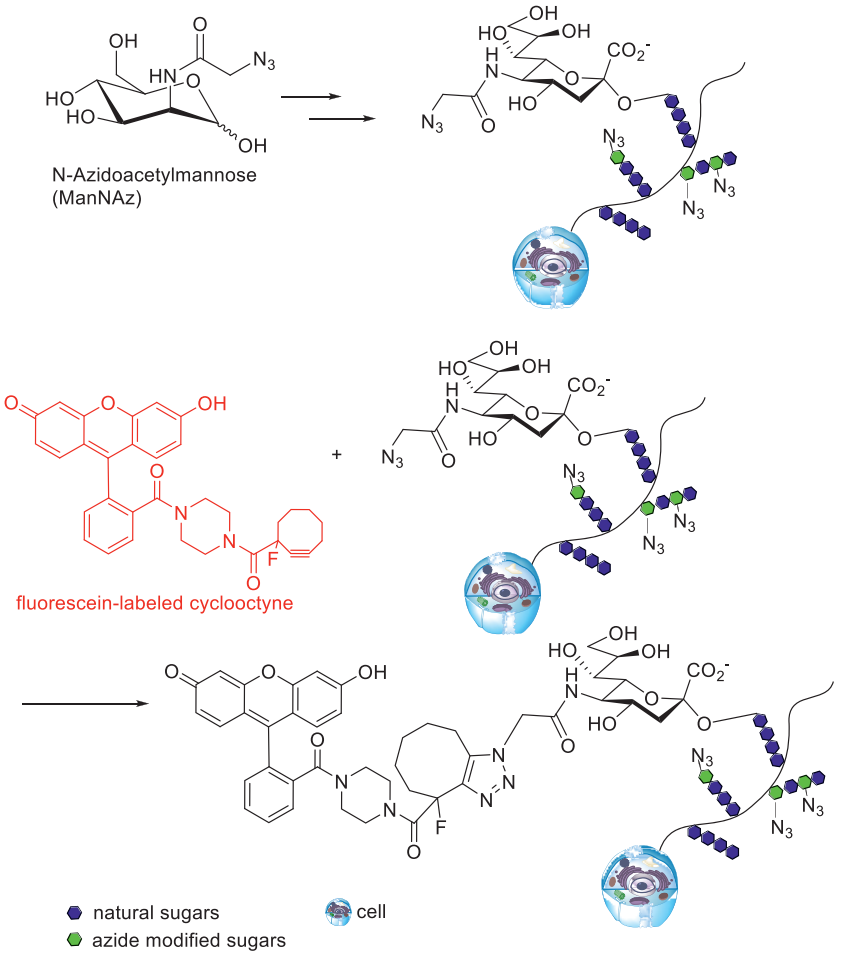

Figure 4.5: Labeling of cell surface glycans using the azide modified mannose ManNAz and a fluorescein labeled cyclooctyne.

.

4.2 Strategy in synthesis

The lead structure **4.1** in the synthesis of a combinatorial library of potential melanoma markers consists mainly of 3 building blocks: a) a cyclooctyne moiety, b) a piperazine linker, and c) a fluorescein as a dye (**Scheme 4.1**).

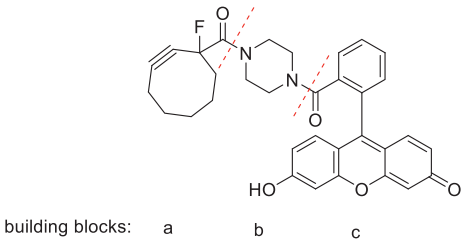

4.1

Scheme 4.1: Lead structure in the synthesis of a combinatorial library consisting of 3 building blocks: a) cyclooctyne moiety, b) piperazine linker, c) fluorescein dye

In the first library we synthesized, the cyclooctyne building block a) was varied to different kinds of aliphatic and aromatic moieties and in the second library not only building block a) but also the piperazine linker b) was modified. The results were compared to a third library with variations of linker b) and the fluorophore c) that was synthesized in an earlier work.[290]

4.2.1 Synthesis of combinatorial library 1: varying the cyclooctyne building block a) of the lead structure

In order to investigate a potential influence of the cyclooctyne moiety on the cellular uptake in melanoma cells, this building block was substituted by various aliphatic and aromatic residues: alkane and alkene structures, linear, branched, and circular, 3-, 5-, 6-, 7-, and 8-membered rings, aromatic, halogenated, and heterocyclic structures. Therefore, a 4-step synthetic methodology was developed (**Scheme 4.2**).

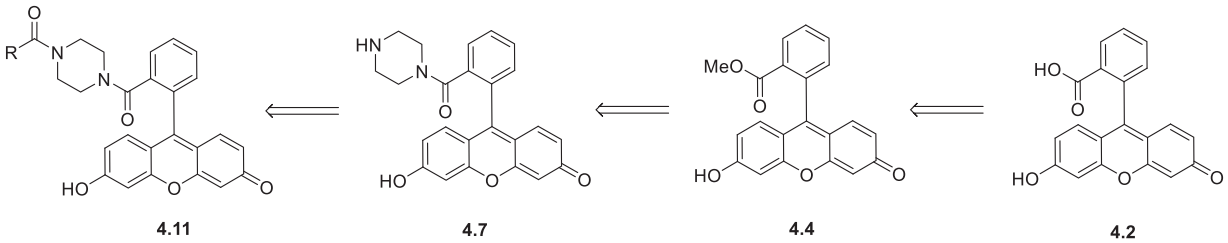

Scheme 4.2: Retrosynthetic methodology in the synthesis of library 1.

In the first step of the synthesis, the commercially available fluorescein dye **4.2**, first described by Baeyer in 1871[91], was converted into the fluorescein methyl ester **4.4** using sulfuric acid, molecular sieves and methanol, or thionyl chloride and methanol (**Scheme 4.3**).[291] Since as a free acid, the carboxy group of fluorescein can undergo an intramolecular cyclization with the xanthene moiety of the dye to build the spirolactone form **4.3**, the esterification allows for a better accessibility of the functional group for further modifications.

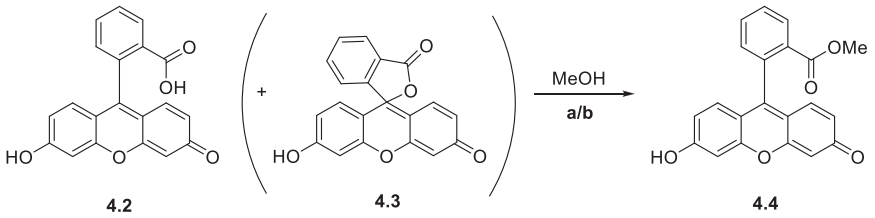

Scheme 4.3: Synthesis of fluorescein methyl ester. a) H_2SO_4, molecular sieves 3A, reflux, 18 h; b) $SOCl_2$, reflux, 16 h.

In the next step, one of the secondary amine groups of piperazine was selectively activated using trimethylaluminum, and the fluorescein piperazine amide **4.7** was formed in a two-step-one-pot approach (**Scheme 4.4**).

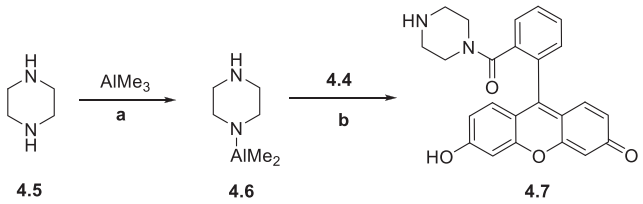

Scheme 4.4: Synthesis of fluorescein piperazine amide. a) DCM, rt, 14 h; b) DCM, reflux, 18 h.

To perform the subsequent coupling to (mostly commercially available) carboxylic acids, their carboxy group was activated first, again in a two-step-one-pot approach, as pentafluorophenyl ester **4.10** using pentafluorophenyl trifluoroacetate **4.9** before

coupling to the fluorescein piperazine amide **4.7** (**Scheme 4.5**). The resulting derivatives of lead structure **4.1** could be obtained in low to moderate yields (10-50%).

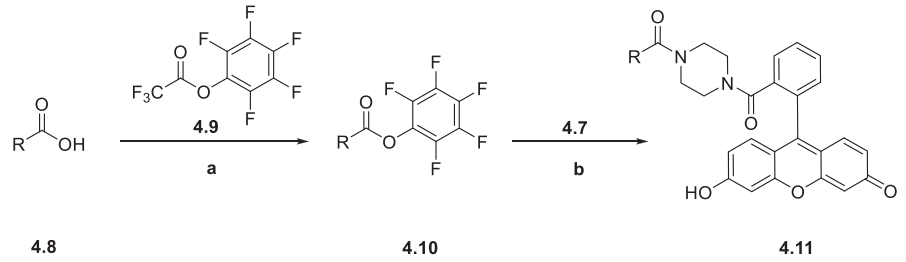

Scheme 4.5: Activation of carboxylic acids as pentafluorophenyl ester and subsequent coupling to fluorescein piperazine amide. a) DIPEA, DCM, 0 °C – rt, 1.5 h; b) DIPEA, DMF, rt, 2 h.

All the carboxylic acids that were used as building blocks in the synthesis of the combinatorial library 1 (shown in **Scheme 4.6**) were commercially available, except the cyclooctene carboxylic acid used to obtain fluorescent derivative **4.23**, which had to be synthesized in two steps from the unfunctionalized (*Z*)-cyclooctene, as depicted in (**Scheme 4.7**), using ninhydrin and periodic acid for a subsequent oxidative cleavage.[292]

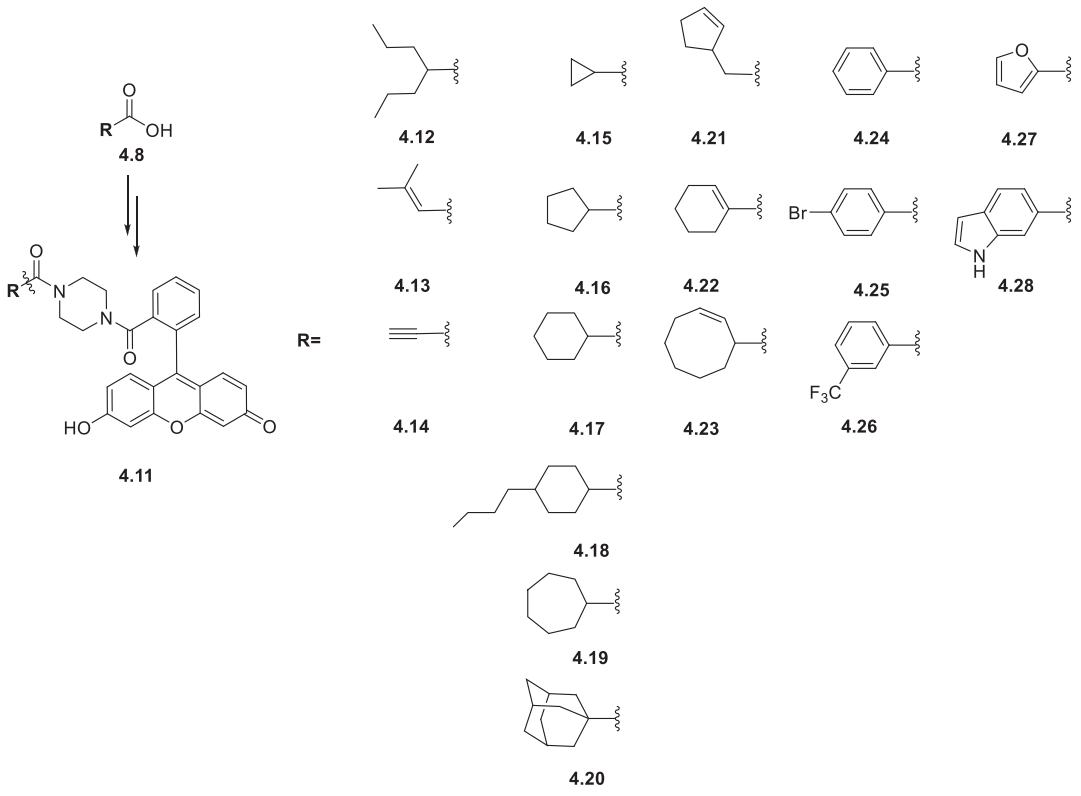

Scheme 4.6: Compounds synthesized in library 1. All carboxylic acids were commercially available, except the cyclooctenecarboxylic acid used for **4.23** which had to be synthesized in a separate approach (**Scheme 4.7**).

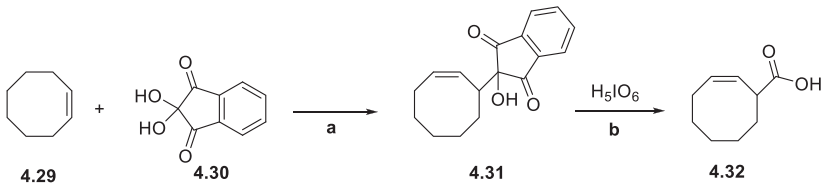

Scheme 4.7: Synthesis of cyclooctene carboxylic acid in two steps from (*Z*)-cyclooctene using ninhydrin and periodic acid. a) Toluene, 140 °C, 40 h; b) Et_2O, 0 °C - rt, 5 h.

An alternative approach for the coupling of aliphatic or aromatic moieties to the fluorescein piperazine amide **4.7** using a direct reaction from an acyl chloride in one step with triethylamine and the amide was not successful.[293] The desired product was formed, yet with numerous side products it could not be isolated successfully. Since not only amines but also alcohols react easily with acyl chlorides, it is likely that one side reaction was the esterification on the xanthene hydroxyl group of fluorescein.

4.2.2 Synthesis of combinatorial library 2: Varying the piperazine linker b) (and the cyclooctyne building block a)) of the lead structure

After synthesizing a library of compounds containing derivatives with variations in building block a), the influence of the piperazine linker was investigated by the introduction of a small variation. Instead of the 6-membered piperazine ring, the 7-membered homopiperazine was used as a linker between dye and aliphatic building block (**Scheme 4.8**).

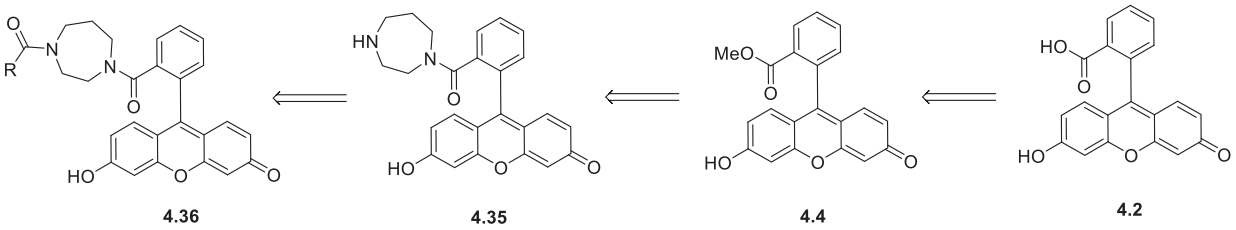

Scheme 4.8: Retrosynthetic methodology in the synthesis of library 2.

The synthesis followed the same principles and reactions that were used in library 1 (chapter 4.2.1), starting with the esterification of fluorescein, followed by a selective activation of one of the secondary amines in homopiperazine with trimethylaluminum and coupling to the fluorescein methyl ester (**Scheme 4.9**).

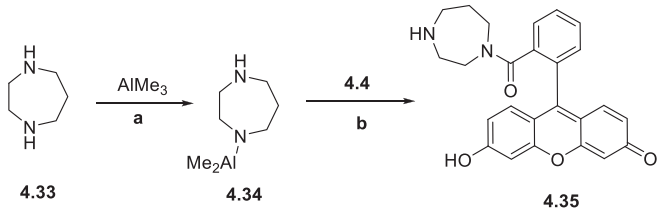

Scheme 4.9: Synthesis of fluorescein homopiperazine amide. a) DCM, rt, 14 h; b) DCM, reflux, 10 h.

In the following step, carboxylic acids, already used in library 1 as building block a), were coupled to the fluorescein homopiperazine amide **4.35** using the two-step-one pot activated coupling with pentafluorophenyl trifluoroacetate (**Scheme 4.10**, **A**), and also using a standard peptide coupling method with hydroxybenzotriazole (HOBt) and diisopropylcarbodiimide (DIC) (**Scheme 4.10**; **B**), resulting in slightly higher yields of 40-50% on route **B** compared to 10-50% (20-25% on average) on route **A**.

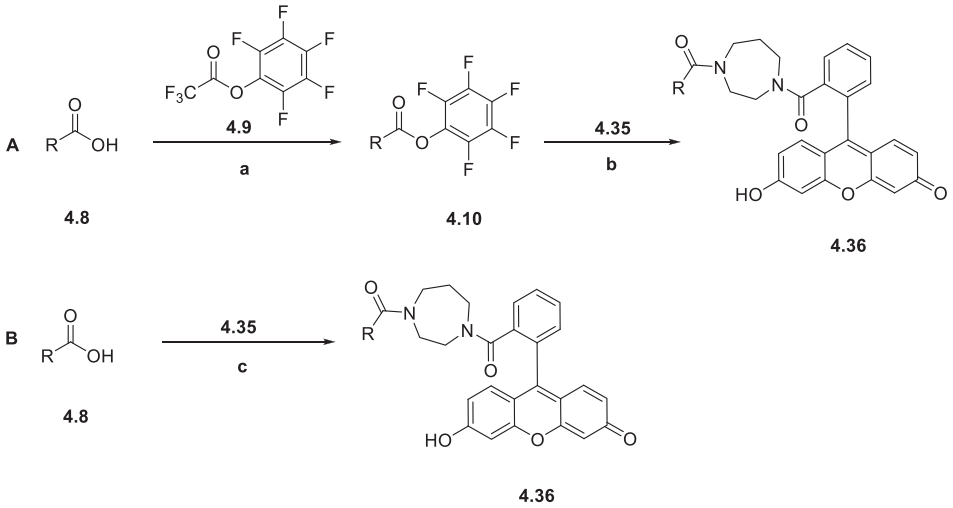

Scheme 4.10: Coupling of aliphatic building blocks to the fluorescein homopiperazine amide 4.35 using either an activation of carboxylic acids as pentafluorophenyl ester 4.10 and subsequent coupling to fluorescein piperazine amide (upper line, A) or a direct peptide coupling method with HOBt and DIC (lower line, B). a) DIPEA, DCM, 0 °C – rt, 1.5 h; b) DIPEA, DMF, rt, 2 h; c) DIPEA, DMF, rt, 12 h.

As aliphatic building blocks in library 2, the commercially available cyclohexanecarboxylic acid, 2-propylpentancarbooxylic acid, 1-adamantanecarboxylic acid, and the synthesized 1-fluorocyclooct-2-yne-1-carboxylic acid were chosen to represent a broad variety of building blocks in only few examples. Additionally, the 1-(adamantane-1-carbonyl)-pyrrolidine-2-carboxylic acid was selected to include an additional spacer between building blocks a) and b) (**Scheme 4.11**). The insertion of an additional pyrrolidin spacer in the adamantane derivative **4.41** did not have a negative impact on the cellular uptake.

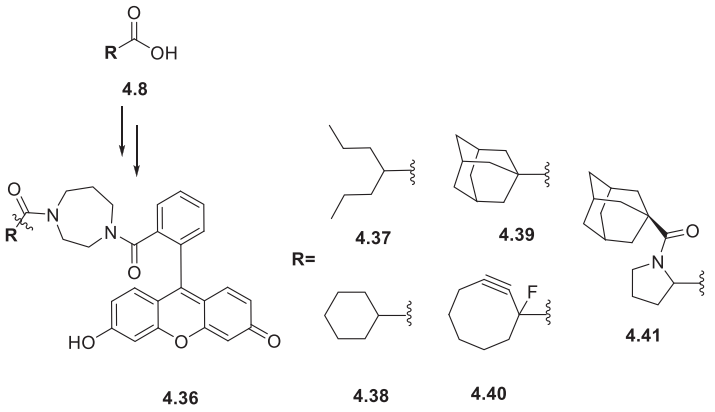

Scheme 4.11: Compounds synthesized in library 2. All carboxylic acids were commercially available, except the cyclooctynecarboxylic acid used for **4.40** which had to be synthesized in a separate approach (**Scheme 4.12**).

The fluorinated cyclooctynecarboxylic acid **4.47**, that was used in the synthesis of **4.40,** was synthesized in a separate approach, following a route starting from cyclooctanone **4.42** (**Scheme 4.12**).[294]

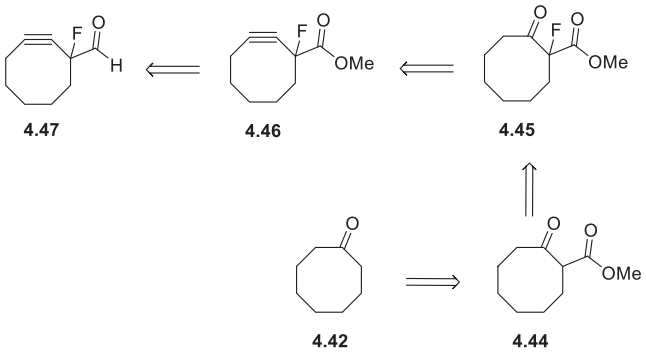

Scheme 4.12: Retrosynthetic strategy in the synthesis of the fluorinated cyclooctynecarboxylic acid **4.47**.[290,294]

Using dimethyl carbonate and sodium hydride as a strong base, the cyclooctanone **4.42** could be converted into the corresponding cyclooctanonemethyl ester **4.44** in the ketone α-position resulting in a mixture of tautomeric forms (**Scheme 4.13**).

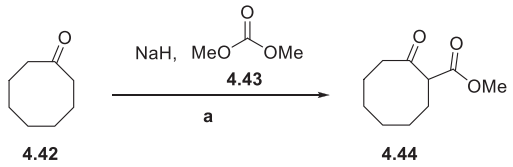

Scheme 4.13: Synthesis of cyclooctanonemethyl ester. a) Toluene, 80 °C, 3 h.

Since this building block in the lead structure **4.1** was formerly used in strain-promoted "click reactions" (SPAAC) with azide modified sugar units within cell surface glycans, a fluorine atom was installed in the propargylic position that has been shown to increase the rate of the SPAAC due to its electron withdrawing properties.[295-297] Selectfluor®, first described in 1992[298], is a commercially-available fluorinating reagent that was applied in this reaction (**Scheme 4.14**).

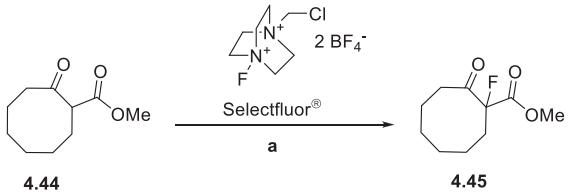

Scheme 4.14: Introduction of a fluorine atom using Selectfluor® to obtain the fluorinated cyclooctanonemethyl ester. a) ACN, 0 °C – 55 °C, overnight.

In the next step, the formation of the alkyne bond could be achieved via the introduction and subsequent elimination of an enol triflate using potassium bis(trimethylsilyl)amide (KHMDS), *N*-phenyl-bis(trifluoromethanesulfonimide) and lithium diisopropylamide (LDA) (**Scheme 4.15**).

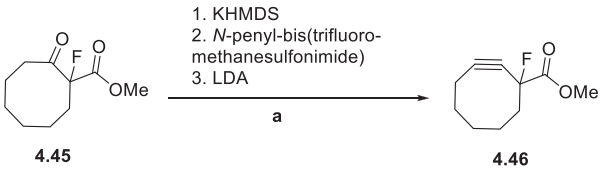

Scheme 4.15: Introduction of the alkyne bond to obtain the fluorinated cyclooctynemethyl ester. a) abs. THF, -78 °C – rt, overnight.

In the final step, the methyl ester **4.46** was hydrolyzed using lithium hydroxide (LiOH) to obtain the free carboxylic acid **4.47**.

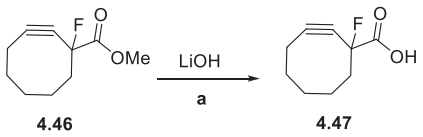

4.46 **4.47**

Scheme 4.16: Hydrilization of the fluorinated cyclooctynemethyl ester using LiOH to obtain the free carboxylic acid. a) MeOH/H_2O, 50 °C, 2 h.

4.2.3 Combinatorial library 3: Varying the piperazine linker b) and the fluorophore building block c) of the lead structure

In an earlier work[xv], a similar combinatorial library has been synthesized that substitutes the piperazine linker (building block b)) of lead structure **4.1** with a diaminobutane linker and the fluorescein building block c) with several (as NHS esters) commercially available dyes: Alexa Fluor™ 488 (**4.49**), Alexa Fluor™ 594 (**4.50**), Alexa Fluor™ 700 (**4.51**, structure not published), ATTO 488 (**4.52**), ATTO 532 (**4.53**), ATTO 655 (**4.54**, structure not published), carboxy-fluorescein (**4.55**), Cy3 (**4.56**), and Cy5 (**4.57**) (**Scheme 4.17**). Results in the cellular uptake of compounds from the synthesized libraries 1 and 2 were compared to those from the earlier library 3.

[xv] Olshausen, B. *Neue Fluorophor-Verbindungen als mögliche Werkzeuge zur Detektion von malignen Melanomen*, (2014).

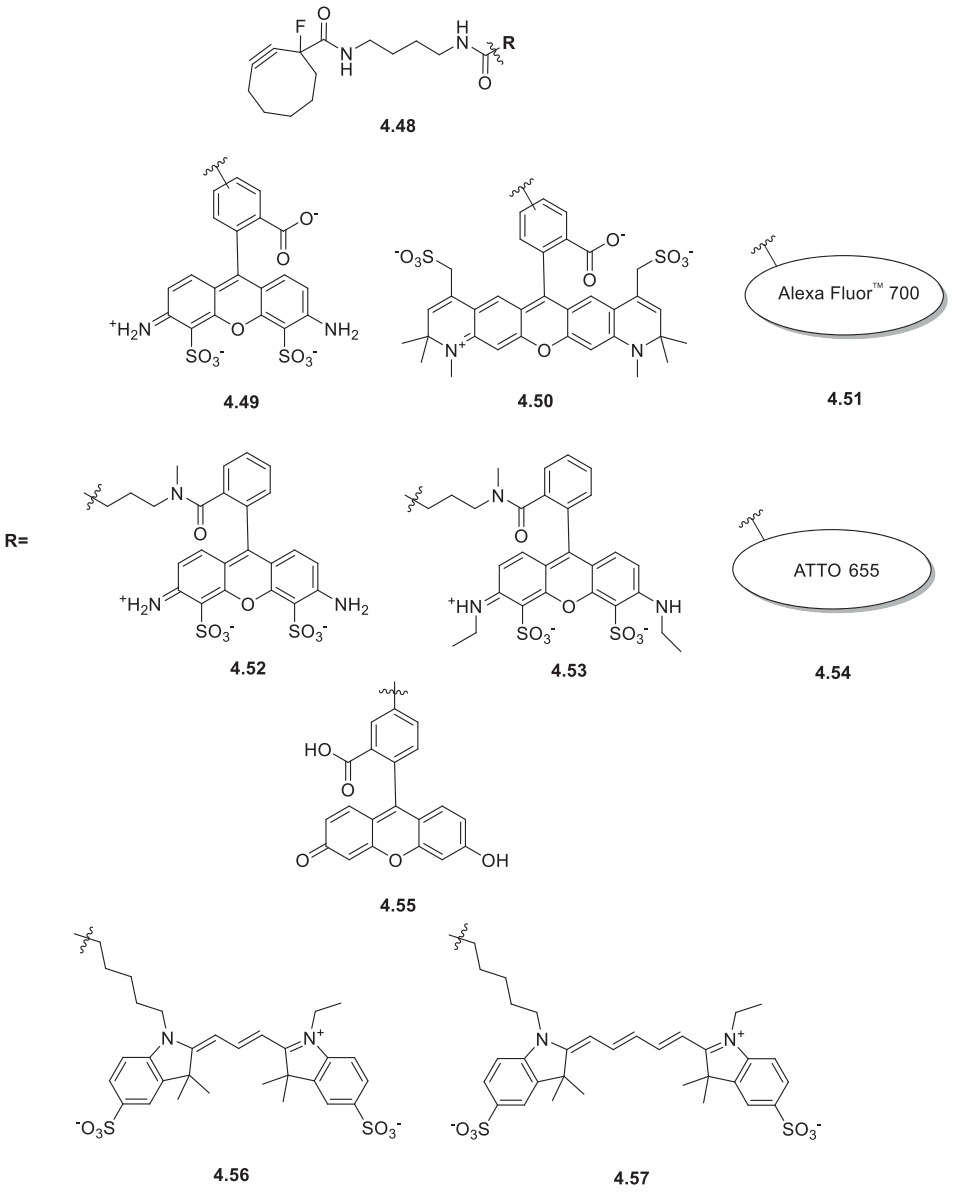

Scheme 4.17: Combinatorial library 3 with variations of linker building block b) and fluorophore building block c).

4.3 Investigating the cellular uptake of compounds from libraries 1 - 3

4.3.1 2D cell screenings via confocal microscopy

In order to investigate the uptake of the synthesized compounds in 2-dimensional cell cultures, cells of the human melanoma cell line SK-Mel 28, primary normal human epidermal melanocytes (NHEM), and HeLa cells (human cervical adenocarcinoma) were treated with the synthesized fluorescent derivatives (for details see chapter 6.2.5.1) and their accumulation in the cells was evaluated via confocal laser scanning microscopy (CLSM).

4.3.1.1 Determination of screening parameters

Prior to the screening of the synthesized lead structure derivatives, the general screening parameters, including compound concentration and incubation time, were optimized for the lead structure **4.1** (**Scheme 4.18**) in SK-Mel 28 cells to allow for a direct comparison between lead and candidates under defined conditions.

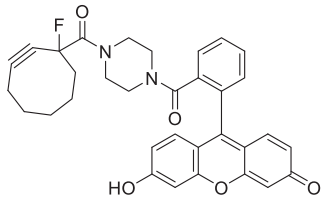

4.1

Scheme 4.18: Lead structure **4.1** that was used to determine optimal screening parameters for the synthesized compounds.

In a first experiment, the melanoma cells were incubated with 20 µM **4.1** for 1 h, 2 h, 3 h, 4 h (**Figure 4.6 a, b, c, d**), 5 h, 6 h, and overnight (21 h) (**Figure 4.7 a, b, c**) to optimize incubation time. The concentration of 20 µM was known from earlier studies to allow for sufficient cell labeling. Since no fluorescence signal could be detected for the incubation times of 1-3 h and there was no significant improvement in intensity observed for incubation times >5 h, the optimal time span for the following screening was set to 4-5 h incubation. In a subsequent experiment, the concentration of **4.1** was reduced to determine the lowest possible concentration while retaining sufficient cell staining. For 5 h, SK-Mel 28 cells were incubated with 20 µM, 15 µM, 10 µM, and 5 µM of lead structure **4.1** (**Figure 4.8 a, b, c, d**). A reduction of concentration could not be achieved without a reduction of the fluorescence signal and therefore the optimal concentration for the following screening was determined as 20 µM.

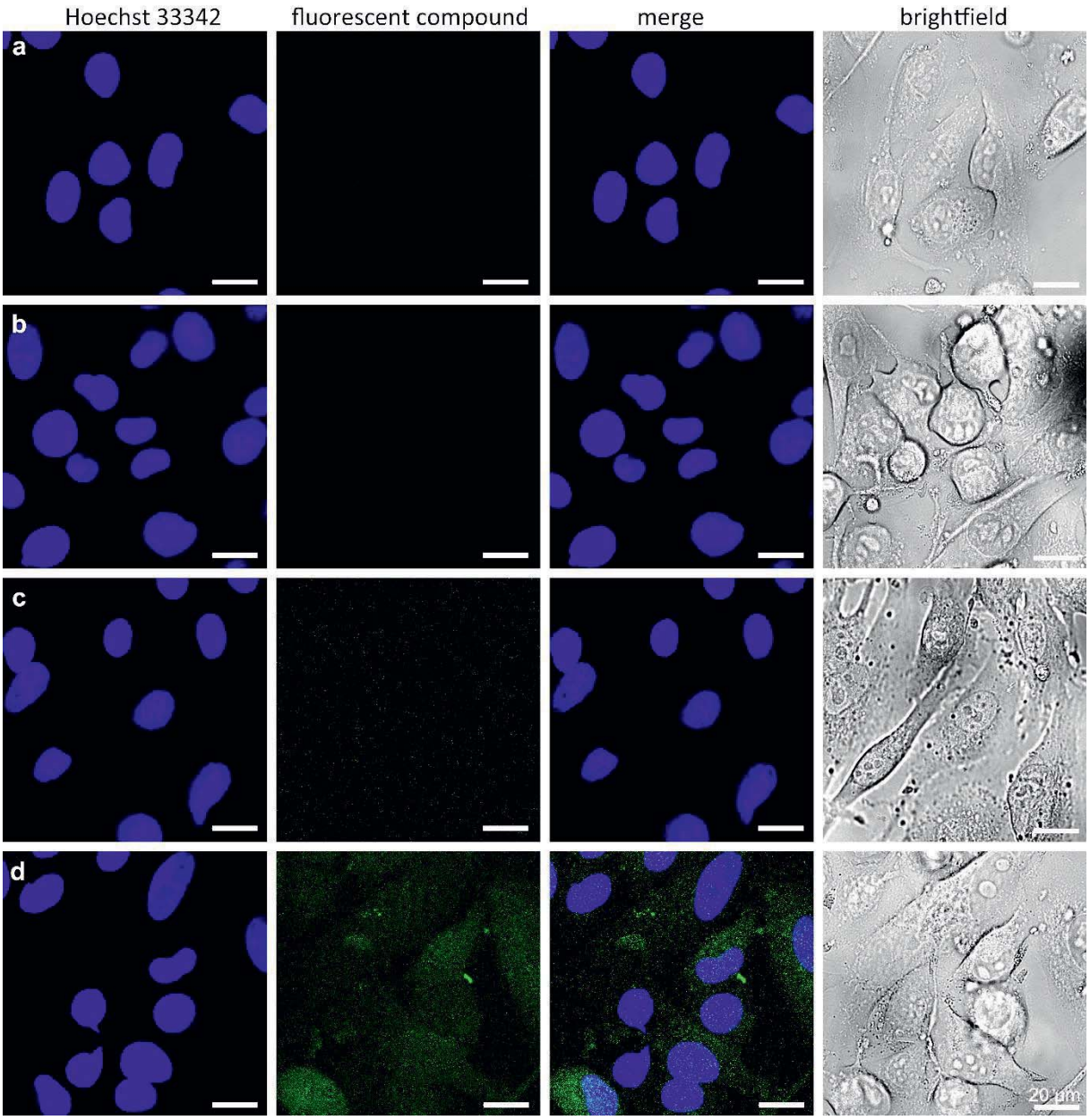

Figure 4.6: Confocal laser scanning microscopy of SK-Mel 28 cells after incubation with 20 µM lead structure 4.1 for a) 1 h, b) 2 h, c) 3 h, and d) 4 h. 8x10^4 SK-Mel 28 cells were seeded in an 8-well chamber slide 3 h prior to treatment with 20 µM **4.1** for 1 h, 2 h, 3 h and 4 h. Cells were washed three times with PBS before staining the nuclei with Hoechst 33342 (Invitrogen, 0.5 µg/ml for 20 min). The visualization was performed using a Leica TCS-SP-5 (DMI6000) inverted microscope with an HCX PL APO 63x/1.20 water UV objective. Fluorophores were excited using an UV laser (λ_{exc}= 351 and 364 nm) for the Hoechst 33342 staining and an argon ion laser (λ_{exc}= 488 nm) for the fluorescent compound. The images were taken in a sequential mode to avoid an overlap of emission spectra from Hoechst 33342 and fluorescein. Using the acquisition software Leica Application Suite (LAS) AF 2.2.2.4842, the picture ratio was adjusted to 1024 × 1024 pixels 8 bit depth. Scale bar: 20 µm.

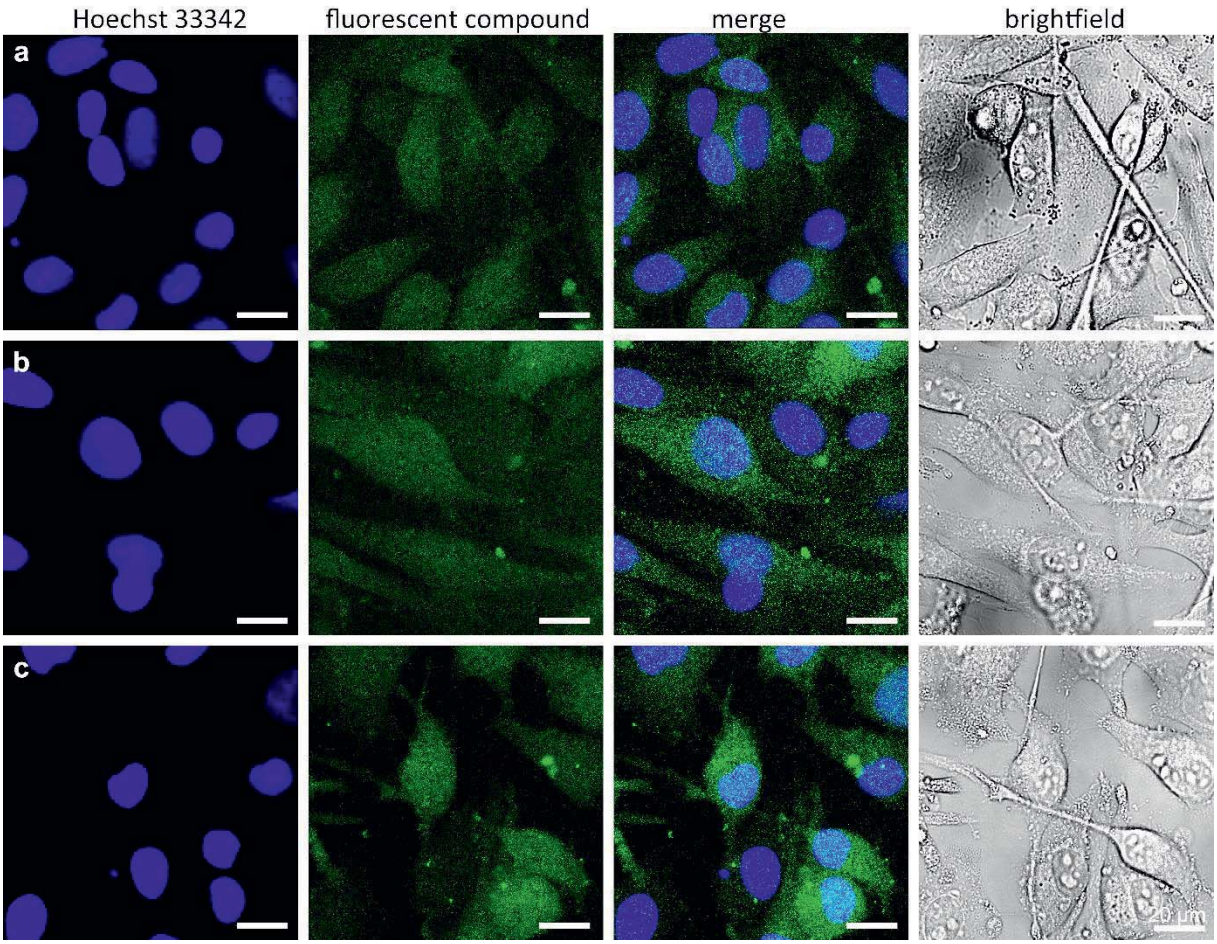

Figure 4.7: Confocal laser scanning microscopy of SK-Mel 28 cells after incubation with 20 µM lead structure 4.1 for a) 5 h, b) 6 h, and c) overnight (21 h). 8x10^4 SK-Mel 28 cells were seeded in an 8-well chamber slide 3 h prior to treatment with 20 µM **4.1** for 5 h, 6 h, and 21 h. Cells were washed three times with PBS before staining the nuclei with Hoechst 33342 (Invitrogen, 0.5 µg/ml for 20 min). The visualization was performed using a Leica TCS-SP-5 (DMI6000) inverted microscope with an HCX PL APO 63x/1.20 water UV objective. Fluorophores were excited using an UV laser (λ_{exc}= 351 and 364 nm) for the Hoechst 33342 staining and an argon ion laser (λ_{exc}= 488 nm) for the fluorescent compound. The images were taken in a sequential mode to avoid an overlap of emission spectra from Hoechst 33342 and fluorescein. Using the acquisition software Leica Application Suite (LAS) AF 2.2.2.4842, the picture ratio was adjusted to 1024 × 1024 pixels 8 bit depth. Scale bar: 20 µm.

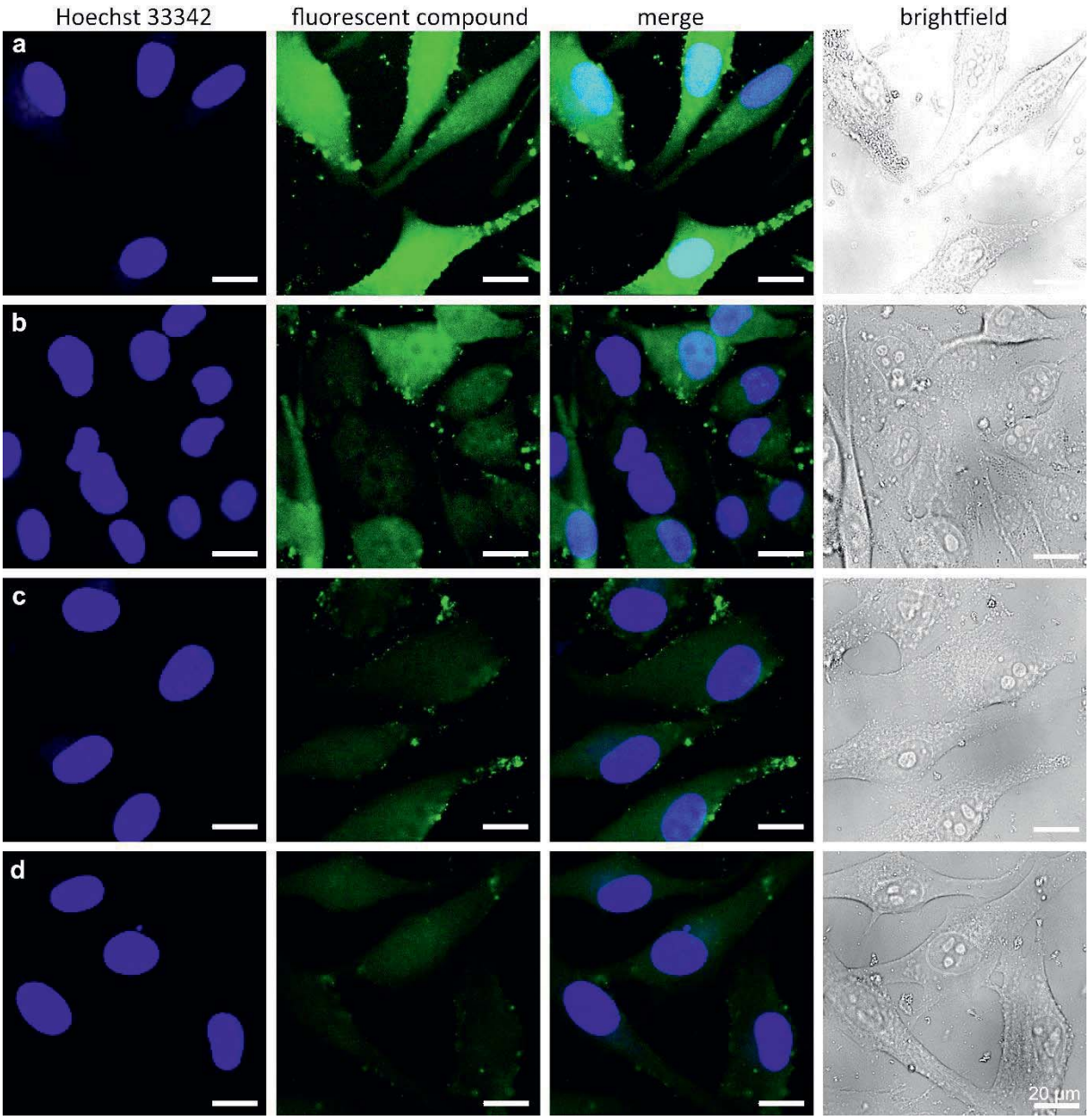

Figure 4.8: Confocal laser scanning microscopy of SK-Mel 28 cells after incubation with a) 20 µM, b) 15 µM, c) 10 µM, and d) 5 µM of lead structure 4.1 for 5 h. 8x10^4 SK-Mel 28 cells were seeded in an 8-well chamber slide 3 h prior to treatment with 20 µM **4.1** for 5 h. Cells were washed three times with PBS before staining the nuclei with Hoechst 33342 (Invitrogen, 0.5 µg/ml for 20 min). The visualization was performed using a Leica TCS-SP-5 (DMI6000) inverted microscope with an HCX PL APO 63x/1.20 water UV objective. Fluorophores were excited using an UV laser (λ_{exc}= 351 and 364 nm) for the Hoechst 33342 staining and an argon ion laser (λ_{exc}= 488 nm) for the fluorescent compound. The images were taken in a sequential mode to avoid an overlap of emission spectra from Hoechst 33342 and fluorescein. Using the acquisition software Leica Application Suite (LAS) AF 2.2.2.4842, the picture ratio was adjusted to 1024 × 1024 pixels 8 bit depth. Scale bar: 20 µm.

4.3.2 Negative screening results

All the compounds shown in library 1 (**Scheme 4.6**), 2 (**Scheme 4.11**), and 3 (**Scheme 4.17**), as well as their precursors fluorescein, fluorescein methyl ester, fluorescein piperazine amide, and fluorescein homopiperazine amide, were investigated for their florescent staining ability in SK-Mel 28 melanoma cells, “healthy” melanocytes NHEM, and as a control HeLa cells, at a concentration of 20 µM for 4-5 h. The majority of the screened derivatives did not show a fluorescent staining of either of the cell lines, nor did fluorescein alone, the fluorescein methyl ester, or the fluorescein piperazine amide **4.7**. Exemplary confocal images from the screening of cyclohexane derivative **4.17** are shown in **Figure 4.9**. No significant fluorescent signal is observed in column two (signal of the fluorescent compound) for the melanoma and the control cells in line **a** and **c**. A weak signal in the NHEM cells (panel **b**) is also detected during the visualization of untreated melanocytes (**Figure 4.10**, panel **b**) and is therefore considered a background fluorescence of the cells.

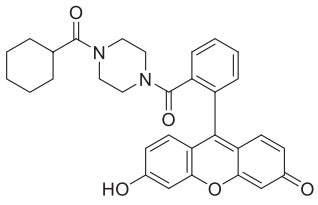

4.17

Scheme 4.19: Structure of cyclohexane derivative **4.17**.

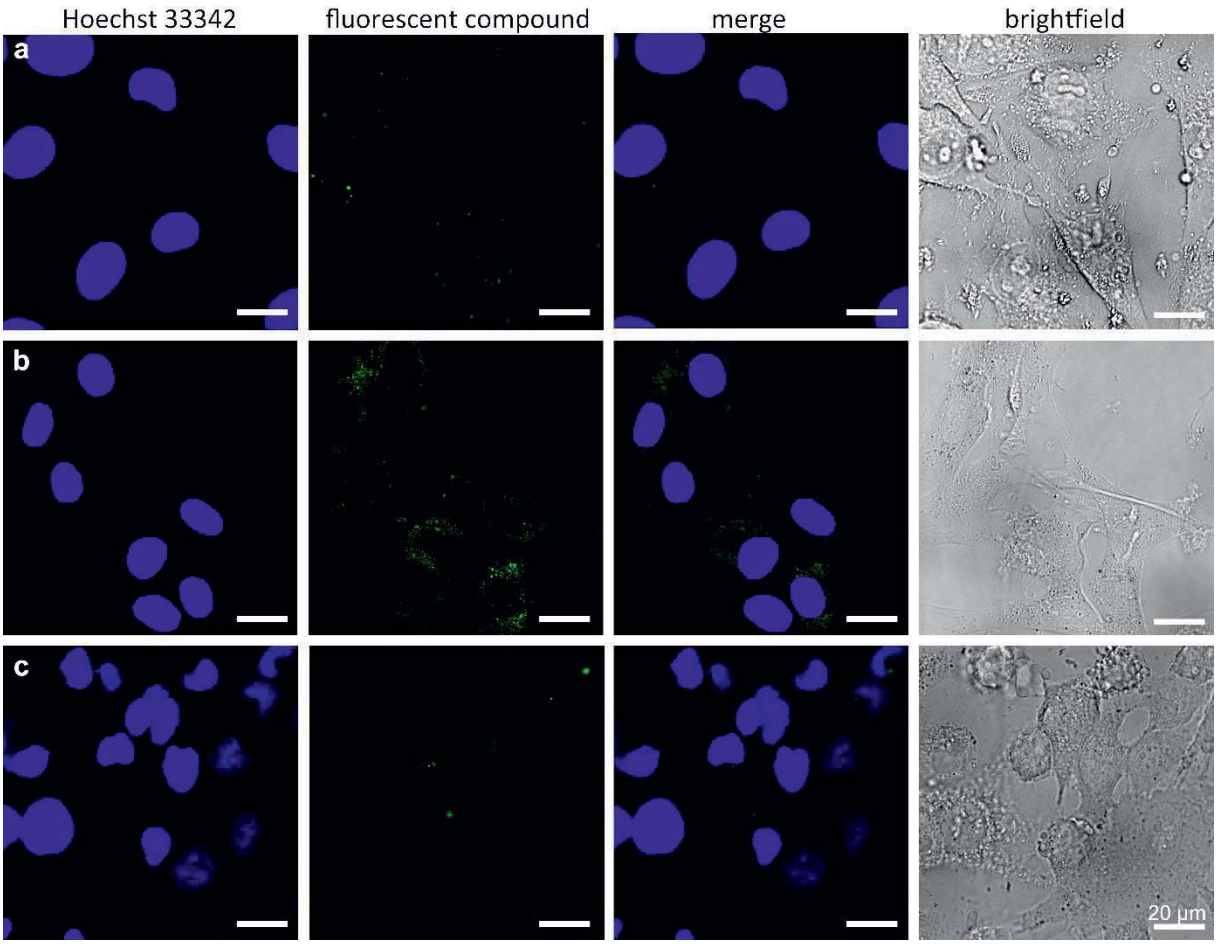

Figure 4.9: Confocal laser scanning microscopy of a) SK-Mel 28 cells, b) NHEM, and c) HeLa cells after incubation with 20 µM of derivative 4.17 for 5 h. 4x10^4 of the respective cell line/primary cells were seeded in an 8-well chamber slide 2 d prior to treatment with 20 µM **4.17** for 5 h. Cells were washed three times with PBS before staining the nuclei with Hoechst 33342 (Invitrogen, 0.5 µg/ml for 20 min). The visualization was performed using a Leica TCS-SP-5 (DMI6000) inverted microscope with an HCX PL APO 63x/1.20 water UV objective. Fluorophores were excited using an UV laser (λ_{exc}= 351 and 364 nm) for the Hoechst 33342 staining and an argon ion laser (λ_{exc}= 488 nm) for the fluorescent compound. The images were taken in a sequential mode to avoid an overlap of emission spectra from Hoechst 33342 and fluorescein. Using the acquisition software Leica Application Suite (LAS) AF 2.2.2.4842, the picture ratio was adjusted to 1024 × 1024 pixels 8 bit depth. Scale bar: 20 µm.

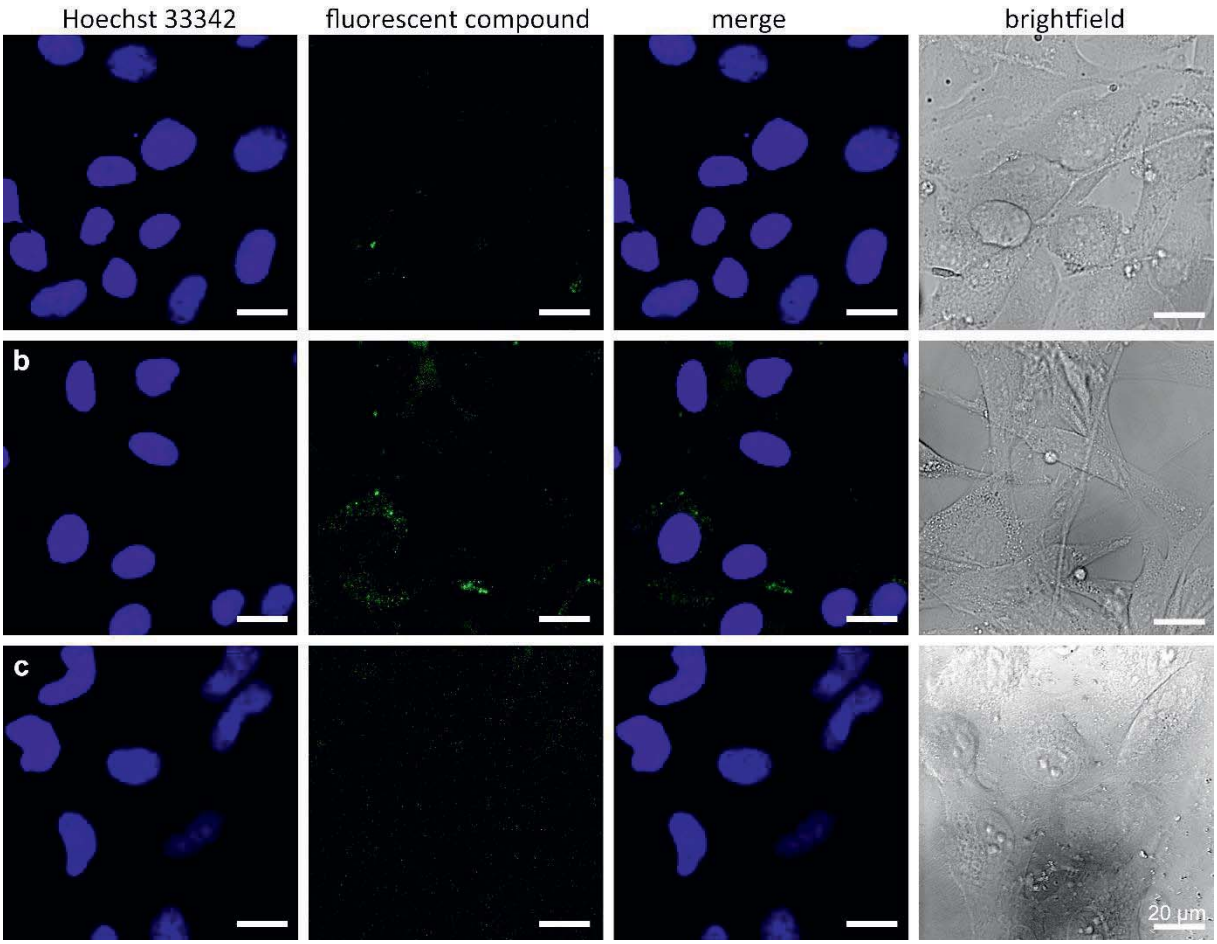

Figure 4.10: Confocal laser scanning microscopy of untreated a) SK-Mel 28 cells, b) NHEM, and c) HeLa cells. 4x10^4 of the respective cell line/primary cells were seeded in an 8-well chamber slide 2 d prior to visualization. Nuclei were stained with Hoechst 33342 (Invitrogen, 0.5 µg/ml for 20 min). The visualization was performed using a Leica TCS-SP-5 (DMI6000) inverted microscope with an HCX PL APO 63x/1.20 water UV objective. Fluorophores were excited using an UV laser (λ_{exc}= 351 and 364 nm) for the Hoechst 33342 staining and an argon ion laser (λ_{exc}= 488 nm) for the fluorescent compound. The images were taken in a sequential mode to avoid an overlap of emission spectra from Hoechst 33342 and fluorescein. Using the acquisition software Leica Application Suite (LAS) AF 2.2.2.4842, the picture ratio was adjusted to 1024 × 1024 pixels 8 bit depth. Scale bar: 20 µm.

The derivatives and precursors from all libraries that did not show any staining ability under the investigated conditions are summarized in **Scheme 4.20**.

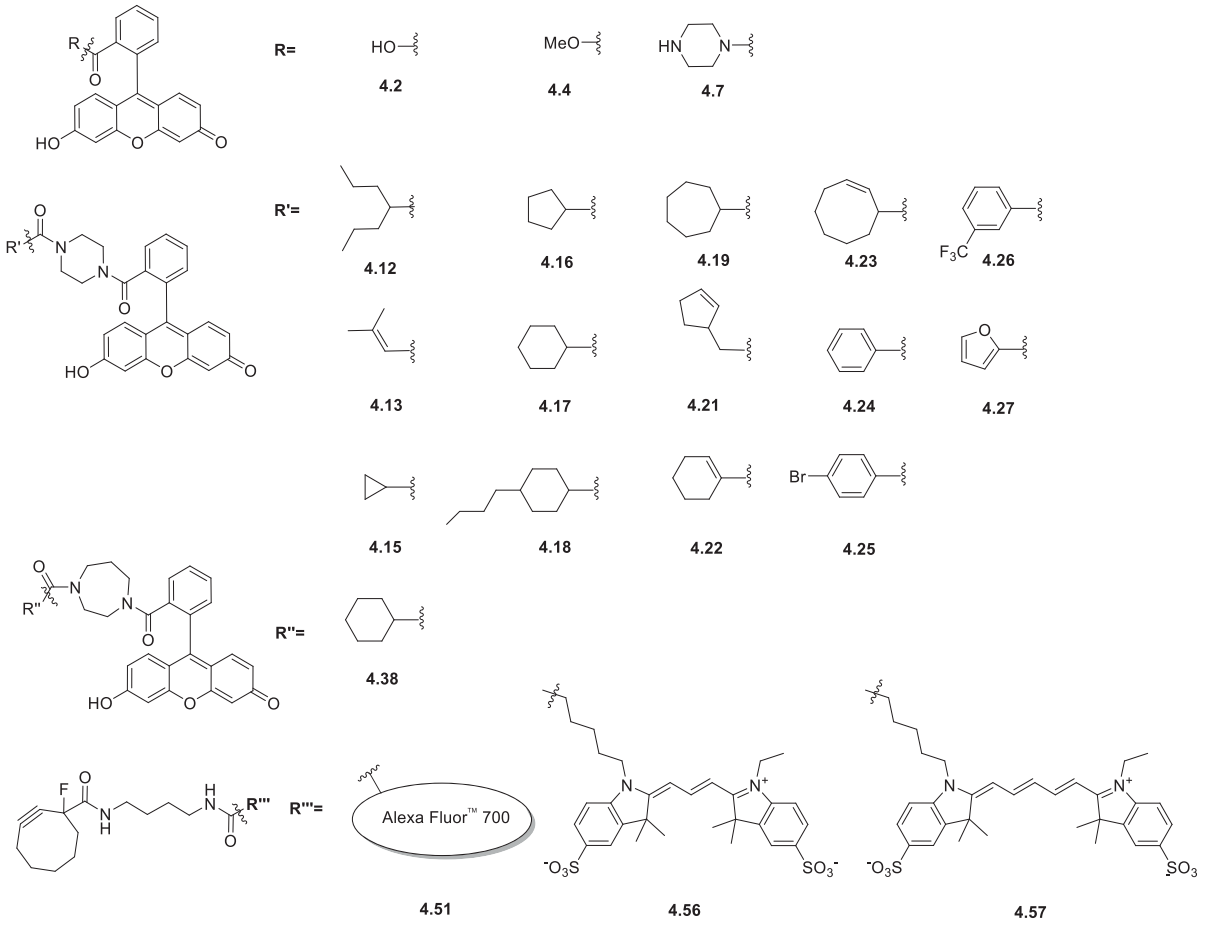

Scheme 4.20: Negative screening. Derivatives and precursors that did not show any cellular uptake in the screening.

4.3.3 Positive screening hits in library 1

The compounds that were screened positive (including the lead structure) revealed a cell staining not only for the melanoma cell line SK-Mel 28, but if detectable there, in general also for the primary melanocytes NHEM under the defined screening conditions. Additionally, the staining patterns were diverse, complicating conclusions regarding a uniform uptake mechanism. While the lead structure resulted in a homogenous staining of the cytoplasm of melanoma cells and melanocytes (**Figure 4.11**), some of the derivatives showed accumulations in vesicular structures and perinuclear regions.

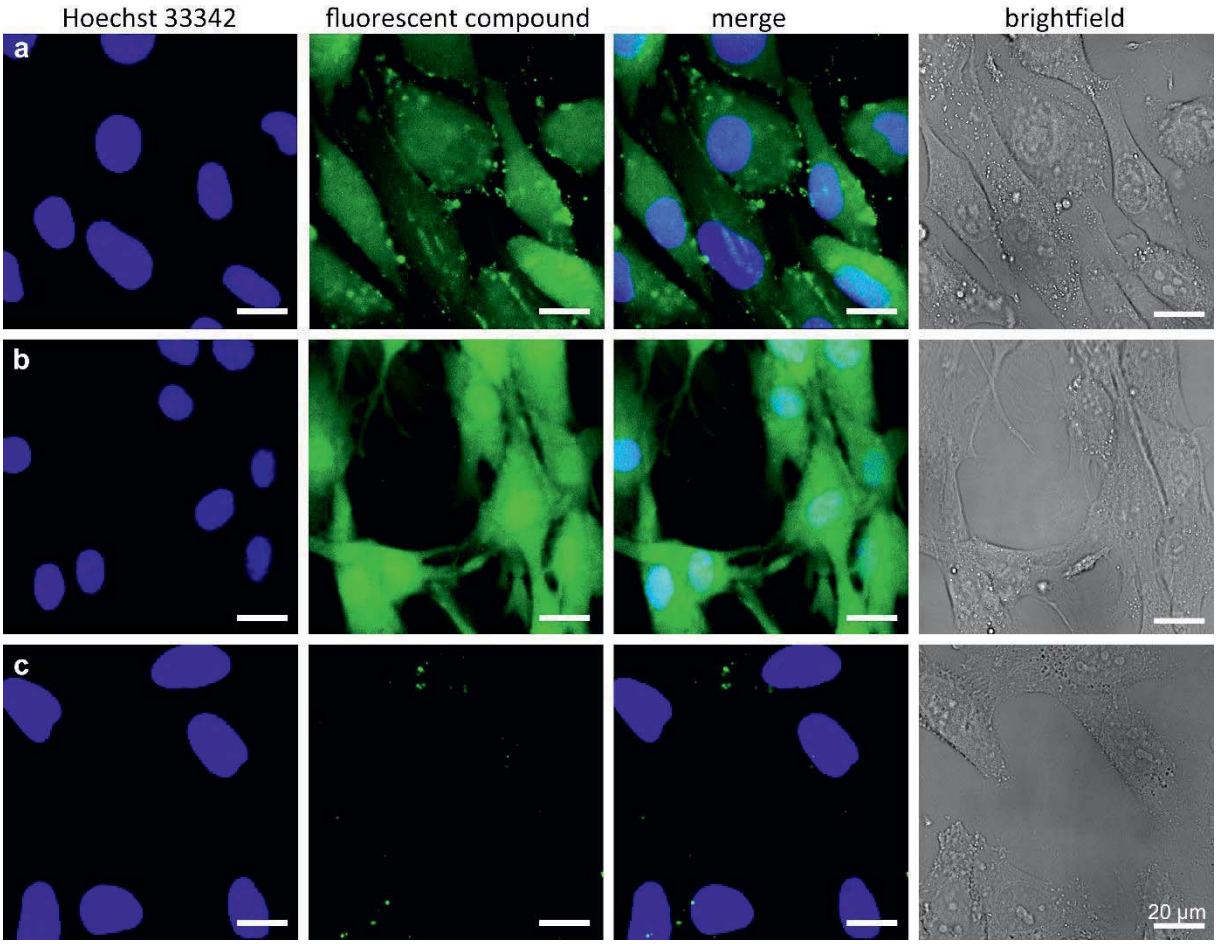

Figure 4.11: Confocal laser scanning microscopy of a) SK-Mel 28 cells, b) NHEM, and c) HeLa cells after incubation with 20 µM of lead structure 4.1 for 5 h. 4x10^4 of the respective cell line/primary cells were seeded in an 8-well chamber slide 2 d prior to treatment with 20 µM **4.1** for 5 h. Cells were washed three times with PBS before staining the nuclei with Hoechst 33342 (Invitrogen, 0.5 µg/ml for 20 min). The visualization was performed using a Leica TCS-SP-5 (DMI6000) inverted microscope with an HCX PL APO 63x/1.20 water UV objective. Fluorophores were excited using an UV laser (λ_{exc}= 351 and 364 nm) for the Hoechst 33342 staining and an argon ion laser (λ_{exc}= 488 nm) for the fluorescent compound. The images were taken in a sequential mode to avoid an overlap of emission spectra from Hoechst 33342 and fluorescein. Using the acquisition software Leica Application Suite (LAS) AF 2.2.2.4842, the picture ratio was adjusted to 1024 × 1024 pixels 8 bit depth. Scale bar: 20 µm.

Propioloylpiperazine fluoresceinamide 4.14

The first positive hit in the screening was the propioloylpiperazine fluoresceinamide **4.14**. Like the lead structure **4.1**, the derivative contains an alkyne bond, yet terminal and not part of a cyclic structure (**Scheme 4.21**). The staining pattern appears cytoplasmic for NHEM (**Figure 4.12**, panel **b**) but more located to perinuclear regions in SK-Mel 28 (panel **a**). A weak perinuclear accumulation is also detectable for the incubation with HeLa cells (panel **c**), indicating a general endocytic uptake.

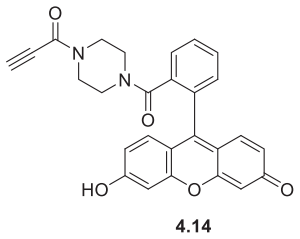

4.14

Scheme 4.21: Structure of propioloylpiperazine fluoresceinamide **4.14.**

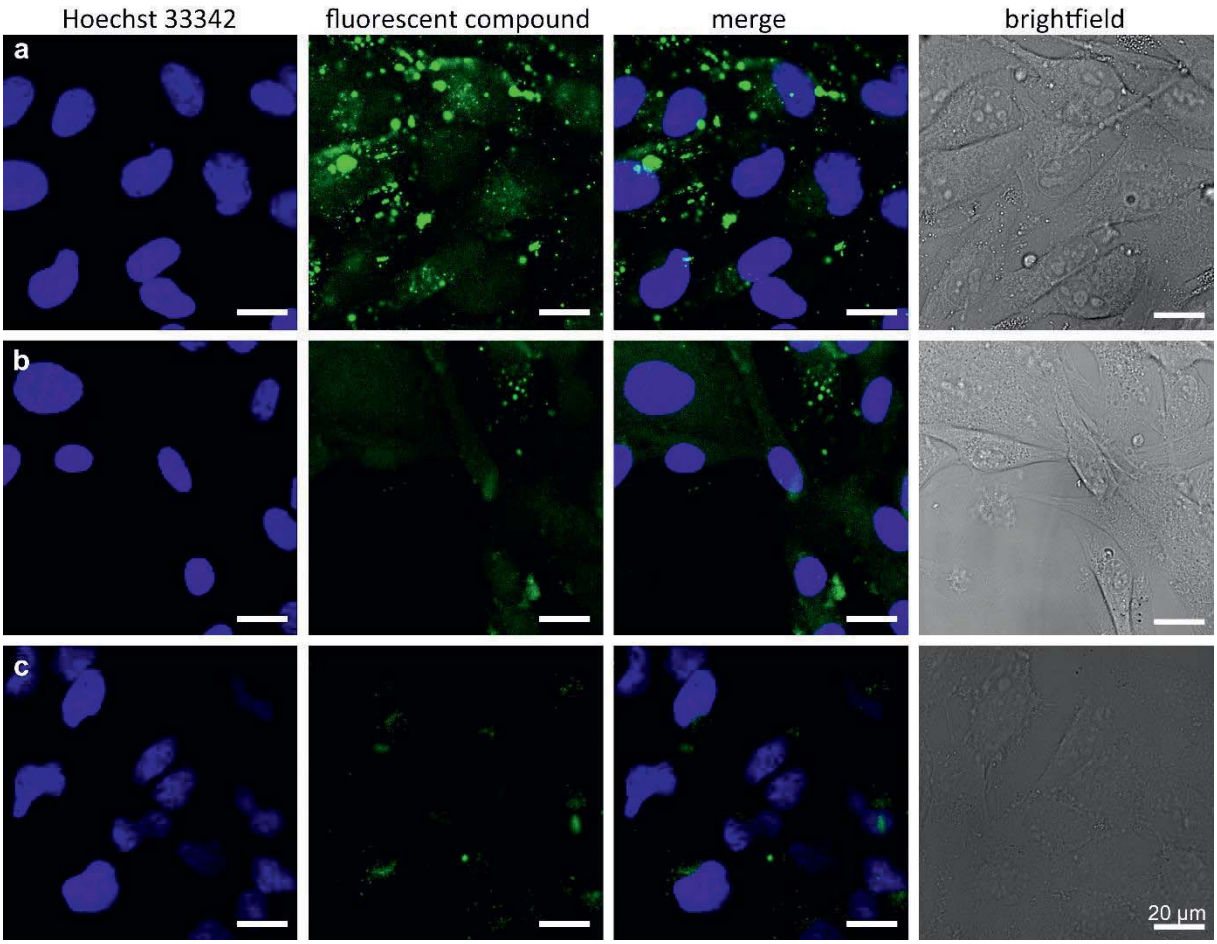

Figure 4.12: Confocal laser scanning microscopy of a) SK-Mel 28 cells, b) NHEM, and c) HeLa cells after incubation with 20 µM of derivative 4.14 for 5 h. 4x10^4 of the respective cell line/primary cells were seeded in an 8-well chamber slide 2 d prior to treatment with 20 µM **4.14** for 5 h. Cells were washed three times with PBS before staining the nuclei with Hoechst 33342 (Invitrogen, 0.5 µg/ml for 20 min). The visualization was performed using a Leica TCS-SP-5 (DMI6000) inverted microscope with an HCX PL APO 63x/1.20 water UV objective. Fluorophores were excited using an UV laser (λ_{exc}= 351 and 364 nm) for the Hoechst 33342 staining and an argon ion laser (λ_{exc}= 488 nm) for the fluorescent compound. The images were taken in a sequential mode to avoid an overlap of emission spectra from Hoechst 33342 and fluorescein. Using the acquisition software Leica Application Suite (LAS) AF 2.2.2.4842, the picture ratio was adjusted to 1024 × 1024 pixels 8 bit depth. Scale bar: 20 µm.

Adamantane-piperazine fluoresceinamide 4.20

A second positive hit was achieved with the screening of the adamantane derivative **4.20**. Like the lead structure moiety cyclooctyne, adamantane is a cyclic system, consisting of three connected cyclohexane rings in their armchair configuration, yet containing only single bonds and, as a simple diamondoid, bulky in the spatial structure, unlike the twisted structure of cyclooctyne (**Scheme 4.22**)[299]. The observed staining pattern appears homogenous and accumulation is observed in the whole cytoplasm for SK-Mel 28 and particularly NHEM (**Figure 4.13**, panel **a** and **b**). No apparent staining is noticed for HeLa cells (panel **c**).

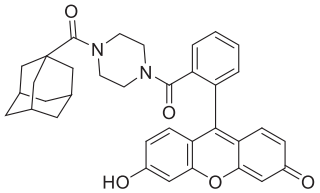

4.20

Scheme 4.22: Structure of adamantane-piperazine fluoresceinamide **4.20**.

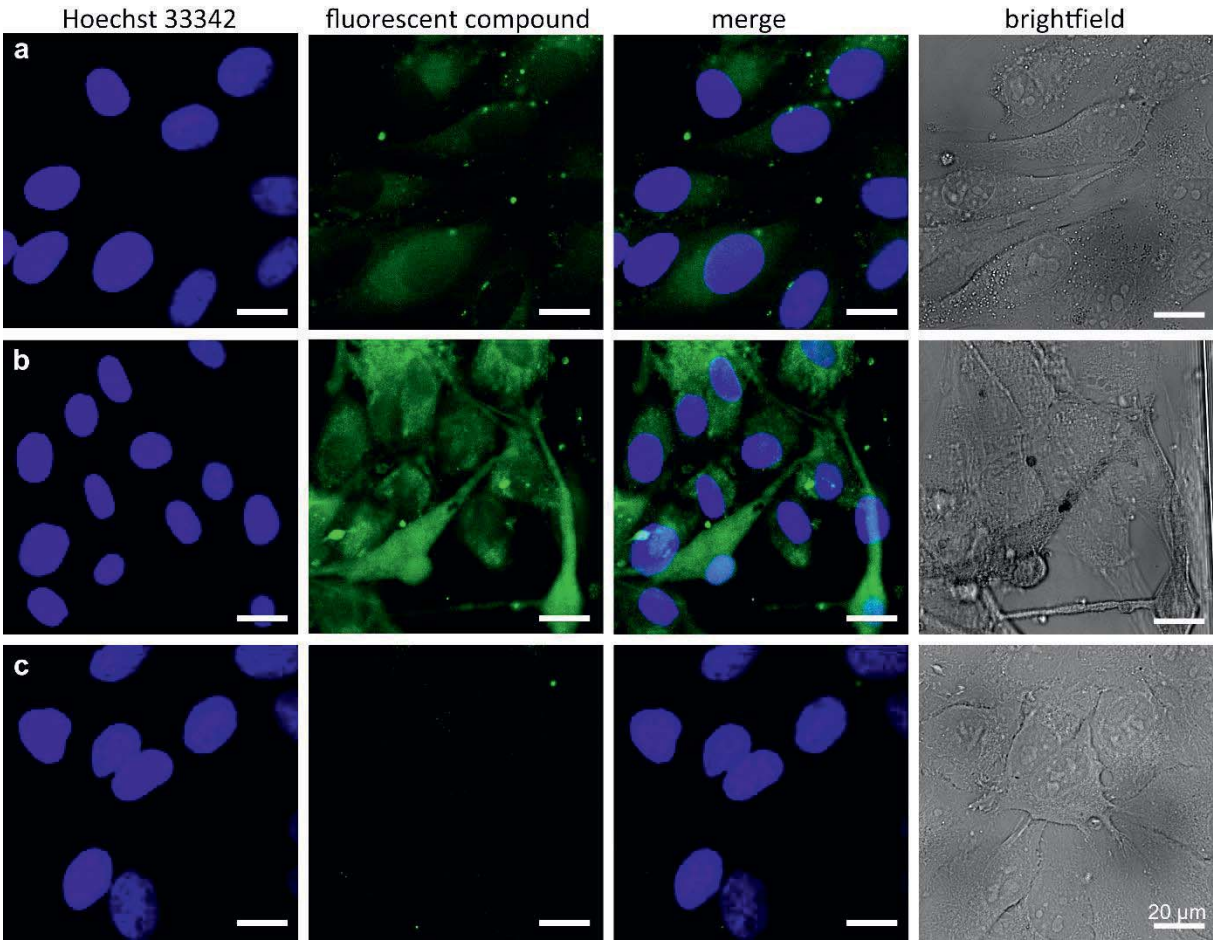

Figure 4.13: Confocal laser scanning microscopy of a) SK-Mel 28 cells, b) NHEM, and c) HeLa cells after incubation with 20 µM of derivative 4.20 for 5 h. 4x10^4 of the respective cell line/primary cells were seeded in an 8-well chamber slide 2 d prior to treatment with 20 µM **4.20** for 5 h. Cells were washed three times with PBS before staining the nuclei with Hoechst 33342 (Invitrogen, 0.5 µg/ml for 20 min). The visualization was performed using a Leica TCS-SP-5 (DMI6000) inverted microscope with an HCX PL APO 63x/1.20 water UV objective. Fluorophores were excited using an UV laser (λ_{exc}= 351 and 364 nm) for the Hoechst 33342 staining and an argon ion laser (λ_{exc}= 488 nm) for the fluorescent compound. The images were taken in a sequential mode to avoid an overlap of emission spectra from Hoechst 33342 and fluorescein. Using the acquisition software Leica Application Suite (LAS) AF 2.2.2.4842, the picture ratio was adjusted to 1024 × 1024 pixels 8 bit depth. Scale bar: 20 µm.

Indole-piperazine fluorescein amide 4.28

The last positive hit in library 1, varying the aliphatic building block a) of the lead structure, is the indole derivative **4.28**. Again, like in the lead structure **4.1**, the aliphatic moiety is cyclic in this derivative, yet aromatic, containing a hetero atom, and planar in its 3-dimensional structure.[300] The staining pattern is irregular and accumulation is primarily in vesicular structures detected for SK-Mel 28 and NHEM (**Figure 4.14**, panel **a** and **b**). No apparent staining is noticed for HeLa cells (panel **c**).

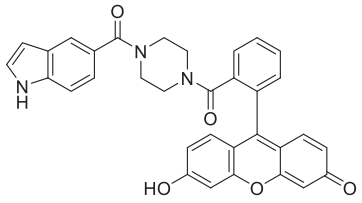

4.28

Scheme 4.23: Structure of indole-piperazine fluoresceinamide **4.28**.

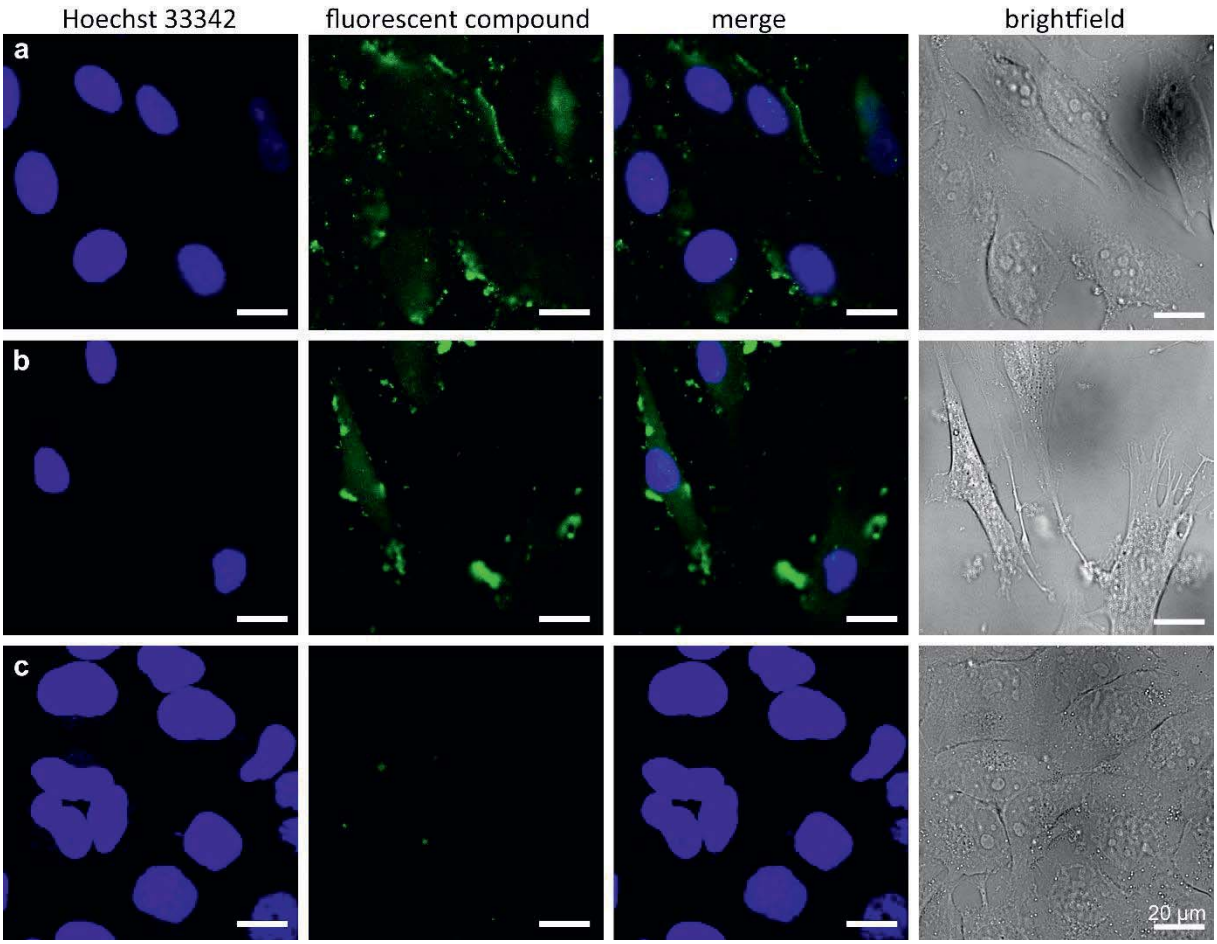

Figure 4.14: Confocal laser scanning microscopy of a) SK-Mel 28 cells, b) NHEM, and c) HeLa cells after incubation with 20 µM of derivative 4.20 for 5 h. $4x10^4$ of the respective cell line/primary cells were seeded in an 8-well chamber slide 2 d prior to treatment with 20 µM **4.20** for 5 h. Cells were washed three times with PBS before staining the nuclei with Hoechst 33342 (Invitrogen, 0.5 µg/ml for 20 min). The visualization was performed using a Leica TCS-SP-5 (DMI6000) inverted microscope with an HCX PL APO 63x/1.20 water UV objective. Fluorophores were excited using an UV laser (λ_{exc}= 351 and 364 nm) for the Hoechst 33342 staining and an argon ion laser (λ_{exc}= 488 nm) for the fluorescent compound. The images were taken in a sequential mode to avoid an overlap of emission spectra from Hoechst 33342 and fluorescein. Using the acquisition software Leica Application Suite (LAS) AF 2.2.2.4842, the picture ratio was adjusted to 1024 × 1024 pixels 8 bit depth. Scale bar: 20 µm.

4.3.4 Positive screening hits in library 2

The screening of the derivatives in library 2 (**Scheme 4.11**) and their precursor, the fluorescein homopiperazine amide **4.35,** showed almost overall positive hits for the cell staining in melanoma cells and melanocytes, while no accumulation was detectable in the control HeLa cells (**Scheme 4.24**).

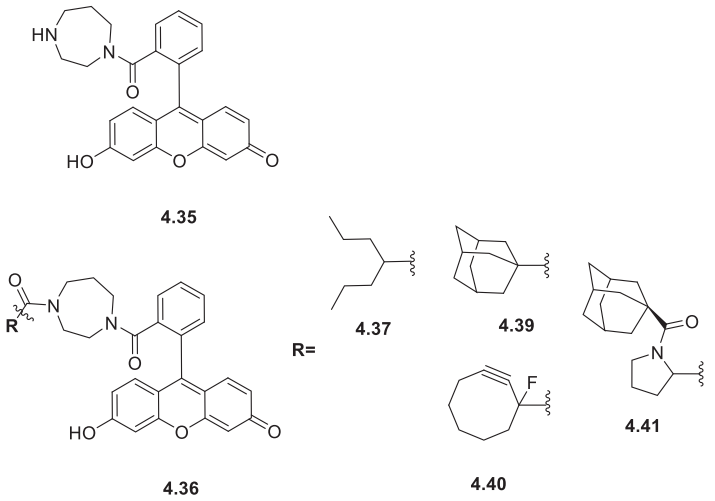

Scheme 4.24: Positive screening hits in library 2.

For the cyclooctyne- and adamantane-containing compounds **4.39** and **4.40** this result is not surprising, since already their piperazine linker equivalents **4.1** and **4.20** were screened as positive and the change from the 6- to the 7-membered linker appears to be comparatively small. Interestingly, this small point variation made a difference in the uptake of the 2-propylpentane derivative **4.37**, which was a positive hit, while its piperazine equivalent **4.12** was screened as negative. A similar picture was obtained in the screening of the piperazine and homopiperazine precursors **4.7** and **4.35**. While the former did not show any detectable accumulation in either of the cell lines, the latter accumulated in the cytoplasm of SK-Mel 28 and NHEM. Whereas for cyclohexane derivatives **4.16** and **4.38**, both variations with piperazine and homopiperazine linker were screened as negative and the linker variation did not cause an enhanced uptake. Still, an influence of the linker variation on the cellular uptake is indicated. The staining patterns for all derivatives in library 2 were homogenous in the cytoplasm, comparable to the results of the lead structure **4.1** (**Figure 4.8**) or the adamantane-piperazine compound **4.20** (**Figure 4.13**). While also the intensity of the fluorescence under similar microscopic parameters was comparable or inferior to the lead structure for most of the screened compounds, the adamantane-homopiperazine fluoresceinamide **4.39** showed an even more intense staining with a brighter fluorescent signal for melanoma cells, compared to lead structure **4.1** (**Figure 4.15**).

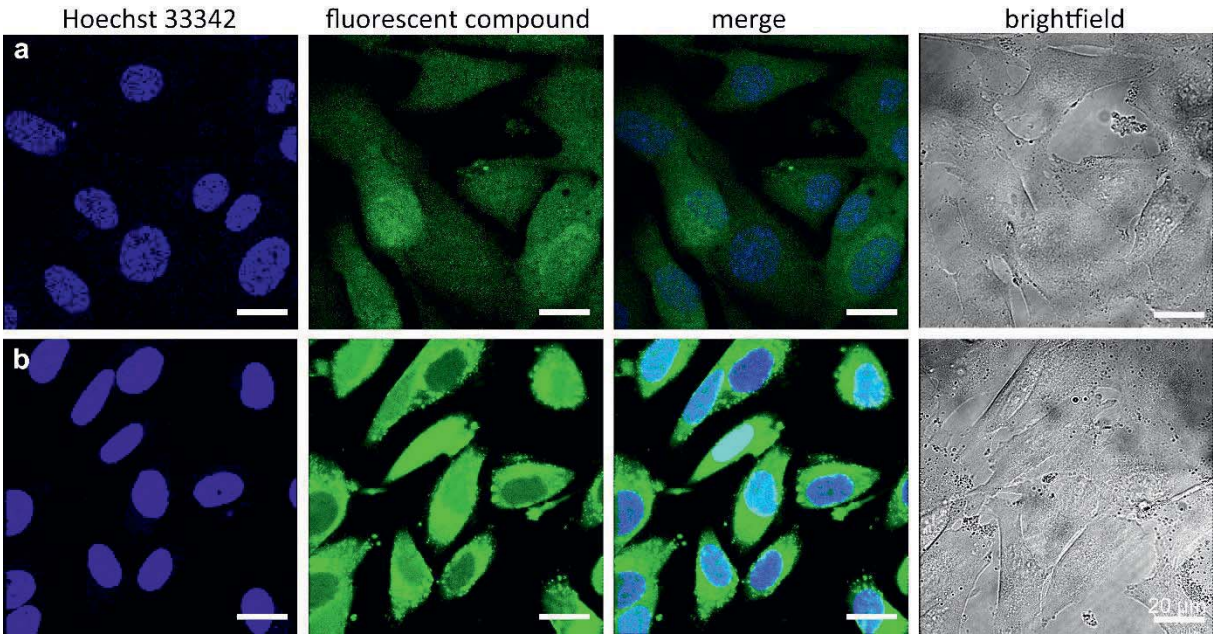

Figure 4.15: Confocal laser scanning microscopy of SK-Mel 28 cells after incubation with 20 µM of a) lead structure 4.1 and b) derivative 4.39 for 5 h. 4x10^4 of the respective cell line/primary cells were seeded in an 8-well chamber slide 2 d prior to treatment with 20 µM **4.1** or **4.39** for 5 h. Cells were washed three times with PBS before staining the nuclei with Hoechst 33342 (Invitrogen, 0.5 µg/ml for 20 min). The visualization was performed using a Leica TCS-SPE (DMI8) inverted microscope with an ACS APO 63x/1.30 oil objective. Fluorophores were excited using an UV laser (λ_{exc}= 405 nm) for the Hoechst 33342 staining and an argon ion laser (λ_{exc}= 488 nm) for the fluorescent compound. The images were taken in a sequential mode to avoid an overlap of emission spectra from Hoechst 33342 and fluorescein. Using the acquisition software Leica Application Suite (LAS) X 2.0.1.14392, the picture ratio was adjusted to 1024 × 1024 pixels 8 bit depth. Scale bar: 20 µm.

4.3.5 Positive screening hits in library 3

From the compounds in the previously synthesized library 3, consisting of the original cyclooctyne moiety, a diaminobutane linker and a variety of different commercially available dyes (**Scheme 4.17**), most derivatives showed a fluorescent signal in the melanoma cells, in the melanocytes, and also in HeLa cells with an endocytic staining pattern, indicating an unspecific uptake of the charged molecules via endocytosis. Only the Cy3- (**4.56**), Cy5- (**4.57**), and Alexa Fluor™ 700 (**4.51**) derivatives did not accumulate in the cells. The positive hits are summarized in **Scheme 4.25**, a representative example for the staining pattern typical for this library is given in **Figure 4.16** with the ATTO 532 derivative **4.53**.

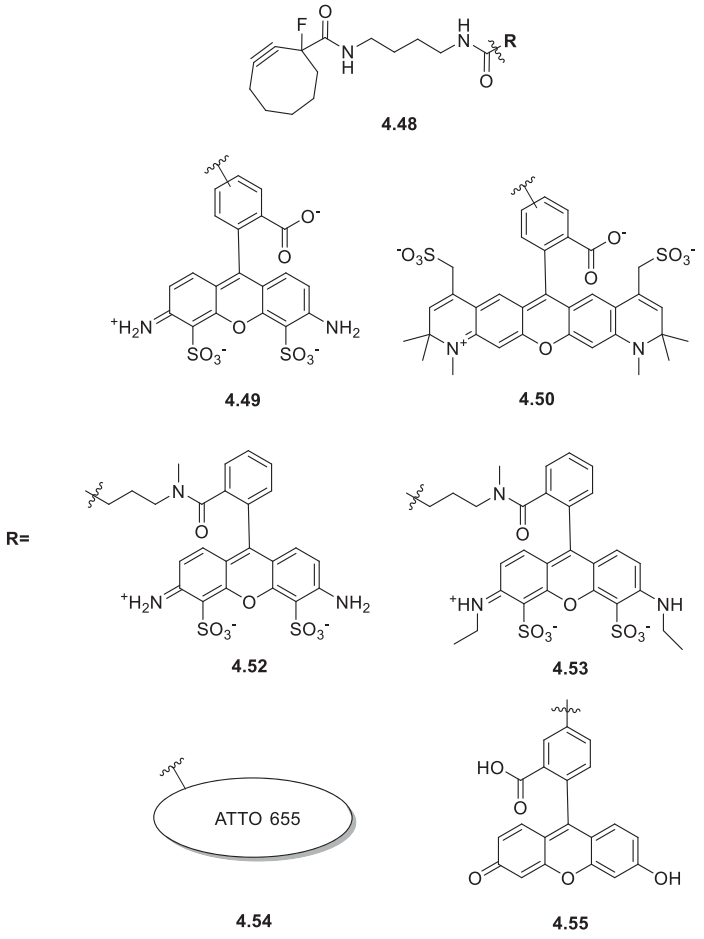

Scheme 4.25: Positive screening hits in library 3.

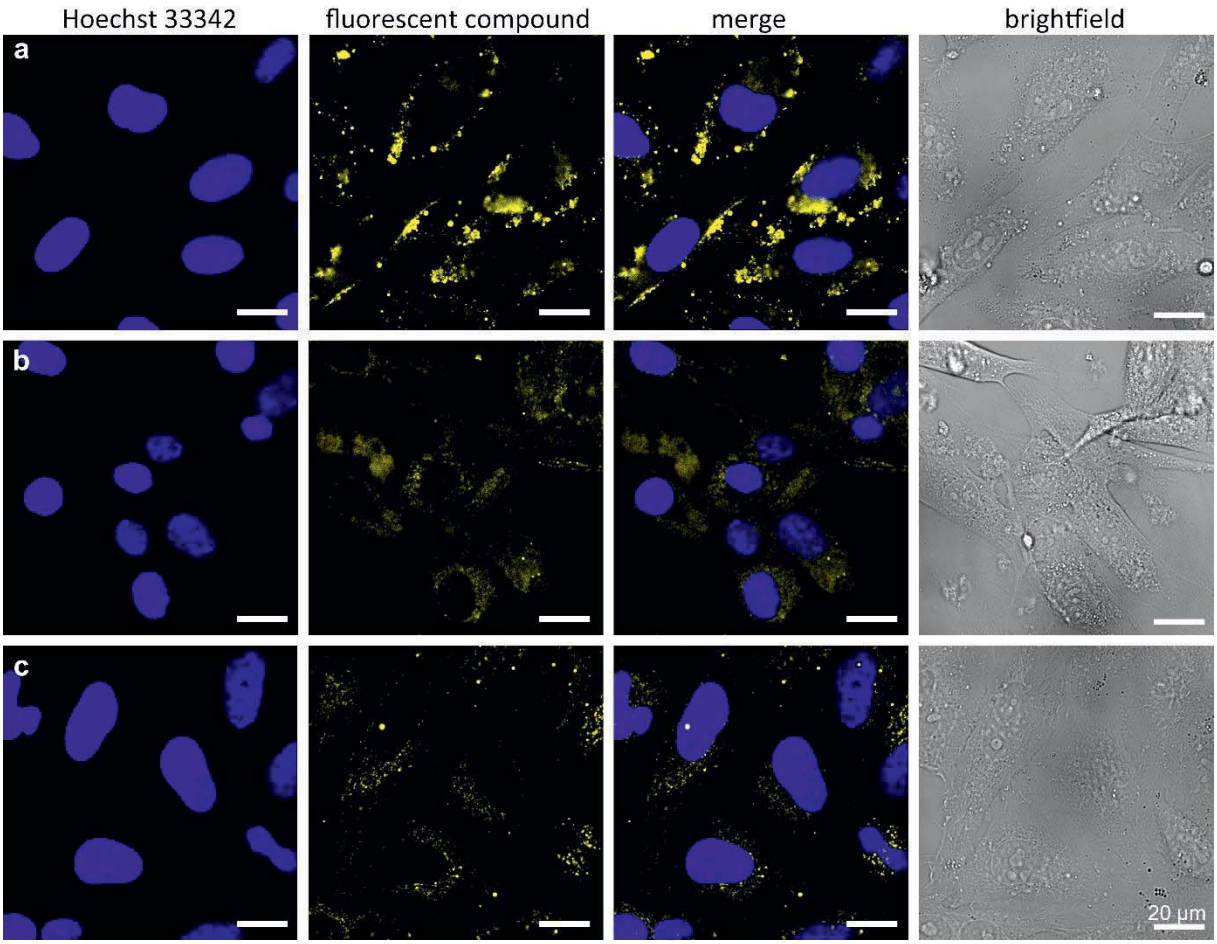

Figure 4.16: Confocal laser scanning microscopy of a) SK-Mel 28 cells, b) NHEM, and c) HeLa cells after incubation with 20 µM of derivative 4.53 for 5 h. $4x10^4$ of the respective cell line/primary cells were seeded in an 8-well chamber slide 2 d prior to treatment with 20 µM **4.53** for 5 h. Cells were washed three times with PBS before staining the nuclei with Hoechst 33342 (Invitrogen, 0.5 µg/ml for 20 min). The visualization was performed using a Leica TCS-SP-5 (DMI6000) inverted microscope with an HCX PL APO 63x/1.20 water UV objective. Fluorophores were excited using an UV laser (λ_{exc}= 351 and 364 nm) for the Hoechst 33342 staining and an argon ion laser (λ_{exc}= 532 nm) for the fluorescent compound. The images were taken in a sequential mode to avoid an overlap of emission spectra from Hoechst 33342 and fluorescein. Using the acquisition software Leica Application Suite (LAS) AF 2.2.2.4842, the picture ratio was adjusted to 1024 × 1024 pixels 8 bit depth. Scale bar: 20 µm.

4.3.6 Investigations of the uptake mechanism – active vs passive transport

In order to achieve a sufficient cell staining and a broad accumulation of the fluorescent compound within the cells, the compounds need to cross the cell membranes as outer layer of the cells first. This process is broadly described as permeation and includes a variety of mechanisms, both active (requires energy effort) and passive transports (along a concentration gradient). Since passive transport and carrier-mediated active mechanisms are both considered to contribute to the cellular uptake of small molecules[301], a simple experiment was performed to elucidate the predominant mode of action for the lead structure **4.1**, the derivative with the most promising staining capacity, the adamantane-homopiperazine fluoresceinamide **4.39**, and its piperazine linker counterpart **4.20**. SK-Mel 28 melanoma cells (**Figure 4.17**) and normal melanocytes (NHEM, **Figure 4.18**) were again treated with 20 µM of a) lead structure 4.1, b) derivative 4.20, and c) derivative 4.39 for 5 h, but at a reduced temperature of 4 °C instead of the physiological 37 °C. The temperature reduction to a sub-physiological level is expected to efficiently inhibit any kind of active, carrier-mediated transport by decreasing reaction rates. For all three compounds in both melanoma cells and melanocytes, an efficient staining of the cytoplasm and the nucei is still observed, with the highest fluorescence intensity present in the cells treated with adamantane-homopiperazine fluoresceinamide **4.39** (**Figure 4.17**, **Figure 4.18**, panel **c**).

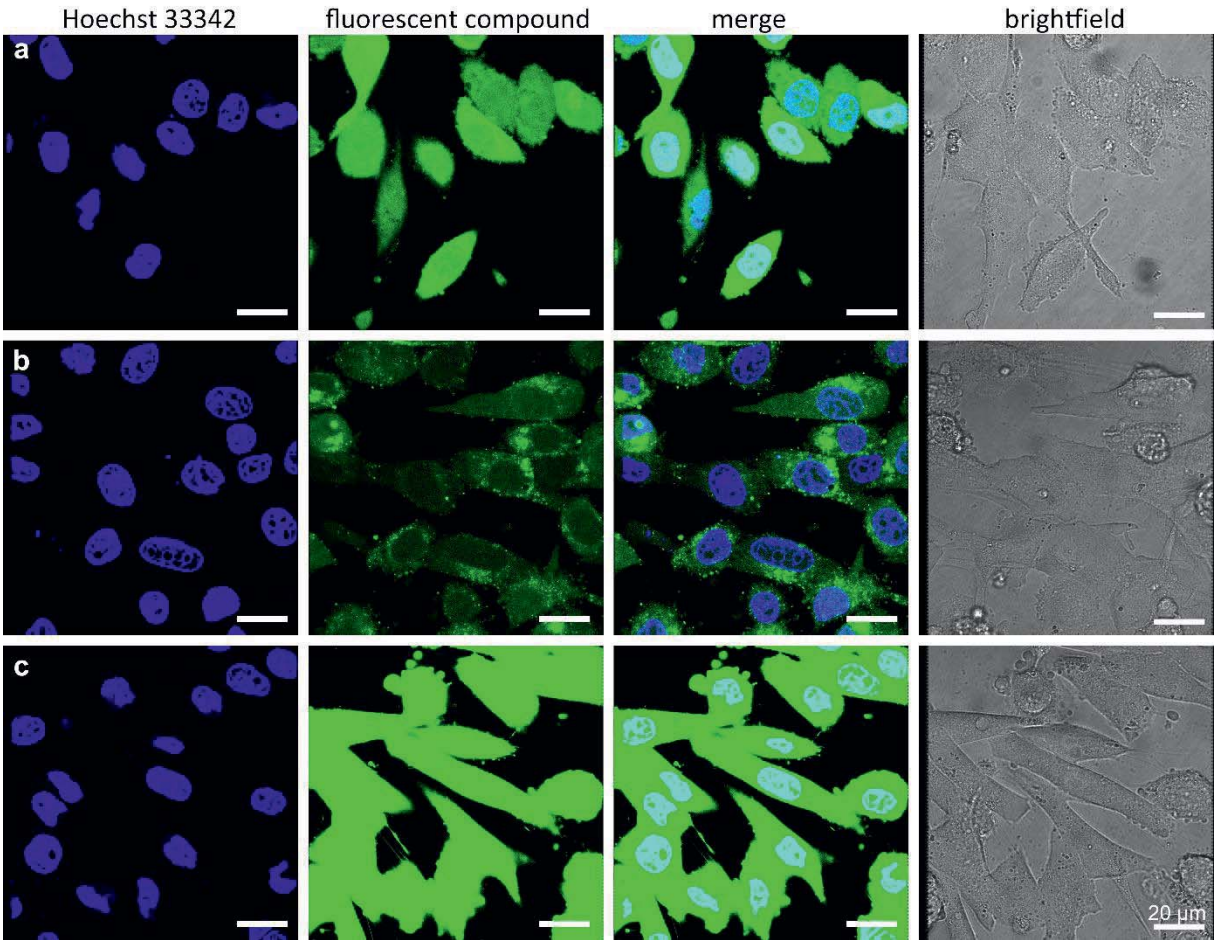

Figure 4.17: Confocal laser scanning microscopy of SK-Mel 28 cells after incubation with 20 µM of a) lead structure 4.1, b) derivative 4.20, and c) derivative 4.39 for 5 h at 4 °C. 4x10^4 of the respective cell line were seeded in an 8-well chamber slide 2 d prior to treatment with 20 µM **4.1, 4.20** or **4.39** for 5 h at 4 °C. Cells were washed three times with PBS before staining the nuclei with Hoechst 33342 (Invitrogen, 0.5 µg/ml for 20 min). The visualization was performed using a Leica TCS-SPE (DMI8) inverted microscope with an ACS APO 63x/1.30 oil objective. Fluorophores were excited using an UV laser (λ_{exc}= 405 nm) for the Hoechst 33342 staining and an argon ion laser (λ_{exc}= 488 nm) for the fluorescent compound. The images were taken in a sequential mode to avoid an overlap of emission spectra from Hoechst 33342 and fluorescein. Using the acquisition software Leica Application Suite (LAS) X 2.0.1.14392, the picture ratio was adjusted to 1024 × 1024 pixels 8 bit depth. Scale bar: 20 µm.

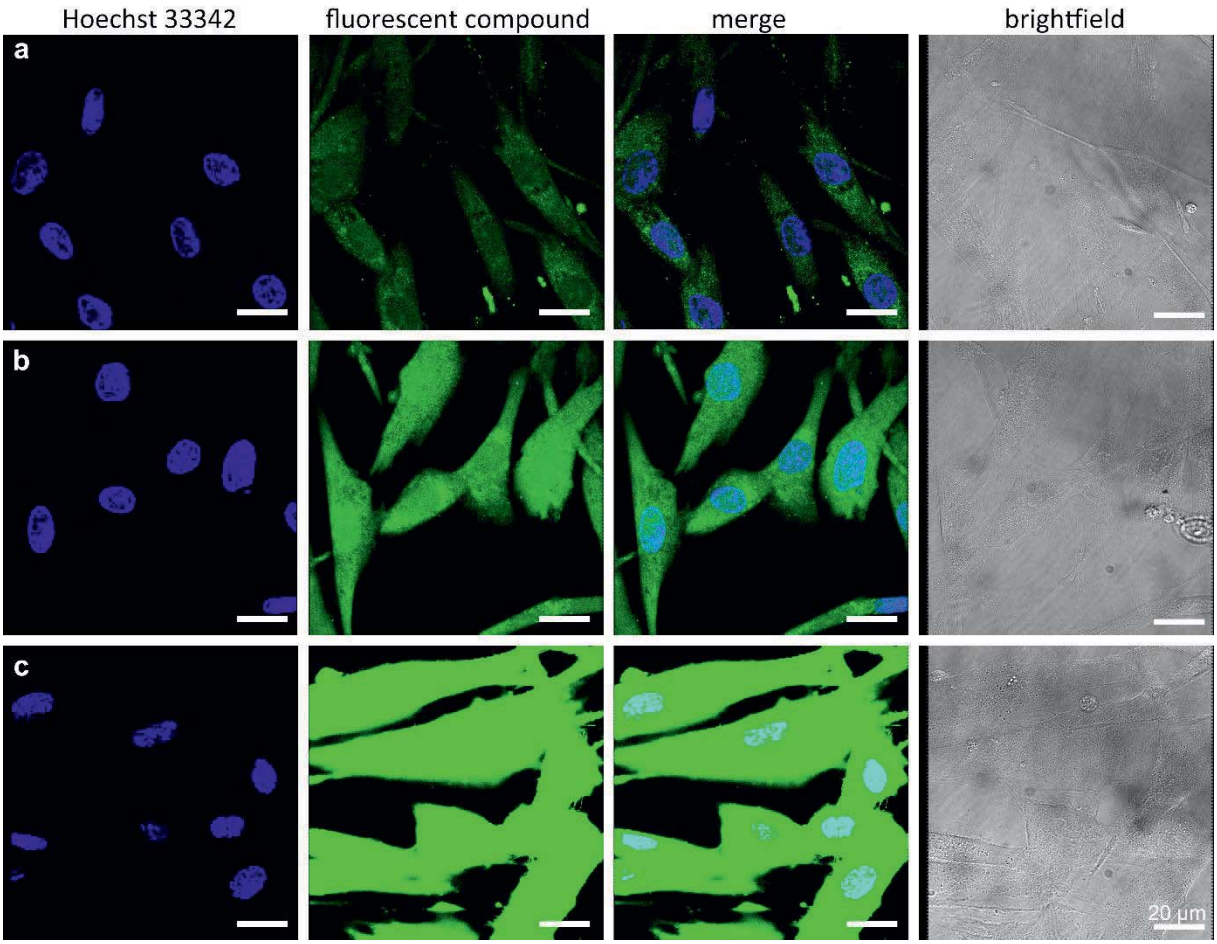

Figure 4.18: Confocal laser scanning microscopy of NHEM after incubation with 20 µM of a) lead structure 4.1, b) derivative 4.20, and c) derivative 4.39 for 5 h at 4 °C. 4x10^4 of primary melanocytes were seeded in an 8-well chamber slide 2 d prior to treatment with 20 µM **4.1, 4.20** or **4.39** for 5 h at 4 °C. Cells were washed three times with PBS before staining the nuclei with Hoechst 33342 (Invitrogen, 0.5 µg/ml for 20 min). The visualization was performed using a Leica TCS-SPE (DMI8) inverted microscope with an ACS APO 63x/1.30 oil objective. Fluorophores were excited using an UV laser (λ_{exc}= 405 nm) for the Hoechst 33342 staining and an argon ion laser (λ_{exc}= 488 nm) for the fluorescent compound. The images were taken in a sequential mode to avoid an overlap of emission spectra from Hoechst 33342 and fluorescein. Using the acquisition software Leica Application Suite (LAS) X 2.0.1.14392, the picture ratio was adjusted to 1024 × 1024 pixels 8 bit depth. Scale bar: 20 µm.

4.3.7 Expanding screening conditions – from 2-dimensional monolayer cell culture to 3-dimensional spheroid cultures

In common 2-dimensional cell cultures, as used in the previous chapters, tumor cells grow in conditions that demand an unnatural behavior. While under physiological conditions they form conglomerates and are surrounded by an extracellular matrix (ECM), but under culture conditions they grow in monolayers on a cell culture-compatible polystyrene surface.[302] This allows for easy culturing and microscopy, and maintains cell proliferation rates, yet changes their natural microenvironment. To overcome this obvious discrepancy between model and reality, and to create a more realistic model system, efforts have been made over the last decade to establish various 3-dimensional culture models.[303-305] The simplest model for tumor systems is growing the respective cells in cell aggregates, called spheroids, which have been shown to mimic tissue-like properties of tumors.[306] In order to investigate the applicability of 3-dimensional spheroid cultures in the screenings of potential melanoma markers, in collaboration with V. Kappings (Schepers group, KIT), a spheroid model of SK-Mel 28 melanoma cells was established and the accumulation of lead structure **4.1** (panel **a-c**) in the tumor tissue was observed in comparison to fluorescein (**4.2**, panel **d**) as a control (**Figure 4.19**). The incubation of the spheroids for 72 h with 50 µM (panel **a**) and 15 µM (panel **b**) of the lead structure results in a strong fluorescent signal, indicating sufficient accumulation of the fluorescent compound in the tumorous tissue for convenient visualization. Even at the lowest concentration of 1 µM **4.1** a signal is still detectable (panel **c**), unlike the control incubation wit 1 µM fluorescein **4.2** (panel **d**).

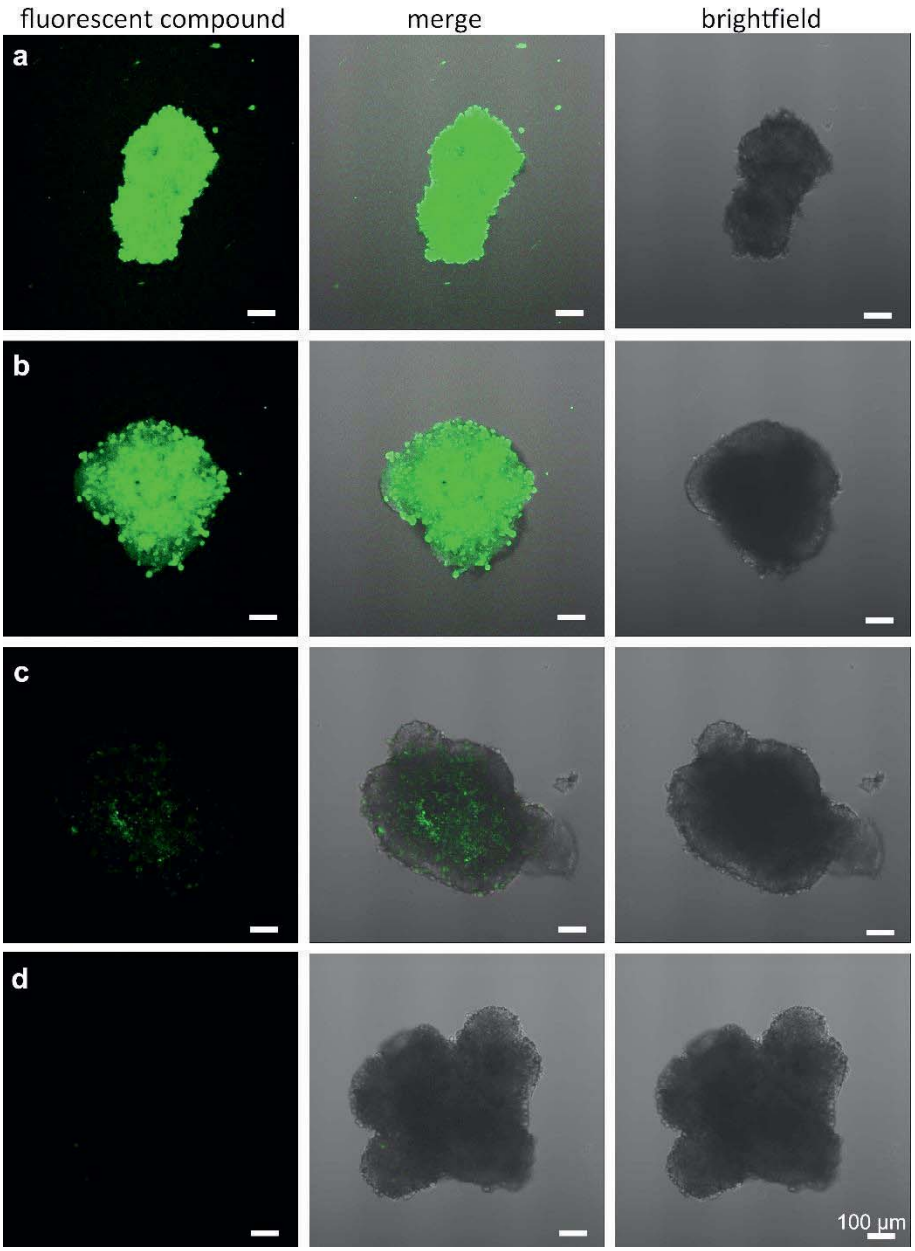

Figure 4.19: Confocal laser scanning microscopy of SK-Mel 28 spheroids after incubation with a) 50 µM, b) 15 µM, c) 1 µM of lead structure 4.1, and d) 1 µM 4.2 (fluorescein) for 72 h. 4x10^3 of SK-Mel 28 were seeded in agarose wells 5 d prior to treatment with 50 µM, 15 µM, 1 µM **4.1**, and 1 µM **4.2** for 72 h at 37 °C. Cells were washed with PBS. The visualization was performed using a Leica TCS-SPE (DMI8) inverted microscope with an ACS APO 63x/1.30 oil objective. The fluorophore was excited using an argon ion laser (λ_{exc}= 488 nm. Using the acquisition software Leica Application Suite (LAS) X 2.0.1.14392, the picture ratio was adjusted to 1024 × 1024 pixels 8 bit depth. Scale bar: 100 µm.

4.3.8 Towards a functional organ – from the 3-dimensional spheroid culture to an organotypic full skin-melanoma spheroid model

After having shown that the accumulation of lead structure **4.1** can successfully be detected within a 3-dimensional tumor spheroid model (chapter 4.3.7), the next step towards a more realistic screening setting was the investigation of compound accumulation in an organotypic full skin-melanoma spheroid model. Organotypic skin models are well-studied, advanced, 3-dimensional cell culture systems and already widely used in the cosmetics industry to close the gap between 2-dimensional cell cultures and human application while preventing the use of animal models. However, their value is not only limited to cosmetics testing. They inhibit the potential of growing tissue *in vitro* for subsequent skin transplantations, as well as a wide potential application in drug development for systemically acting drugs that are applied via the skin surface, or for drugs in skin diseases (such as allergies, irritations, burns, wounds etc.).[307] Their complexity varies from reconstructed human epidermis (RHE), consisting of only one cell type, to full thickness (FT) skin models with a keratinocyte epidermis on top of a fibroblast dermis layer, to full thickness models including also other cell types. The more complex the model is, the better it reflects the *in vivo* situation. However, various problems arise from complexity, ranging from costs over maintenance to reproducibility issues. In the simplest form, the RHE, keratinocytes derived from mammary tissue or juvenile foreskin are cultured for up to 14 days at an air-liquid interface (ALI) to form the typical stratified epithelium.[308-310] While coming with a high reproducibility, these systems have been shown to exceed human or animal epidermis in permeability due to a decreased barrier function.[311] FT skin models are based on a dermis layer, created by culturing primary fibroblasts in a gel matrix, usually collagen I. After several days of cultivation, the fibroblasts adhere to the collagen fibers, thus contracting the gel. Subsequent addition of keratinocytes on the top and cultivation at the ALI to enable stratification and cornification allows for the formation of an epidermis layer above the dermis, thus creating an artificial skin model highly similar to the layers of human skin (**Figure 4.20**, **Figure 4.21**[xvi]).[312] These full thickness models have been shown to better represent the *in vivo* barrier function. While the RHE models were 10 times more permeable than human cadaver control skin for drugs like caffeine or hydrocortisone, the permeability of FT models was 3-4 times higher.[313] Models of even greater complexity and closer to the *in vivo* situation are created by the addition of other cell types to the full thickness skin models. Co-culturing melanocytes alongside with the keratinocytes during epidermis formation results in pigmented skin models, with keratinocytes and melanocytes in close interactions.[314,315] Other possibilities are the addition of Langerhans' cells, tissue stem cells, or hair follicles to the FT models in order to derive different (or more complex) models or the creation of disease models.[307,316-318]Besides many more skin disease models, the development of a 3-dimensional organotypic skin melanoma model that closely mimics the *in vivo* situation of cutaneous melanoma metastasis, is of unquestionable value for melanoma

[xvi] Reprinted from „Artificial skin in perspective: concepts and applications“, Volume 24, C. A. Brohem, L. B. da Silva Cardeal, M. Tiago, M. S. Soengas, S. B. de Moraes Barros, S. S. Maria-Engler, Pigment Cell Melanoma Res., Pages 35-50, Copyright (2010), with permission from John Wiley & Sons A/S.

drug development and could also be used in the development of novel diagnostic methods. In general, there are two ways of creating a melanoma model. Either melanoma cells of different progression stages (radial/vertical growth phase, metastasis) are seeded on top of the dermal layer before adding the keratinocytes, or melanoma spheroids of a defined size and cell number are inserted into the fibroblast/collagen I scaffold on day one and co-cultured with the model. Skin melanoma models have successfully been shown to recapitulate key features of human cutaneous melanoma metastasis and early tumor invasion, and therefore represent a suitable system for melanoma drug screenings.[319,320]

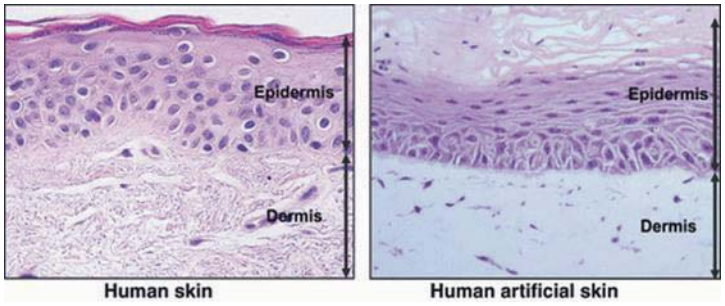

Figure 4.20: HE stain and optical microscopy of human facial skin and artificial skin with dermis and epidermis very similar in thickness and layers. Reprinted from Brohem et al.[321] Copyright (2010), with permission from John Wiley & Sons A/S.

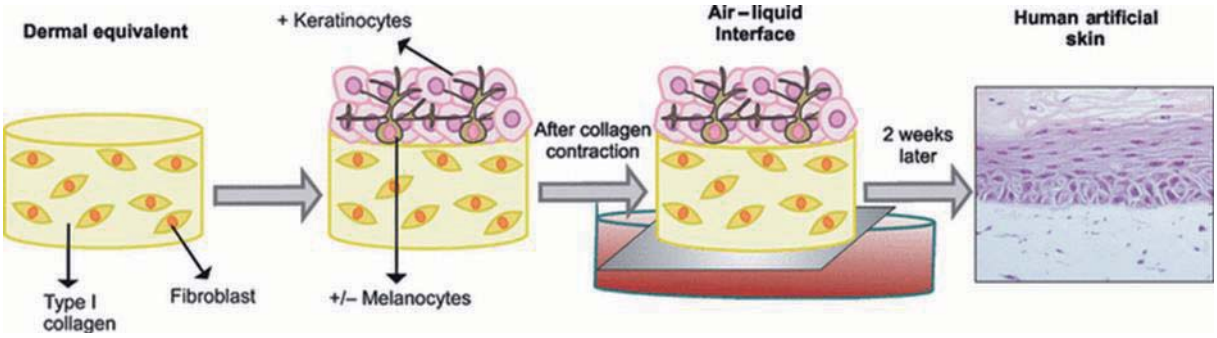

Figure 4.21: Construction process of an artificial full thickness skin model. Fibroblasts are cultivated in collagen I matrix, forming the dermis layer. Subsequent addition of keratinocytes (and melanocytes in more advanced models) on the top and cultivation at the ALI to enable stratification and cornification, allows for the formation of an epidermis layer above the dermis. Reprinted from Brohem et al.[321] Copyright (2010), with permission from John Wiley & Sons A/S.

Similar to the described models, V. Kappings (Schepers group, KIT) established a melanoma model by culturing normal human dermal fibroblasts (NHDF), together with SK-Mel 28 melanoma spheroids in a gelatin methycryloyl (GelMA) matrix to mimic the invasion of a matured melanoma tumor in the dermis layer. Normal human epidermal keratinocytes (NHEK) were seeded on top and cultured at an air-liquid interface (ALI)

to enable differentiation and stratification in the formation of an epidermal layer. In a second model, keratinocytes were seeded on top of the dermis alongside with normal human epidermal melanocytes (NHEM) to generate a more sophisticated pigmented skin-melanoma model. As a control model, the same melanocyte-including skin set-up was used but with spheroids derived from the hepatocellular carcinoma cells HepG2 instead of melanoma spheroids. After successful cultivation of the skin models, lead structure **4.1** was applied on the epidermis in a concentration of 50 µM for 24 h and the accumulation of the fluorescent compound in different tissue layers was investigated via CLSM. **Figure 4.22** shows in panel **a** the dermis layer of the simpler skin-melanoma model with the melanoma spheroid. A fluorescent signal is detected that indicates an accumulation of lead structure **4.1** in the tumor. Panel **b** shows the same model but an image of the epidermis layer, in the simpler version only consisting of keratinocytes. Within the keratinocyte layer, no signal is observed. Panel **c** shows the epidermis layer of the more sophisticated model consisting of keratinocytes and melanocytes and a detectable signal, which is coherent with findings from the 2-dimensional cell culture screenings, where an accumulation of the compound in melanocytes was stated. Results from the control model with a HepG2 spheroid and a mixed keratinocyte/melanocyte epidermis are shown in **Figure 4.23**. While there is a fluorescent signal observed in panel **b** for the melanocytes containing epidermis, no signal is detectable in the dermis layer with the hepatocellular carcinoma tumor (panel **a**).

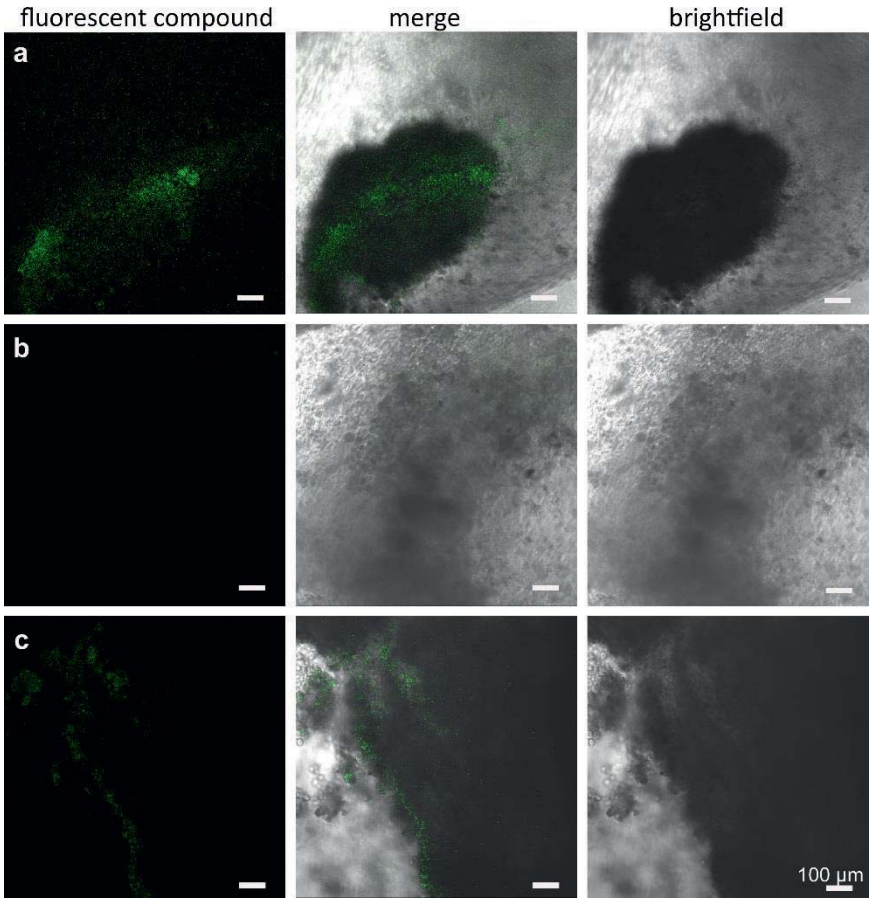

Figure 4.22: Confocal laser scanning microscopy of full skin-melanoma models with SK-Mel 28 spheroids after incubation with 50 µM of lead structure 4.1 for 24 h. a) shows the dermis with a fluorescent signal in the melanoma spheroid, b) shows the epidermis consisting of only keratinocytes and no detectable signal, c) shows the epidermis with keratinocytes and melanocytes, a signal is detected. $4x10^3$ of SK-Mel 28 melanoma cells were seeded and grown to spheroids in agarose wells 7 d prior to implantation in a dermis model with 5 x 10^5 NHDF in 5% GelMA and 0.3% LAP in a transwell filter system. After 7 days culture, 7 x 10^5 NHEK (panels a, b and c) and 2 x 10^5 NHEM (panel c) were seeded on top of the dermis. After 7 days, the surface was lifted to the ALI and cultivated there for another 14 days before being treated with 50 µM lead structure **4.1** for 24 h. Models were washed with PBS and fixated with 4% PFA. The visualization was performed using a Leica TCS-SPE (DMI8) inverted microscope with an ACS APO 63x/1.30 oil objective. The fluorophore was excited using an argon ion laser (λ_{exc}= 488 nm. Using the acquisition software Leica Application Suite (LAS) X 2.0.1.14392, the picture ratio was adjusted to 1024 × 1024 pixels 8 bit depth. Scale bar: 100 µm.

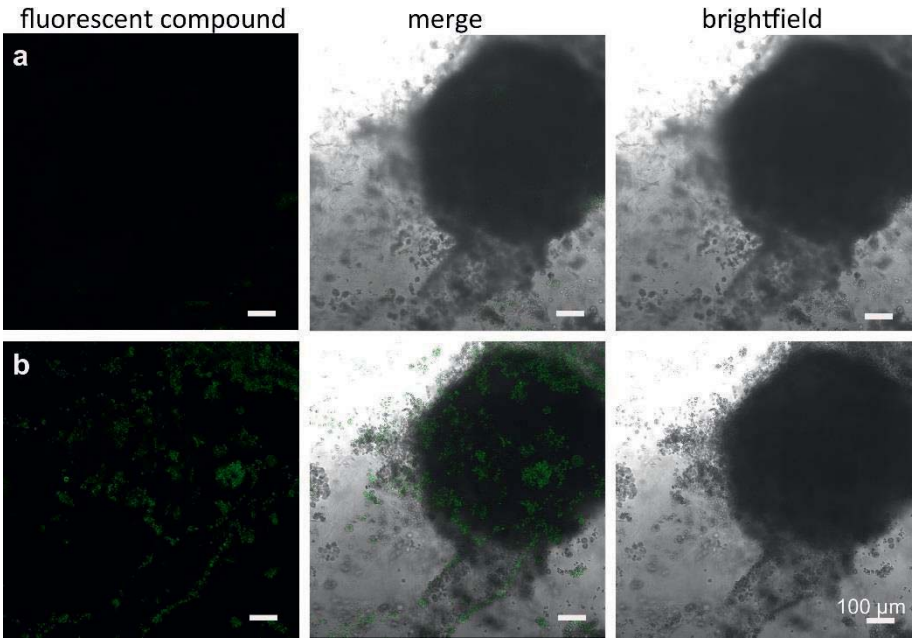

Figure 4.23: Confocal laser scanning microscopy of full skin models with HepG2 spheroids after incubation with 50 µM of lead structure 4.1 for 24 h. a) shows the dermis with no fluorescent signal detectable in the HepG2 hepatocellular carcinoma spheroid, b) shows the epidermis with keratinocytes and melanocytes, a fluoresent signal is detected. $4x10^3$ of HepG2 cells were seeded and grown to spheroids in agarose wells 7 d prior to implantation in a dermis model with 5×10^5 NHDF in 5% GelMA and 0.3% LAP in a transwell filter system. After 7 days culture, 7×10^5 NHEK and 2×10^5 NHEM were seeded on top of the dermis. After 7 days, the surface was lifted to the ALI and cultivated there for another 14 days before being treated with 50 µM lead structure **4.1** for 24 h. Models were washed with PBS and fixated with 4% PFA. The visualization was performed using a Leica TCS-SPE (DMI8) inverted microscope with an ACS APO 63x/1.30 oil objective. The fluorophore was excited using an argon ion laser (λ_{exc}= 488 nm. Using the acquisition software Leica Application Suite (LAS) X 2..1.14392, the picture ratio was adjusted to 1024 × 1024 pixels 8 bit depth. Scale bar: 100 µm.

4.4 Conclusion

It has been shown that the fluorescent labeling of certain cell types and especially cancer cells is of significant value in the elucidation of disease mechanisms and in the detection of diseases.[218] Since melanoma of the skin is a widespread disease with often lethal outcome and growing incidence and mortality rates, a fluorescent labeling of melanoma cells would bear a great potential in early diagnostics.[226-228] Similar strategies have already been developed for non-melanoma skin cancers (NMSCs). The treatment of malignant lesions with 5-aminolevulinic acid (5-ALA) is an approach in photodynamic therapy (PDT). The photosensitizer is topically applied and, after cell permeation, transformed into protoporphyrin IX (PpIX) which causes phototoxicity in the tumor tissue by light exposure. This transformation of 5-ALA can also be monitored non-invasively by the detection of PpIX fluorescence at 634 nm.[322-324] However, there is no specificity in the cellular uptake. 5-ALA concentrations are higher in the tumor tissue due to an enhanced infiltration effect but it is also found in remote skin.[325] Considering the induced phototoxicity, the system lacks in a broad applicability on large, sun-exposed skin areas. Another fluorescence-based detection system for NMSCs that has been published recently is the use of the indomethacin-based fluorescent probe fluorocoxib A that specifically binds the cyclooxygenase-2 (COX-2) enzyme. COX-2 is highly overexpressed in inflammatory and tumorous tissues and can therefore be used in the visualization of cancer cells.[223,224] The applicability of the system in diagnostics has been investigated in a basal cell carcinoma (BCC) allograft hairless mouse model, as well as in a spontaneous BCC mouse model. After systemic administration of fluorocoxib A via retro-orbital injection, the mouse models with different tumor development states were imaged via *in vivo* fluorescence microscopy. For macroscopic tumors, a sensitivity of 88% and a specificity of 100% was reached; for microscopic tumors, a sensitivity and specificity of 85% and 56%, respectively.[326] Despite these efforts, to date there is no fluorescence-based detection system for melanoma skin cancer with a topical probe administration available.

Here we present the discovery of a potential lead structure in the development of such a system, its derivatization to libraries of probe candidates via combinatorial synthesis, the evaluation of these candidates using confocal fluorescence microscopy, and the development and evaluation of different screening settings using 3-dimensional cell culture and organ models. The lead structure that had been found to accumulate in melanoma cells in an earlier project, while not showing this tendency in many other cell lines, consists of three building blocks: an aliphatic cyclooctyne moiety, a piperazine linker, and fluorescein as a fluorophore moiety. Importantly in this context, fluorescein is excited at 490 nm and emits at 525 nm, a wavelength range in the visible light spectrum, that is considered to be biocompatible and does not result in photodamage to the tissue. In three different libraries, two of them synthesized within the scope of this work and one in an earlier work[290], either one or two of these building blocks were altered. In a 2-dimensional cell culture and CLSM imaging approach using melanoma cells, melanocytes, and a control cell line, it was found that the lead structure does not only show a homogenous cytoplasm staining in melanoma cells but also has the same effect in non-melanoma melanocytes. The control cell line (HeLa, human cervix carcinoma) was not affected. The uptake of the compound is apparently

related not to any alteration during the degeneration process of the cancer cells but to a special characteristic of normal as well as degenerated melanocytes compared to other cell types. The same effect was observed in all positive hits among the screened derivatives. Some of the compounds, most of them synthesized in library 3 and with an alteration of the fluorophore and the linker building block, showed a fluorescent signal, and therefore an undesired uptake of the compound, in all three cell lines with an apparent endosomal staining pattern. In library 1 and 2, several molecules were found to reproduce the properties of the lead structure, an uptake in melanoma cells, and melanocytes with homogenous cytoplasm staining and no uptake in HeLa cells. These are considered to be successful candidates and are summarized in **Scheme 4.26**, in particular compound **4.39**, with an adamantane moiety as aliphatic building block and a homopiperazine linker, showed an enhanced fluorescent signal compared to the lead structure and therefore is considered the most promising novel compound for the purpose of melanoma imaging. While the exact structure-function relationships are not resolved yet, the exchange of the piperazine to the homopiperazine linker seemed to have some influence, since compounds **4.35** and **4.37** showed a successful uptake and staining whereas their exact counterparts, with piperazine instead of homopiperazine, did not.

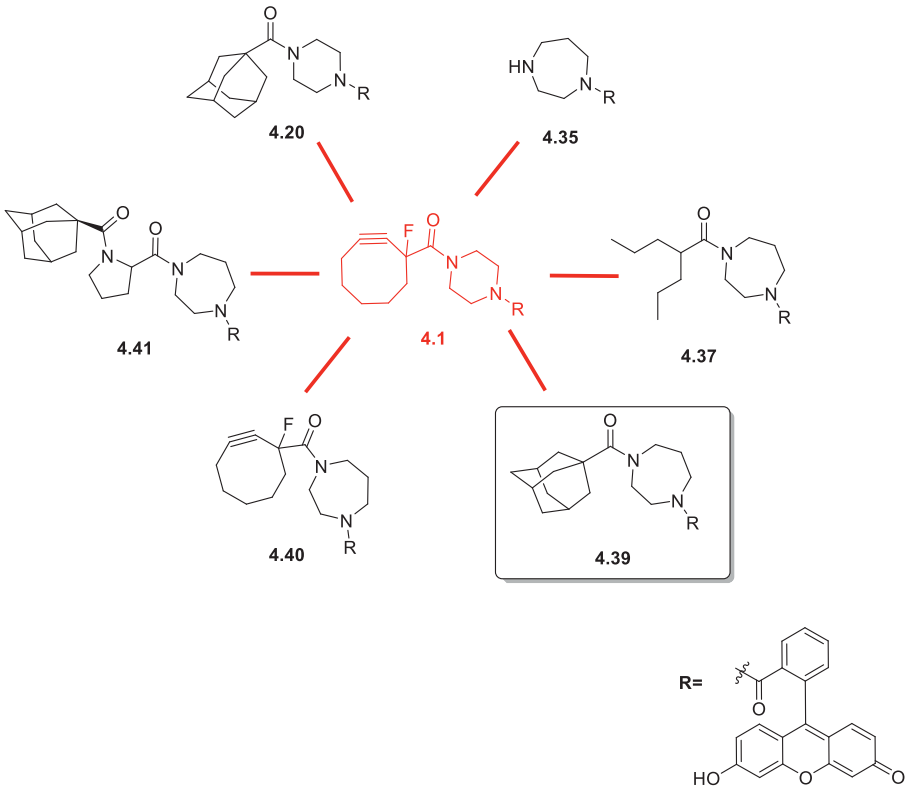

Scheme 4.26: Lead structure **4.1**, the summary of the synthesized and successfully screened derivatives with melanoma and melanocyte uptake, and the most promising candidate **4.39**.

A simple experiment gave insight into the mechanism of transport into the cells. Cell permeation can be achieved either passively, depending on physicochemical properties of the molecules, or in an active, carrier-mediated way. Both mechanisms are usually considered to coexist and contribute both to the uptake of molecules (i.e. drugs) in cells.[301] The lead structure **4.1**, the successful candidate **4.20,** and the most promising candidate **4.39** all showed a successful cell staining when incubated at a temperature of 4 °C with melanoma cells and melanocytes, when the low temperature is expected to sufficiently block active transport pathways by decreasing biochemical reaction rates tremendously. Therefore, a passive transport into the cells is most likely.

To determine the probability of a molecule's cell permeability by its physicochemical properties, Lipinski's rule of 5 is used as a rule of thumb in drug development. It states that a molecule/ drug is less likely to pass a cell membrane when it

1. contains more than 5 hydrogen bond donors (number of OH- and NH-bonds),
2. contains more than 10 hydrogen bond acceptors (total sum of all O and N atoms),
3. the molecular weight is over 500 g/mol and
4. the Log P (water/octanol distribution coefficient) is over 5.

Compound classes that are substrates for biological transporters are exceptions to the rule.[21,22]

Considering the lead structure and its successful derivatives, it becomes obvious that not all of them fit exactly into these rules (mostly due to a slightly too high molecular weight) but with the derivatization, the molecules get closer to this range, especially for the calculated cLogP values that could be reduced. While the lead structure violates the rules twice with a molecular weight of 552.6 g/mol and a calculated cLogP of 5.20 (calculated with ChemDraw Professional 15.0, CambridgeSoft Corporation), the derivatives show only one or no violation (**Table 4.1**).

compound number	number of H-bond donors	number of H-bond acceptors	molecular weight [g/mol]	cLogP	number of violations
4.1	1	7	552,60	5,20	2
4.20	1	7	562,67	4,78	1
4.35	2	6	414,16	2,40	0
4.37	1	7	540,66	4,67	1
4.39	1	7	576,69	4,38	1
4.40	1	7	566,63	4,80	1
4.41	1	9	673,81	4,77	1

Table 4.1: Considerations of the lead structure **4.1** and its as successful screened derivatives under Lipinski's rule of 5.

Since **4.39**shows the best melanoma cells staining results but not **4.35**, which fits exactly into the rule without a violation, this explanation might be not sufficient, but contributive to the whole picture and the process of understanding the mode of action in the apparently melanocyte-specific uptake.

The fact that uptake and accumulation was observed also in the healthy primary melanocytes for all successful candidates contradicts the original assumption to find a structure that is purely melanoma-specific. However, monocultures of melanocytes do not necessarily mimic their behavior in biological systems, since melanocytes and keratinocytes have been shown to closely interact with and influence each other.[327,328] Therefore, the extension of the screening conditions from 2D to 3D and from mono- to mixed cultures had to be established to create a more realistic setting. In order to create the highest possible comparability, the lead structure has been chosen for the first experiments with 3D models. We showed successfully that the lead structure could be detected in spheroids, small tumor-like cell aggregates derived from melanoma cells. Even down to the lowest concentration of 1 µM, the fluorescent signal of our compound was detectable, which established the basis for further development. In the next step we showed successfully that in a full skin-melanoma model with a fibroblast dermis, including an implanted melanoma spheroid and a keratinocyte epidermis, our compound was also accumulated and detectable exclusively in the tumor region after administration via the epidermis. Neither the fibroblasts nor the keratinocytes showed an enrichment that could be detected via confocal microscopy. However, when melanocytes were added to the epidermis, these cells also revealed a fluorescent staining. In a control model with a liver carcinoma derived spheroid, the tumor did not show a detectable accumulation of our marker compound, but here also, the melanocytes in the epidermis layer were stained. However, the epidermis layer in the model does not completely represent the biological tissue properties of human skin. The melanocytes were seeded in a higher density than would occur in the human skin. Furthermore, the brightfield images of the epidermis layer show a not completely confluent, dense layer and treatment concentrations and incubation times were not optimized yet. It is still to be determined how the uptake would appear under optimized conditions in a realistic skin model with only few melanocytes, attached to the basal layer and covered by dense layers of keratinocytes.

To conclude, we presented a promising new approach to the early detection of melanoma via non-invasive fluorescence microscopy after topical administration of a novel fluorescent probe. The lead structure could be optimized and the screening settings could be further developed and extended. In the next steps, both optimizations of the system should be combined and the behavior of the optimized probe in a full skin-melanoma model has to be investigated. Additionally, the step towards an *in vivo* model is becoming important at this point. If and how melanoma formation in a nude mouse melanoma model could be visualized and traced, as well as if and how much the accumulation in healthy melanoma cells and benign lesions can be observed, is of tremendous significance. An equivalent staining of benign melanocytic lesions *in* vivo would unquestionably present a drawback in a potential diagnostic setting for melanoma. Nevertheless, also a specific fluorescent melanocyte marker would be valuable, in histopathologic staining, differential diagnostics, the development of further

artificial skin models, co-staining approaches in fluorescence microscopy, and many further applications.

5 Fluorescent labeling of drug delivery systems

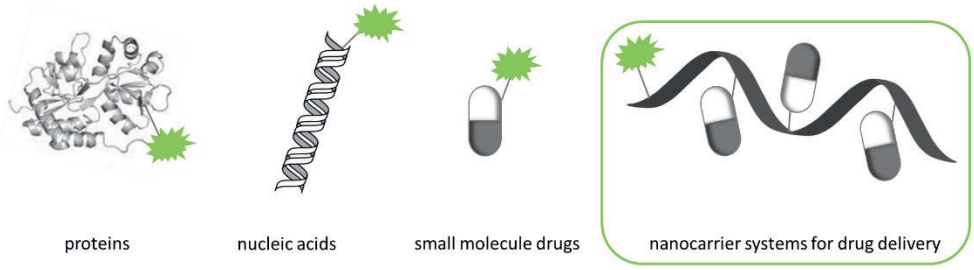

From the broad variety of available drug delivery systems (DDS), including micelles, liposomes, dendrimers, nanoparticles (NPs), and lipoproteins, biocompatible and biodegradable polymeric nanocarriers have gained increasing attention over recent years (**Figure 5.1**). The feasibility of modifications and adaptions, as well as their degradation via hydrolysis or enzymatic activity and therefore clearance from the body after cargo delivery, makes them attractive tools in nanomedicine.[329-331] Combining a (hydrophobic) drug with a (hydrophilic) polymer can significantly enhance drug efficacy through improved biodistribution, as well as restrict drug release in a site-specific manner, or avoid undesired degradation in certain environments (i.e., gastrointestinal tract).[332-335] When generating drug-polymer conjugates, the drug can be either loaded on a platform or encapsulated, as in polymeric nanoparticles or polymeric micelles, or it can be covalently linked to a polymeric backbone, which enables a higher drug loading.[336-338] After arriving at the site-of-interest, a cleavage of these bonds (or degradation of the carrier) and therefore a triggered release of the drug can be achieved via different stimuli-dependent strategies. Thermosensitive polymer systems release their cargo at elevated temperatures, thus being a useful tool in cancer therapy. While tumor tissue already exhibits a slightly warmer microenvironment than healthy tissue (1-2 °C warmer), hyperthermia is a widely used approach in management and treatment of solid tumors.[339-341] Since the elevated temperatures increase the permeability of the tumor vasculature, not only is the release triggered at the tumor site, but drug delivery and accumulation there is also enhanced.[342] Another stimulus-responsive delivery approach are enzyme-triggered release systems. In many diseases, certain types of enzymes are upregulated and overexpressed. By using a peptide moiety that mimics the biochemical substrate of these enzymes, a linker between cargo and delivery system a site-specific release is possible.[343] Further examples of stimuli-triggered release systems include the sensitivity towards ions[344], ultrasound[345-347], magnetic fields[348-350], or redox conditions[351], as well as light-triggered cleavages.[352-354] Additionally, pH-sensitive polymers belong to the most popular release systems. Amino-groups carrying cationic polymers, sensitive to a low stomach pH, are widely used to mask unpleasant taste of orally administered drugs by preventing their release in the oral cavity.[355-357] Anionic polymers, sensitive to basic pH values, prevent a gastric degradation of the drug and thus provide colon drug delivery.[358,359] However, the most important class of pH-sensitive drug carriers are those responding to a lower pH in tumor environment. Due to an enhanced

permeability and retention (EPR) effect, nanosized particles and polymers accumulate in tumorous tissue after intravenous injection (see chapter 1.1).[40,360] Since tumor microenvironments have been shown to be more acidic than healthy tissue (pH= 6.5-7.0 compared to pH= 7.4), the utilization of pH-sensitive groups in the carrier, such as imidazole groups and PEG-*b*-poly (β-amino ester), has been found to be beneficial, reacting to a low extracellular pH value.[361-364] Polymers containing acetal-, ortho ester, vinyl ether, or hydrazone linkages are sensitive towards a lower intracellular pH. After accumulation in the tumor environment via EPR and incorporation in the targeted cells via endocytosis, the release of the drug is triggered in lysosomal compartments (pH= 5).[365]

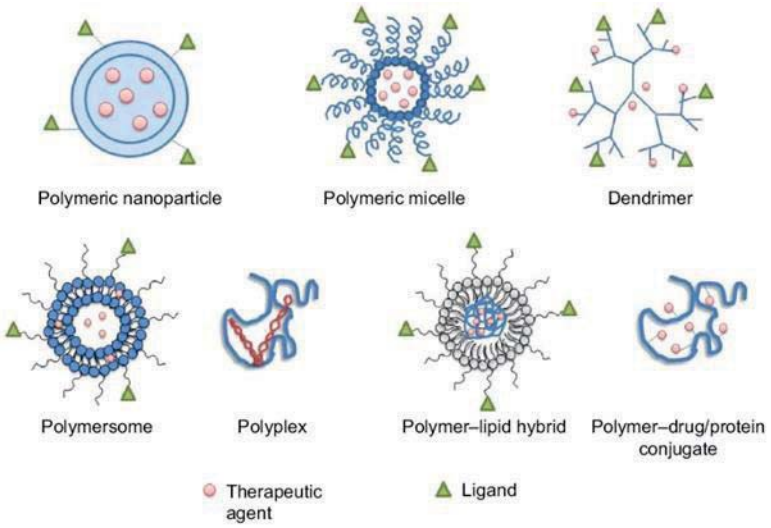

Figure 5.1: Schematic illustration of different polymeric nanocarrier platforms.[366] Republished with permission from Prabhu et al. ©2015 by DOVE medical press

By fluorescent labeling of the delivery systems, or using polymers or drugs with intrinsic fluorescent properties, the drug delivery to and accumulation at the targeted site can be imaged *in vitro* or *in vivo* in real-time.[367] However, imaging the cargo release remains challenging. A potential possibility to overcome this obstacle is the utilization of a fluorescence silencing – fluorescence recovery principle. Nitroxide molecules that exhibit radical character can efficiently mask the fluorescence of fluorophores when situated in close spatial proximity by forming profluorescent nitroxide molecules.

The term nitroxide describes an *N,N*-bissubstituted nitrogen-oxygen (NO) radical with an unpaired, delocalized electron shared between the nitrogen and the oxygen atom.[368] The bond length between N and O (1.23-1.29 Å) is reportedly shorter than in NO single bonds (1.44 Å), thus exploiting a double bond character.[369] Due to their paramagnetic characteristics, nitroxide molecules can be conveniently analyzed via electron paramagnetic resonance (EPR) spectroscopy.[370] In their solid state, most nitroxides are very stable and can be stored for years. Since the first report in 1845 and through today, these molecules have been studied intensively and a broad variety of applications has been found. Besides their application in synthesis and polymerization[371,372], they have been used as antioxidants[373], as well as probes in EPR

spectroscopy[374,375], and imaging[376-378]. When tethered to a fluorophore, nitroxides have been found to efficiently quench fluorescence in an intra- and intermolecular mechanism, thus generating profluorescent nitroxides (**Figure 5.2**).[379] Instead of emitting a photon from an excited singlet state (termed fluorescence, chapter 1.3), electron-exchange interactions between the paramagnetic nitroxide and the excited-state fluorophore lead to enhanced intersystem crossing (ISC) processes to an excited triplet state and therefore decreased fluorescence (**Figure 5.3**). The interactions cause a change in spin multiplicity, thus producing doublet states from the excited singlet states which turns the former forbidden transition process ISC into a spin-allowed process.[380] Due to the long life span of the generated triplet states, a lot of energy is lost to non-radiative environment interactions and not emitted as phosphorescence. Spatial proximity of an unpaired electron to a fluorophore results in a significant reduction of fluorescence quantum yield.[381] Since the reaction of the nitroxide free radical removes this quenching by forming a diamagnetic species and leads to a fluorescence increase, profluorescent nitroxides have been used to intracellularly detect and monitor reactive oxygen species (ROS, oxidative stress) in one- and two-photon microscopy, as well as in the detection of free radicals formed during degradation and aging of polymeric materials.[382-384]

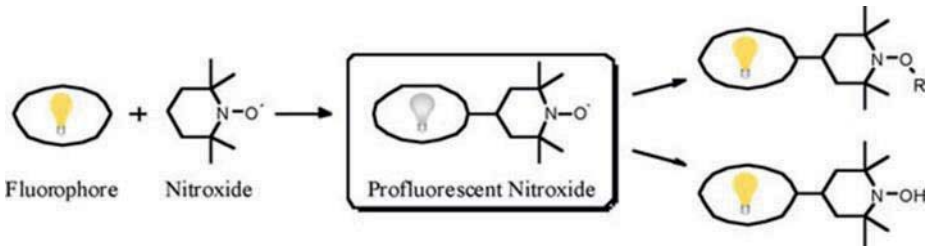

Figure 5.2: Tethering of a nitroxide to a fluorophore leads to a fluorescence quenching/masking. Removal of the spin by a radical reaction results in return of fluorescence. Reproduced from Blinco et al (2011), with permission from CSIRO Publishing.[379]

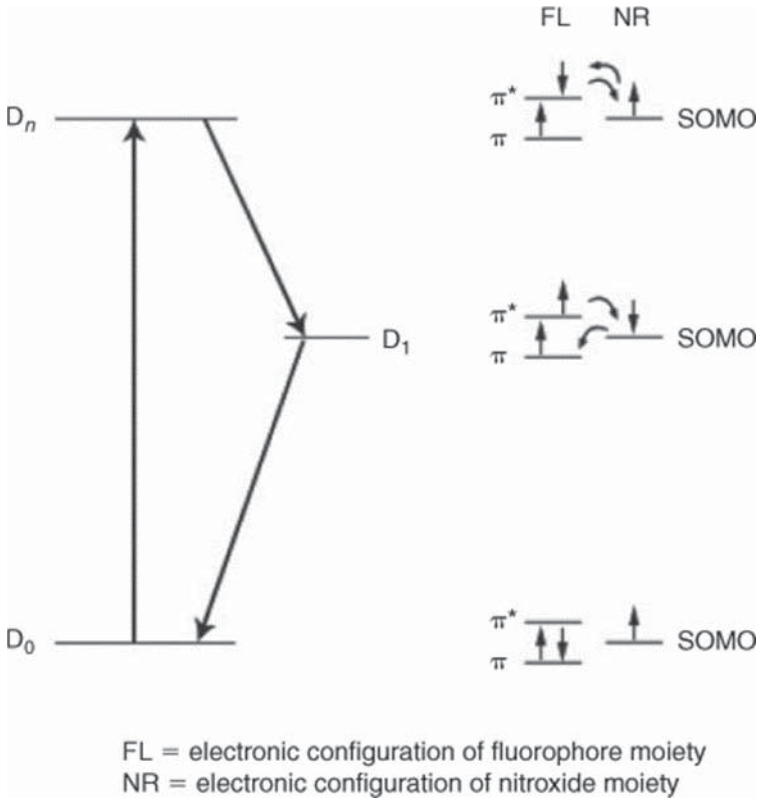

Figure 5.3: Electron exchange interactions between nitroxide and fluorophore in the doublet state. (SOMO= singly occupied molecular orbital). Reproduced from Blinco et al (2011), with permission from CSIRO Publishing.[379]

Since the imaging and tracking of drug delivery is already established in many different ways, but the visualization as well as the quantification of the stimuli-triggered release from drug delivery nanocarrier platforms remains challenging, it was the aim of this study to develop an innovative, fluorescence-based system for the tracking of delivery and release.[385-387] On a water-soluble polymeric backbone, nitroxide moieties were installed in close proximity to a doxorubicin molecule, attached to the backbone via a pH-labile linker. Doxorubicin, a cytostatic that is frequently used in chemotherapy, exhibits, due to a conjugated π-system, intrinsic fluorescence in the visible (red) range (λ_{exc}= 480nm, λ_{em}= 560-590 nm).[388] After injection of the carrier system *in vivo*, the nanosized polymer should accumulate at the tumor site, taking advantage of the EPR effect (see chapter 1.1). The fluorescent drug doxorubicin is covalently linked to the backbone via a pH-labile hydrazone bond and its fluorescence is quenched by an adjacent nitroxide (**Figure 5.4**). As soon as the carrier system is permeating the tumor cells via endocytosis, the hydrazone bond between cargo and carrier is cleaved due to hydrolysis caused by low pH values within the lysosome compartments. Doxorubicin as a free drug accumulates in the nuclei of the cancer cells, while recovering its fluorescent signal. By installing all the components in a way that switching on one fluorophore is related to the successful delivery of one molecule, not only a visualization but also a quantitative measurement of release would be possible.

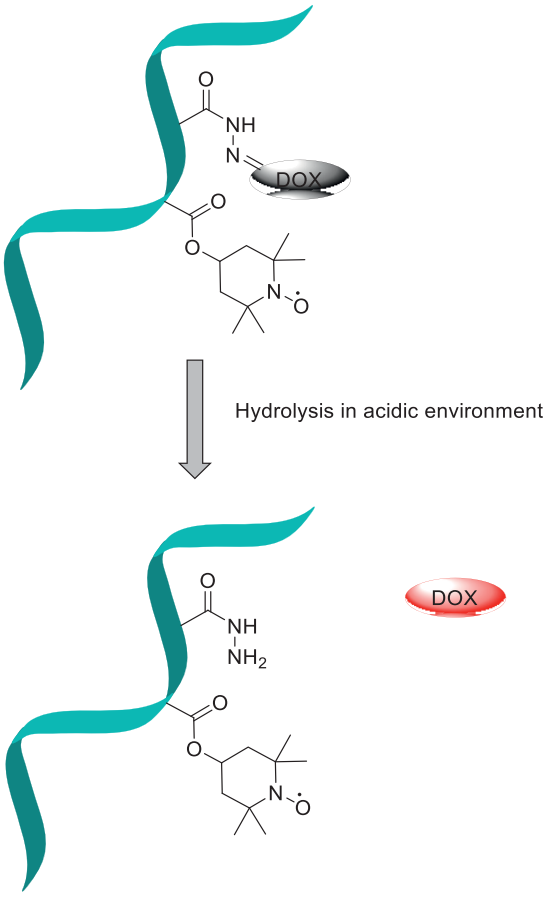

Figure 5.4: Design of the polymeric nanocarrier platform. Doxorubicin (DOX) is attached to the polymer backbone (blue) via a pH-labile hydrazone bond and its fluorescence is silenced through electron exchange interactions with the adjacent nitroxide moiety. In acidic environment, as in lysosomes after endocytosis, the hydrazone bond is cleaved via hydrolysis and the DOX is released under fluorescence recovering.

5.1 Synthesis of a small molecule release model system

In order to investigate the quenching effects of the nitroxide on doxorubicin (DOX) and the required release conditions, the synthesis of a small molecule model system was defined as a first step towards our nanocarrier platform. In the model system, DOX was coupled directly to a previously synthesized tetramethylisoindoline nitroxide (TMIO) moiety via a pH-labile hydrazone bond (**Scheme 5.1**).

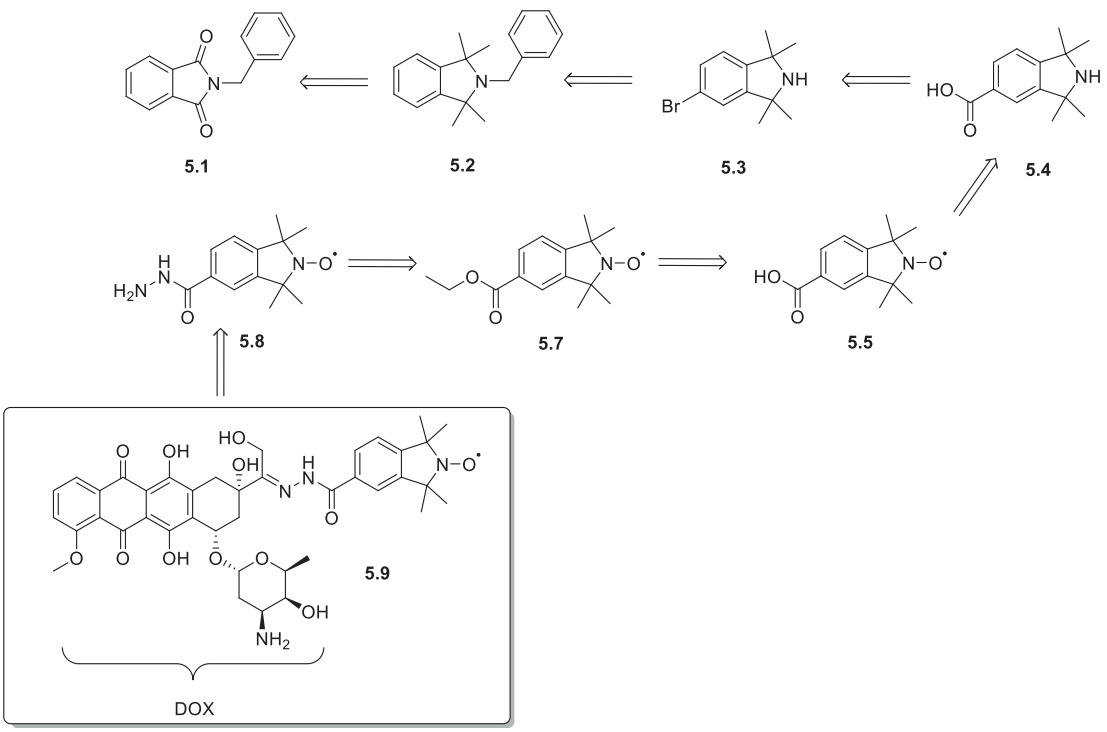

Scheme 5.1: Retrosynthetic strategy in the synthesis of a DOX-nitroxide small molecule model system.

In the first step of the synthesis, the *N*-benzylphtalimide **5.1** was alkylated under Grignard reaction conditions using methyl magnesium iodide to form the benzyl-protected tetramethylisoindoline **5.2** (**Scheme 5.2**). First published in 1900 by the French chemist F. A. V. Grignard, the reaction describes the addition of an organomagnesium halide to a ketone or aldehyde to form carbon-carbon bonds.[389] In a large-scale approach starting with 50 g **5.1**, the desired product could be obtained in a moderate yield of 26%, after the formation of the Grignard reagent from methyl iodide and magnesium chips.

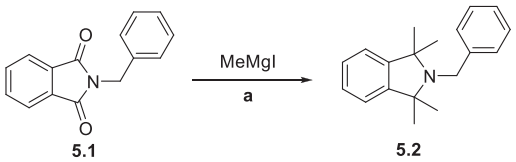

Scheme 5.2: Synthesis of the benzyl-protected tetramethylisoindoline under Grignard reaction conditions. a) Et_2O, toluene, hexanes, reflux, 2 d.

Subsequently, the deprotection of the secondary amine was performed in a two-step-one-pot reaction with a bromination, preparing the following carboxylation on the phenyl ring. Aluminum chloride ($AlCl_3$) is used as a strong Lewis acid to catalyze the bromination before the benzyl ether is cleaved with hydrogen peroxide (H_2O_2)

(**Scheme 5.3**). While in comparatively small scales (3 g) the desired product **5.3** could be obtained in good to excellent yields of up to 92%, the yield was significantly decreased to a moderate 43% for scales >10 g, indicating limitations in upscaling the reaction.

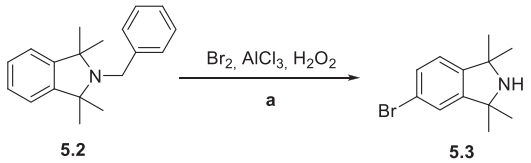

Scheme 5.3: Two-step-one-pot bromination and benzyl-deprotection. a) abs. DCM, 0 °C, 2 h.

Using n-butyllithium (n-BuLi) as a highly reactive nucleophile in presence of carbon dioxide (CO_2), the previously brominated phenyl-position could be transformed into a carboxylic acid in the next step (**Scheme 5.4**).[390] Due to the formation of a large amount of inorganic salts and the difficulties of separating a carboxylic acid from those, the yield could not be determined in this reaction step.

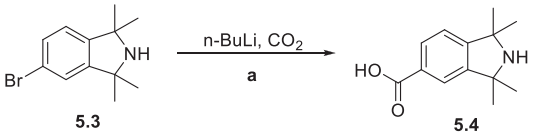

Scheme 5.4: Carboxylation of the brominated phenyl ring position using n-butyllithium (n-BuLi) and CO_2. a) abs. THF, -78 °C-rt, 45 min.

From the tetramethylisoindoline carboxylic acid **5.4** the next crucial step was the oxidation to obtain the nitroxide in the amine position. In a first attempt, sodium tungstate dihydrate ($Na_2WO_4 \cdot H_2O$) and hydrogen peroxide were used (**Scheme 5.5**). However, after several days of reaction and repeated oxidation steps adding more Na_2WO_4 dihydrate and H_2O_2, the respective mass of the starting material was still found in mass spectrometry (additionally to the desired product mass) and the NMR still exhibited an amine signal.

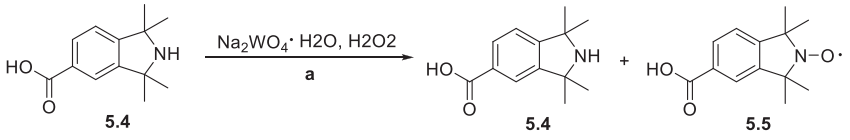

Scheme 5.5: Oxidation of the amine position using sodium tungstate to obtain the nitroxide. a) H_2O/MeOH, rt, 5 d.

Since the complete oxidation could not be achieved by using this method, a second oxidation step using meta-chloroperoxybenzoic acid (mCPBA) was applied after first protecting the carboxylic acid as an ethyl ester in the next step. Solving the carboxylic acids **5.4** and **5.5** in EtOH and heating for 72 h in presence of sulfuric acid results in reliable ethyl ester formation (**Scheme 5.6**).

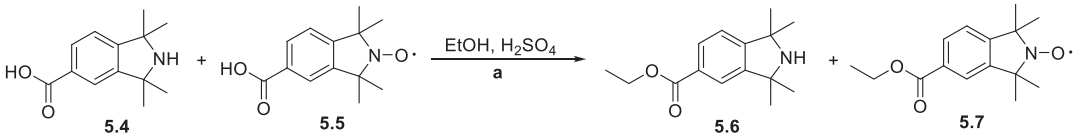

Scheme 5.6: Esterification of the carboxylic acid using EtOH and H_2SO_4. a) 70 °C, 72 h.

In order to complete the oxidation of the amine, the mixture of nitroxide and amine **5.6** and **5.7** was separated and the amine ester **5.6** was treated with mCPBA. After 3 h reaction time, a complete product conversion could be achieved indicating a more efficient oxidation strategy then the previously applied one using sodium tungstate and hydrogen peroxide. Hence, in later approaches the tetramethylisoindoline carboxylic acid **5.4** was first esterified and then oxidized with mCPBA to obtain the TMIO ethyl ester **5.7**.

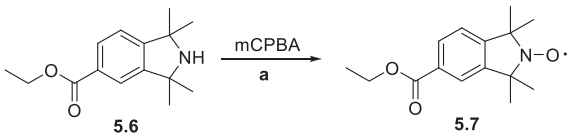

Scheme 5.7: Oxidation of the ethyl ester amine side product **5.6** to the desired TMIO ethyl ester **5.7** using mCPBA. a) DCM, 0 °C-rt, 3 h.

After building up the nitroxide moiety, the ester had to be converted to the respective hydrazide to achieve the desired hydrazone linkage to DOX in the following step (**Scheme 5.8**). Refluxing the ester **5.7** with hydrazine monohydrate for several hours resulted in the formation of the desired hydrazide **5.8** in a good yield of 57%.

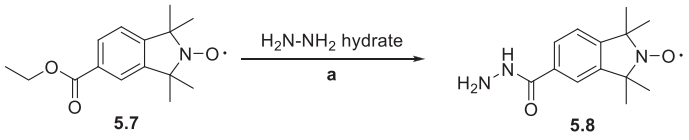

Scheme 5.8: Formation of the TMIO hydrazide **5.8** from the ethyl ester **5.7** using hydrazine monohydrate. a) iPrOH, 95 °C, 2.5 h.

An exchange from the oxygen in the doxorubicin ketone functionality with the terminal hydrazide nitrogen results in the formation of the desired hydrazone linked DOX-TMIO **5.9** (**Scheme 5.9**).

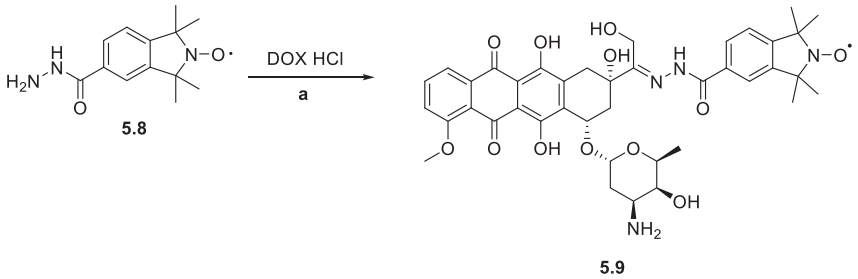

Scheme 5.9: Coupling of DOX to obtain the desired hydrazone linked DOX-TMIO **5.9**. a) abs. MeOH, 80 °C, 19 h.

However, several reaction conditions had to be investigated to achieve this coupling (**Table 5.1**). The different conditions were screened via analytical HPLC using ACN and H_2O as eluents, without the common addition of 0.1% trifluoroacetic acid (TFA) or formic acid (FA), since the acidic additives could cause hydrolysis of the newly-obtained hydrazone bond.

entry	solvent	additive	temperature	time
1	iPrOH	AcOH	95 °C	17 h
2	EtOH	-	90 °C	17 h
3	EtOH	EDCI	90 °C	17 h
4	abs. EtOH	-	rt	1 h
5	abs. EtOH	-	80 °C	1 h
6	abs. EtOH	-	80 °C	3 h
7	abs. EtOH	-	80 °C	19 h
8	abs. EtOH	-	80 °C	25 h
9	abs. EtOH	-	80 °C	46 h
10	abs. MeOH	-	rt	1 h
11	abs. MeOH	-	80 °C	1 h
12	abs. MeOH	-	80 °C	3 h
13	**abs. MeOH**	**-**	**80 °C**	**19 h**
14	abs. MeOH	-	80 °C	25 h
15	abs. MeOH	-	80 °C	46 h

Table 5.1: Screened reaction conditions for the DOX coupling. Evaluation of the reactions via analytical HPLC gave the best product conversion for 19 h reaction time at 80 °C in abs. MeOH. Eluents: ACN/H_2O without acidic additives.

The at least partially successful product formation could be shown via analytical HPLC, LC/MS, and MALDI-TOF mass spectrometry. NMR spectroscopy is, due to the paramagnetic properties, in general extremely difficult and very often not successful for nitroxide compounds. An additional drawback in analytics and purification of the DOX-TMIO **5.9** was the labile hydrazone bond. Especially the LC/MS measurements, which require the addition of a small amount TFA in the eluent, were not ideally suited for the product analysis and it was impossible to distinguish between an incomplete coupling and bond cleavage occurring during the measurements. Fragmentation and dissociation could also be observed in analytical as well as preparative HPLC, and during MALDI-TOF measurements with a non-acidic matrix. Purification attempts via preparative HPLC failed due to hydrolysis of the linkage, as well as an attempted cleavage in acidic solvent to demonstrate the DOX release via HPLC. Since the release occurred very fast and each HPLC run took about 20 min, there was no difference detectable between the runs.

5.2 Synthesis of the polymeric nanocarrier platform

In order to create a water-soluble polymeric platform carrying nitroxide moieties adjacent to hydrazone-linked doxorubicin molecules as a cargo and that is therefore comparable to the previously described small molecule model system, a terpolymer was synthesized in a reversible addition-fragmentation chain-transfer (RAFT) polymerization from three different precursor methacrylate monomers that could be adapted in a post-polymerization approach.[xvii] The application of RAFT agents in the polymerization process allows for a precise control of chain length and dispersity, and has been widely used in biomedical applications and in particular as drug delivery nanocarriers.[391] The monomers, employed in a ratio of 6.5:1:1 in the polymerization, were triethylene glycol methacrylate (TEGMA) **5.10** to ensure water-solubility, *tert*-butyloxycarbonyl-hydrazidomethacrylate (bHMA) **5.11** as a protected hydrazide anchor for subsequent DOX-coupling, and tetramethyl-piperidyl-methacrylate (TMPMA) **5.12** as a nitroxide precursor for subsequent oxidization (**Scheme 5.10**).

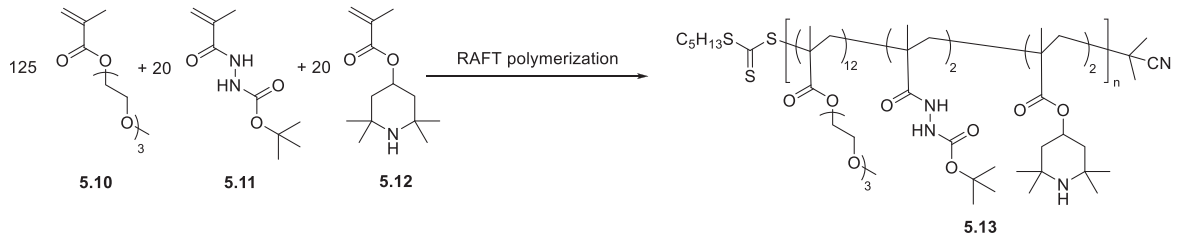

Scheme 5.10: RAFT polymerization using the 3 different methacrylate monomers TEGMA, bHMA and TMPMA.

Oxidization of the TMPMA amine with mCPBA to the nitroxide, similar to the optimized oxidation step in the small molecule system, deprotection of the hydrazide anchor, and subsequent doxorubicin coupling (in contrast to the small molecule system under slightly acidic conditions), resulted in the desired polymeric system **5.14** (**Scheme 5.11**).

[xvii] All polymer-related synthesis, analytics and fluorescence measurements were conducted by M. Eing, Barner-Kowollik group, KIT & QUT (Queensland University of Technology, Brisbane, AUS)

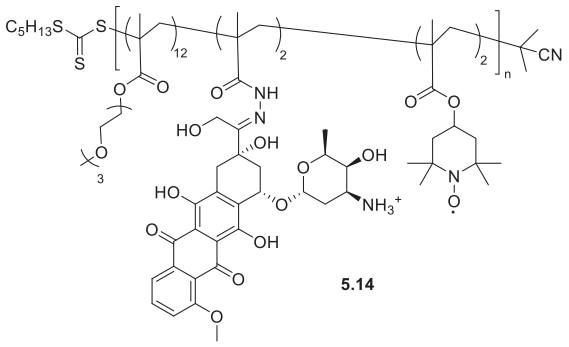

Scheme 5.11: Desired water-soluble DOX-nitroxide polymeric nanocarrier platform **5.14**.

In a release test reaction, a highly diluted sample of the DOX-nitroxide polymer **5.14** (6.25 µg/ml in PBS) was acidified using 30 µl glacial acid and the fluorescence development was tracked over the course of the next 7 days (**Figure 5.5**). While the polymer **5.14** showed a significant quenching of fluorescence compared to free DOX, the signal was almost completely recovered after the release. The observation of fluorescence intensity development over time showed a very fast increase in signal intensity, especially within the first minutes.

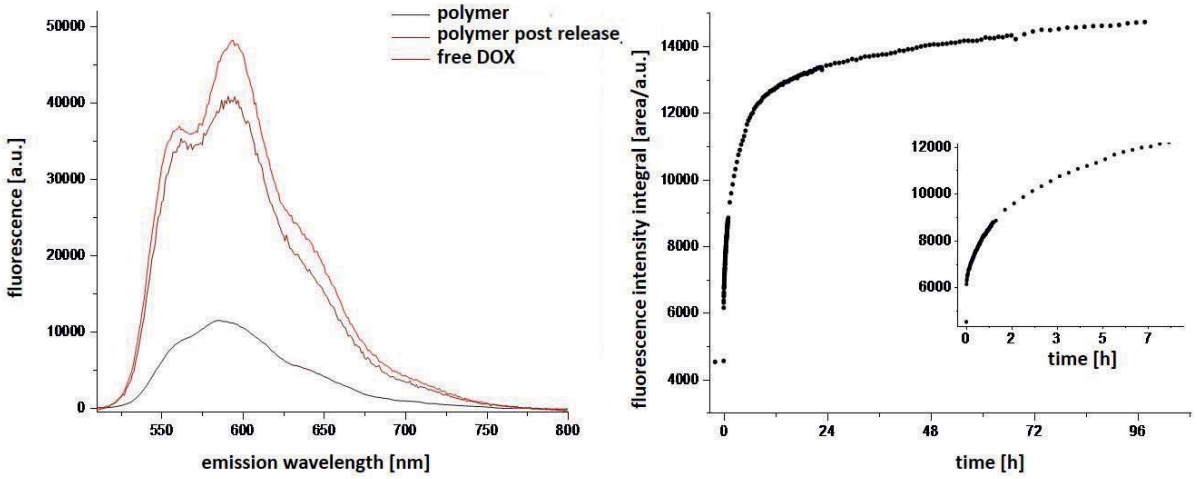

Figure 5.5: A comparison of the fluorescence of free DOX and DOX-nitroxide polymer **5.14** before and after release shows almost complete fluorescence recovery after hydrazone linkage hydrolysis. Observations over time showed a very fast increase in fluorescence intensity (measured as integral area/a.u.) within the first minutes of the release. Reproduced with permission from M. Eing, Barner-Kowollik group, KIT.

5.3 In vitro studies of the polymeric nanocarrier platform

5.3.1 Cytotoxicity studies in HeLa cells

The synthesized polymeric nanocarrier platform **5.18**, its precursor before the DOX coupling **5.16**, free doxorubicin hydrochloride **5.17**, as well as the most abundant monomer TEGMA **5.10,** and a control nitroxide molecule 4-amino-2,2,6,6-tetramethylpipridine-1-oxyl (4-amino TEMPO) were investigated for their influence on cell viability using a standard MTT assay in HeLa cells (as described in chapter 3.3.1). LD_{50} values, describing the concentration of a chemical that leads to 50% cell viability, were calculated where applicable. The monomer TEGMA **5.10** and the control nitroxide 4-amino TEMPO **5.19** (**Scheme 5.12**) were incubated with HeLa cells for 72 h in a concentration range of 100 µM to 2.5 mM (**Figure 5.6**). Both investigated molecules did not show significant cytotoxic effects up to a concentration of 500 µM. The LD_{50} value could be calculated for TEGMA by applying a fit curve as 891 µM[xviii]. The LD_{50} for 4-amino TEMPO was found to be >2.5 mM.

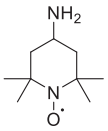

5.19

Scheme 5.12: Structure of the control nitroxide 4-amino TEMPO.

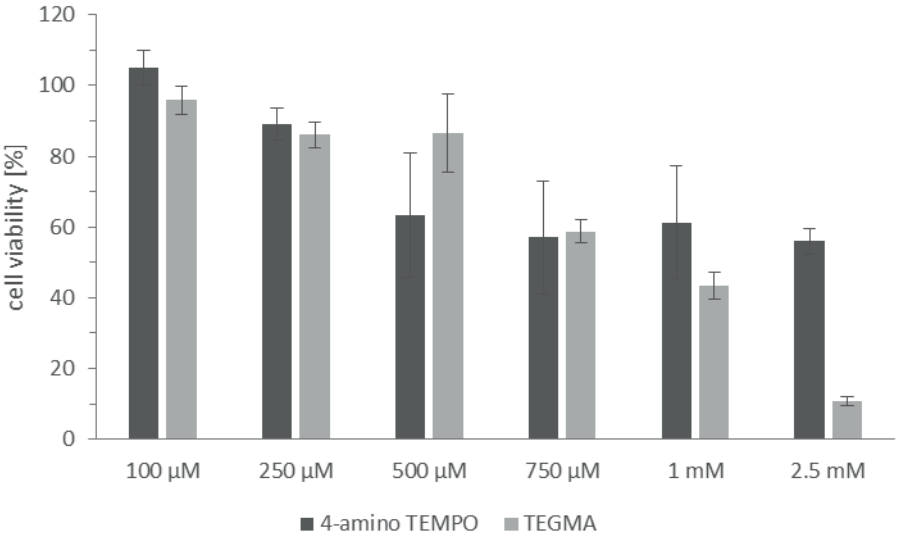

Figure 5.6: Cytotoxicity assay of the monomer TEGMA and the control nitroxide 4-amino TEMPO after 72 h incubation of HeLa cells in the concentration range 100 µM – 2.5 mM. Statistical error bars were calculated as standard deviations from a sextuplicate of *n*=6 experiments.

[xviii] Applied fit curve: DoseResp in OriginPro 8.6G.

The target polymer **5.18**, its precursor polymer **5.16** and the free DOX **5.17** were investigated in a significantly lower concentration range of 1 µg/ml – 1 mg/ml for the polymers and a DOX concentration of 0.01 µM – 10 µM (**Figure 5.7**). These DOX concentrations were chosen corresponding to the DOX load in the investigated target polymer **5.18**. Considering the percentage of hydrazide anchor monomers and effective DOX loading, in a polymer concentration of 1 mg/ml, DOX molecules are contained equivalent to a 10 µM free DOX HCl dilution. The DOX loaded polymer **5.18** revealed a higher toxicity at lower concentrations compared to the same amount of free DOX **5.17** while the precursor polymer **5.16**, not carrying DOX as a cargo, was significantly less toxic. The LD_{50} values were calculated as 12.6 µg/ml for **5.18**[xix] and 0.488 µM for **5.17**[xx]. The cell viability range necessary to calculate the LD_{50} for precursor polymer **5.16** was not reached, it is expected to be >1 mg/ml.

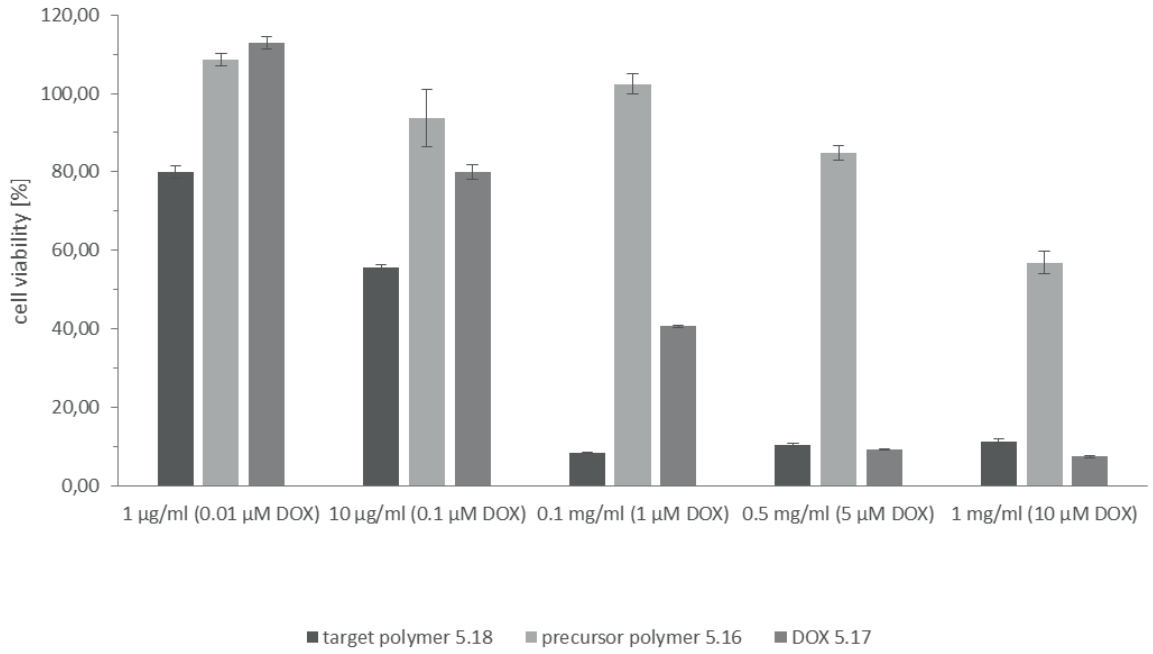

Figure 5.7: Cytotoxicity assay of the target polymer **5.18**, the precursor polymer **5.16** and the free DOX HCl **5.17** after 72 h incubation of HeLa cells in the concentration range 1 µg/ml – 1 mg/ml (0.01 µM – 10 µM DOX, respectively). Statistical error bars were calculated as standard deviations from a triplicate of *n*=3 experiments.

[xix] Applied fit curve: exponential fit in OriginPro 8.6G.
[xx] Applied fit curve: logarithmic fit in OriginPro 8.6G.

5.3.2 Confocal microscopy - cellular uptake and release studies

In order to investigate the synthesized polymeric nanocarrier platform **5.18** for cell permeation and release within a biological system, HeLa cells were treated in two concentrations with the target polymer **5.18** and free DOX **5.17** (50 µg/ml and 100 µg/ml **5.18**, and corresponding 0.5 µM and 1 µM **5.17**) for 45 min, and the cellular uptake as well as fluorescence development were observed via confocal microscopy (**Figure 5.8**). The revealed fluorescence signal in the cell nuclei was significantly stronger for the polymer-bound DOX than for the free DOX in both concentrations (panel **a** and **c**), indicating an enhanced uptake for the polymeric nanocarrier system. Due to a fast uptake in cells, release of the DOX, and migration in the nucleus, a visualization of the endocytosis with subsequent release in the lysosomal compartments was not successful.

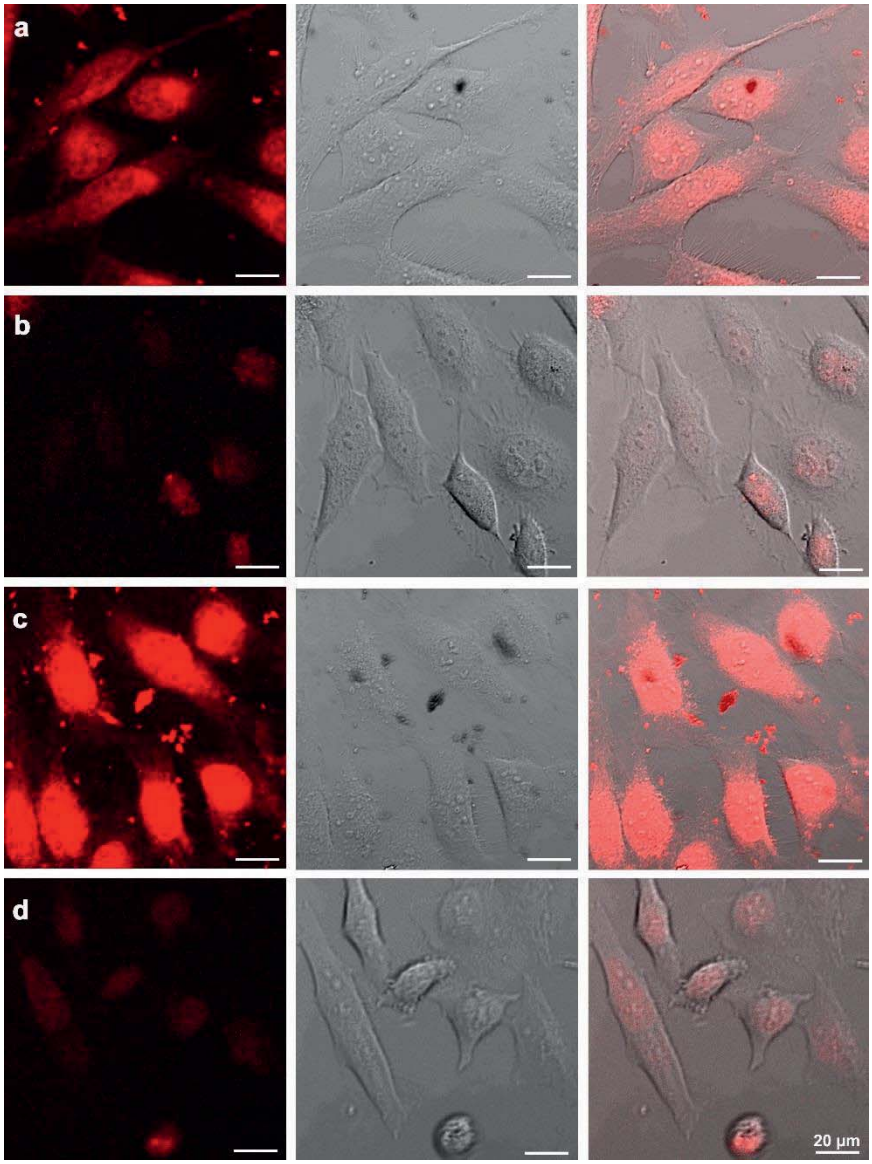

Figure 5.8: Confocal laser scanning microscopy of HeLa cells after incubation with a) 50 µg/ml polymer 5.18, b) 0.5 µM DOX 5.17, c) 100 µg/ml polymer 5.18, and d) 1 µM DOX 5.17 for 45 min. $4x10^4$ HeLa cells were seeded in an 8-well chamber slide 24 h prior to treatment. The visualization was performed using a Zeiss LSM 800 inverted microscope with a plan-neofluar 10x/0.30 objective. DOX was excited using an argon ion laser (λ_{exc}= 488 nm). The picture ratio was adjusted to 1024 × 1024 pixels 8 bit depth. Scale bar: 20 µm.

5.4 Conclusion

Extensive efforts have been made in the development of drug delivery systems (DDSs) over previous years. Especially in cancer therapy, a targeted drug delivery can not only improve drug efficacy but also significantly reduce systemic side effects like nausea, vomiting, diarrhea, mucositis, alopecia, and constipation, that frequently occur in chemotherapy.[392] Many systems have been proposed for the delivery of doxorubicin, a common cytostatic that additionally exhibits intrinsic fluorescence and therefore facilitates the tracking of the delivery, including liposomal delivery, hydrogels, and nanoparticles.[393] However, the successful tracking of the drug delivery process is not only depending on the site-specific arrival of the cargo-carrier construct, but also on the release of the cargo from the carrier platform. To date, the imaging of this release remains challenging. Several groups have been working on methods to visualize and quantify drug release from a cargo *in vivo*, almost all of them based on magnetic resonance imaging (MRI).[394] Here we present a novel approach for the *in vitro* and *in vivo* fluorescence imaging of drug delivery and release. On a water-soluble polymeric nanocarrier platform, a doxorubicin (DOX) payload has been installed via a pH labile linker and in close proximity to a nitroxide unit. The unpaired electron of the nitroxide interferes with the excited states of the fluorescent DOX in electron exchange interactions, thus silencing its fluorescence. After successful delivery to and accumulation of the system at a tumor-site, taking advantage of the EPR effect, the carrier system is permeating the target cells via endocytosis and the cargo is released due to acidic pH values in lysosomal compartments. The free DOX accumulates in the cell nuclei by intercalating in the DNA under recovery of its fluorescence.[393] We have successfully synthesized a small molecule model system, connecting DOX and a nitroxide moiety directly via a hydrazone linkage. Due to the very fragile bond, however, purification and analytics were challenging. A verification of the bond cleavage in a HPLC set-up to demonstrate the release was not successful. Release experiments in a fluorescence measurement based set-up with the successfully synthesized polymeric platform showed a very fast release mechanism with the largest increase in fluorescence intensity within the first minutes. Given the lower accessibility of the hydrazone bond within a polymeric system compared to small molecules in solution, it is supposed that the cleavage would be even faster in the model system. Hence, an HPLC set-up with measurements every 20 min and separation conditions that can already lead to bond cleavage is not ideally suited for this system. First *in vitro* studies investigating the cytotoxicity of the polymeric system have shown an enhanced toxicity for the carrier-bound DOX as compared to free DOX and a comparatively low toxicity of the polymer itself and its components. While the LD_{50} value for free DOX was found to be 0.488 µM, the LD_{50} for the DOX carrier system was 12.6 µg/ml which, based on the number of hydrazide anchors and their respective loading density, relates to an amount of DOX corresponding to 0.126 µM. The cytotoxic effect and therefore the drug efficacy of DOX was increased almost by factor 4 after delivery by our system. An accelerated uptake could be an explanation of this effect. Imaging of cells after treatment with our system and free DOX in the corresponding concentrations via confocal microscopy, detecting the DOX fluorescence, revealed a significantly stronger fluorescent signal in the cell nuclei, the DOX target destination, for our system. Even

though we were not able to visualize the release of DOX in lysosomal compartments due to a very fast uptake, release, and migration in the nucleus, the strong signal supports our hypothesis of increased drug efficacy by enhanced uptake within the developed platform and demonstrates fluorescence recovery.

To conclude, we successfully synthesized the proposed polymeric nanocarrier platform and demonstrated not only fluorescence silencing and recovery but also superior drug delivery and therefore enhanced efficacy. 3-dimensional cell culture based tumor studies as well as *in vivo* studies in mice are considered to be the next relevant steps to demonstrate the applicability of our system

Experimental section

6 Experimental section

6.1 Chemistry

6.1.1 General

6.1.1.1 Analytics and equipment

Nuclear Magnetic Resonance (NMR)

NMR spectra were recorded using the following equipment: ^{1}H-NMR: Bruker AV 300 (300 MHz) and Bruker Ascend™ (400 MHz), ^{13}C-NMR: BRUKER Ascend™ (101 MHz). All spectra were recorded at room temperature. Deuterated solvents were purchased from Eurisotop: chloroform-d_1, dimethylsulfoxid-d_6, water-d_2 and methanol-d_4. Chemical shifts for protons δ are reported in parts per million (ppm) and are referenced to residual solvent peaks for DMSO (^{1}H: δ = 2.50 ppm, ^{13}C: δ = 40.76 ppm), $CHCl_3$ (^{1}H: δ = 7.26 ppm, ^{13}C: δ = 77.0 ppm), H_2O (^{1}H: δ = 4.79 ppm) and CH_3OH (^{1}H: δ = 3.31. ppm).[395] The multiplicities of the signals were abbreviated as follows: s = singlet, d = doublet, t = triplet, q = quartet, hept = heptet, bs = broad singlet, m = multiplet b = broad (unresolved) and combinations thereof. All coupling constants *J* are stated as modulus in Hertz [Hz]. Assignment of ^{13}C NMR spectra signals is according to DEPT technique (Distortionless Enhancement by Polarisation Transfer) as given in **Table 6.1**.

carbon atom	DEPT signal	abbreviation
primary or tertiary	positive	+
secondary	negative	–
quaternary	no	C_q

Table 6.1: Assignment of signals from DEPT spectra.

Infrared spectroscopy (IR)

IR spectra were recorded on a Bruker alpha-p. Samples (solids and oils) were measured via ATR technique (attenuated total reflection). Band intensities were characterized as follows: vs= very strong (0-10% T), s= strong (11-40% T), m= medium (41-70% T), w= weak (71-90% T) and vw= very weak (90-100% T). Position of absorption bands are given as wave numbers ($\tilde{\nu}$) in the unit [cm^{-1}].

Mass spectrometry (EI-MS)

Samples were measured via electron ionization EI-MS on a Finnigan MAT 95. Molecular fragments are given as mass-to-charge ratio [m/z], the intensity of signals is

given as percentage relative to the base signal (100%). For the molecule ion, the abbreviation $[M]^+$ is used.

Analytical LC-ELSD-MS

Analytical LC-ELSD-MS was performed on a Waters 2545 HPLC equipped with a 2998 diode array detector, a Waters 3100 ESI-MS module, using a XTerraMS C18 5 µm, 4.6 x 50 mm column at a flow rate of 5 mL/min with a linear gradient (95% A: 5% B to 100% B with 90 seconds and 30 seconds hold at 100% B, solvent A = water +0.1% formic acid, solvent B = acetonitrile + 0.1% formic acid).

Flash purifications

Purifications were performed on a Biotage Isolera 4 Purification System equipped with a 200-400 nm diode array detector using Biotage SNAP Flash Chromatography Cartridges.

Thin Layer Chromatography (TLC)

Thin layer chromatography was performed with precoated aluminum backed TLC plates obtained from VWR: Aluminum Oxide 60, Neutral F254 & Silica Gel 60, Neutral F254 and from Merck: Silica Gel 60, Neutral F254. Visualization of TLC plates was performed with ninhydrin, potassium permanganate, or an UVGL25, Compact UV Lamp 254/365 UV (UVP 115V~60Hz/0.16 Amps).

6.1.1.2 Preparative work

For air- or humidity-sensitive reactions, glass vessels were heat-dried and evacuated before flooding with argon. Reactions were conducted under argon as inert gas using Schlenk technique. Liquids were transferred using syringes and cannulas, solids were used as powders. Reactions at 0 °C were cooled with an ice/water mixture, reactions at -20 °C with an ice/sodium chloride mixture and reactions at -78 °C with an isopropanol/dry ice mixture in Isotherm dewar vessels.

Reaction control was conducted via TLC, solvents were removed under reduced pressure using a rotary evaporator. Solvent mixtures were measured volumetrically, solutions of inorganic salts are saturated aqueous solutions unless otherwise noted.

Crude products were purified as flash purifications (6.1.1.1) or in a column chromatography procedure established by Stille et al.[395] As column material Silica Gel 60 (0.040–0.063 mm, 230–400 ASTM, Merck) and quartz sand (fine granular, washed and calcined, Merck) were used. As eluents, solvents in p.a. (*pro analysi*) quality were used.

All chemicals and solvents (p.a. quality) were purchased from Chem-Impex International, ABCR, Acros, Alfa Aesar, Fluka, Iris, and Sigma Aldrich Co. or were available in the lab and were used without further purification unless otherwise noted.

6.1.2 Synthesis of BODIPY derivatives

Monomethoxy BODIPY (5-fluoro-5-methoxy-1,3,7,9,10-pentamethyl-5H-4l4,5l4-dipyrrolo[1,2-c:2',1'-f][1,3,2]diazaborinine (2.4))

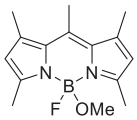

In a 500 ml round-bottom flask, 100 mg of 5,5-Difluoro-1,3,7,9,10-pentamethyl-BODIPY (382 µmol, 1.00 equiv.) were dissolved in 200 ml DCM (to a final concentration of 1.9 mM) and cooled in an ice bath**.** 345 µl of TMSOTf (424 mg, 1.91 mmol, 5.00 equiv.) were added very slowly as 3.45 ml of a precooled 10% (v/v) solution in chloroform and the mixture was allowed to react for exactly 2.5 min**.** Subsequently, an ice-cold mixture of 1.54 ml MeOH (1.22 g, 38.2 mmol, 100 equiv.) and 665 µl DIPEA (493 mg, 3.82 mmol, 10.0 equiv.) was added quickly and the reaction was stirred for 1 h at 0 °C. After completion of the reaction, the reaction mixture was partitioned between 100 ml DCM/H_2O 1:1. The organic layer was washed with brine (3x 50 ml) and the aqueous layer was back-extracted with DCM. The combined organic layers were dried over Na_2SO_4 before removing the solvent under reduced pressure. The crude product was subsequently purified via column flash chromatography in toluene/acetonitrile. 47.7 mg (174 µmol, 46%) of the desired product could be obtained as a dark red powder.

R_f = 0.57 (Tol/ACN 1:1). – ^{1}H-NMR: (400 MHz, $CDCl_3$): δ (ppm) = 6.03 (s, 2H, C*H*-Ar), 2.86 (s, 3H, OCH_3), 2.56 (s, 3H, CH_3), 2.50 (s, 6H, CH_3), 2.40 (s, 6H, CH_3). – ^{13}C-NMR (100 MHz, $CDCl_3$), δ (ppm) = 153.78 ($C_{quart.}$, *C*-Ar), 141.28 ($C_{quart.}$, *C*-Ar), 140.23 ($C_{quart.}$, *C*-Ar), 132.90 ($C_{quart.}$, *C*-Ar), 121.28 (+., *C*H-Ar), 49.13 (+., O*C*H_3), 17.52 (+., *C*H_3), 16.53 (+., *C*H_3), 14.54 (+., *C*H_3). –MS (ESI): $C_{15}H_{20}BFN_2O$, *m/z* calculated for [(M-H)$^-$]: 273.16, Found: 273.37.

Bis-Fmoc-azetidine BODIPY (bis((9H-fluoren-9-yl)methyl) 3,3'-((1,3,7,9,10-pentamethyl-5H-4l4,5l4-dipyrrolo[1,2-c:2',1'-f][1,3,2]diazaborinine-5,5-diyl)bis(oxy))bis(azetidine-1-carboxylate)) (2.6)

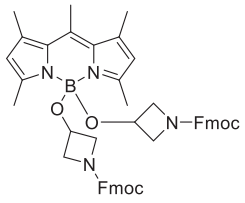

In a 50 ml round-bottom flask, 116 mg of monomethoxy BODIPY **2.4** (0.423 mmol, 1.00 equiv.) and 323 mg 1-Fmoc-3-Hydroxyazetidine (1.09 mmol, 2.58 equiv.) were dissolved in 10 ml toluene before 6.00 g of 5A molecular sieves were added (50mg/mg fluorophore). The reaction mixture was heated to 60 °C and stirred overnight. After gravity filtration, the solvent was removed under reduced pressure and the crude product was purified via tituration with ice-cold MeOH

at -20 °C. 368 mg (330 µmol, 78 %) of the desired product could be obtained as a dark red powder.

R_f = 0.63 (Tol/ACN 1:1). – ^{1}H-NMR: (400 MHz, $CDCl_3$): δ (ppm) = 7.74 (d, *J* = 7.6 Hz, 4H, C*H*-Ar), 7.53 (d, *J* = 7.6 Hz, 4H, C*H*-Ar), 7.39 (t, *J* = 7.5 Hz, 4H, C*H*-Ar), 7.31 – 7.25 (m, 4H, C*H*-Ar), 6.12 (s, 2H, C*H*-Ar), 4.24 (d, *J* = 7.4 Hz, 4H, COOCH_2), 4.18 (d, *J* = 7.3 Hz, 2H, $COOCH_2CH$), 3.93 (q, *J* = 6.1 Hz, 2H, BOC*H*), 3.79 (s, 8H, BOCHCH_2), 2.64 (s, 3H, CH_3), 2.54 (s, 6H, CH_3), 2.47 (s, 6H, CH_3).– ^{13}C-NMR (100 MHz, $CDCl_3$), δ (ppm) = 156.64 ($C_{quart.}$, *C*O), 144.13 ($C_{quart.}$, *C*-Ar), 141.47 ($C_{quart.}$, *C*-Ar), 141.39 ($C_{quart.}$, *C*-Ar), 133.07 ($C_{quart.}$, *C*-Ar), 127.77 (+.,*C*H-Ar), 127.09 (+.,*C*H-Ar), 125.30 (+.,*C*H-Ar), 120.05 (+.,*C*H-Ar), 67.13 (-., *C*H_2), 60.45 (+., *C*H), 47.31 (+., *C*H), 17.76 (+., *C*H_3), 16.75 (+., *C*H_3), 15.32 (+., *C*H_3). –MS (ESI): $C_{50}H_{49}BN_4O_6$, *m/z* calculated for [(M-H)$^-$]: 811.37, Found: 811.39.

Fmoc-azetidine-oxetane BODIPY ((9H-fluoren-9-yl)methyl 3-((1,3,7,9,10-pentamethyl-5-(oxetan-3-yloxy)-5H-4l4,5l4-dipyrrolo[1,2-c:2',1'-f][1,3,2]diazaborinin-5-yl)oxy)azetidine-1-carboxylate) (2.7)

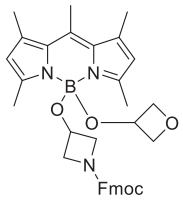

In a 20 ml scintillation vial, 218 mg of bis-Fmoc-azetidine BODIPY **2.6** (268 µmol, 1.00 equiv.) and 111 µl 3-Hydroxyoxetane (129 mg, 1.74 mmol, 6.50 equiv.) were dissolved in 15 ml toluene (predried over MS). Subsequently, 10.9 g of 5A molecular sieves (50 mg/mg fluorophore) were added**.** The reaction was stirred overnight at room temperature. After gravity filtration, the solvent was removed under reduced pressure and the crude product was purified via flash column chromatography (gradient Tol/ACN 1-100%). 25.3 mg (42.8 µmol, 16 %) of the desired product could be obtained as a red powder.

R_f = 0.24 (Tol/ACN 1:1). – ^{1}H-NMR: (400 MHz, $CDCl_3$): δ (ppm) = 7.74 (d, *J* = 7.5 Hz, 2H, C*H*-Ar), 7.53 (d, *J* = 7.5 Hz, 2H, C*H*-Ar), 7.38 (t, *J* = 7.5 Hz, 2H, C*H*-Ar), 7.29 (d, *J* = 7.4 Hz, 2H , C*H*-Ar), 6.08 (s, 2H, C*H*-Ar), 4.52 (t, *J* = 6.3 Hz, 2H, COOCH_2), 4.31 (t, *J* = 6.2 Hz, 2H, $COOCH_2CH$), 4.20 (dq, *J* = 14.3, 6.8 Hz, 4H, BOCHCH_2), 3.96 – 3.65 (m, 5H, *BOCHCH*$_2$), 2.62 (s, 3H, CH_3), 2.51 (s, 6H, CH_3), 2.45 (s, 6H, CH_3).– ^{13}C-NMR (100 MHz, $CDCl_3$), δ (ppm) = 156.63 ($C_{quart.}$, *C*O), 144.14 ($C_{quart.}$, *C*-Ar), 141.38 ($C_{quart.}$, *C*-Ar), 141.37 ($C_{quart.}$, *C*-Ar), 133.04 ($C_{quart.}$, *C*-Ar), 127.75 (+.,*C*H-Ar), 127.08 (+.,*C*H-Ar), 125.30 (+.,*C*H-Ar), 120.04 (+.,*C*H-Ar), 80.84 (-., *C*H_2), 67.11 (-., *C*H_2), 64.28 (+., *C*H), 60.42 (+., *C*H), 47.31 (+., *C*H), 17.73 (+., *C*H_3), 16.71 (+., *C*H_3), 15.24 (+., *C*H_3). – MS (ESI): $C_{35}H_{38}BN_3O_5$, *m/z* calculated for [(M-H)$^-$]: 590.28, Found: 590.22.

Azetidine-oxetane BODIPY (5-(azetidin-3-yloxy)-1,3,7,9,10-pentamethyl-5-(oxetan-3-yloxy)-5H-4l4,5l4-dipyrrolo[1,2-c:2',1'-f][1,3,2]diazaborinine) (2.8)

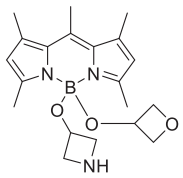

In a 3 ml vial, 5.00 mg of Fmoc-azetidine-oxetane BODIPY **6** (8.45 µmol, 1.00 equiv.) were dissolved in 1 ml piperidine in DMF 20% (v/v) and stirred for 2 min at room temperature before quenching the reaction by addition of 1 ml H_2O. The completion of the reaction was verified via LC/MS. The reaction was immediately further purified via reversed phase flash chromatography (gradient H_2O/ACN 1-100%) without removing the solvents under reduced pressure before. The collected aqueous fraction was extracted with DCM (3x 30 ml) and the combined organic layers were dried over Na_2SO_4 before removing the solvent under reduced pressure at room temperature. Due to the low stability of the desired product and immediate degradation processes a yield could not be determined.

MS (ESI): $C_{20}H_{28}BN_3O_3$, *m/z* calculated for [(M-H)$^-$]: 368.21, Found: 368.21.

Acetyl BODIPY (1-(3-((1,3,7,9,10-pentamethyl-5-(oxetan-3-yloxy)-5H-4l4,5l4-dipyrrolo[1,2-c:2',1'-f][1,3,2]diazaborinin-5-yl)oxy)azetidin-1-yl)ethan-1-one) (2.13)

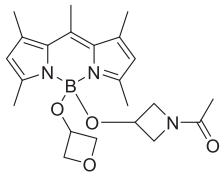

In a 3 ml vial, 5.00 mg of Fmoc-azetidine-oxetane BODIPY **6** (8.45 µmol, 1.00 equiv.) were dissolved in 1 ml piperidine in DMF 20% (v/v) and stirred for 2 min at room temperature before quenching the reaction by adding of 1ml H_2O. The completion of the reaction was verified via LC/MS. The reaction was immediately further purified via reversed phase flash chromatography without removing the solvents under reduced pressure before. The collected aqueous fraction was extracted with DCM (3x 30 ml) and the combined organic layers were dried over Na_2SO_4 before removing the solvent under reduced pressure at room temperature. The resulting deprotection product was used directly in a reprotection without further purification by the addition of 26.6 mg acetyl-NHS (2,5-Dioxopyrrolidin-1-yl acetate, 169 µmol, 20.0 equiv.) in 2ml DMF. The reaction was stirred overnight at room temperature and completion of the reaction was verified via LC/MS. Again, without removing the solvent the reaction mixture was purified via reversed phase flash chromatography. Due to formation of an unidentified byproduct during column chromatography, the desired product could not be isolated in sufficient purity.

MS (ESI): $C_{22}H_{30}BN_3O_4$, *m/z* calculated for [(M-H)$^-$]: 410.23, Found: 410.25.

Cyclobutanecarboxylic acid BODIPY (3-((5-fluoro-1,3,7,9,10-pentamethyl-5H-4l4,5l4-dipyrrolo[1,2-c:2',1'-f][1,3,2]diazaborinin-5-yl)oxy)cyclobutane-1-carboxylic acid) (2.15)

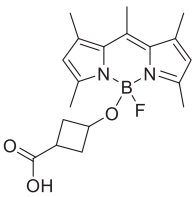

In a 20 ml scintillation vial, 31.6 mg of monomethoxy BODIPY **2.4** (115 µmol, 1.00 equiv.) and 33.5 mg 3-Hydroxycyclobutane-1-carboxylic acid (288 µmol, 2.50 equiv.) were dissolved in 10 ml toluene before 1.58 g of 5A molecular sieves were added (50mg/mg fluorophore). The reaction mixture was heated to 60 °C and stirred for 5 min, completion of the reaction was verified via LC/MS. The solvent was removed under reduced pressure followed by an aqueous workup with diluted $NaHCO_3$ solution (pH= 8) and EtOAc. The organic layer was extracted with $NaHCO_3$ solution (pH= 8) 3x20 ml and the combined aqueous layers were saturated with NaCl. The product was back extracted from the aqueous layer with DCM 1x20 ml and DCM/MeOH 2x20 ml. After drying the combined organic layers over Na_2SO_4 and removing the solvent under reduced pressure, more impurities were removed by a 2nd aqueous workup with diluted $NaHCO_3$ solution (pH= 8) and hexanes. The organic layer was extracted with $NaHCO_3$ solution (pH8) 3x 20 ml and the combined aqueous layers were saturated with NaCl. The product was back extracted from the aqueous layer with DCM. Further purification was achieved via tituration with hexanes overnight at -20 °C. 12.5 mg (34.9 µmol, 30 %) of the desired product could be obtained as an orange powder.

R_f = 0.51 (Tol/ACN 1:2). – ^{1}H-NMR: (400 MHz, $CDCl_3$): δ (ppm) = 6.04 (s, 2H, C*H*-Ar), 3.37 (p, *J* = 7.7 Hz, 1H, BOC*H*), 2.59 (s, 3H, CH_3), 2.51 (s, 6H, CH_3), 2.42 (s, 6H, CH_3), 2.36 – 2.32 (m, 1H, C*H*COOH), 2.02 (dd, *J* = 12.4, 5.9 Hz, 4H, BOCHCH_2). –^{13}C-NMR (100 MHz, $CDCl_3$), δ (ppm) = 154.13 ($C_{quart.}$, *C*O), 140.56 ($C_{quart.}$, *C*-Ar), 132.65 ($C_{quart.}$, *C*-Ar), 121.51 *C*H-Ar), 35.99 (-., *C*H_2), 29.85 (+., *C*H), 17.60 (+., *C*H_3), 16.58 (+., *C*H_3), 14.87 (+., *C*H_3). –MS (ESI): $C_{19}H_{24}BFN_2O_3$, *m/z* calculated for [(M-H)$^-$]: 357.18, Found: 357.25.

Bis-oxetane BODIPY (1,3,7,9,10-pentamethyl-5,5-bis(oxetan-3-yloxy)-5H-4l4,5l4-dipyrrolo[1,2-c:2',1'-f][1,3,2]diazaborinine) (2.11)

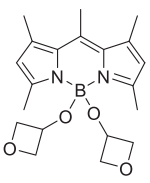

In a 20 ml scintillation vial, 10.0 mg of monomethoxy BODIPY **2.4** (36.5µmol, 1.00 equiv.) and 13.5 mg 3-Hydroxyoxetane (182 µmol, 5.00 equiv.) were dissolved in 4 ml toluene before 500 mg of 5A molecular sieves were added (50mg/mg fluorophore). The reaction mixture was stirred for 2 d at room temperature before adding another 2.50 equiv. of 3-Hydroxyoxetane and stirring for 4d at 50 °C, followed by the addition of additional 2.50 equiv. 3-Hydroxyoxetane and reaction overnight at 80 °C to achieve maximum conversion. The solvent was removed under reduced pressure and purified via column flash chromatography. 1.60 mg (4.32 µmol, 12 %) of the desired product could be obtained as a red powder.

R_f = 0.24 (Tol/ACN 1:1). – MS (ESI): $C_{20}H_{27}BN_2O_4$, *m/z* calculated for [(M-H)$^-$]: 369.20, Found: 369.25.

Cyclobutanecarboxylic acid-oxetane BODIPY (3-((1,3,7,9,10-pentamethyl-5-(oxetan-3-yloxy)-5H-4l4,5l4-dipyrrolo[1,2-c:2',1'-f][1,3,2]diazaborinin-5-yl)oxy)cyclobutane-1-carboxylic acid) (2.14)

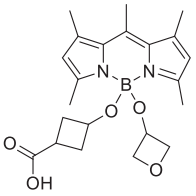

In a 3 ml vial, 5.00 mg of bisoxetane BODIPY **2.11** (13.5 µmol, 1.00 equiv.) and 3.92 mg 3-Hydroxycyclobutane-1-carboxylic acid (33.8 µmol, 2.50 equiv.) were dissolved in 2 ml toluene before 250 mg of 5A molecular sieves were added (50mg/mg fluorophore). The reaction mixture was stirred for 24 h at room temperature, the solvent was removed under reduced pressure, and the crude product was purified via reversed phase flash chromatography (gradient H_2O/ACN 1-100%). The desired product could be isolated as a red solid in a yield <1 mg.

^{1}H-NMR: (400 MHz, $CDCl_3$): δ (ppm) = 6.04 (s, 2H, C*H*-Ar), 4.47 (t, *J* = 6.2 Hz, 2H, BOCHC*H*$_2$O), 4.27 (t, *J* = 6.3 Hz, 2H, BOCHC*H*$_2$O), 4.14 (dd, *J* = 6.5 Hz, 1H, BOC*H*CH$_2$O), 3.38 (p, 1H, BOC*H*CH$_2$CH), 2.60 (s, 3H, C*H*$_3$), 2.50 (s, 6H, C*H*$_3$), 2.44 (s, 6H, C*H*$_3$), 2.37 – 2.30 (m, 1H, CH$_2$C*H*COOH), 2.11 – 2.00 (m, 4H, C*H*$_2$CHCOOH). –MS (ESI): $C_{22}H_{29}BN_2O_5$, *m/z* calculated for [(M-H)$^-$]: 411.21, Found: 411.25.

Cyclobutanecarboxylic acid Halo ligand (N-(2-(2-((6-chlorohexyl)oxy)ethoxy)ethyl)-3-hydroxycyclobutane-1-carboxamide) (2.22)

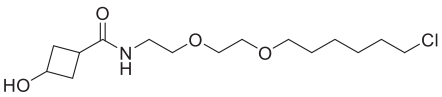

In a 20 ml scintillation vial, 20.0 mg of 3-Hydroxycyclobutane-1-carboxlic acid (172 µmol, 1.00 equiv.) and 53.8 mg Halo-Ligand 2-(2-((6-chlorohexyl)oxy)ethoxy)ethan-1-amine (207 µmol, 1.20 equiv.) were dissolved in 4 ml DMF and 150 µl DIPEA (861 µmol, 5.00 equiv.) were added. Subsequently**,** 112 mg of PyBOP (215 µmol, 1.25 equiv.) were added to the reaction mixture. The reaction mixture was stirred for 1 h at room temperature, and completion of the reaction was assessed via LC/MS. After removing the solvent under reduced pressure the reaction was purified via a slightly basic aqueous workup (pH= 8) and extracted 3x 20 ml with DCM. The combined organic layers were dried over Na_2SO_4 and the solvent was removed under reduced pressure. Further purification of the product was performed via flash column chromatography (gradient DCM/MeOH 1-30%). 25.9 mg (80.5 µmol, 47 %) of the desired product could be obtained as a colorless oil.

R_f = 0.31 (DCM/MeOH 20%). – ^{1}H-NMR: (400 MHz, $CDCl_3$): δ (ppm) = 6.24 (s, 1H, N*H*), 4.14 (p, *J* = 7.1 Hz, 1H, C*H*OH), 3.67 (tt, *J* = 6.7, 3.5 Hz, 1H, COC*H*CH$_2$), 3.60 (dd, *J* = 5.8, 3.1 Hz, 2H, OC*H*$_2$CH$_2$NH), 3.57 – 3.51 (m, 4H, ClC*H*$_2$, Cl(CH$_2$)$_5$C*H*$_2$), 3.48 – 3.42 (m, 4H, OC*H*$_2$C*H*$_2$O), 3.20 – 3.07 (m, 2H, OCH$_2$C*H*$_2$NH), 2.59 – 2.43 (m, 4H,

COCHC*H*$_2$), 1.79 – 1.73 (m, 2H, ClCH$_2$C*H*$_2$), 1.59 (p, *J* = 7.0 Hz, 2H, Cl(CH$_2$)$_4$C*H*$_2$), 1.49 – 1.30 (m, 4H, Cl(CH$_2$)$_2$C*H*$_2$ C*H*$_2$). –^{13}C-NMR (100 MHz, $CDCl_3$), δ (ppm) = 174.98 ($C_{quart.}$, *C*O), 71.37 (-., *C*H$_2$), 70.31 (*C*H$_2$), 70.07 (*C*H$_2$), 69.82 (*C*H$_2$), 64.03 (-, *C*H$_2$), 46.55 (*C*H$_2$), 45.17 (*C*H$_2$), 39.47 (-,*C*H$_2$), 36.86 (*C*H$_2$), 26.46 (-,*C*H$_2$), 25.49 (-,*C*H$_2$), 18.63 (-,*C*H$_2$), 17.18 (*C*H$_2$). –MS (ESI): $C_{15}H_{28}ClNO_4$, *m/z* calculated for [(M+H)$^+$]: 322.18, Found: 322.41, *m/z* calculated for [(M+FA)$^-$]: 366.17, Found: 366.29.

Halo ligand BODIPY (N-(2-(2-((6-chlorohexyl)oxy)ethoxy)ethyl)-3-((5-fluoro-1,3,7,9,10-pentamethyl-5H-4l4,5l4-dipyrrolo[1,2-c:2',1'-f][1,3,2]diazaborinin-5-yl)oxy)cyclobutane-1-carboxamide) (2.21)

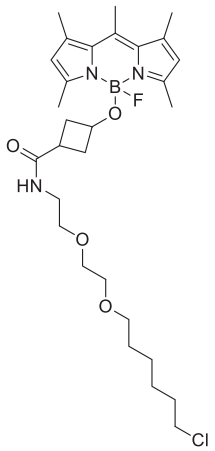

Method A:

In a 3 ml vial, 4.00 mg Halo-Ligand 2-(2-((6-chlorohexyl)oxy)ethoxy)ethan-1-amine (15.4 µmol, 1.10 equiv.) were dissolved in 1 ml DMF and 2.70 µl DIPEA (15.4 µmol, 1.10 equiv.) were added. Then the solution of 5.00 mg of cyclobutanecarboxylic acid BODIPY **14** (14.0 µmol, 1.00 equiv.) in 1 ml DMF was added to the reaction mixture, followed by the addition of the solution of 7.99 mg of PyBOP (15.4 µmol, 1.10 equiv.) in 1 ml DMF. The reaction mixture was stirred for 10 min at room temperature. After completion of the reaction the solvent was removed under reduced pressure followed by a slightly basic aqueous workup with H_2O/$NaHCO_3$ (pH= 8) and diethyl ether. The combined organic layers were dried over Na_2SO_4 and the solvent was removed under reduced pressure. The resulting crude product was further purified via preparative TLC.

Method B:

In a 3 ml vial, 3.70 mg of monomethoxy-BODIPY **2.4** (13.5 µmol, 1.00 equiv.) and 10.6 mg cyclobutanecarboxylic acid Halo ligand **2.22** (32.9 µmol, 2.44 equiv.) were dissolved in 1 ml toluene before 185 mg of 5A molecular sieves were added (50 mg/mg fluorophore). The reaction mixture was heated to 60 °C and stirred overnight, and the completion of reaction was verified via LC/MS**.** After 26 h the solvent was removed under reduced pressure and the crude product was purified via preparative TLC. 2.30 mg (4.08 µmol, 30 %) of the desired product could be obtained as a dark red powder.

R_f = 0.49 (Tol/ACN 1:1). – ^{1}H-NMR: (400 MHz, $CDCl_3$): δ (ppm) = 6.04 (d, *J* = 4.4 Hz, 2H, C*H*-Ar), 5.84 (s, 1H, BOC*H*), 4.17 (p, *J* = 6.3 Hz, 1H, C*H*CONH), 3.68 – 3.28 (m, 12H, NHC*H*$_2$C*H*$_2$OC*H*$_2$C*H*$_2$OC*H*$_2$(CH$_2$)$_4$C*H*$_2$Cl), 2.59 (s, 3H, C*H*$_3$), 2.52 (s, 6H, C*H*$_3$), 2.43 (s, 6H, C*H*$_3$), 2.15 (ddt, *J* = 18.1, 13.3, 6.2 Hz, 2H, BOCHC*H*$_2$), 1.99 – 1.89 (m, 2H, BOCHC*H*$_2$), 1.65 – 1.55 (m, 4H, OCH$_2$C*H*$_2$(CH$_2$)$_2$C*H*$_2$CH$_2$Cl), 1.48 – 1.32 (m, 4H,

$O(CH_2)_2(CH_2)_2(CH_2)_2Cl$). –MS (ESI): $C_{29}H_{44}BClFN_3O_4$, *m/z* calculated for [$(M-H)^-$]: 562.30, Found: 562.42.

6.1.3 Synthesis of melanocyte-specific fluorescent probes

Methyl 2-(6-hydroxy-3-oxo-3H-xanthen-9-yl)benzoate (4.4)

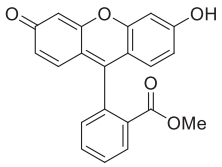

In a 100 ml round bottom flask, 10.0 g fluorescein (30.1 mmol, 1.00 equiv.) were suspended in 30 ml MeOH and 7.5 ml concentrated H_2SO_4 were added. Between flask and cooler, a dropping funnel filled with molecular sieves (3A) was installed and the reaction mixture was refluxed for 18 h. After cooling to room temperature, 10 g ice and 30 g $NaHCO_3$ were added, the suspension was filtered and washed with water. The resulting red solid was resuspended in a 2% aqueous $NaHCO_3$ solution, filtered and washed 4 times before being resuspended in1% acetic acid, filtered, washed with water and dried. 9.93 g (28.7 mmol, 95%) of the desired product was obtained as a red powder.

Alternative route:

In a 20 ml scintillation vial, 500 mg fluorescein (1.51 mmol, 1.00 equiv.) were solved in 3 ml MeOH and 450 µl thionyl chloride (6.47 mmol, 4.30 equiv.) were added. After refluxing overnight, the solvent was removed under reduced pressure. 470 mg (1.36 mmol, 90%) of the desired product was obtained as a yellow-brown powder.

R_f = 0.67 (DCM/MeOH 4:1). – 1H NMR (300 MHz, DMSO-*d*6), δ (ppm)= 8.31 (d, J = 7.6 Hz, 1H, C*H*-Ar), 7.93 (dt, J = 21.9, 7.6 Hz, 2H, C*H*-Ar), 7.55 (d, J = 7.5 Hz, 1H, C*H*-Ar), 7.33 (dd, J = 9.2, 3.4 Hz, 2H, C*H*-Ar), 7.28 (d, J = 2.1 Hz, 2H, C*H*-Ar), 7.13 (dd, J = 9.2, 2.2 Hz, 2H, C*H*-Ar), 3.57 (s, 3H, OCH_3). – MS (FAB, 3-NBA), *m/z* (%): 347.0 [M^+] (100).

6-Hydroxy-9-(2-(piperazine-1-carbonyl)phenyl)-3H-xanthen-3-one (4.7)

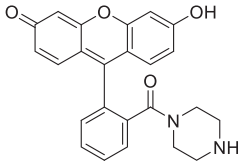

In a 50 ml Schlenk flask, 2.90 g piperazine (33.7 mmol, 3.90 equiv.) were solved in 13 ml abs. DCM, before 8.45 ml $AlMe_3$ (2M in heptane) (16.9 mmol, 1.95 equiv.) were added and the reaction mixture was stirred overnight (precipitation of a white solid). 3.00 g methyl 2-(6-hydroxy-3-oxo-3H-xanthen-9-yl)benzoate (**4.4**) (8.64 mmol, 1.00 equiv.) suspended in 10 ml DCM were added and the mixture was refluxed for 10 h, protecting the reaction mixture from the light. After cooling to room temperature, 80 ml MeOH and 195 ml HCl (1M) were added until no further gas evolution could be observed. The solvent was removed under reduced pressure and the crude product was purified via column chromatography (DCM/MeOH 4:1). 3.06 g (7.64 mmol, 88 %) of the desired product could be obtained as orange-yellow powder.

R_f = 0.13 (DCM/MeOH 4:1). – 1H NMR (300 MHz, methanol-*d*4), δ (ppm)= 7.83 (s, 3H, C*H*-Ar), 7.66 (d, J = 9.2 Hz, 2H, C*H*-Ar), 7.60 (s, 1H, C*H*-Ar), 7.36 (d, J = 2.2 Hz, 2H, C*H*-Ar), 7.26 (dd, J = 9.2, 2.1 Hz, 2H, C*H*-Ar), 3.68 (d, J = 52.5 Hz, 4H, CO-N-CH_2), 3.31 (s, 1H, N*H*), 3.11 (s, 4H, CH_2-CH_2-NH).– IR (ATR) ũ (cm^{-1}) = 2722 (w), 1643 (w), 1595 (m), 1415 (w), 1386 (w), 1323 (w), 1288 (w), 1258 (w), 1230 (w), 1163 (w), 1111 (w), 1039 (w), 1006 (w), 917 (w), 847 (w), 822 (w), 782 (w), 761 (w), 713 (w), 659 (w), 632 (vw), 601 (w), 570 (w), 454 (m).– MS (FAB, 3-NBA), *m/z* (%): 401.2 [M^+] (70).– HRMS ($C_{24}H_{21}N_2O_4$): calculated 401.1496; found 401.1495.

6-Hydroxy-9-(2-(4-(2-propylpentanoyl)piperazine-1-carbonyl)phenyl)-3H-xanthen-3-one (4.12)

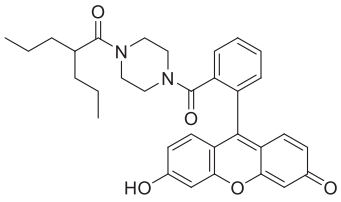

In a 10 ml round bottom flask, 111 µl 2-propylpentanecarboxylic acid (100 mg, 0.693 mmol, 2.00 equiv.) were solved in 3 ml DCM and cooled to 0 °C. 143 µl pentafluorophenyl trifluoroacetate (233 mg, 0.832 mmol, 2.40 equiv.) were added and stirred for 10 min, before 146 µl DIPEA (108 mg, 0.832 mmol, 2.40 equiv.) were added and the reaction was allowed to warm to room temperature while stirring for 1.5 h. The mixture was filtered over silica gel and the solvent was removed under reduced pressure. The obtained intermediate product was used in the next step without further purification.

In a 10 ml round bottom flask, 139 mg 6-hydroxy-9-(2-(piperazine-1-carbonyl)phenyl)-3H-xanthen-3-one (**4.7**) (0.347 mmol, 1.00 equiv.) and 146 µl DIPEA (108 mg, 0.832 mmol, 2.40 equiv.) were solved in 3 ml DMF and the mixture was cooled to 0 °C, then the solution of the previously obtained pentafluorophenyl-ester intermediate in 1 ml DMF was added. After stirring the reaction mixture for 10 min, the ice bath was removed, the mixture was allowed to warm to room temperature and stirred for another 2 h. The solvent was removed under reduced pressure and the crude product was

purified via flash column chromatography (EE/MeOH 10:1). 54.6 mg (104 µmol, 30 %) of the desired product could be obtained as an orange oil.

R_f = 0.10 (EE/MeOH 10:1). –^{1}H NMR (300 MHz, DMSO-d_6), δ (ppm)= 7.74 – 7.59 (m, 3H, C*H*-Ar), 7.58 – 7.43 (m, 1H, C*H*-Ar), 6.93 (d, *J* = 9.2 Hz, 2H, C*H*-Ar), 6.55 (d, *J* = 9.7 Hz, 4H, C*H*-Ar), 3.27 (b, 8H, N-CH_2-CH_2-N), 2.69 (m, *J* = 19.5 Hz, 1H, CO-C*H*), 1.49 – 1.32 (m, 2H, CH-CH_2-CH_2), 1.20 – 1.06 (m, 6H, CH-CH_2-CH_2), 0.80 (t, *J* = 7.1 Hz, 6H, CH_3). –IR (ATR) ũ (cm^{-1}) = 2958 (w), 1752 (w), 1675 (w), 1608 (m), 1506 (w), 1451 (m), 1317 (w), 1283 (w), 1248 (m), 1176 (m), 1109 (m), 1023 (m), 994 (m), 825 (w), 798 (w), 761 (w), 719 (w), 694 (w), 577 (w). –MS (FAB, 3-NBA), *m/z* (%): 527.0 [M$^+$] (100).

6-Hydroxy-9-(2-(4-(3-methylbut-2-enoyl)piperazine-1-carbonyl)phenyl)-3H-xanthen-3-one (4.13)

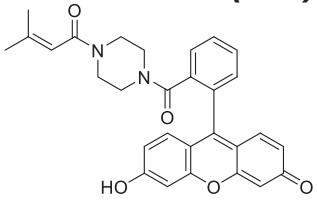

In a 10 ml round bottom flask, 100 mg 3-methyl-2-butenoic acid (1.00 mmol, 2.00 equiv.) were solved in 3 ml DCM and cooled down to 0 °C. Then 206 µl pentafluorophenyl trifluoroacetate (336 mg, 1.20 mmol, 2.40 equiv.) were added and the mixture was further stirred for 10 min, followed by the addition of 209 µl DIPEA (155 mg, 1.20 mmol, 2.40 equiv.). The reaction then was allowed to warm to room temperature while stirring for additional 1.5 h. The mixture was filtered over silica gel and the solvent was removed under reduced pressure. The obtained intermediate product was used in the next step without further purification.

In a 10 ml round bottom flask, 200 mg 6-hydroxy-9-(2-(piperazine-1-carbonyl)phenyl)-3H-xanthen-3-one (**4.7**) (0.500 mmol, 1.00 equiv.) and 209 µl DIPEA (155 mg, 1.20 mmol, 2.40 equiv.) were solved in 3 ml DMF and the mixture was cooled to 0 °C, before the previously obtained pentafluorophenyl-ester intermediate was solved in 1 ml DMF and added. After stirring the reaction mixture for 10 min, the ice bath was removed, the mixture was allowed to warm to room temperature and stirred for another 2 h. The solvent was removed under reduced pressure, followed by an aqueous workup with diluted NaOH solution (pH=9) and DCM. The aqueous layer was extracted with DCM 4x 20 ml and the combined organic layers were dried over $NaSO_4$. The solvent removed under reduced pressure and the crude product was purified via column chromatography (DCM/MeOH 15:1→10:1). 19.7 mg (40.8 µmol, 8 %) of the desired product could be obtained as an orange-red powder.

R_f = 0.24 (DCM/MeOH 10:1). – ^{1}H NMR (300 MHz, methanol-d_4), δ (ppm)= 7.76 (dd, *J* = 5.8, 3.2 Hz, 2H, C*H*-Ar), 7.67 (dd, *J* = 5.9, 3.2 Hz, 1H, C*H*-Ar), 7.52 (dd, *J* = 5.6, 3.3 Hz, 1H, C*H*-Ar), 7.19 (d, *J* = 9.5 Hz, 2H, C*H*-Ar), 6.77 – 6.70 (m, 4H, C*H*-Ar), 5.82 (s, 1H, CO-C*H*=C), 3.40 (b, 8H, N-CH_2-CH_2-N), 1.90 – 1.77 (m, 6H, CH_3). –MS (FAB, 3-NBA): *m/z* (%): 483.2 [M$^+$] (100).

6-Hydroxy-9-(2-(4-propioloylpiperazine-1-carbonyl)phenyl)-3H-xanthen-3-one (4.14)

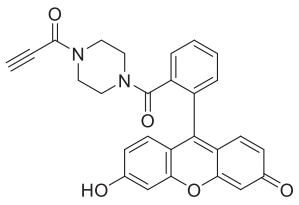

In a 10 ml round bottom flask, 124 µl propiolic acid (140 mg, 2.00 mmol, 2.00 equiv.) were dissolved in 5 ml DCM and cooled to 0 °C. 412 µl pentafluorophenyl trifluoroacetate (672 mg, 2.40 mmol, 2.40 equiv.) were added and stirred for 10 min, before 418 µl DIPEA (310 mg, 2.40 mmol, 2.40 equiv.) were added and the reaction was allowed to warm to room temperature while stirring for 1.5 h. The mixture was filtered over silica gel and the solvent was removed under reduced pressure. The obtained intermediate product was used in the next step without further purification.

In a 10 ml round bottom flask, 400 mg 6-hydroxy-9-(2-(piperazine-1-carbonyl)phenyl)-3H-xanthen-3-one (**4.7**) (1.00 mmol, 1.00 equiv.) and 418 µl DIPEA (310 mg, 2.40 mmol, 2.40 equiv.) were solved in 5 ml DMF and the mixture was cooled to 0 °C, before the previously obtained pentafluorophenyl-ester intermediate was solved in 1 ml DMF and added. After stirring the reaction mixture for 10 min, the ice bath was removed, the mixture was allowed to warm to room temperature and stirred for another 2.5 h. The solvent was removed under reduced pressure, followed by an aqueous workup with diluted NaOH solution (pH=9) and DCM. The aqueous layer was extracted with DCM 4x 30 ml and the combined organic layers were dried over $NaSO_4$. The solvent removed under reduced pressure and the crude product was purified via column chromatography (DCM/MeOH 15:1→10:1). 44.6 mg (98.6 µmol, 10 %) of the desired product could be obtained as an orange-red powder.

R_f = 0.24 (DCM/MeOH 10:1). – ^{1}H NMR (300 MHz, methanol-d_4), δ (ppm)= 7.76 (dd, *J* = 5.8, 3.2 Hz, 2H, C*H*-Ar), 7.68 (dd, *J* = 5.9, 3.2 Hz, 1H, C*H*-Ar), 7.56 – 7.50 (m, 1H, C*H*-Ar), 7.22 – 7.16 (m, 2H, C*H*-Ar), 6.74 (d, *J* = 7.9 Hz, 4H, C*H*-Ar), 3.64 (b, 2H, N-CH_2-CH_2-N), 3.46 (d, *J* = 16.6 Hz, 6H, N-CH_2-CH_2-N), 3.01 (s, 1H, C*H*). –MS (FAB, 3-NBA): *m/z* (%): 453.1 [M$^+$] (15).

(4-(Cyclopropanecarbonyl)piperazin-1-yl)(2-(3,6-dihydroxy-9H-xanthen-9-yl)phenyl)methanone (4.15)

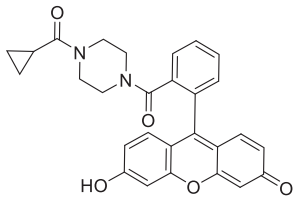

In a 10 ml round bottom flask, 92.5 µl cyclopropanecarboxylic acid (100 mg, 1.16 mmol, 2.00 equiv.) were solved in 3 ml DCM and cooled to 0 °C. 239 µl pentafluorophenyl trifluoroacetate (389 mg, 1.39 mmol, 2.40 equiv.) were added and stirred for 10 min, before 243 µl DIPEA (180 mg, 1.39 mmol, 2.40 equiv.) were added and the reaction was allowed to warm to room temperature while stirring for 1.5 h. The mixture was filtered over silica gel and the solvent was removed under reduced pressure. The obtained intermediate product was used in the next step without further purification.

In a 10 ml round bottom flask, 232 mg 6-hydroxy-9-(2-(piperazine-1-carbonyl)phenyl)-3H-xanthen-3-one (**4.7**) (0.580 mmol, 1.00 equiv.) and 243 µl DIPEA (180 mg, 1.39 mmol, 2.40 equiv.) were solved in 3 ml DMF and the mixture was cooled to 0 °C, before the previously obtained pentafluorophenyl-ester intermediate was solved in 1 ml DMF and added. After stirring the reaction mixture for 10 min, the ice bath was removed, the mixture was allowed to warm to room temperature and stirred for another 2 h. The solvent was removed under reduced pressure and the crude product was purified via column chromatography (DCM/MeOH 10:1). 29.8 mg (63.6 µmol, 13 %) of the desired product could be obtained as a red powder.

R_f = 0.13 (DCM/MeOH 10:1). – ^{1}H NMR (300 MHz, methanol-d_4), δ (ppm)= 7.89 – 7.74 (m, 3H, C*H*-Ar), 7.62 (s, 1H, C*H*-Ar), 7.58 (d, *J* = 5.1 Hz, 2H, C*H*-Ar), 7.25 (d, *J* = 2.2 Hz, 2H, C*H*-Ar), 7.17 (dd, *J* = 9.2, 2.2 Hz, 2H, C*H*-Ar), 3.71 – 3.33 (m, 8H, N-CH_2-CH_2-N), 1.27 (s, 1H, C*H*), 0.91 – 0.73 (m, 4H, CHCH_2). –IR (ATR) ũ (cm^{-1}) = 2918 (w), 1682 (w), 1628 (m), 1557 (m), 1428 (m), 1381 (m), 1232 (m), 1195 (s), 1109 (m), 1003 (s), 912 (m), 842 (s), 752 (m), 710 (m), 592 (m), 568 (w), 477 (s), 455 (s).– MS (FAB, 3-NBA): *m/z* (%): 469.1 [M$^+$] (45).

9-(2-(4-(Cyclopentanecarbonyl)piperazine-1-carbonyl)phenyl)-6-hydroxy-3H-xanthen-3-one (4.16)

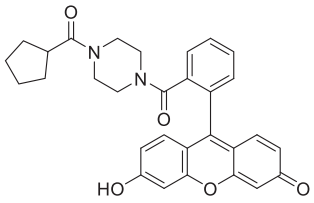

In a 10 ml round bottom flask, 114 mg cyclopentanecarboxylic acid (1.00 mol, 2.00 equiv.) were solved in 3 ml DCM and cooled to 0 °C. 206 µl pentafluorophenyl trifluoroacetate (336 mg, 1.20 mmol, 2.40 equiv.) were added and stirred for 10 min, before 209 µl DIPEA (155 mg, 1.20 mmol, 2.40 equiv.) were added and the reaction was allowed to warm to room temperature while stirring for 1.5 h. The mixture was filtered over silica gel and the solvent was removed under reduced pressure. The obtained intermediate product was used in the next step without further purification.

In a 10 ml round bottom flask, 200 mg 6-hydroxy-9-(2-(piperazine-1-carbonyl)phenyl)-3H-xanthen-3-one (**4.7**) (0.500 mmol, 1.00 equiv.) and 209 µl DIPEA (155 mg, 1.20 mmol, 2.40 equiv.) were solved in 3 ml DMF and the mixture was cooled to 0 °C, before the previously obtained pentafluorophenyl-ester intermediate was solved in 1 ml DMF and added. After stirring the reaction mixture for 10 min, the ice bath was removed, the mixture was allowed to warm to room temperature and stirred for another 2 h. The solvent was removed under reduced pressure, followed by an aqueous workup with diluted NaOH solution (pH= 9) and DCM. The aqueous layer was extracted with DCM 4x 20 ml and the combined organic layers were dried over $NaSO_4$. The solvent removed under reduced pressure and the crude product was purified via column chromatography (DCM/MeOH 15:1→10:1). 50.7 mg (0.102 mmol, 20%) of the desired product could be obtained as a red powder.

R_f = 0.33 (DCM/MeOH 10:1). – ^{1}H NMR (300 MHz, methanol-d_4), δ (ppm)= 7.74 (s, 2H, C*H*-Ar), 7.68 (s, 1H, C*H*-Ar), 7.52 (s, 1H, C*H*-Ar), 7.20 (d, *J* = 9.5 Hz, 2H, C*H*-Ar), 6.73 (d, *J* = 7.7 Hz, 4H, C*H*-Ar), 3.39 (d, *J* = 11.8 Hz, 8H, N-CH_2-CH_2-N), 2.97 (b, 1H, C*H*), 1.86 – 1.52 (m, 8H, CH-CH_2). –IR (ATR) ũ (cm^{-1}) = 2946 (vw), 2859 (vw), 1633 (w), 1591 (w), 1454 (w), 1381 (w), 1259 (w), 1202 (w), 1106 (w), 1005 (w), 913 (vw), 846 (vw), 757 (vw), 664 (vw), 593 (vw), 569 (vw), 506 (vw), 478 (vw), 449 (w). –MS (FAB, 3-NBA): *m/z* (%): 497.2 [M$^+$] (100).

(4-(Cyclohexanecarbonyl)piperazin-1-yl)(2-(3,6-dihydroxy-9H-xanthen-9-yl)phenyl)methanone (4.17)

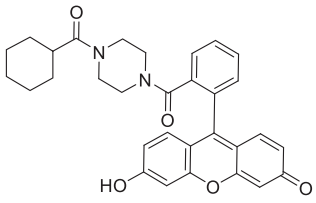

In a 10 ml round bottom flask, 111 µl cyclohexanecarboxylic acid (120 mg, 0.936 mmol, 2.00 equiv.) were dissolved in 3 ml DCM and cooled to 0 °C. 193 µl pentafluorophenyl trifluoroacetate (314 mg, 1.12 mmol, 2.40 equiv.) were added and stirred for 10 min, before 195 µl DIPEA (145 mg, 1.12 mmol, 2.40 equiv.) were added and the reaction was allowed to warm to room temperature while stirring for 1.5 h. The mixture was filtered over silica gel and the solvent was removed under reduced pressure. The obtained intermediate product was used in the next step without further purification.

In a 10 ml round bottom flask, 187 mg 6-hydroxy-9-(2-(piperazine-1-carbonyl)phenyl)-3H-xanthen-3-one (**4.7**) (0.468 mmol, 1.00 equiv.) and 195 µl DIPEA (145 mg, 1.12 mmol, 2.40 equiv.) were solved in 3 ml DMF and the mixture was cooled to 0 °C, before the previously obtained pentafluorophenyl-ester intermediate was solved in 1 ml DMF and added. After stirring the reaction mixture for 10 min, the ice bath was removed, the mixture was allowed to warm to room temperature and stirred for another 2 h. The solvent was removed under reduced pressure and the crude product was purified via column chromatography (DCM/MeOH 15:1→5:1). 89.7 mg (0.175 mmol, 38 %) of the desired product could be obtained as an orange powder.

R_f = 0.13 (DCM/MeOH 15:1). ^{1}H NMR (300 MHz, methanol-d_4), δ (ppm)= 7.72 (d, *J* = 3.2 Hz, 2H, C*H*-Ar), 7.65 (d, *J* = 4.7 Hz, 1H, C*H*-Ar), 7.49 (s, 1H, C*H*-Ar), 7.17 (d, *J* = 9.4 Hz, 2H, C*H*-Ar), 6.71 (d, *J* = 8.2 Hz, 4H, C*H*-Ar), 3.37 (d, *J* = 14.3 Hz, 8H, N-CH_2-CH_2-N), 2.54 (b, 1H, C*H*), 1.69 (dd, *J* = 30.7, 8.6 Hz, 5H, CH-CH_2), 1.44 – 1.16 (m, 5H, CH_2). –IR (ATR) ũ (cm^{-1}) = 2924 (w), 2436 (vw), 1632 (w), 1557 (w), 1512 (w), 1427 (w), 1379 (w), 1244 (w), 1196 (m), 1107 (w), 999 (w), 910 (w), 840 (w), 752 (w), 710 (w), 661 (w), 591 (w), 568 (w), 475 (w), 445 (w). –MS (FAB, 3-NBA): *m/z* (%): 511.2 [M$^+$] (100).

9-(2-(4-(4-Butylcyclohexane-1-carbonyl)piperazine-1-carbonyl)phenyl)-6-hydroxy-3H-xanthen-3-one (4.18)

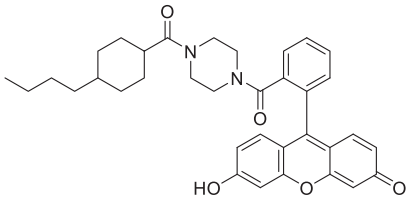

In a 10 ml round bottom flask, 166 mg 4-butylcyclohexanecarboxylic acid (0.900 mmol, 2.00 equiv.) were solved in 3 ml DCM and cooled to 0 °C. 186 µl pentafluorophenyl trifluoroacetate (302 mg, 1.08 mmol, 2.40 equiv.) were added and stirred for 10 min, before 188 µl DIPEA (140 mg, 1.08 mmol, 2.40 equiv.) were added and the reaction was allowed to warm to room temperature while stirring for 1.5 h. The mixture was filtered over silica gel and the solvent was removed under reduced pressure. The obtained intermediate product was used in the next step without further purification.

In a 10 ml round bottom flask, 180 mg 6-hydroxy-9-(2-(piperazine-1-carbonyl)phenyl)-3H-xanthen-3-one (**4.7**) (0.450 mmol, 1.00 equiv.) and 188 µl DIPEA (140 mg, 1.08 mmol, 2.40 equiv.) were solved in 3 ml DMF and the mixture was cooled to 0 °C, before the previously obtained pentafluorophenyl-ester intermediate was solved in 1 ml DMF and added. After stirring the reaction mixture for 10 min, the ice bath was removed, the mixture was allowed to warm to room temperature and stirred for another 2 h. The solvent was removed under reduced pressure, followed by an aqueous workup with diluted NaOH solution (pH= 9) and DCM. The aqueous layer was extracted with DCM 4x 20 ml and the combined organic layers were dried over $NaSO_4$. The solvent removed under reduced pressure and the crude product was purified via column chromatography (DCM/MeOH 15:1→10:1). 142 mg (0.251 mmol, 56%) of the desired product could be obtained as a red powder.

R_f = 0.30 (DCM/MeOH 10:1). – ^{1}H NMR (300 MHz, methanol-d_4), δ (ppm)= 7.74 (dt, *J* = 7.6, 4.0 Hz, 2H, C*H*-Ar), 7.65 (dd, *J* = 5.9, 3.0 Hz, 1H, C*H*-Ar), 7.55 – 7.47 (m, 1H, C*H*-Ar), 7.20 (t, *J* = 11.0 Hz, 2H, C*H*-Ar), 6.74 (dd, *J* = 11.0, 8.9 Hz, 4H, C*H*-Ar), 3.43 – 3.33 (m, 8H, N-CH_2-CH_2-N), 2.52 (s, 1H, C*H*), 1.73 (dd, *J* = 35.1, 11.6 Hz, 4H, CH_2), 1.50 – 1.14 (m, 11H, C*H*, CH_2), 0.95 – 0.86 (m, 3H, CH_3). –IR (ATR) ũ (cm^{-1}) = 2915 (w), 2850 (w), 1635 (w), 1590 (w), 1419 (w), 1378 (w), 1246 (w), 1201 (w), 1102 (w), 1003 (w), 911 (w), 846 (w), 756 (w), 663 (vw), 634 (vw), 592 (w), 569 (w), 518 (vw), 475 (vw), 446 (w). –MS (FAB, 3-NBA): *m/z* (%): 567.3 [M^+] (100).

9-(2-(4-(Cycloheptanecarbonyl)piperazine-1-carbonyl)phenyl)-6-hydroxy-3H-xanthen-3-one (4.19)

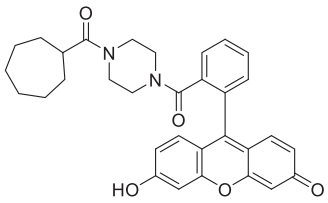

In a 10 ml round bottom flask, 116 µl cycloheptanecarboxylic acid (120 mg, 0.844 mmol, 2.00 equiv.) were solved in 3 ml DCM and cooled to 0 °C. 174 µl pentafluorophenyl trifluoroacetate (283 mg, 1.01 mmol, 2.40 equiv.) were added and stirred for 10 min, before 177 µl DIPEA (131 mg, 1.01 mmol, 2.40 equiv.) were added and the reaction was allowed to warm to room

temperature while stirring for 1.5 h. The mixture was filtered over silica gel and the solvent was removed under reduced pressure. The obtained intermediate product was used in the next step without further purification.

In a 10 ml round bottom flask, 169 mg 6-hydroxy-9-(2-(piperazine-1-carbonyl)phenyl)-3H-xanthen-3-one (**4.7**) (0.422 mmol, 1.00 equiv.) and 177 µl DIPEA (131 mg, 1.01 mmol, 2.40 equiv.) were solved in 3 ml DMF and the mixture was cooled to 0 °C, before the previously obtained pentafluorophenyl-ester intermediate was solved in 1 ml DMF and added. After stirring the reaction mixture for 10 min, the ice bath was removed, the mixture was allowed to warm to room temperature and stirred for another 2 h. The solvent was removed under reduced pressure and the crude product was purified via column chromatography (DCM/MeOH 15:1→5:1). 81.9 mg (0.156 mmol, 37 %) of the desired product could be obtained as an orange powder.

R_f = 0.25 (DCM/MeOH 10:1). – ^{1}H NMR (300 MHz, methanol-d_4), δ (ppm)= 7.68 (dt, *J* = 25.9, 4.5 Hz, 3H, C*H*-Ar), 7.48 (d, *J* = 3.4 Hz, 1H, C*H*-Ar), 7.17 (d, *J* = 9.5 Hz, 2H, C*H*-Ar), 6.70 (d, *J* = 8.2 Hz, 4H, C*H*-Ar), 3.48 – 3.29 (m, 8H, N-CH_2-CH_2-N), 2.69 (d, *J* = 7.8 Hz, 1H, C*H*), 1.56 (dd, *J* = 33.2, 25.7 Hz, 12H, CH-CH_2). –IR (ATR) ũ (cm^{-1}) = 2915 (w), 1631 (w), 1589 (m), 1419 (m), 1378 (m), 1257 (m), 1200 (m), 1102 (m), 1002 (m), 911 (w), 846 (w), 756 (w), 664 (w), 634 (w), 592 (w), 569 (w), 517 (vw), 445 (w). –MS (FAB, 3-NBA): *m/z* (%): 525.0 [M$^+$] (75).

9-(2-(4-((3r,5r,7r)Aadamantane-1-carbonyl)piperazine-1-carbonyl)phenyl)-6-hydroxy-3H-xanthen-3-one (4.20)

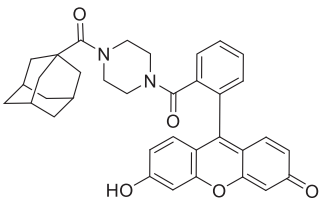

In a 10 ml round bottom flask, 150 mg adamantanecarboxylic acid (0.832 mmol, 2.00 equiv.) were dissolved in 3 ml DCM and cooled to 0 °C. 172 µl pentafluorophenyl trifluoroacetate (280 mg, 0.998 mmol, 2.40 equiv.) were added and stirred for 10 min, before 174 µl DIPEA (129 mg, 0.998 mmol, 2.40 equiv.) were added and the reaction was allowed to warm to room temperature while stirring for 1.5 h. The mixture was filtered over silica gel and the solvent was removed under reduced pressure. The obtained intermediate product was used in the next step without further purification.

In a 10 ml round bottom flask, 167 mg 6-hydroxy-9-(2-(piperazine-1-carbonyl)phenyl)-3H-xanthen-3-one (**4.7**) (0.416 mmol, 1.00 equiv.) and 174 µl DIPEA (129 mg, 0.998 mmol, 2.40 equiv.) were dissolved in 3 ml DMF and the mixture was cooled to 0 °C, then the solution of the previously obtained pentafluorophenyl-ester intermediate in 1 ml DMF was added. After stirring the reaction mixture for 10 min, the ice bath was removed, the mixture was allowed to warm to room temperature and stirred for another 2 h. The solvent was removed under reduced pressure and the crude product was purified via column chromatography (EE/MeOH 10:1→6:1). 180 mg (0.320 mmol, 77 %) of the desired product could be obtained as an orange powder (with impurities).

R_f = 0.03 (EE/MeOH 10:1). – ^{1}H NMR (300 MHz, methanol-d_4) , δ (ppm)= 7.69 (dt, *J* = 5.9, 2.9 Hz, 2H, C*H*-Ar), 7.58 (dd, *J* = 5.8, 3.2 Hz, 1H, C*H*-Ar), 7.45 (dd, *J* = 5.7, 3.2 Hz, 1H, C*H*-Ar), 7.03 (dd, *J* = 9.2, 2.5 Hz, 2H, C*H*-Ar), 6.61 – 6.45 (m, 4H, C*H*-Ar), 3.30 (b, 8H, N-CH_2- CH_2-N), 2.52 (d, *J* = 28.8 Hz, 3H, C*H*), 2.08 – 1.94 (m, 6H, CH_2), 1.89 (d, *J* = 2.8 Hz, 2H, CH_2), 1.83 – 1.70 (m, 4H, CH_2–MS (FAB, 3-NBA): *m/z* (%): 585.1 [M+Na$^+$] (35).

9-(2-(4-(2-(Cyclopent-2-en-1-yl)acetyl)piperazine-1-carbonyl)phenyl)-6-hydroxy-3H-xanthen-3-one (4.21)

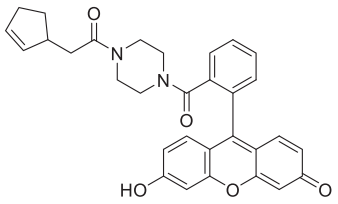

In a 10 ml round bottom flask, 115 µl 2-cyclopentene-1-acetic acid (120 mg, 0.952 mmol, 2.00 equiv.) were solved in 3 ml DCM and cooled to 0 °C. 196 µl pentafluorophenyl trifluoroacetate (319 mg, 1.14 mmol, 2.40 equiv.) were added and stirred for 10 min, before 198 µl DIPEA (147 mg, 1.14 mmol, 2.40 equiv.) were added and the reaction was allowed to warm to room temperature while stirring for 1.5 h. The mixture was filtered over silica gel and the solvent was removed under reduced pressure. The obtained intermediate product was used in the next step without further purification.

In a 10 ml round bottom flask, 191 mg 6-hydroxy-9-(2-(piperazine-1-carbonyl)phenyl)-3H-xanthen-3-one (**4.7**) (0.476 mmol, 1.00 equiv.) and 198 µl DIPEA (147 mg, 1.14 mmol, 2.40 equiv.) were solved in 3 ml DMF and the mixture was cooled to 0 °C, before the previously obtained pentafluorophenyl-ester intermediate was solved in 1 ml DMF and added. After stirring the reaction mixture for 10 min, the ice bath was removed, the mixture was allowed to warm to room temperature and stirred for another 2 h. The solvent was removed under reduced pressure, followed by an aqueous workup with diluted NaOH solution (pH = 9) and DCM. The aqueous layer was extracted with DCM 4x 20 ml and the combined organic layers were dried over $NaSO_4$. The solvent removed under reduced pressure and the crude product was purified via column chromatography (DCM/MeOH 15:1→10:1). 23.5 mg (46.2 µmol, 10 %) of the desired product could be obtained as an orange powder.

R_f = 0.18 (DCM/MeOH 10:1). – ^{1}H NMR (300 MHz, methanol-d_4) , δ (ppm)= 7.72 (d, *J* = 3.1 Hz, 2H, C*H*-Ar), 7.66 (s, 1H, C*H*-Ar), 7.49 (s, 1H, C*H*-Ar), 7.17 (d, *J* = 9.6 Hz, 2H, C*H*-Ar), 6.70 (d, *J* = 7.9 Hz, 4H, C*H*-Ar), 5.73 (s, 1H, C*H*=CH), 5.63 (s, 1H, CH=C*H*), 3.35 (d, *J* = 8.6 Hz, 8H, N-CH_2- CH_2-N), 2.98 (s, 1H, CO-CH$_2$-C*H*), 2.46 – 2.19 (m, 4H, CH-CH_2), 2.07 (d, *J* = 7.5 Hz, 1H, CO-CH_2-C*H*), 1.41 (d, *J* = 6.7 Hz, 1H, CO-CH_2-C*H*). –IR (ATR) ũ (cm^{-1}) = 3055 (vw), 2850 (vw), 1636 (w), 1594 (vw), 1560 (w), 1494 (vw), 1428 (w), 1380 (w), 1280 (w), 1250 (w), 1198 (w), 1161 (w), 1108 (w), 1004 (w), 967 (vw), 911 (w), 844 (w), 783 (vw), 763 (vw), 710 (vw), 683 (vw), 660 (vw), 593 (w), 570 (vw), 481 (w), 451 (w). –MS (FAB, 3-NBA): *m/z* (%): 509.3 [M$^+$] (25).

9-(2-(4-(Cyclohex-1-ene-1-carbonyl)piperazine-1-carbonyl)phenyl)-6-hydroxy-3H-xanthen-3-one (4.22)

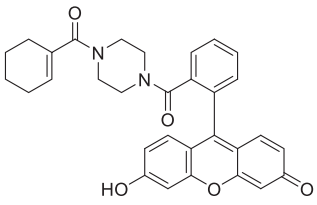

In a 10 ml round bottom flask, 109 µl 1-cyclohexene-1-carboxylic acid (120 mg, 0.952 mmol, 2.00 equiv.) were solved in 3 ml DCM and cooled to 0 °C. 196 µl pentafluorophenyl trifluoroacetate (319 mg, 1.14 mmol, 2.40 equiv.) were added and stirred for 10 min, before 198 µl DIPEA (147 mg, 1.14 mmol, 2.40 equiv.) were added and the reaction was allowed to warm to room temperature while stirring for 1.5 h. The mixture was filtered over silica gel and the solvent was removed under reduced pressure. The obtained intermediate product was used in the next step without further purification.

In a 10 ml round bottom flask, 191 mg 6-hydroxy-9-(2-(piperazine-1-carbonyl)phenyl)-3H-xanthen-3-one (**4.7**) (0.476 mmol, 1.00 equiv.) and 198 µl DIPEA (147 mg, 1.14 mmol, 2.40 equiv.) were solved in 3 ml DMF and the mixture was cooled to 0 °C, before the previously obtained pentafluorophenyl-ester intermediate was solved in 1 ml DMF and added. After stirring the reaction mixture for 10 min, the ice bath was removed, the mixture was allowed to warm to room temperature and stirred for another 2 h. The solvent was removed under reduced pressure and the residues were resuspended in 10 ml H_2O and extracted with 4 x 20 ml DCM. The combined organic layers were dried over $NaSO_4$, the solvent removed under reduced pressure and the crude product was purified via column chromatography (DCM/MeOH 15:1→10:1). 23.5 mg (46.2 µmol, 10 %) of the desired product could be obtained as an orange powder.

R_f = 0.22 (DCM/MeOH 10:1). ^{1}H NMR (300 MHz, methanol-d_4), δ (ppm)= 7.73 (d, *J* = 3.2 Hz, 2H, C*H*-Ar), 7.65 (d, *J* = 4.8 Hz, 1H, C*H*-Ar), 7.49 (d, *J* = 4.1 Hz, 1H, C*H*-Ar), 7.17 (d, *J* = 8.8 Hz, 2H, C*H*-Ar), 6.71 (d, *J* = 8.0 Hz, 4H, C*H*-Ar), 5.77 (s, 1H, C=C*H*), 3.45 – 3.31 (m, 8H, N-CH_2-CH_2-N), 2.12 (d, *J* = 16.4 Hz, 4H, CH_2-CH_2), 1.64 (s, 4H, CH_2-CH_2). –IR (ATR) ũ (cm^{-1}) = 2927 (vw), 1622 (w), 1559 (w), 1512 (w), 1426 (w), 1379 (w), 1243 (m), 1196 (m), 1107 (w), 999 (w), 911 (w), 842 (w), 752 (w), 711 (w), 661 (w), 591 (w), 569 (w), 475 (w), 445 (m). –MS (FAB, 3-NBA): *m/z* (%): 509.3 [M^+] (100).

(Z)-9-(2-(4-(Cyclooct-2-ene-1-carbonyl)piperazine-1-carbonyl)phenyl)-6-hydroxy-3H-xanthen-3-one (4.23)

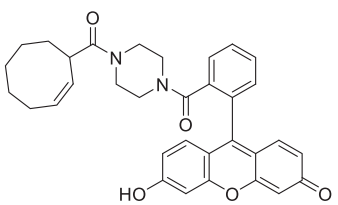

In a 10 ml round bottom flask, 140 mg (Z)-cyclooct-2-ene-1-carboxylic acid (**4.32**) (0.908 mmol, 2.00 equiv.) were solved in 3 ml DCM and cooled to 0 °C. 187 µl pentafluorophenyl trifluoroacetate (305 mg, 1.09 mmol, 2.40 equiv.) were added and stirred for 10 min, before 190 µl DIPEA (141 mg, 1.09 mmol, 2.40 equiv.) were added and the reaction was allowed to warm to room

temperature while stirring for 1.5 h. The mixture was filtered over silica gel and the solvent was removed under reduced pressure. The obtained intermediate product was used in the next step without further purification.

In a 10 ml round bottom flask, 182 mg 6-hydroxy-9-(2-(piperazine-1-carbonyl)phenyl)-3H-xanthen-3-one (**4.7**) (0.454 mmol, 1.00 equiv.) and 190 µl DIPEA (141 mg, 1.09 mmol, 2.40 equiv.) were solved in 3 ml DMF and the mixture was cooled to 0 °C, before the previously obtained pentafluorophenyl-ester intermediate was solved in 1 ml DMF and added. After stirring the reaction mixture for 10 min, the ice bath was removed, the mixture was allowed to warm to room temperature and stirred for another 2 h. The solvent was removed under reduced pressure, followed by an aqueous workup with diluted NaOH solution (pH = 9) and DCM. The aqueous layer was extracted with DCM 4x20 ml and the combined organic layers were dried over $NaSO_4$. The solvent removed under reduced pressure and the crude product was purified via column chromatography (DCM/MeOH 15:1→10:1). 128 mg (0.239 mmol, 53%) of the desired product could be obtained as an orange powder.

R_f = 0.26 (DCM/MeOH 10:1). ^{1}H NMR (300 MHz, methanol-d_4), δ (ppm)= 7.73 (dd, *J* = 5.5, 3.3 Hz, 2H, C*H*-Ar), 7.67 – 7.58 (m, 1H, C*H*-Ar), 7.49 (dd, *J* = 5.2, 3.1 Hz, 1H, C*H*-Ar), 7.17 (d, *J* = 9.1 Hz, 2H, C*H*-Ar), 6.71 (d, *J* = 5.9 Hz, 4H, C*H*-Ar), 5.76 (d, *J* = 8.6 Hz, 1H, C*H*=CH), 5.38 (d, *J* = 5.4 Hz, 1H, CH=C*H*), 3.73 – 3.30 (m, 8H, N-CH_2-CH_2-N), 2.19 (s, 1H, CO-C*H*), 2.09 (s, 1H, CH_2-CH_2), 1.75 – 1.24 (m, 9H, CH_2-CH_2). – IR (ATR) ũ (cm^{-1}) = 2913 (w), 1632 (w), 1590 (w), 1420 (w), 1376 (w), 1253 (w), 1197 (w), 1102 (w), 1001 (w), 910 (w), 843 (w), 754 (w), 661 (w), 634 (w), 591 (w), 569 (w), 475 (w), 445 (w). –MS (FAB, 3-NBA): *m/z* (%): 537.3 [M^+] (90).

9-(2-(4-Benzoylpiperazine-1-carbonyl)phenyl)-6-hydroxy-3H-xanthen-3-one (4.24)

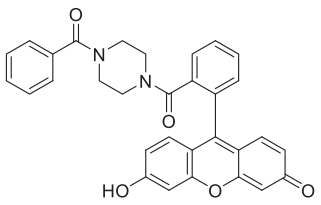

In a 10 ml round bottom flask, 120 mg benzoic acid (0.984 mmol, 2.00 equiv.) were solved in 3 ml DCM and cooled to 0 °C. 202 µl pentafluorophenyl trifluoroacetate (330 mg, 1.18 mmol, 2.40 equiv.) were added and stirred for 10 min, before 206 µl DIPEA (153 mg, 1.18 mmol, 2.40 equiv.) were added and the reaction was allowed to warm to room temperature while stirring for 1.5 h. The mixture was filtered over silica gel and the solvent was removed under reduced pressure. The obtained intermediate product was used in the next step without further purification.

In a 10 ml round bottom flask, 197 mg 6-hydroxy-9-(2-(piperazine-1-carbonyl)phenyl)-3H-xanthen-3-one (**4.7**) (0.492 mmol, 1.00 equiv.) and 206 µl DIPEA (153 mg, 1.18 mmol, 2.40 equiv.) were solved in 3 ml DMF and the mixture was cooled to 0 °C, before the previously obtained pentafluorophenyl-ester intermediate was solved in 1 ml DMF and added. After stirring the reaction mixture for 10 min, the ice bath was

removed, the mixture was allowed to warm to room temperature and stirred for another 2 h. The solvent was removed under reduced pressure, followed by an aqueous workup with diluted NaOH solution (pH= 9) and DCM. The aqueous layer was extracted with DCM 4x20 ml and the combined organic layers were dried over $NaSO_4$. The solvent removed under reduced pressure and the crude product was purified via column chromatography (DCM/MeOH 15:1→10:1). 85.2 mg (0.169 mmol, 43%) of the desired product could be obtained as an orange powder.

R_f = 0.24 (DCM/MeOH 10:1). ^{1}H NMR (300 MHz, methanol-d_4), δ (ppm)= 7.74 (s, 2H, C*H*-Ar), 7.68 (s, 1H, C*H*-Ar), 7.48 (dd, *J* = 19.7, 5.5 Hz, 4H, C*H*-Ar), 7.38 (s, 2H, C*H*-Ar), 7.19 (d, *J* = 9.6 Hz, 2H, C*H*-Ar), 6.73 (s, 4H, C*H*-Ar), 3.43 (b, 8H, N-CH_2-CH_2-N). –IR (ATR) ũ (cm^{-1}) = 1632 (w), 1560 (w), 1490 (w), 1425 (w), 1380 (w), 1277 (w), 1248 (w), 1197 (w), 1109 (w), 1000 (w), 914 (w), 842 (w), 779 (w), 760 (w), 707 (w), 662 (w), 593 (w), 570 (w), 528 (vw), 477 (w), 447 (m).–MS (FAB, 3-NBA): *m/z* (%): 505.3 [M^+] (100).

9-(2-(4-(4-Bromobenzoyl)piperazine-1-carbonyl)phenyl)-6-hydroxy-3H-xanthen-3-one (4.25)

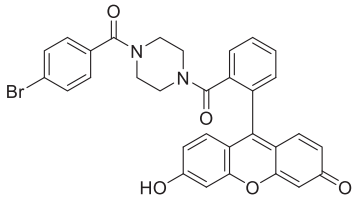

In a 10 ml round bottom flask, 201 mg 4-bromo-benzoic acid (1.00 mmol, 2.00 equiv.) were solved in 3 ml DCM and cooled to 0 °C. 206 µl pentafluorophenyl trifluoroacetate (336 mg, 1.20 mmol, 2.40 equiv.) were added and stirred for 10 min, before 209 µl DIPEA (155 mg, 1.20 mmol, 2.40 equiv.) were added and the reaction was allowed to warm to room temperature while stirring for 1.5 h. The mixture was filtered over silica gel and the solvent was removed under reduced pressure. The obtained intermediate product was used in the next step without further purification.

In a 10 ml round bottom flask, 200 mg 6-hydroxy-9-(2-(piperazine-1-carbonyl)phenyl)-3H-xanthen-3-one (**4.7**) (0.500 mmol, 1.00 equiv.) and 209 µl DIPEA (155 mg, 1.20 mmol, 2.40 equiv.) were solved in 3 ml DMF and the mixture was cooled to 0 °C, before the previously obtained pentafluorophenyl-ester intermediate was solved in 1 ml DMF and added. After stirring the reaction mixture for 10 min, the ice bath was removed, the mixture was allowed to warm to room temperature and stirred for another 2 h. The solvent was removed under reduced pressure, followed by an aqueous workup with diluted NaOH solution (pH= 9) and DCM. The aqueous layer was extracted with DCM 4x 20 ml and the combined organic layers were dried over $NaSO_4$. The solvent removed under reduced pressure and the crude product was purified via column chromatography (DCM/MeOH 15:1→10:1). 61.9 mg (0.106 mmol, 21 %) of the desired product could be obtained as an orange-red powder.

R_f = 0.45 (DCM/MeOH 10:1). – ^{1}H NMR (300 MHz, methanol-d_4), δ (ppm)= 7.75 (s, 2H, C*H*-Ar), 7.68 (s, 1H, C*H*-Ar), 7.63 (d, *J* = 8.1 Hz, 2H, C*H*-Ar), 7.52 (s, 1H, C*H*-Ar),

7.32 (d, *J* = 7.8 Hz, 2H, C*H*-Ar), 7.20 (d, *J* = 9.3 Hz, 2H, C*H*-Ar), 6.74 (s, 4H, C*H*-Ar), 3.46 (s, 8H, N-CH_2-CH_2-N). –IR (ATR) ũ (cm^{-1}) = 2589 (vw), 1588 (w), 1455 (w), 1419 (w), 1378 (w), 1251 (w), 1203 (w), 1104 (w), 999 (w), 912 (vw), 847 (vw), 751 (vw), 664 (vw), 634 (vw), 590 (vw), 569 (vw), 506 (vw), 448 (vw),.–MS (FAB, 3-NBA): *m/z* (%): 583.1 [M^+] (95).

6-Hydroxy-9-(2-(4-(3-(trifluoromethyl)benzoyl)piperazine-1-carbonyl)phenyl)-3H-xanthen-3-one (4.26)

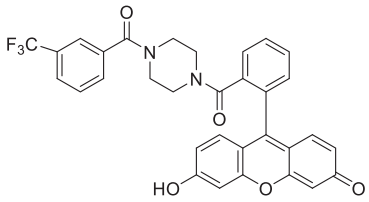

In a 10 ml round bottom flask, 190 mg 3-trifluoromethylbenzoic acid (1.00 mmol, 2.00 equiv.) were solved in 3 ml DCM and cooled to 0 °C. 206 µl pentafluorophenyl trifluoroacetate (336 mg, 1.20 mmol, 2.40 equiv.) were added and stirred for 10 min, before 209 µl DIPEA (155 mg, 1.20 mmol, 2.40 equiv.) were added and the reaction was allowed to warm to room temperature while stirring for 1.5 h. The mixture was filtered over silica gel and the solvent was removed under reduced pressure. The obtained intermediate product was used in the next step without further purification.

In a 10 ml round bottom flask, 200 mg 6-hydroxy-9-(2-(piperazine-1-carbonyl)phenyl)-3H-xanthen-3-one (**4.7**) (0.500 mmol, 1.00 equiv.) and 209 µl DIPEA (155 mg, 1.20 mmol, 2.40 equiv.) were solved in 3 ml DMF and the mixture was cooled to 0 °C, before the previously obtained pentafluorophenyl-ester intermediate was solved in 1 ml DMF and added. After stirring the reaction mixture for 10 min, the ice bath was removed, the mixture was allowed to warm to room temperature and stirred for another 2 h. The solvent was removed under reduced pressure, followed by an aqueous workup with diluted NaOH solution (pH= 9) and DCM. The aqueous layer was extracted with DCM 4x 20 ml and the combined organic layers were dried over $NaSO_4$. The solvent removed under reduced pressure and the crude product was purified via column chromatography (DCM/MeOH 15:1→10:1). 29.2 mg (51.0 µmol, 10 %) of the desired product could be obtained as an orange-red powder.

R_f = 0.24 (DCM/MeOH 10:1). – ^{1}H NMR (300 MHz, methanol-d_4), δ (ppm)= 7.75 (d, *J* = 9.2 Hz, 4H, C*H*-Ar), 7.70 – 7.59 (m, 3H, C*H*-Ar), 7.51 (d, *J* = 4.6 Hz, 1H, C*H*-Ar), 7.19 (d, *J* = 9.4 Hz, 2H, C*H*-Ar), 6.72 (s, 4H, C*H*-Ar), 3.41 (d, *J* = 36.1 Hz, 8H, N-CH_2-CH_2-N). –IR (ATR) ũ (cm^{-1}) = 2914 (vw), 1632 (w), 1589 (w), 1458 (w), 1419 (w), 1380 (w), 1328 (w), 1247 (w), 1204 (w), 1164 (w), 1105 (w), 1069 (w), 1001 (w), 911 (w), 850 (w), 815 (w), 787 (w), 747 (w), 701 (vw), 663 (vw), 634 (vw), 592 (vw), 570 (vw), 507 (vw), 449 (w).–MS (FAB, 3-NBA): *m/z* (%): 573.1 [M^+] (95).

9-(2-(4-(Furan-2-carbonyl)piperazine-1-carbonyl)phenyl)-6-hydroxy-3H-xanthen-3-one (4.27)

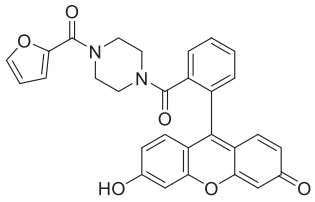

In a 10 ml round bottom flask, 112 mg furan-2-carboxylic acid (1.00 mmol, 2.00 equiv.) were solved in 3 ml DCM and cooled to 0 °C. 206 µl pentafluorophenyl trifluoroacetate (336 mg, 1.20 mmol, 2.40 equiv.) were added and stirred for 10 min, before 209 µl DIPEA (155 mg, 1.20 mmol, 2.40 equiv.) were added and the reaction was allowed to warm to room temperature while stirring for 1.5 h. The mixture was filtered over silica gel and the solvent was removed under reduced pressure. The obtained intermediate product was used in the next step without further purification.

In a 10 ml round bottom flask, 200 mg 6-hydroxy-9-(2-(piperazine-1-carbonyl)phenyl)-3H-xanthen-3-one (**4.7**) (0.500 mmol, 1.00 equiv.) and 209 µl DIPEA (155 mg, 1.20 mmol, 2.40 equiv.) were dissolved in 3 ml DMF and the mixture was cooled to 0 °C, before the previously obtained pentafluorophenyl-ester intermediate was solved in 1 ml DMF and added. After stirring the reaction mixture for 10 min, the ice bath was removed, the mixture was allowed to warm to room temperature and stirred for another 2 h. The solvent was removed under reduced pressure, followed by an aqueous workup with diluted NaOH solution (pH=9) and DCM. The aqueous layer was extracted with DCM 4x20 ml and the combined organic layers were dried over $NaSO_4$. The solvent removed under reduced pressure and the crude product was purified via column chromatography (DCM/MeOH 15:1→10:1). 46.4 mg (93.8 µmol, 19 %) of the desired product could be obtained as an orange-red powder.

R_f = 0.11 (DCM/MeOH 10:1). – ^{1}H NMR (300 MHz, methanol-d_4), δ (ppm)= 7.99 (d, *J* = 1.9 Hz, 1H, C*H*-Ar), 7.74 (d, *J* = 3.1 Hz, 2H, C*H*-Ar), 7.70 – 7.61 (m, 1H, C*H*-Ar), 7.52 (s, 1H, C*H*-Ar), 7.26 – 7.12 (m, 2H, C*H*-Ar), 6.72 (s, 4H, C*H*-Ar), 6.37 (d, *J* = 12.1 Hz, 1H, C*H*-Ar), 6.23 (d, *J* = 12.1 Hz, 1H, C*H*-Ar), 3.37 (dd, *J* = 18.9, 12.4 Hz, 8H, N-CH_2-CH_2-N). –IR (ATR) ũ (cm^{-1}) = 2419 (w), 1611 (m), 1560 (w), 1488 (w), 1425 (m), 1380 (m), 1249 (m), 1195 (m), 1110 (m), 1002 (m), 913 (m), 842 (m), 751 (m), 711 (w), 662 (w), 591 (m), 568 (w), 474 (m), 447 (m).–MS (FAB, 3-NBA): *m/z* (%): 495.2 [M^+] (25).

9-(2-(4-(1H-Indole-5-carbonyl)piperazine-1-carbonyl)phenyl)-6-hydroxy-3H-xanthen-3-one (4.28)

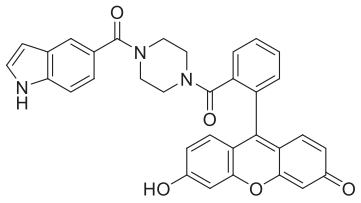

In a 10 ml round bottom flask, 161 mg indole-5-carboxylic acid (1.00 mmol, 2.00 equiv.) were solved in 3 ml DCM and cooled to 0 °C. 206 µl pentafluorophenyl trifluoroacetate (336 mg, 1.20 mmol, 2.40 equiv.) were added and stirred for 10 min, before 209 µl DIPEA (155 mg, 1.20 mmol, 2.40 equiv.) were added and the reaction was allowed to warm to room temperature while stirring for 1.5 h. The mixture was filtered over silica gel and the solvent was removed under reduced pressure. The obtained intermediate product was used in the next step without further purification.

In a 10 ml round bottom flask, 200 mg 6-hydroxy-9-(2-(piperazine-1-carbonyl)phenyl)-3H-xanthen-3-one (**4.7**) (0.500 mmol, 1.00 equiv.) and 209 µl DIPEA (155 mg, 1.20 mmol, 2.40 equiv.) were solved in 3 ml DMF and the mixture was cooled to 0 °C, before the previously obtained pentafluorophenyl-ester intermediate was solved in 1 ml DMF and added. After stirring the reaction mixture for 10 min, the ice bath was removed, the mixture was allowed to warm to room temperature and stirred for another 2 h. The solvent was removed under reduced pressure, followed by an aqueous workup with diluted NaOH solution (pH= 9) and DCM. The aqueous layer was extracted with DCM 4x 20 ml and the combined organic layers were dried over $NaSO_4$. The solvent removed under reduced pressure and the crude product was purified via column chromatography (DCM/MeOH 15:1→10:1). 28.8 mg (53.0 µmol, 11 %) of the desired product could be obtained as an orange-red powder.

R_f = 0.13 (DCM/MeOH 10:1). – ^{1}H NMR (300 MHz, methanol-d_4), δ (ppm)= 7.73 (s, 2H, C*H*-Ar), 7.69 (s, 1H, C*H*-Ar), 7.63 (s, 1H, C*H*-Ar), 7.50 (s, 1H, C*H*-Ar), 7.43 (d, *J* = 8.6 Hz, 1H, C*H*-Ar), 7.32 (d, *J* = 3.1 Hz, 1H, C*H*-Ar), 7.16 (dd, *J* = 18.8, 9.1 Hz, 3H, C*H*-Ar), 6.73 (d, *J* = 6.8 Hz, 4H, C*H*-Ar), 6.52 (d, *J* = 2.7 Hz, 1H, C*H*-Ar), 3.46 (s, 8H, N-CH_2-CH_2-N). –IR (ATR) ũ (cm^{-1}) = 2915 (w), 1746 (vw), 1588 (w), 1455 (w), 1419 (w), 1380 (w), 1319 (w), 1244 (w), 1202 (w), 1164 (w), 1103 (w), 1001 (w) 911 (vw), 849 (w), 748 (vw), 663 (vw), 590 (vw), 569 (vw), 508 (vw), 448 (w).–MS (FAB, 3-NBA): *m/z* (%): 544.2 [M^+] (100).

(Z)-2-(Cyclooct-2-en-1-yl)-2-hydroxy-1H-indene-1,3(2H)-dione (4.31)

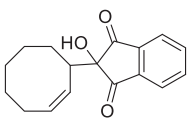

In a 250 ml round bottom flask equipped with a Dean-Stark apparatus, 2.19 ml cyclooctene (1.85 g, 16.8 mmol, 3.00 equiv.) and 1.00 g ninhydrin (5.61mmol, 1.00 equiv.) were solved in 100 ml toluene and the mixture was refluxed for 40 h under water removal. A color change from dark to light green was observed. The solvent was removed under reduced pressure and the crude product was purified via column chromatography (CH/EE 3:1). 883 mg (3.27 mmol, 58 %) of the desired product could be obtained as a white powder.

R_f = 0.26 (CH/EE 3:1). – ^{1}H NMR (300 MHz, chloroform-*d*), δ (ppm)= 8.04 – 7.95 (m, 2H, C*H*-Ar), 7.93 – 7.84 (m, 2H, C*H*-Ar), 5.93 – 5.80 (m, 1H, C*H*=CH), 5.61 (t, *J* = 10.0 Hz, 1H, CH=C*H*), 3.24 – 3.12 (m, 1H, C*H*), 2.26 – 1.98 (m, 2H, CH-CH_2), 1.72 – 1.09 (m, 8H, CH_2-CH_2).

(Z)-Cyclooct-2-ene-1-carboxylic acid (4.32)

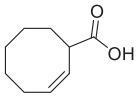

In a 100 ml round bottom flask, 600 mg (Z)-2-(cyclooct-2-en-1-yl)-2-hydroxy-1H-indene-1,3(2H)-dione (**4.31**) (2.22 mmol, 1.00 equiv.) were solved in 22 ml diethyl ether and the mixture was cooled to 0 °C. 1.04 g periodic acid (4.55 mol, 2.05 equiv.) were added portionwise over 2 min. The reaction mixture was allowed to slowly warm to room temperature, avoiding a sudden exothermal reaction of H_5IO_6. The reaction mixture was stirred for 5 h at room temperature before being filtered over celite and the solvent was removed under reduced pressure. The crude product was purified via column chromatography (DCM/CH 4:1 → CH/EE 2:1). 222 mg (1.44 mmol, 65 %) of the desired product could be obtained as a yellow oil.

R_f = 0.21 (CH/EE 3:1). – ^{1}H NMR (300 MHz, chloroform-*d*), δ (ppm)= 5.80 (q, *J* = 8.9, 7.9 Hz, 1H, C*H*=CH), 5.72 – 5.63 (m, 1H, CH=C*H*), 3.58 – 3.38 (m, 1H, C*H*), 2.16 (dd, *J* = 22.3, 9.3 Hz, 2H, CH-CH_2), 2.03 – 1.91 (m, 1H, CH_2-CH_2), 1.86 – 1.48 (m, 5H, CH_2-CH_2), 1.48 – 1.22 (m, 2H, CH_2-CH_2).

9-(2-(1,4-Diazepane-1-carbonyl)phenyl)-6-hydroxy-3H-xanthen-3-one (4.35)

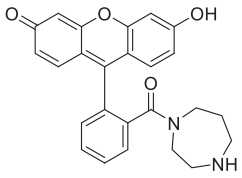

In a 50 ml Schlenk flask, 3.38 g homopiperazine (33.7 mmol, 3.90 equiv.) were solved in 13 ml abs. DCM, before 8.45 ml $AlMe_3$ (2M in heptane) (16.9 mmol, 1.95 equiv.) were added and the reaction mixture was stirred overnight (precipitation of a white solid). 3.00 g methyl 2-(6-hydroxy-3-oxo-3H-xanthen-9-yl)benzoate (**4.4**) (8.64 mmol, 1.00 equiv.) suspended in 10 ml DCM were added and the mixture was refluxed for 10 h in the dark. After cooling to room temperature, 80 ml MeOH + 195 ml HCl (1M) were added until no further gas evolution could be observed. The solvent was removed under reduced pressure and the crude product was purified via column chromatography (DCM/MeOH 4:1). 824 mg (1.97 mmol, 23 %) of the desired product could be obtained as orange-yellow powder.

R_f = 0.13 (DCM/MeOH 4:1). – ^{1}H NMR (300 MHz, methanol-d_4), δ (ppm)= 7.83 (s, 3H, C*H*-Ar), 7.62 (d, *J* = 23.7 Hz, 3H, C*H*-Ar), 7.36 (s, 2H, C*H*-Ar), 7.31 – 7.20 (m, 2H, C*H*-Ar), 3.59 (d, *J* = 35.9 Hz, 4H, N-CH_2), 3.10 (d, *J* = 31.7 Hz, 4H, CH_2-NH), 2.06 (d, *J* = 31.5 Hz, 2H, CH_2-CH_2-CH_2). –^{13}C-NMR (100 MHz, Methanol-d_4): δ = 173.01 ($C_{quart.}$, *C*O), 161.06 (C_{quart}, N-*C*O), 135.09 (+,*C*H-Ar), 131.82 (-, *C*H_2), 129.26 ($C_{quart.}$, *C*-Ar),

121.46 (+,*C*H-Ar), 118.38 (+,*C*H-Ar), 103.33 (+,*C*H-Ar). –IR (ATR) ũ (cm^{-1}) =3346 (m, w), 1588 (s), 1536 (m), 1452 (m), 1375 (m), 1297 (m), 1263 (m), 1203 (m), 1172 (m), 1117 (m), 917 (w), 850 (w), 759 (w), 662 (w), 631 (w), 571 (w), 500 (w), 449 (w). – MS (FAB, 3-NBA): *m/z* (%): 415.2 [M^+] (100).

6-Hydroxy-9-(2-(4-(2-propylpentanoyl)-1,4-diazepane-1-carbonyl)phenyl)-3H-xanthen-3-one (4.37)

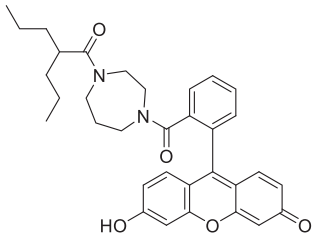

In a 10 ml round bottom flask, 144 mg 2-propylpentanecarboxylic acid (1.00 mmol, 2.00 equiv.) were solved in 3 ml DCM and cooled to 0 °C. 206 µl pentafluorophenyl trifluoroacetate (336 mg, 1.20 mmol, 2.40 equiv.) were added and stirred for 10 min, before 209 µl DIPEA (155 mg, 1.20 mmol, 2.40 equiv.) were added and the reaction was allowed to warm to room temperature while stirring for 1.5 h. The mixture was filtered over silica gel and the solvent was removed under reduced pressure. The obtained intermediate product was used in the next step without further purification.

In a 10 ml round bottom flask, 207 mg 9-(2-(1,4-Diazepane-1-carbonyl)phenyl)-6-hydroxy-3H-xanthen-3-one (**4.35**) (0.500 mmol, 1.00 equiv.) and 209 µl DIPEA (155 mg, 1.20 mmol, 2.40 equiv.) were solved in 3 ml DMF and the mixture was cooled to 0 °C, before the previously obtained pentafluorophenyl-ester intermediate was solved in 1 ml DMF and added. After stirring the reaction mixture for 10 min, the ice bath was removed, the mixture was allowed to warm to room temperature and stirred for another 2 h. The solvent was removed under reduced pressure, followed by an aqueous workup with diluted NaOH solution (pH = 9) and DCM. The aqueous layer was extracted with DCM 4x 20 ml and the combined organic layers were dried over $NaSO_4$. The solvent removed under reduced pressure and the crude product was purified via column chromatography (DCM/MeOH 15:1→10:1). 45.7 mg (84.5 µmol, 17 %) of the desired product could be obtained as an orange-red powder.

R_f = 0.22 (DCM/MeOH 10:1). – ^{1}H NMR (300 MHz, methanol-d_4), δ (ppm)= 7.78 – 7.66 (m, 2H, C*H*-Ar), 7.61 – 7.44 (m, 2H, C*H*-Ar), 7.26 – 7.13 (m, 2H, C*H*-Ar), 6.71 (d, *J* = 8.3 Hz, 4H, C*H*-Ar), 3.53 (d, *J* = 26.4 Hz, 4H, N-CH_2), 3.48 – 3.31 (m, 4H, CH_2-N), 2.72 (d, *J* = 19.7 Hz, 1H, CO-C*H*), 1.72 (s, 2H, CH_2-CH_2-CH_2), 1.61 – 1.15 (m, 8H, CH-CH_2-CH_2), 0.87 (dt, *J* = 14.7, 7.2 Hz, 6H, CH_3). –IR (ATR) ũ (cm^{-1}) = 2927 (vw), 2870 (vw), 1590 (w), 1452 (w), 1377 (w), 1259 (w), 1202 (w), 1104 (w), 911 (vw), 848 (vw), 758 (vw), 664 (vw), 634 (vw), 593 (vw), 569 (vw), 506 (vw), 448 (vw).– MS (FAB, 3-NBA): *m/z* (%): 541.2 [M^+] (70).

9-(2-(4-(cyclohexanecarbonyl)-1,4-diazepane-1-carbonyl)phenyl)-6-hydroxy-3H-xanthen-3-one (4.38)

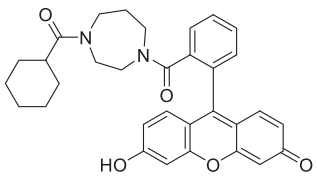

In a 10 ml round bottom flask, 128 mg cyclohexanecarboxylic acid (1.00 mmol, 2.00 equiv.) were solved in 3 ml DCM and cooled to 0 °C. 206 µl pentafluorophenyl trifluoroacetate (336 mg, 1.20 mmol, 2.40 equiv.) were added and stirred for 10 min, before 209 µl DIPEA (155 mg, 1.20 mmol, 2.40 equiv.) were added and the reaction was allowed to warm to room temperature while stirring for 1.5 h. The mixture was filtered over silica gel and the solvent was removed under reduced pressure. The obtained intermediate product was used in the next step without further purification.

In a 10 ml round bottom flask, 207 mg 9-(2-(1,4-Diazepane-1-carbonyl)phenyl)-6-hydroxy-3H-xanthen-3-one (**4.35**) (0.500 mmol, 1.00 equiv.) and 209 µl DIPEA (155 mg, 1.20 mmol, 2.40 equiv.) were solved in 3 ml DMF and the mixture was cooled to 0 °C, before the previously obtained pentafluorophenyl-ester intermediate was solved in 1 ml DMF and added. After stirring the reaction mixture for 10 min, the ice bath was removed, the mixture was allowed to warm to room temperature and stirred for another 2 h. The solvent was removed under reduced pressure, followed by an aqueous workup with diluted NaOH solution (pH = 9) and DCM. The aqueous layer was extracted with DCM 4x20 ml and the combined organic layers were dried over $NaSO_4$. The solvent removed under reduced pressure and the crude product was purified via column chromatography (DCM/MeOH 15:1→10:1). 103 mg (0.196 mmol, 39 %) of the desired product could be obtained as an orange-red powder.

R_f = 0.19 (DCM/MeOH 10:1). – ^{1}H NMR (300 MHz, methanol-d_4), δ (ppm)= 7.72 (s, 2H, C*H*-Ar), 7.48 (s, 2H, C*H*-Ar), 7.18 (d, *J* = 8.3 Hz, 2H, C*H*-Ar), 6.71 (d, *J* = 8.0 Hz, 4H, C*H*-Ar), 3.53 (s, 4H, N-CH_2), 3.35 (d, *J* = 2.0 Hz, 4H, CH_2-N), 2.54 (d, *J* = 36.5 Hz, 1H, CO-C*H*), 1.73 (s, 7H, CH_2-CH_2), 1.33 (d, *J* = 24.0 Hz, 5H, CH_2-CH_2). –IR (ATR) ũ (cm^{-1}) = 2920 (w), 2851 (w), 1588 (w), 1453 (w), 1417 (w), 1378 (w), 1259 (w), 1203 (w), 1104 (w), 955 (vw), 911 (w), 847 (w), 757 (vw), 665 (w), 634 (w), 591 (vw), 569 (w), 505 (vw), 446 (w). – MS (FAB, 3-NBA): *m/z* (%): 525.2 [M^+] (100).

9-(2-(4-((3r,5r,7r)-Adamantane-1-carbonyl)-1,4-diazepane-1-carbonyl)phenyl)-6-hydroxy-3H-xanthen-3-one (4.39)

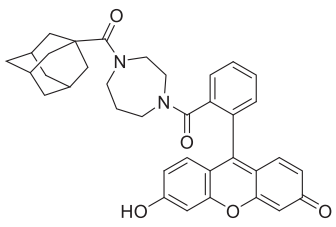

In a 10 ml round bottom flask, 65.2 mg 1-adamantanecarboxylic acid (0.362 mmol, 2.00 equiv.) were solved in 2 ml DCM and cooled to 0 °C. 74.6 µl pentafluorophenyl trifluoroacetate (122 mg, 0.434 mmol, 2.40 equiv.) were added and stirred for 10 min, before 75.6 µl DIPEA (56.1 mg, 0.434 mmol, 2.40 equiv.) were added and the reaction was allowed to warm to room temperature while stirring for

1.5 h. The mixture was filtered over silica gel and the solvent was removed under reduced pressure. The obtained intermediate product was used in the next step without further purification.

In a 10 ml round bottom flask, 75.0 mg 9-(2-(1,4-Diazepane-1-carbonyl)phenyl)-6-hydroxy-3H-xanthen-3-one (**4.35**) (0.181 mmol, 1.00 equiv.) and 75.6 µl DIPEA (56.1 mg, 0.434 mmol, 2.40 equiv.) were solved in 2 ml DMF and the mixture was cooled to 0 °C, before the previously obtained pentafluorophenyl-ester intermediate was solved in 1 ml DMF and added. After stirring the reaction mixture for 10 min, the ice bath was removed, the mixture was allowed to warm to room temperature and stirred for another 2 h. The solvent was removed under reduced pressure, followed by an aqueous workup with diluted NaOH solution (pH= 9) and DCM. The aqueous layer was extracted with DCM 4x 20 ml and the combined organic layers were dried over $NaSO_4$. The solvent removed under reduced pressure and the crude product was purified via column chromatography (DCM/MeOH 15:1→10:1). 20.0 mg (34.7 µmol, 19 %) of the desired product could be obtained as an orange-red powder.

R_f = 0.39 (DCM/MeOH 4:1). – ^{1}H NMR (300 MHz, methanol-d_4), δ (ppm)= 7.72 (tt, *J* = 6.0, 2.9 Hz, 3H, C*H*-Ar), 7.54 – 7.43 (m, 1H, C*H*-Ar), 7.40 (d, *J* = 2.2 Hz, 1H, C*H*-Ar), 7.23 (ddd, *J* = 22.0, 9.4, 4.7 Hz, 1H, C*H*-Ar), 7.09 – 6.97 (m, 1H, C*H*-Ar), 6.56 (ddt, *J* = 17.8, 10.6, 2.1 Hz, 2H, C*H*-Ar), 6.41 (t, *J* = 3.5 Hz, 1H, C*H*-Ar), 3.54 – 3.33 (m, 4H, N-CH_2), 2.95 – 2.68 (m, 4H, CH_2-N), 2.06 (d, *J* = 5.5 Hz, 9H, C*H*, CH_2), 1.92 – 1.69 (m, 6H, C*H*, CH_2), 1.39 – 1.22 (m, 2H, 2H, CH_2-CH_2-CH_2). –IR (ATR) ũ (cm^{-1}) = 2902 (w), 2848 (vw), 1748 (vw), 1634 (w), 1593 (w), 1453 (w), 1418 (w), 1387 (w), 1325 (w), 1301 (w), 1198 (w), 1175 (w), 1103 (w), 1035 (w), 912 (vw), 851 (vw), 756 (vw), 678 (vw), 632 (vw), 596 (vw), 569 (vw), 507 (vw), 448 (w). – MS (FAB, 3-NBA): *m/z* (%): 577.5 [M^+] (40).

9-(2-(4-(1-Fluorocyclooct-2-yne-1-carbonyl)-1,4-diazepane-1-carbonyl)phenyl)-6-hydroxy-3H-xanthen-3-one (4.40)

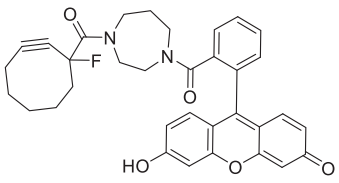

In a 10 ml round bottom flask, 20.0 mg 1-Fluorocyclooct-2-yne-1-carboxylic acid (**4.47**) (118 µmol, 1.00 equiv.), 30.7 µl DIPEA (22.8 mg, 176 µmol, 1.50 equiv.), 23.8 mg HOBt (176 µmol, 1.50 equiv.) and 73.1 mg 9-(2-(1,4-Diazepane-1-carbonyl)phenyl)-6-hydroxy-3H-xanthen-3-one (**4.35**) (176 µmol, 1.50 equiv.) were solved in 2 ml abs. DCM. 27.3 µl DIC (22.2 mg, 176 µmol, 1.50 equiv.) were added and the reaction mixture was stirred for 24 h. Subsequently, the mixture was diluted with H_2O and extracted with 3x 10 ml EE. The combined organic layers were washed with brine, dried over $NaSO_4$ and the solvent was removed under reduced pressure. The crude product was purified via column chromatography (DCM/MeOH 10:1). 34.0 mg (60.0 µmol, 51 %) of the desired product could be obtained as an orange-red powder.

IR (ATR) ũ (cm^{-1}) = 3338 (w), 2966 (m), 2928 (w), 2449 (w), 1750 (w), 1597 (s), 1479 (s), 1382 (m), 1360 (m), 1248 (w), 1154 (m), 1129 (m), 995 (w), 924 (w), 854 (w), 766 (m), 744 (w), 634 (vw), 596 (vw), 475 (m), 401 (w). –MS (FAB, 3-NBA): *m/z* (%): 567.5 [M^+] (45).

9-(2-(4-(((3r,5r,7r)-Adamantane-1-carbonyl)prolyl)-1,4-diazepane-1-carbonyl)phenyl)-6-hydroxy-3H-xanthen-3-one (4.41)

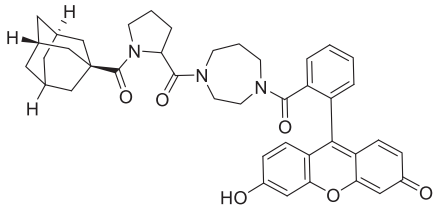

In a 10 ml round bottom flask, 30.0 mg adamantane-1-carbonylproline (108 µmol, 1.00 equiv.), 28.3 µl DIPEA (21.0mg, 162 µmol, 1.50 equiv.), 21.9 mg HOBt (162 µmol, 1.50 equiv.) and 67.2 mg 9-(2-(1,4-Diazepane-1-carbonyl)phenyl)-6-hydroxy-3H-xanthen-3-one (**4.35**) (162 µmol, 1.50 equiv.) were solved in 2 ml abs. DMF. 25.1 µl DIC (20.5 mg, 162 µmol, 1.50 equiv.) were added and the reaction mixture was stirred for 24 h. Subsequently, the mixture was diluted with H_2O and extracted with 3x 10 ml EE. The combined organic layers were washed with brine, dried over $NaSO_4$ and the solvent was removed under reduced pressure. The crude product was purified via column chromatography (DCM/MeOH 10:1). 28.0 mg (41.6 µmol, 38 %) of the desired product could be obtained as an orange-red powder.

^{1}H NMR (500 MHz, methanol-d_4), δ (ppm)= 7.76 – 7.66 (m, 3H, C*H*-Ar), 7.46 (tt, *J* = 6.8, 4.1 Hz, 1H, C*H*-Ar), 7.22 – 7.12 (m, 2H, C*H*-Ar), 6.74 – 6.66 (m, 4H, C*H*-Ar), 3.97 (tt, *J* = 10.3, 5.5 Hz, 1H, CO-C*H*), 3.76 (dq, *J* = 14.5, 8.0, 7.4 Hz, 4H, N-CH_2), 3.30 (p, *J* = 1.6 Hz, 4H, CH_2-N), 1.99 (d, *J* = 18.4 Hz, 12H, m, C*H*, CH_2), 1.75 (t, *J* = 5.3 Hz, 8H, C*H*, CH_2), 1.27 (s, 3H, C*H*, CH_2). –IR (ATR) ũ (cm^{-1}) = 2918 (w), 2849 (w), 1589 (w), 1504 (w), 1454 (w), 1419 (w), 1379 (w), 1261 (w), 1204 (w), 1177 (w), 1104 (w), 974 (vw), 914 (vw), 850 (w), 758 (vw), 666 (vw), 634 (vw), 593 (vw), 569 (w), 506 (vw), 449 (w), 44. – MS (FAB, 3-NBA): *m/z* (%): 674.3 [M^+] (15).

Methyl 2-oxocyclooctane-1-carboxylate (4.44)

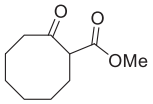

In a 500 ml 3-neck flask, 19.0 g NaH (2.00 equiv., 475 mmol, as a 60% suspension in mineral oil) were suspended in 150 ml toluene. 60.1 ml dimethyl carbonate (3.00 equiv., 713 mmol, 64.2 g) were added in one portion and the mixture was heated to 80 °C. 30.0 g cyclooctanone (1.00 equiv., 238 mmol) were solved in 80 ml toluene and added dropwise over 1 h (precipitation of a white solid). When no further gas evolution could be observed, the reaction mixture was cooled to 0 °C, 20 ml dH_2O and 48 ml glacial acid were added. Icecold HCl was added until the solid was completely solved. The reaction mixture was partitioned and extracted with 2 x 100 ml toluene. Combined organic layers were washed with $NaHCO_3$ solution, dried over $NaSO_4$ and the solvent was removed under reduced pressure. The crude product was distilled at 0 mbar/75 °C. 25.7 g (140 mmol, 59%) of the desired product could be obtained as a clear liquid.

R_f = 0.21 (CH/2% EE). – ^{1}H NMR (300 MHz, chloroform-*d*), δ (ppm)= 3.65 (s, 3H, C*H*$_3$), 3.60 – 3.53 (m, 1H, CO-C*H*), 2.39 – 2.28 (m, 2H, CO-C*H*$_2$), 2.07 (ddd, *J* = 8.8, 6.3, 3.9 Hz, 1H, C*H*$_2$- C*H*$_2$), 1.85 (dt, *J* = 9.8, 4.2 Hz, 1H, C*H*$_2$- C*H*$_2$), 1.73 – 1.62 (m, 2H, C*H*$_2$-C*H*$_2$), 1.54 – 1.31 (m, 6H, C*H*$_2$-C*H*$_2$).

Methyl 1-fluoro-2-oxocyclooctane-1-carboxylate (4.45)

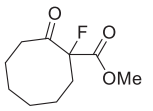

In a 500 ml round bottom flask, 4.33 g methyl 2-oxocyclooctane-1-carboxylate (**4.44**) (1.00 equiv., 23.5 mmol) were solved in 170 ml acetonitrile and cooled to 0 °C. 10.0 g Selectfluor® (1.20 equiv., 28.2 mmol) were added and the reaction mixture was stirred over night at 55°C. After cooling to room temperature, the reaction was quenched with 160 ml H_2O and the aqueous layer was extracted with 4x120 ml EE. The combined organic layers were dried over $NaSO_4$ trocknen and the solvent was removed under reduced pressure. The resulting oil was suspended in DCM, filtered over silica gel and again the solvent was removed under reduced pressure. 4.37 g (21.6 mmol, 92%) of the desired product could be obtained as a clear oil that precipitated to a white solid at 4 °C.

R_f = 0.06 (CH/2% EE). – ^{1}H NMR (300 MHz, chloroform-*d*), δ (ppm)= 3.78 (s, 3H, C*H*$_3$), 2.77 – 2.43 (m, 3H, C*H*$_2$), 2.23 (dddd, *J* = 15.6, 8.1, 4.3, 3.5 Hz, 1H, C*H*$_2$), 2.08 – 1.92 (m, 1H, C*H*$_2$), 1.93 – 1.80 (m, 1H, C*H*$_2$), 1.65 (dddd, *J* = 24.9, 14.9, 7.4, 4.1 Hz, 3H, C*H*$_2$), 1.44 (dtdd, *J* = 21.0, 10.7, 6.6, 3.6 Hz, 3H, C*H*$_2$).

Methyl 1-fluorocyclooct-2-yne-1-carboxylate (4.46)

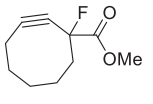

In a 100 ml Schlenk flask, 1.00 g Methyl-1-fluoro-2-oxocyclooctane-1-carboxylate (**4.45**) (4.94 mmol, 1.00 equiv.) were solved in 38 ml abs. THF and cooled to -78 °C. 10.9 ml KHMDS solution (0.5 M in toluene) (1.09 g, 5.44 mmol, 1.10 equiv.) were added over 1.5 h via syringe pump and the reaction

mixture was stirred for further 30 min. 1.94 g *N*-phenyl-bis(trifluoromethanesulfonimide) (4.44 mmol, 1.10 equiv.) were solved in 5 ml THF, added over 1 h and the reaction mixture was stirred for 1 h. in the meantime, fresh LDA was prepared: in a 50 ml Schlenk flask, 1.05 ml diisopropylamine (0.756 g, 7.47 mmol, 1.51 equiv.) were solved in 5 ml THF and cooled to -78 °C before 2.87 ml n-butyllithium (0.459 g, 7.17 mmol, 1.45 equiv.) were added portion wise over 30 min and the mixture was allowed to warm to room temperature. The fresh LDA was added to the reaction mixture, which was allowed to warm to room temperature and stirred overnight. The reaction was quenched with MeOH and the solvents were removed under reduced pressure. The crude product was purified via column chromatography (CH/2%EE, 2 cm x 20 cm). 323 mg (1.75 mmol, 35%) of the desired product was obtained as a yellow oil.

R_f = 0.05 (CH/EE 30:1). – ^{1}H NMR (300 MHz, chloroform-*d*), δ (ppm)= 3.83 (s, 3H, C*H*$_3$), 2.47 – 2.19 (m, 4H, C*H*$_2$), 2.12 – 1.81 (m, 4H, C*H*$_2$), 1.73 (dd, *J* = 7.8, 1.7 Hz, 1H, C*H*$_2$), 1.53 – 1.37 (m, 1H, C*H*$_2$).

1-Fluorocyclooct-2-yne-1-carboxylic acid (4.47)

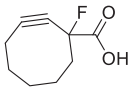

In a 25 ml round bottom flask, 259 mg Methyl 1-fluorocyclooct-2-yne-1-carboxylate (**4.46**) (1.41 mmol, 1.00 equiv.) were solved in 4.00 ml H_2O/MeOH (1:1). 69.0 mg lithiumhydroxide (2.88 mmol, 2.05 equiv.) were added and the reaction mixture was heated to 50°C for 10 min, before it was allowed to cool to room temperature and was stirred for another 2 h. Subsequently, the mixture was cooled to 0 °C, diluted with H_2O and brought to pH= 2 with conc. HCl. The aqueous layer was extracted with 3x 20 ml EE, the combined organic layers were dried over $NaSO_4$ and the solvent was removed under reduced pressure. 208 mg (1.22 mmol, 87%) of the desired product was obtained as a yellow oil.

^{1}H NMR (300 MHz, chloroform-*d*), δ (ppm)= 5.17 (s, 1H, O*H*), 2.46 – 2.23 (m, 4H, C*H*$_2$), 2.10 – 1.82 (m, 4H, C*H*$_2$), 1.73 (dt, *J* = 15.8, 7.6 Hz, 1H, C*H*$_2$), 1.49 (dd, *J* = 15.3, 7.5 Hz, 1H, C*H*$_2$).

6.1.4 Synthesis of a DOX-nitroxide small molecule model system

2-Benzyl-1,1,3,3-tetramethylisoindoline (5.2)

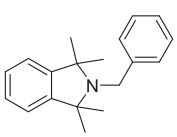

A 2 l 3-necked round bottom flask equipped with a dropping funnel, a cooler, and a Dean-Stark-apparatus, was filled with 44.6 g predried magnesium chips (1.84 mol, 8.70 equiv.), evacuated and heated with a heatgun before flooding with argon. A few iodine crystals were added, the set-up was sealed and heated again until the iodine crystals were completely sublimed. The magnesium chips were dissolved in 270 ml abs. Et_2O and a solution of

89.5 ml methyl iodine (1.44 mol, 6.80 equiv.) in 130 ml abs. Et_2O was added slowly over 1.5 h over the dropping funnel while the flask was cooled in an ice bath. Temperature was controlled to not exceed 30 °C and evaporation of ether was kept constant. 50.0 g n-benzylphtalimide (211 mmol, 1.00 equiv.) were solved in 500 ml warm toluene and added through the dropping funnel before the ice bath was replaced by an oil bath. The reaction mixture was heated to 110 °C under constant removal of ether through the Dean-Stark apparatus. Subsequently, the mixture was heated to 130 °C and refluxed overnight. 200 ml of the 500 ml total toluene in the flask were removed via the Dean-Stark apparatus and the solution was cooled to room temperature. 400 ml hexanes were added and again refluxed under scratching the walls of the flask with a spatula, until the residues in the flask were soft. Solution and residues were filtered over Celite until the residue was not yellow anymore and the flask was rinsed with hexanes. Residues in flask and Celite filter were quenched cautiously. The combined organic filtrates were bubbled with air for 72 h until the solvent was evaporated. The remaining solvent was removed under reduced pressure. The residue was solved in hexanes and purified via basic aluminum oxide column chromatography before the solvent was removed under reduced pressure and the resulting crude product was recrystallized from MeOH. 13.7 g of the desired product (51.6 mmol, 26%) could be obtained as white needles.

^{1}H NMR (400 MHz, chloroform-*d*), δ (ppm)= 7.45 (s, 2H, C*H*-Ar), 7.28 (s, 2H, C*H*-Ar), 7.23 (d, *J* = 7.8 Hz, 3H, C*H*-Ar), 7.13 (s, 2H, C*H*-Ar), 3.99 (s, 2H, CH_2), 1.30 (s, 12H, CH_3).

5-Bromo-1,1,3,3-tetramethylisoindoline (5.3)

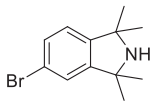

In a 250 ml round bottom flask, 3.00 g 2-Benzyl-1,1,3,3-tetramethylisoindoline (**5.2**) (11.3 mmol, 1.00 equiv.) were solved in 45 ml abs. DCM and cooled to 0 °C before 1.21 ml bromine (3.79 g, 23.7 mmol, 2.10 equiv.) in 30 ml abs. DCM were added dropwise. After the addition of 5.43 g $AlCl_3$ (40.7 mmol, 3.60 equiv.) the solution was stirred for 1 h at 0 °C. The reaction mixture was added to 150 ml ice and stirred for another 30 min. The mixture was basified using 10M NaOH (pH= 14) and extracted with 3x 100 ml DCM. The combined organic layers were washed with brine and the solvent was removed under reduced pressure. The residue was solved in 70 ml MeOH, 225 mg $NaHCO_3$ were added and, in $NaHCO_3$ excess, 18 ml conc. H_2O_2 (35%) were added before the whole mixture was acidified using 1 M H_2SO_4. The reaction mixture was washed with 3x 40 ml DCM, the DCM was back extracted with H_2SO_4. The combined aqueous layers were basified again (10M N

1,1,3,3-Tetramethylisoindoline-5-carboxylic acid (5.4)

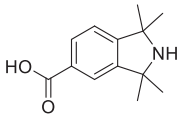

In a 500 ml Schlenk flask, 4.64 g 5-Bromo-1,1,3,3-tetramethylisoindoline (**5.3**) (18.3 mmol, 1.00 equiv.) were dissolved in 90 ml abs. THF and the solution was cooled to -78 °C. 17.6 ml n-butyllithium (2.5M in hexanes, 2.81 g, 42.9 mmol, 2.40 equiv.) were added over 30 min and the solution was stirred for another 15 min, before a mixture of dry ice in 250 ml abs. THF was added and the mixture was allowed to warm to room temperature. The solvent was removed under reduced pressure and the residue was solved in 150 ml 2M HCl. The aqueous layer was washed with 3x 60 ml diethyl ether, neutralized with $NaHCO_3$ and again washed with 3x 60 ml Et_2O. The solvent was removed via lyophilization.

^{1}H NMR (300 MHz, deuterium oxide), δ (ppm)= 7.93 (s, 1H, C*H*-Ar), 7.79 (s, 1H, C*H*-Ar), 7.43 (s, 1H, C*H*-Ar), 1.66 (s, 12H, CH_3).

1,1,3,3-Tetramethylisoindoline-2-yloxyl-5-carboxylic acid (5.5)

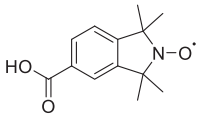

In a 1 l round bottom flask, 4.01 g 1,1,3,3-Tetramethylisoindoline-5-carboxylic acid (**5.4**) (18.3 mmol, 1.00 equiv.) were solved in mixture of H_2O/MeOH (95 ml/8.5 ml) and 1.44 g $NaHCO_3$ (17.2 mmol, 0.94 equiv.), 785 mg sodium tungstate dihydrate (2.38 mmol, 0.13 equiv.), and 10.6 ml conc. H_2O_2 (35%, 123 mmol, 6.73 equiv.) were added. After stirring for 24 h, another 250 mg sodium tungstate dihydrate (1.06 mmol, 0.058 equiv.) and 5.40 ml H_2O_2 (35%, 61.5 mmol, 3.36 equiv.) were added. The reaction mixture was stirred for further 48 h, basified with 1M NAOH and washed with 3x 80 ml diethyl ether. The aqueous layer was acidified with 1M HCl and extracted with 3x 150 ml diethyl ether before the combined organic layers were washed with brine, dried over Na_2SO_4 and the solvent removed under reduced pressure. The remaining aqueous layer was neutralized with $NaHCO_3$ and again 907 mg sodium tungstate dihydrate (2.75 mmol, 0.15 equiv.), 9.85 ml H_2O_2 (35%, 113 mmol, 6.21 equiv.) and 8 ml MeOH were added. The mixture was purified as before and the whole procedure was repeated several times. 1.70 g of the desired product (7.26 mmol, 40%) could be obtained as a white solid.^{1}H NMR (300 MHz, DMSO-d_6), δ (ppm)= 11.57 (s, 1H, O*H*), 8.01 – 7.75 (m, 2H, C*H*-Ar), 7.47 (dd, *J* = 20.3, 7.5 Hz, 1H, C*H*-Ar), 1.68 (s, *J* = 7.2, 3.6 Hz, 6H), 1.42 (s, 6H, CH_3). – MS (EI): $C_{13}H_{16}NO_3$•, *m/z* calculated for [M^+]: 234.11, Found: 234.2.

Ethyl 1,1,3,3-tetramethylisoindoline-5-carboxylate (5.6)

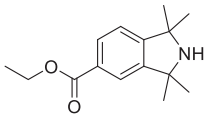

I n a 100 ml round bottom flask, 2.08 g 1,1,3,3-tetramethylisoindoline-5-carboxylic acid (**5.4**) (9.50 mmol, 1.00 equiv.) were solved in 55 ml EtOH and 3.54 ml conc. H_2SO_4 (98%, 66.5 mmol, 7.00 equiv.) were added. The mixture was heated to 70 °C and stirred for 72 h. Subsequently, the reaction mixture was allowed to cool to room temperature and neutralized by dropwise addition of $NaHCO_3$ solution. The aqueous layer was extracted with 3x 160 ml DCM and the combined organic layers were washed with brine before they were dried over Na_2SO_4 and the solvent was removed under reduced pressure. 0.731 g of the desired product (2.96 mmol, 31%) could be obtained as a white solid.

R_f= (CH/EE 2:1): 0.06. – ^{1}H NMR (300 MHz, chloroform-*d*), δ (ppm)= 7.95 (dt, *J* = 7.9, 1.2 Hz, 1H, C*H*-Ar), 7.83 – 7.75 (m, 1H, C*H*-Ar), 7.16 (d, *J* = 7.9 Hz, 1H, C*H*-Ar), 4.38 (qd, *J* = 7.1, 0.9 Hz, 2H, CH_2), 2.36 (s, 1H, N*H*), 1.48 (dd, *J* = 4.7, 0.9 Hz, 12H, CH_3), 1.39 (td, *J* = 7.1, 0.9 Hz, 3H, CH_3).– MS (EI): $C_{15}H_{21}NO_2$, *m/z* calculated for [M^+]: 247.16, Found: 247.1.

1,1,3,3-Tetramethylisoindoline-2-yloxyl-5-ethylcarboxylat (5.7)

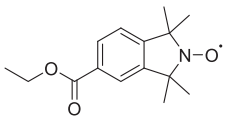

Route A:

In a 100 ml round bottom flask, 1.31 g 1,1,3,3-Tetramethylisoindoline-2-yloxyl-5-carboxylic acid (**5.5**) (5.60 mmol, 1.00 equiv.) were solved in 32 ml EtOH and 2.10 ml conc. H_2SO_4 (98%, 39.2 mmol, 7.00 equiv.) were added. The mixture was heated to 70 °C and stirred for 72 h. Subsequently, the reaction mixture was allowed to cool to room temperature and neutralized by dropwise addition of $NaHCO_3$ solution. The aqueous layer was extracted with 3x 80 ml DCM and the combined organic layers were washed with brine before they were dried over Na_2SO_4 and the solvent was removed under reduced pressure. 1.22 g of the desired product (4.66 mmol, 89%) could be obtained as a white solid.

Route B:

In a 50 ml round bottom flask, 533 mg ethyl 1,1,3,3-tetramethylisoindoline-5-carboxylate (**5.6**) (2.15 mmol, 1.00 equiv.) were solved in 25 ml DCM and the solution was cooled to 0 °C before 723 mg mCPBA (3.23 mmol, 1.50 equiv.) were added portion-wise. The solution was allowed to warm to room temperature and was stirred for 3.5 h. Subsequently, the reaction mixture was washed with 3x 10 ml $NaHCO_3$ solution and dried over Na_2SO_4. The solvent was removed under reduced pressure.

R_f= (CH/EE 2:1): 0.63. – MS (EI): $C_{15}H_{20}NO_3$•, *m/z* calculated for [M^+]: 262.14, Found: 262.1.

2-Yloxyl-1,1,3,3-tetramethylisoindoline-5-carbohydrazide (5.8)

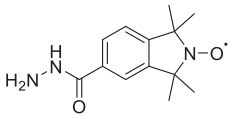

In a 100 ml round bottom flask equipped with a cooler, 100 mg 1,1,3,3-tetramethylisoindoline-2-yloxyl-5-ethylcarboxylat (**5.7**) (381 mmol, 1.00 equiv.) were solved in a 1:1 mixture (v/v) hydrazine monohydrate and isopropanol (6.00 ml each, excess). The reaction mixture was heated to 95 °C and refluxed for 2 h. After the mixture was cooled to room temperature, 50 ml diethyl ether were added and precipitation of the product was allowed to proceed overnight at 4 °C. After filtration, 49.0 mg of the desired product (197 mmol, 52%) could be obtained as white needles.

^{1}H NMR (300 MHz, DMSO-d_6), δ (ppm)= 9.69 (s, 1H, N*H*), 7.66 (dd, *J* = 12.5, 6.1 Hz, 2H, C*H*-Ar), 7.26 (d, *J* = 7.9 Hz, 1H, C*H*-Ar), 4.46 (s, 2H, NH_2), 1.30 (s, 12H, CH_3).– MS (ESI): $C_{13}H_{20}N_3O_2$+, *m/z* calculated for [(M+2H)$^+$]: 250.16, Found: 250.155.

Doxorubicin-2-Yloxyl-1,1,3,3-tetramethylisoindoline-5-carbohydrazide (5.9)

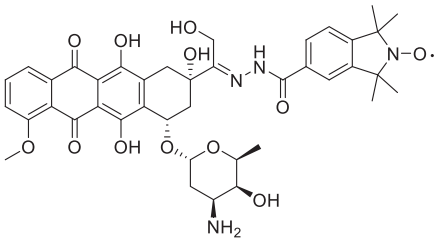

In a 20 ml scintillation vial, 10.0 mg 2-Yloxyl-1,1,3,3-tetramethylisoindoline-5-carbohydrazide (**5.8**) (0.0400 mmol, 1.00 equiv.) and 23.3 mg doxorubicin HCl (0.0400 mmol, 1.00 equiv.) were solved in 10 ml abs. MeOH before heated to 80 °C and stirred for 17 h. The reaction was followed via analytical HPLC.

MS (MALDI-TOF): $C_{13}H_{20}N_3O_2$+, *m/z* calculated for [(M+H+Na)$^+$]: 797.30, Found: 797.311.

6.2 Biological Methods

6.2.1 Biochemical and in vitro *studies of the BODIPY HaloSNAP system*

6.2.1.1 *HaloSNAP protein expression*

E. coli bacteria of the strain BL21(DE3) expressing HaloSNAP fusion protein were streaked out on a LB with ampicillin plate from a frozen glycerol stock and incubated at 37 °C overnight. Afterwards, one colony was picked into 5 ml starter culture of LB with ampicillin and again incubated at 37°C overnight. The starter culture was then expanded in 100 ml LB with ampicillin and grown at 37 °C until an optical density of 0.3 was reached at 600 nm measurement (OD_{600}). After decreasing the temperature to 15 °C, the protein expression was induced by adding 0.5 mM IPTG and bacteria were grown at 15 °C overnight.

6.2.1.2 HaloSNAP protein isolation and labeling with Halo-BODIPY ligand

After expression of the HaloSNAP protein (according to chapter 6.2.1.1), bacteria were pelleted and the supernatant was discarded. The pellet was resuspended in 1 ml bacterial protein extraction reagent (B-PER, ThermoFisher) supplemented with ethylenediaminetetraacetic acid (EDTA)-free protease inhibitor tablet (Roche) and nuclease (Benzonase®, Sigma-Aldrich) (1 tablet + 1 µl nuclease per 10 ml B-PER), and the lysate was incubated at room temperature for 10-15 min. 1 ml of dH_2O were added to a total volume of 2 ml, gently mixed and aliquoted across 2 microfuge tubes. After centrifugation at ≥10,000 x g for 30 min at 4 °C, the supernatant (total soluble protein) was collected. 20 µl of the protein solution were incubated with either 0.1 mM Halo-BODIPY ligand or Halo-TAMRA ligand for 15 min at room temperature. For the competition assay, 20 µl of the protein solution were incubated with 0.1 mM of Halo H3 ac peptide for 1h at room temperature before incubating with either 0.1 mM Halo-BODIPY ligand or Halo-TAMRA ligand for 15 min at room temperature.

6.2.1.3 SDS-PAGE of HaloSNAP protein labeling with Halo-BODIPY ligand

After protein expression, isolation, and labeling following the procedures in chapter 6.2.1.1 and 6.2.1.2, samples for the SDS-PAGE were prepared by adding 7 µl of loading buffer (Invitrogen™ Novex™ NuPAGE™ LDS Sample Buffer (4X)) and 3 µl of reducing agent (Invitrogen™ Novex™ NuPAGE™ Sample Reducing Agent (10X)) to each 20 µl of labeled protein sample and incubated at 90 °C for approximately 5 min. 10-30 µl of each sample were loaded on a polyacrylamide gel and ran for about 1 h at 160 V. After rinsing with dH_2O, fluorescence signal was detected using a Typhoon Phosphorimager (Cy2 and Cy3 settings, 400 PMT). For further staining, after rinsing with dH_2O, 25 ml of SimplyBlue™ Coomassie stain (ThermoFisher) were added and staining was allowed to develop for 30-60 min while gently shaking.

6.2.1.4 In vitro HaloSNAP labeling and fluorescence imaging

After expression and induction of the HaloSNAP protein in bacteria (procedure according to chapter 6.2.1.1), 100 µl/well bacteria were added in a 96-well transparent bottom plate, also including control samples that were not treated with IPTG to induce protein expression. Samples were incubated overnight with 10 µM and 100 µM Halo-BODIPY ligand at room temperature with constant shaking. A washing step was performed, centrifuging the plate for 1 min at 4000 x g, replacing media and shaking for 1 h at room temperature, centrifuging and replacing media again. The visualization

was performed using a Zeiss Axiovert 100M inverted epifluorescence microscope with a 40x objective.

6.2.2 Used cell lines/ primary cells

- HeLa cells (human cervix carcinoma)
- HeLa GFP cells (GFP expressing human cervix carcinoma cell)
- HepG2 cells (human hepatocellular carcinoma)
- SK-Mel 28 cells (human malignant melanoma)
- NHEM (normal human epidermal melanocytes)
- NHDF (normal human dermal fibroblasts)
- NHEK (normal human epidermal keratinocytes)

6.2.3 Cell culture

Human cervix carcinoma cells (HeLa cells), GFP-expressing human cervix carcinoma cells (HeLa GFP cells) and human melanoma cells (SK-Mel 28) were cultured in 75 cm^2 cell culture flasks using Dulbecco's modified Eagle medium (DMEM), supplemented with 10% fetal calf serum and 1% penicillin/streptomycin, at 37 °C in a 5% CO_2 atmosphere. Normal human epidermal melanocytes (NHEM) were cultured in MGM-4 (melanocytes growth medium, + endothelin-3), normal human dermal fibroblasts (NHDF) in FGM-2 (fibroblasts growth medium) and normal human epidermal keratinocytes (NHEK) in KGM-Gold (keratinocytes growth medium).

Subculturing was performed at 90% confluency by washing with Dulbeccos's Phosphate Buffered Saline (PBS) and treatment with 1 ml 0.25% Trypsin-EDTA. After 1-3 min the trypsinization was stopped by the addition of 2 ml of the respective medium. Cells were counted in a Neubauer chamber and, after resuspending the cells in the respective amount of fresh medium, they were transferred into a new cell culture vessel.

6.2.4 In vitro *studies of the DNA-/RNA-constructs and dyes*

6.2.4.1 Transfection DNA

24 h before transfection, 4 × 10^4 HeLa cells per well were seeded in an 8-well chamber slide (µ Slide 8 well ibiTreat, IBIDI, Martinsried, Germany) in 200 µL of media. For the transfection of DNA oligonucleotides into HeLa cells, a 2-step method using previously-seeded cells was performed. 15 pmol of the respective oligonucleotides were diluted

in ScreenFect®A Dilution Buffer (ScreenFect, Eggenstein-Leopoldshafen, Germany) to a final volume of 9 µl. 12 µl of a 1:10 dilution of ScreenFect®A in Dilution Buffer were added to the diluted DNA/siRNA and rapidly mixed. A subsequent incubation time of 20 min at room temperature allowed for the formation of lipoplexes (liposome-DNA complexes). The transfection mixture was then added to the previously-seeded and attached cells in each well of the 8-well chamber slide. The cells were incubated for 24 h with the respective transfection mixture at 37 °C in a 5% CO_2 atmosphere.

6.2.4.2 Transfection RNA

48 h before transfection, 4 × 10^4 HeLa GFP cells/HeLa GFP cells per well were seeded in an 8-well chamber slide (µ Slide 8 well ibiTreat, IBIDI, Martinsried, Germany) in 200 µL of media. For the transfection of DNA and siRNA oligonucleotides into HeLa cells, a 2-step method using previously-seeded cells was performed. 15 pmol of the respective oligonucleotides were diluted in ScreenFect®A Dilution Buffer (ScreenFect, Eggenstein-Leopoldshafen, Germany) to a final volume of 9 µl. 12 µl of a 1:10 dilution of ScreenFect®A in Dilution Buffer were added to the diluted DNA/siRNA and rapidly mixed. A subsequent incubation time of 20 min at room temperature allowed for the formation of lipoplexes (liposome-DNA complexes). The transfection mixture was then added to the previously-seeded and attached cells in each well of the 8-well chamber slide. The cells were incubated for 24 h with the respective transfection mixture at 37 °C in a 5% CO_2 atmosphere.

6.2.4.3 CLSM imaging of DNA

The visualization was performed using a Leica TCS-SPE (DMi8) inverted microscope with an ACS APO 63x/1.30 oil objective. Fluorophores were excited using an UV laser (λ_{exc}= 405 nm) for duplexes DNA**3.4**dye**3.5**(donor)- DNA**3.9**dye**3.11**(acceptor) and DNA**3.3**dye**3.5**(donor)- DNA**3.10**dye**3.14**(acceptor) and an argon ion laser (λ_{exc}= 488 nm) for duplexes DNA**3.4**dye**3.6**(donor)- DNA**3.10**dye**3.14**(acceptor) and DNA**3.3**dye**3.8**(donor)- DNA**3.10**dye**3.14**(acceptor). The emission detection bandwidths were at λ_{em}= 435-470 nm (blue) and λ_{em}= 575-750 nm (yellow) for DNA**3.4**dye**3.5**(donor)- DNA**3.9**dye**3.11**(acceptor), λ_{em}= 415-550 nm (blue) and λ_{em}= 575-750 nm (red) for DNA**3.3**dye**3.5**(donor)- DNA**3.10**dye**3.14**(acceptor), λ_{em}= 490-550 nm (green) and λ_{em}= 550-675 nm (red) for DNA**3.4**dye**3.6**(donor)-DNA**3.10**dye**3.14**(acceptor), λ_{em}= 490-550 nm (green) and λ_{em}= 675-800 nm (red) for DNA**3.3**dye**3.8**(donor)- DNA**3.10**dye**3.14**(acceptor). Using the acquisition software Leica Application Suite (LAS) X 2.0.1.14392, the picture ratio was adjusted to 1024 × 1024 pixels 8 bit depth.

6.2.4.4 CLSM imaging of siRNA

The visualization was performed using a Leica TCS-SPE (DMi8) inverted microscope with an ACS APO 63x/1.30 oil objective. Fluorophores were excited using an argon ion laser (λ_{exc}= 488 nm). The emission detection bandwidths were at λ_{em}= 490-515 nm (green) and λ_{em}= 675-800 nm (red). Using the acquisition software Leica Application Suite (LAS) X 2.0.1.14392, the picture ratio was adjusted to 1024 × 1024 pixels 8 bit depth.

6.2.4.5 GFP knockdown imaging

$7x10^4$ HeLa cells were seeded in an 8-well chamber slide 4 h prior to transfection. 15 pmol of siRNA duplexes were then transiently transfected into cells for 24 h, as described in chapter 6.2.4.2. The visualization was performed using a Leica TCS-SP8 inverted microscope with an HCPL APO CS2 40x/1.10 water objective. Fluorophores were excited using an argon ion laser (λ_{exc}= 488 nm). The emission detection bandwidths were at λ_{em}= 535-567 nm (GFP, green) and λ_{em}= 675-800 nm (siRNA, red). Using the acquisition software Leica Application Suite (LAS) X 1.1.0.12420, the picture ratio was adjusted to 1024 × 1024 pixels 8 bit depth.

6.2.4.6 Cytotoxicity assay dyes

To determine the toxic effect of the respective fluorophores (used in the DNA FRET pair constructs) in HeLa cells, the viability was tested using the CellTiter 96® Non-Radioactive Cell Proliferation Assay (Promega) according to the manufacturer's instructions. This assay is based on the intracellular reduction of a yellow tetrazolium salt (3-(4,5-dimethylthiazole-2-yl)-2,5-diphenyltetrazoliumbromide), MTT) into a violet formazan product by mitochondrial dehydrogenases, which only takes place in metabolically-active cells. Therefore the amount of the generated formazan which can be determined by absorbance measurements is directly linked to cell viability.

1×10^4 HeLa cells were seeded in each well of a 96 well plate (Costar 3596, 96 Well Cell Culture Cluster, sterile) and cultured in 100 µL Dulbecco's modified Eagle's medium (DMEM, Gibco) supplemented with 10% fetal calf serum (FCS, Sigma-Aldrich) and 1% penicillin/streptomycin at 37 °C, 5% CO_2. After 24 hours the cells were treated with different concentrations of the dyes (0.0375 µM - 0.30 µM). For each amount 4 wells were prepared and as a positive control (living cells) 6 wells were treated with respected DMSO concentrations to 0.30 µM dye samples. After an incubation time of 72 h, another 6 wells were treated with 5 µl of 20% Triton X-100 (Serva) for 5 min as a negative control for 100% dead cells , before all cells were treated with 15 µl of MTT reagent (Dye Solution according to manufacturer's instructions) per well and incubated

for 2.5 h. Subsequently, 100 µL Solubilization Solution/Stop Mix was added to each well to lyse cells and dissolve the formed formazan crystals. After 24 h incubation at 37°C the absorbance was measured at 595 nm using a 96-well plate reader (Ultra Microplate Reader ELx808, BioTEK Instruments, INC). Mean values and standard deviation were calculated from n=4 experiments.

6.2.4.7 Cytotoxicity assay siRNA

To determine the toxic effect of the respective siRNA strands in HeLa cells, the viability was tested using the CellTiter 96® Non-Radioactive Cell Proliferation Assay (Promega) according to the manufacturer's instructions.

1×10^4 HeLa cells were seeded in each well of a 96-well plate (Costar 3596, 96 Well Cell Culture Cluster, sterile) and cultured in 100 µL Dulbecco's modified Eagle's medium (DMEM, Gibco) supplemented with 10% fetal calf serum (FCS, Sigma-Aldrich) and 1% penicillin/streptomycin at 37 °C, 5% CO_2. After 24 hours the cells were treated with different concentrations of the siRNAs (0.0375 µM - 0.15 µM) and respective concentrations of ScreenFect®A (ScreenFect, Eggenstein-Leopoldshafen, Germany) used in the prior transfections (0.1 µl/pmol siRNA). For each amount 6 wells were prepared, and as a positive control (living cells) 6 wells were treated with respective ScreenFect®A concentrations to 0.15 µM siRNA samples. After an incubation time of 72 h, another 6 wells were treated with 5 µl of 20% Triton X-100 (Serva) as a negative control for 100% dead cells for 5 min, before all cells were treated with 15 µl of MTT reagent (Dye Solution according to manufacturer's instructions) per well and incubated for 2.5 h. Subsequently, 100 µL Solubilization Solution/Stop Mix was added to each well to lyse cells and dissolve the formed formazan crystals. After 24 h incubation at 37°C the absorbance was measured at 595 nm using a 96-well plate reader (Ultra Microplate Reader ELx808, BioTEK Instruments, INC). Mean values and standard deviation were calculated from n=6 experiments.

6.2.5 Cellular uptake studies of melanocyte-specific compounds

6.2.5.1 CLSM imaging 2-dimensional cell screening melanoma

$4x10^4$ of the respective cell line/primary cells were seeded in an 8-well chamber slide (µ-slide 8 well, ibidi®) 2 d prior to treatment with 20 µM of the fluorescent compound for 5 h. Cells were washed three times with PBS before staining the nuclei with Hoechst 33342 (Invitrogen, 0.5 µg/ml for 20 min). The visualization was performed using a Leica TCS-SP-5 (DMI6000) inverted microscope with an HCX PL APO 63x/1.20 water UV objective, or a Leica TCS-SPE (DMI8) inverted microscope with an ACS APO 63x/1.30 oil objective. Fluorophores were excited using an UV laser (λ_{exc}= 351 and 364 nm for TCS-SP-5 and λ_{exc}= 405 nm for TCS-SPE) for the Hoechst 33342 staining

and an argon ion laser (λ_{exc}= 488 nm and 532 nm) for the fluorescent compound. The images were taken in a sequential mode to avoid an overlap of emission spectra from Hoechst 33342 and fluorescein. Using the acquisition software Leica Application Suite (LAS) AF 2.2.2.4842 for the TCS-SP-5 and (LAS) X 2.0.1.14392 for the TCS-SPE, the picture ratio was adjusted to 1024 × 1024 pixels 8 bit depth.

6.2.5.2 Preparation of 3-dimensional melanoma/ liver carcinoma spheroids

$4x10^3$ of SK-Mel 28 or HepG2 cells were seeded in 40 µl DMEM in wells of a 1.5% agarose-coated 96-well plate (flat bottom) and cultivated for up to 14 days at 37 °C and 5% CO_2 atmosphere with adding of 10-15 µl fresh medium every 2-3 days. The spheroids were harvested by aspiration of the whole medium including the spheroid and transferring into µ-slide wells or an Eppendorf tube.

6.2.5.3 CLSM imaging 3-dimensional melanoma spheroids

$4x10^3$ of SK-Mel 28 were seeded in agarose wells 5 d prior to treatment with 50 µM, 15 µM, 1 µM **4.1**, and 1 µM **4.2** for 72 h at 37 °C. Cells were washed with PBS. The visualization was performed using a Leica TCS-SPE (DMI8) inverted microscope with an ACS APO 63x/1.30 oil objective. The fluorophore was excited using an argon ion laser (λ_{exc}= 488 nm. Using the acquisition software Leica Application Suite (LAS) X 2.0.1.14392, the picture ratio was adjusted to 1024 × 1024 pixels 8 bit depth.

6.2.5.4 Preparation of the full skin-melanoma models

The GelMA was prepared by adding 10 g gelatin to 100 ml PBS at 50 °C and, after complete solubilization, dropwise addition of 5 ml methacryl anhydride. After 2 h stirring at 50 °C, the mixture was transferred into 12 kD dialysis tubes and dialyzed for 5-7 days with dH_2O until the methacryl anhydride small disappeared before portion-wise lyophilization.

The GelMa fibroblast hydrogel was prepared as a 5% GelMA and 0.3% LAP photoinitiator solution in EGM-2 medium with $5x10^5$ NHDF and 3 SK-Mel-28 or HepG2 spheroids per transwell filter insert. The cell suspensions were exposed to an UV/blue light source (OSRAM ultra Vitralux 300W E27; 280-315 nm, 3W; 314-400 nm, 13.6W) for 45-60 s to initiate polymerization. 200 µl EGM-2 medium were added on top of the hydrogel and 500 µl into the lower compartment of the transwell filter system. The dermis models were cultured for 7 days at 37 °C and 5% CO_2 atmosphere with a

medium change every 2-3 days. $7x10^5$ NHEK (and $2x10^5$ NHEM) were seeded on top of the dermis in a 0.6 mg/ml collagen I solution and cultured for 3 days at 37 °C and 5% CO_2 atmosphere. The EGM-2 medium was supplemented with 2 mM $CaCl_2$ for 4 days further to induce epidermis differentiation before the medium on top of the epidermis was removed to cultivate the model at the air-liquid interface for the next 14 days and achieve terminal differentiation.

6.2.5.5 Treatment and CLSM imaging of the full skin-melanoma models

The full skin-melanoma models were prepared according to chapter 6.2.5.4 before being treated with 50 µM lead structure **4.1** in KGM-2 medium for 24 h (added on top of the epidermis) at 37 °C and 5% CO_2 atmosphere. Models were washed with PBS and fixated with 1 ml 4% PFA for 1 h. The skin-melanoma models were removed cautiously from the transwell filter inserts using a cannula and transferred to 8-well chamber slides (µ-slide 8 well, ibidi®). The visualization was performed using a Leica TCS-SPE (DMI8) inverted microscope with an ACS APO 63x/1.30 oil objective. The fluorophore was excited using an argon ion laser (λ_{exc}= 488 nm). Using the acquisition software Leica Application Suite (LAS) X 2.0.1.14392, the picture ratio was adjusted to 1024 × 1024 pixels 8 bit depth.

6.2.6 In vitro *studies of the polymeric nanocarrier platform*

6.2.6.1 Cytotoxicity assay polymer precursor and control nitroxide

To determine the toxic effect of the respective polymer precursor and control nitroxide in HeLa cells, the viability was tested using the CellTiter 96® Non-Radioactive Cell Proliferation Assay (Promega) according to the manufacturer's instructions.

1×10^4 HeLa cells were seeded in each well of a 96-well plate (Costar 3596, 96 Well Cell Culture Cluster, sterile) and cultured in 100 µL Dulbecco's modified Eagle's medium (DMEM, Gibco) supplemented with 10% fetal calf serum (FCS, Sigma-Aldrich) and 1% penicillin/streptomycin at 37 °C, 5% CO_2. After 24 hours the cells were treated with different concentrations of the precursor/control nitroxide (100 µM – 2.5 mM). For each amount 6 wells were prepared and as a positive control (living cells), 6 wells were treated with respected DMSO concentrations to 2.5 mM dye samples. After an incubation time of 72 h, another 6 wells were treated with 5 µl of 20% Triton X-100 (Serva) for 5 min as a negative control for 100% dead cells, before all cells were treated with 15 µl of MTT reagent (Dye Solution according to manufacturer's instructions) per well and incubated for 2.5 h. Subsequently, 100 µL Solubilization Solution/Stop Mix was added to each well to lyse cells and dissolve the formed formazan crystals. After 24 h incubation at 37°C the absorbance was measured at 595 nm using a 96-well plate reader (Ultra Microplate Reader ELx808, BioTEK Instruments, INC). Mean values and standard deviation were calculated from n=6 experiments.

6.2.6.2 Cytotoxicity assay polymer platform and DOX

To determine the toxic effect of the polymer-DOX-platform, the polymer before DOX coupling, and free DOX in HeLa cells, the viability was tested using the CellTiter 96® Non-Radioactive Cell Proliferation Assay (Promega) according to the manufacturer's instructions.

1×10^4 HeLa cells were seeded in each well of a 96-well plate (Costar 3596, 96 Well Cell Culture Cluster, sterile) and cultured in 100 µL Dulbecco's modified Eagle's medium (DMEM, Gibco) supplemented with 10% fetal calf serum (FCS, Sigma-Aldrich) and 1% penicillin/streptomycin at 37 °C, 5% CO_2. After 24 hours the cells were treated with different concentrations of the polymer/DOX (1 µg/ml – 1 mg/ml for the polymers, 0.01 µM – 10 µM for DOX) while keeping a DMSO concentration of 1% in each well. For each concentration 3 wells were prepared and as a positive control (living cells), 6 wells were treated with 1% DMSO. After an incubation time of 72 h, the medium in all wells was changed cautiously and another 6 wells were treated with 5 µl of 20% Triton X-100 (Serva) for 5 min as a negative control for 100% dead cells, before all cells were treated with 15 µl of MTT reagent (Dye Solution according to manufacturer's instructions) per well and incubated for 2.5 h. Subsequently, 100 µL Solubilization Solution/Stop Mix was added to each well to lyse cells and dissolve the formed formazan crystals. After 24 h incubation at 37°C the absorbance was measured at 595 nm using a 96-well plate reader (Ultra Microplate Reader ELx808, BioTEK Instruments, INC). Mean values and standard deviation were calculated from n=3 experiments.

6.2.6.3 CLSM imaging polymeric DOX nanocarrier platform

$4x10^4$ of HeLa cells were seeded in an 8-well chamber slide (µ-slide 8 well, ibidi®) 24 h prior to treatment with different concentrations of polymer **5.18** and DOX **5.17**. The visualization was performed using a Zeiss LSM 800 inverted microscope with a plan-neofluar 10x/0.30 objective. DOX was excited using an argon ion laser (λ_{exc}= 488 nm). The picture ratio was adjusted to 1024 × 1024 pixels 8 bit depth.

References

1 Song, C. M., Lim, S. J. & Tong, J. C. Recent advances in computer-aided drug design. *Briefings in bioinformatics* **10**, 579-591 (2009).

2 Macalino, S. J. Y., Gosu, V., Hong, S. & Choi, S. Role of computer-aided drug design in modern drug discovery. *Archives of pharmacal research* **38**, 1686-1701 (2015).

3 Anderson, A. C. The process of structure-based drug design. *Chemistry & biology* **10**, 787-797 (2003).

4 Jamdade, V. S. *et al.* Therapeutic targets of triple-negative breast cancer: a review. *British journal of pharmacology* **172**, 4228-4237 (2015).

5 Johnson, I. M. RNA as a Drug Target: Recent Patents on the Catalytic Activity of Trans-Splicing Ribozymes Derived from Group I Intron RNA. *Recent patents on DNA & gene sequences* **4**, 17-28 (2010).

6 Li, Z. & Rana, T. M. Therapeutic targeting of microRNAs: current status and future challenges. *Nature reviews Drug discovery* **13**, 622-638 (2014).

7 Nakamura, H. & Minegishi, H. HSP60 as a drug target. *Current pharmaceutical design* **19**, 441-451 (2013).

8 Andrews, S. P., Brown, G. A. & Christopher, J. A. Structure-Based and Fragment-Based GPCR Drug Discovery. *ChemMedChem* **9**, 256-275 (2014).

9 Guo, D., Hillger, J. M., IJzerman, A. P. & Heitman, L. H. Drug-Target Residence Time—A Case for G Protein-Coupled Receptors. *Medicinal research reviews* **34**, 856-892 (2014).

10 Kumari, P., Ghosh, E. & Shukla, A. K. Emerging approaches to GPCR ligand screening for drug discovery. *Trends in molecular medicine* **21**, 687-701 (2015).

11 Blagg, J. & Workman, P. Chemical biology approaches to target validation in cancer. *Current opinion in pharmacology* **17**, 87-100 (2014).

12 Frigault, M. M. & Barrett, J. C. Is target validation all we need? *Current opinion in pharmacology* **17**, 81-86 (2014).

13 Sim, D. S. & Kauser, K. in *New Approaches to Drug Discovery* 59-70 (Springer, 2015).

14 Chi, C.-W., Ahmed, A. R., Dereli-Korkut, Z. & Wang, S. Microfluidic cell chips for high-throughput drug screening. (2016).

15 Prével, C., Pellerano, M., Van, T. N. N. & Morris, M. C. Fluorescent biosensors for high throughput screening of protein kinase inhibitors. *Biotechnology journal* **9**, 253-265 (2014).

16 Li, L., Zhou, Q., Voss, T. C., Quick, K. L. & LaBarbera, D. V. High-throughput imaging: Focusing in on drug discovery in 3D. *Methods* **96**, 97-102 (2016).

17 Pepperkok, R. & Ellenberg, J. High-throughput fluorescence microscopy for systems biology. *Nature reviews Molecular cell biology* **7**, 690-696 (2006).

18 Chan, A. I., McGregor, L. M. & Liu, D. R. Novel selection methods for DNA-encoded chemical libraries. *Current opinion in chemical biology* **26**, 55-61 (2015).

19 Kleiner, R. E., Dumelin, C. E. & Liu, D. R. Small-molecule discovery from DNA-encoded chemical libraries. *Chem Soc Rev* **40**, 5707-5717 (2011).

20 Scheuermann, J. & Neri, D. Dual-pharmacophore DNA-encoded chemical libraries. *Current opinion in chemical biology* **26**, 99-103 (2015).

21 Lipinski, C. A. Lead-and drug-like compounds: the rule-of-five revolution. *Drug Discovery Today: Technologies* **1**, 337-341 (2004).

22 Lipinski, C. A., Lombardo, F., Dominy, B. W. & Feeney, P. J. Experimental and computational approaches to estimate solubility and permeability in drug discovery and development settings1. *Advanced drug delivery reviews* **46**, 3-26 (2001).

23 Alonso, H., Bliznyuk, A. A. & Gready, J. E. Combining docking and molecular dynamic simulations in drug design. *Medicinal research reviews* **26**, 531-568 (2006).

24 Shoichet, B. K., McGovern, S. L., Wei, B. & Irwin, J. J. Lead discovery using molecular docking. *Current opinion in chemical biology* **6**, 439-446 (2002).

25 Cavagnaro, J. A. Preclinical safety evaluation of biotechnology-derived pharmaceuticals. *Nature Reviews Drug Discovery* **1**, 469-475 (2002).

26 Silverman, R. B. & Holladay, M. W. *The organic chemistry of drug design and drug action*. (Academic press, 2014).

27 Tibbitt, M. W., Dahlman, J. E. & Langer, R. Emerging frontiers in drug delivery. *Journal of the American Chemical Society* **138**, 704-717 (2016).

28 Huang, Y., Ng, H. C. A., Ng, X. W. & Subbu, V. Drug-eluting biostable and erodible stents. *Journal of Controlled Release* **193**, 188-201 (2014).

29 Liu, J. *et al.* pH-sensitive nano-systems for drug delivery in cancer therapy. *Biotechnology advances* **32**, 693-710 (2014).

30 Mottaghitalab, F., Farokhi, M., Shokrgozar, M. A., Atyabi, F. & Hosseinkhani, H. Silk fibroin nanoparticle as a novel drug delivery system. *Journal of Controlled Release* **206**, 161-176 (2015).

31 Nakase, I. *et al.* Efficient intracellular delivery of nucleic acid pharmaceuticals using cell-penetrating peptides. *Accounts Chem Res* **45**, 1132-1139 (2011).

32 Svensen, N., Walton, J. G. & Bradley, M. Peptides for cell-selective drug delivery. *Trends in pharmacological sciences* **33**, 186-192 (2012).

33 Mussbach, F., Franke, M., Zoch, A., Schaefer, B. & Reissmann, S. Transduction of peptides and proteins into live cells by cell penetrating peptides. *Journal of cellular biochemistry* **112**, 3824-3833 (2011).

34 Yi Xue, H., Guo, P., Wen, W.-C. & Lun Wong, H. Lipid-based nanocarriers for RNA delivery. *Current pharmaceutical design* **21**, 3140-3147 (2015).

35 Koelmel, D. K. *et al.* Cell-penetrating peptoids: Introduction of novel cationic side chains. *European journal of medicinal chemistry* **79**, 231-243 (2014).

36 Althuon, D. *et al.* Functionalized triazolopeptoids–a novel class for mitochondrial targeted delivery. *Organic & biomolecular chemistry* **13**, 4226-4230 (2015).

37 Vollrath, S. B., Fürniss, D., Schepers, U. & Bräse, S. Amphiphilic peptoid transporters–synthesis and evaluation. *Organic & biomolecular chemistry* **11**, 8197-8201 (2013).

38 Kobayashi, H., Turkbey, B., Watanabe, R. & Choyke, P. L. Cancer drug delivery: considerations in the rational design of nanosized bioconjugates. *Bioconjugate Chem* **25**, 2093-2100 (2014).

39 Nichols, J. W. & Bae, Y. H. EPR: evidence and fallacy. *Journal of Controlled Release* **190**, 451-464 (2014).

40 Maeda, H., Nakamura, H. & Fang, J. The EPR effect for macromolecular drug delivery to solid tumors: Improvement of tumor uptake, lowering of systemic toxicity, and distinct tumor imaging in vivo. *Advanced drug delivery reviews* **65**, 71-79 (2013).

41 Noble, G. T., Stefanick, J. F., Ashley, J. D., Kiziltepe, T. & Bilgicer, B. Ligand-targeted liposome design: challenges and fundamental considerations. *Trends in biotechnology* **32**, 32-45 (2014).

42 Sanderson, M. J., Smith, I., Parker, I. & Bootman, M. D. Fluorescence microscopy. *Cold Spring Harbor Protocols* **2014**, pdb. top071795 (2014).

43 Wilson, T. Spinning-disk microscopy systems. *Cold Spring Harbor Protocols* **2010**, pdb. top88 (2010).

44 Ettinger, A. & Wittmann, T. Fluorescence live cell imaging. *Methods in cell biology* **123**, 77 (2014).

45 Stehbens, S., Pemble, H., Murrow, L. & Wittmann, T. Imaging intracellular protein dynamics by spinning disk confocal microscopy. *Methods in enzymology* **504**, 293 (2012).

46 De Los Santos, C., Chang, C. W., Mycek, M. A. & Cardullo, R. A. FRAP, FLIM, and FRET: detection and analysis of cellular dynamics on a molecular scale using fluorescence microscopy. *Molecular reproduction and development* **82**, 587-604 (2015).

47 Renz, M. Fluorescence microscopy—A historical and technical perspective. *Cytometry Part A* **83**, 767-779 (2013).

48 Henriques, R. & Mhlanga, M. M. PALM and STORM: What hides beyond the Rayleigh limit? *Biotechnology journal* **4**, 846-857 (2009).

49 Lakadamyali, M. Super-Resolution Microscopy: Going Live and Going Fast. *ChemPhysChem* **15**, 630-636, doi:10.1002/cphc.201300720 (2014).

50 Gustafsson, M. G. L. Surpassing the lateral resolution limit by a factor of two using structured illumination microscopy. *Journal of Microscopy* **198**, 82-87, doi:10.1046/j.1365-2818.2000.00710.x (2000).

51 Hirano, Y., Matsuda, A. & Hiraoka, Y. Recent advancements in structured-illumination microscopy toward live-cell imaging. *Microscopy* **64**, 237-249 (2015).

52 Hell, S. W. & Wichmann, J. Breaking the diffraction resolution limit by stimulated emission: stimulated-emission-depletion fluorescence microscopy. *Opt. Lett.* **19**, 780-782, doi:10.1364/OL.19.000780 (1994).

53 Chéreau, R., Tønnesen, J. & Nägerl, U. V. STED microscopy for nanoscale imaging in living brain slices. *Methods* **88**, 57-66 (2015).

54 Blom, H. & Widengren, J. STED microscopy—towards broadened use and scope of applications. *Current opinion in chemical biology* **20**, 127-133 (2014).

55 Kamiyama, D. & Huang, B. Development in the STORM. *Developmental cell* **23**, 1103-1110 (2012).

56 Poulter, N. S., Pitkeathly, W. T., Smith, P. J. & Rappoport, J. Z. The physical basis of total internal reflection fluorescence (TIRF) microscopy and its cellular applications. *Advanced Fluorescence Microscopy: Methods and Protocols*, 1-23 (2015).

57 Almada, P., Culley, S. & Henriques, R. PALM and STORM: Into large fields and high-throughput microscopy with sCMOS detectors. *Methods* **88**, 109-121 (2015).

58 Tam, J. & Merino, D. Stochastic optical reconstruction microscopy (STORM) in comparison with stimulated emission depletion (STED) and other imaging methods. *Journal of Neurochemistry* **135**, 643-658, doi:10.1111/jnc.13257 (2015).

59 Helmchen, F. & Denk, W. Deep tissue two-photon microscopy. *Nature methods* **2**, 932-940 (2005).

60 Perry, S. W., Burke, R. M. & Brown, E. B. Two-photon and second harmonic microscopy in clinical and translational cancer research. *Annals of biomedical engineering* **40**, 277-291 (2012).

61 Li, W., Goldstein, D. R. & Kreisel, D. Intravital 2-photon imaging, leukocyte trafficking, and the beating heart. *Trends in cardiovascular medicine* **23**, 287-293 (2013).

62 Molitoris, B. A. Using 2-photon microscopy to understand albuminuria. *Transactions of the American Clinical and Climatological Association* **125**, 343 (2014).

63 Thorling, C. A. *et al.* Multiphoton microscopy in defining liver function. *Journal of biomedical optics* **19**, 090901-090901 (2014).

64 WANG, B. G., König, K. & HALBHUBER, K. J. Two-photon microscopy of deep intravital tissues and its merits in clinical research. *Journal of microscopy* **238**, 1-20 (2010).

65 Herschel, J. F. W. 'Αμορφωτα No. I. On a Case of Superficial Colour Presented by a Homogeneous Liquid Internally Colourless. *Philosophical Transactions of the Royal Society of London*, 143-145 (1845).

66 Jabłoński, A. Über den Mechanismus der Photolumineszenz von Farbstoffphosphoren. *Zeitschrift für Physik* **94**, 38-46, doi:10.1007/bf01330795 (1935).

67 Lakowicz, J. R. & Masters, B. R. Principles of fluorescence spectroscopy. *Journal of Biomedical Optics* **13**, 029901 (2008).

68 Kanaoka, Y. Organic fluorescence reagents in the study of enzymes and proteins. *Angewandte Chemie International Edition* **16**, 137-147 (1977).

69 Dobretsov, G., Syrejschikova, T. & Smolina, N. On mechanisms of fluorescence quenching by water. *Biophysics* **59**, 183-188 (2014).

70 Doose, S., Neuweiler, H. & Sauer, M. Fluorescence quenching by photoinduced electron transfer: a reporter for conformational dynamics of macromolecules. *ChemPhysChem* **10**, 1389-1398 (2009).

71 Abraham, B. G. *et al.* Fluorescent protein based FRET pairs with improved dynamic range for fluorescence lifetime measurements. *PloS one* **10**, e0134436 (2015).

72 Shrestha, D., Jenei, A., Nagy, P., Vereb, G. & Szöllősi, J. Understanding FRET as a research tool for cellular studies. *International journal of molecular sciences* **16**, 6718-6756 (2015).

73 Stokes, G. G. On the change of refrangibility of light. *Philosophical Transactions of the Royal Society of London* **142**, 463-562 (1852).

74 Ghisaidoobe, A. B. & Chung, S. J. Intrinsic tryptophan fluorescence in the detection and analysis of proteins: a focus on Förster resonance energy transfer techniques. *International journal of molecular sciences* **15**, 22518-22538 (2014).

75 Zhdanova, N. G. *et al.* Tyrosine fluorescence probing of the surfactant-induced conformational changes of albumin. *Photochemical & Photobiological Sciences* **14**, 897-908 (2015).

76 Neurauter, G. *et al.* Simultaneous measurement of phenylalanine and tyrosine by high performance liquid chromatography (HPLC) with fluorescence detection. *Clinical biochemistry* **46**, 1848-1851 (2013).

77 Hull, R. V., Conger, P. S. & Hoobler, R. J. Conformation of NADH studied by fluorescence excitation transfer spectroscopy. *Biophysical chemistry* **90**, 9-16 (2001).

78 Churchich, J. E. Fluorescence properties of pyridoxamine 5-phosphate. *Biochimica et Biophysica Acta (BBA)-Biophysics including Photosynthesis* **102**, 280-288 (1965).

79 Hühner, J., Ingles-Prieto, Á., Neusüß, C., Lämmerhofer, M. & Janovjak, H. Quantification of riboflavin, flavin mononucleotide, and flavin adenine dinucleotide in mammalian model cells by CE with LED-induced fluorescence detection. *Electrophoresis* **36**, 518-525 (2015).

80 Li, P., Liu, S., Wang, X., Liu, Z. & He, Y. Fluorescence quenching studies on the interaction of riboflavin with tryptophan and its analytical application. *Luminescence* **28**, 910-914 (2013).

81 Luo, Y. & Liu, Y. J. Bioluminophore and flavin mononucleotide fluorescence quenching of bacterial bioluminescence—a theoretical study. *Chemistry-A European Journal* **22**, 16243-16249 (2016).

82 Murchie, E. H. & Lawson, T. Chlorophyll fluorescence analysis: a guide to good practice and understanding some new applications. *Journal of experimental botany* **64**, 3983-3998 (2013).

83 Stirbet, A., Riznichenko, G. Y. & Rubin, A. Modeling chlorophyll a fluorescence transient: relation to photosynthesis. *Biochemistry (Moscow)* **79**, 291-323 (2014).

84 Hu, J. y., Era, M., Elsegood, M. R. & Yamato, T. Synthesis and Photophysical Properties of Pyrene-Based Light-Emitting Monomers: Highly Pure-Blue-Fluorescent, Cruciform-Shaped Architectures. *European Journal of Organic Chemistry* **2010**, 72-79 (2010).

85 Kocsis, L. S. *et al.* Cyclopenta[b]naphthalene cyanoacrylate dyes: Synthesis and evaluation as fluorescent molecular rotors. *Organic & biomolecular chemistry* **13**, 2965-2973, doi:10.1039/c4ob02563f (2015).

86 Moon, H. *et al.* A Dipolar Anthracene Dye: Synthesis, Optical Properties and Two-photon Tissue Imaging. *Chemistry – An Asian Journal* **11**, 2518-2523, doi:10.1002/asia.201600986 (2016).

87 Vanga, D. G., Santra, M., Keerthi, A. & Valiyaveettil, S. Synthesis and photophysical properties of pyrene-based green fluorescent dyes: butterfly-shaped architectures. *Organic & biomolecular chemistry* **12**, 7914-7918 (2014).

88 Lavis, L. D. & Raines, R. T. Bright building blocks for chemical biology. *Acs Chem Biol* **9**, 855-866 (2014).

89 Chazotte, B. Labeling nuclear DNA using DAPI. *Cold Spring Harbor Protocols* **2011**, pdb. prot5556 (2011).

90 Crowley, L. C., Marfell, B. J. & Waterhouse, N. J. Analyzing cell death by nuclear staining with Hoechst 33342. *Cold Spring Harbor Protocols* **2016**, pdb. prot087205 (2016).

91 Baeyer, A. Ueber eine neue Klasse von Farbstoffen. *European Journal of Inorganic Chemistry* **4**, 555-558 (1871).

92 Murube, J. Fluorescein: The Most Commonly Used Surfocular Vital Stain. *The ocular surface* **11**, 144-149 (2013).

93 Lavis, L. D. & Raines, R. T. Bright ideas for chemical biology. *Acs Chem Biol* **3**, 142-155 (2008).

94 Lavis, L. D., Chao, T.-Y. & Raines, R. T. Synthesis and utility of fluorogenic acetoxymethyl ethers. *Chemical science* **2**, 521-530 (2011).

95 Wysocki, L. M. *et al.* Facile and general synthesis of photoactivatable xanthene dyes. *Angewandte Chemie International Edition* **50**, 11206-11209 (2011).

96 Graber, M. L., DiLillo, D. C., Friedman, B. L. & Pastoriza-Munoz, E. Characteristics of fluoroprobes for measuring intracellular pH. *Analytical biochemistry* **156**, 202-212 (1986).

97 Martin, M. M. & Lindqvist, L. The pH dependence of fluorescein fluorescence. *Journal of Luminescence* **10**, 381-390 (1975).

98 Ceresole, M. Verfahren zur Darstellung von Farbstoffen aus der Gruppe des Meta-amidophenol-Phtaleïns. *DR patent* (1887).

99 Lavis, L. D., Chao, T.-Y. & Raines, R. T. Fluorogenic label for biomolecular imaging. *Acs Chem Biol* **1**, 252-260 (2006).

100 Kolmakov, K. *et al.* Red-emitting rhodamine dyes for fluorescence microscopy and nanoscopy. *Chemistry-A European Journal* **16**, 158-166 (2010).

101 Masuko, M., Ohuchi, S., Sode, K., Ohtani, H. & Shimadzu, A. Fluorescence resonance energy transfer from pyrene to perylene labels for nucleic acid hybridization assays under homogeneous solution conditions. *Nucleic Acids Research* **28**, e34-e34 (2000).

102 Wang, L. *et al.* Fluorescence resonance energy transfer between donor-acceptor pair on two oligonucleotides hybridized adjacently to DNA template. *Biopolymers* **72**, 401-412 (2003).

103 Gonçalves, M. S. T. Fluorescent labeling of biomolecules with organic probes. *Chemical reviews* **109**, 190-212 (2008).

104 Zhang, H., Wu, Q. & Berezin, M. Y. Fluorescence anisotropy (polarization): from drug screening to precision medicine. *Expert Opin Drug Discov* **10**, 1145-1161, doi:10.1517/17460441.2015.1075001 (2015).

105 Germain, R. N., Robey, E. A. & Cahalan, M. D. A decade of imaging cellular motility and interaction dynamics in the immune system. *Science* **336**, 1676-1681, doi:10.1126/science.1221063 (2012).

106 Vernall, A. J., Hill, S. J. & Kellam, B. The evolving small-molecule fluorescent-conjugate toolbox for Class A GPCRs. *Br J Pharmacol* **171**, 1073-1084, doi:10.1111/bph.12265 (2014).

107 Weijer, C. J. Visualizing signals moving in cells. *Science* **300**, 96-100, doi:10.1126/science.1082830 (2003).

108 Cunha, L., Szigeti, K., Mathe, D. & Metello, L. F. The role of molecular imaging in modern drug development. *Drug Discov Today* **19**, 936-948, doi:10.1016/j.drudis.2014.01.003 (2014).

109 Ignatius, M. S., Hayes, M. & Langenau, D. M. In Vivo Imaging of Cancer in Zebrafish. *Adv Exp Med Biol* **916**, 219-237, doi:10.1007/978-3-319-30654-4_10 (2016).

110 Weber, T. & Koster, R. Genetic tools for multicolor imaging in zebrafish larvae. *Methods* **62**, 279-291, doi:10.1016/j.ymeth.2013.07.028 (2013).

111 Dana, H. *et al.* Thy1-GCaMP6 transgenic mice for neuronal population imaging in vivo. *PLoS One* **9**, e108697, doi:10.1371/journal.pone.0108697 (2014).

112 Lin, X. *et al.* Simple and rapid determination of homozygous transgenic mice via in vivo fluorescence imaging. *Oncotarget* **6**, 39073-39087, doi:10.18632/oncotarget.5535 (2015).

113 Dubach, J. M. *et al.* In vivo imaging of specific drug-target binding at subcellular resolution. *Nat Commun* **5**, 3946, doi:10.1038/ncomms4946 (2014).

114 Martinez, N. J., Titus, S. A., Wagner, A. K. & Simeonov, A. High-throughput fluorescence imaging approaches for drug discovery using in vitro and in vivo three-dimensional models. *Expert Opin Drug Discov* **10**, 1347-1361, doi:10.1517/17460441.2015.1091814 (2015).

115 Patterson, A. P., Booth, S. A. & Saba, R. The emerging use of in vivo optical imaging in the study of neurodegenerative diseases. *Biomed Res Int* **2014**, 401306, doi:10.1155/2014/401306 (2014).

116 Li, W., Goldstein, D. R. & Kreisel, D. Intravital 2-photon imaging, leukocyte trafficking, and the beating heart. *Trends Cardiovasc Med* **23**, 287-293, doi:10.1016/j.tcm.2013.04.002 (2013).

117 Hefendehl, J. K. *et al.* Repeatable target localization for long-term in vivo imaging of mice with 2-photon microscopy. *J Neurosci Methods* **205**, 357-363, doi:10.1016/j.jneumeth.2011.10.029 (2012).

118 Stetter, C. *et al.* An experimental protocol for in vivo imaging of neuronal structural plasticity with 2-photon microscopy in mice. *Exp Transl Stroke Med* **5**, 9, doi:10.1186/2040-7378-5-9 (2013).

119 Zheng, B. *et al.* A NIR-remote controlled upconverting nanoparticle: an improved tool for living cell dye-labeling. *Nanotechnology* **26**, 425102, doi:10.1088/0957-4484/26/42/425102 (2015).

120 Luo, S., Zhang, E., Su, Y., Cheng, T. & Shi, C. A review of NIR dyes in cancer targeting and imaging. *Biomaterials* **32**, 7127-7138, doi:10.1016/j.biomaterials.2011.06.024 (2011).

121 Beckmann, N. *et al.* In vivo mouse imaging and spectroscopy in drug discovery. *NMR Biomed* **20**, 154-185, doi:10.1002/nbm.1153 (2007).

122 Hoffman, R. M. Fluorescent proteins as visible in vivo sensors. *Prog Mol Biol Transl Sci* **113**, 389-402, doi:10.1016/B978-0-12-386932-6.00010-7 (2013).

123 Matsuda, T. & Nagai, T. Quantitative measurement of intracellular protein dynamics using photobleaching or photoactivation of fluorescent proteins. *Microscopy (Oxf)* **63**, 403-408, doi:10.1093/jmicro/dfu033 (2014).

124 Hoffman, R. M. Use of fluorescent proteins and color-coded imaging to visualize cancer cells with different genetic properties. *Cancer Metastasis Rev* **35**, 5-19, doi:10.1007/s10555-016-9610-8 (2016).

125 Biju, V., Itoh, T. & Ishikawa, M. Delivering quantum dots to cells: bioconjugated quantum dots for targeted and nonspecific extracellular and intracellular imaging. *Chem Soc Rev* **39**, 3031-3056, doi:10.1039/b926512k (2010).

126 Li, Z. H., Peng, J. & Chen, H. L. Bioconjugated quantum dots as fluorescent probes for biomedical imaging. *J Nanosci Nanotechnol* **11**, 7521-7536 (2011).

127 Peacock, A. F. De Novo Designed Imaging Agents Based on Lanthanide Peptides Complexes. *Methods Enzymol* **580**, 557-580, doi:10.1016/bs.mie.2016.05.051 (2016).

128 Rajendran, M., Yapici, E. & Miller, L. W. Lanthanide-based imaging of protein-protein interactions in live cells. *Inorg Chem* **53**, 1839-1853, doi:10.1021/ic4018739 (2014).

129 Wysocki, L. M. & Lavis, L. D. Advances in the chemistry of small molecule fluorescent probes. *Curr Opin Chem Biol* **15**, 752-759, doi:10.1016/j.cbpa.2011.10.013 (2011).

130 Uppal, T. *et al.* Synthesis, computational modeling, and properties of benzo-appended BODIPYs. *Chemistry* **18**, 3893-3905, doi:10.1002/chem.201103002 (2012).

131 Ulrich, G., Ziessel, R. & Harriman, A. The chemistry of fluorescent bodipy dyes: versatility unsurpassed. *Angew Chem Int Ed Engl* **47**, 1184-1201, doi:10.1002/anie.200702070 (2008).

132 Treibs, A. & Kreuzer, F. H. Di- and Tri-Pyrrylmethene Complexes with Di-Fluoro Boron. *Liebigs Ann Chem* **718**, 208-+ (1968).

133 Pavlopoulos, T. G., Boyer, J. H., Shah, M., Thangaraj, K. & Soong, M. L. Laser action from 2,6,8-position trisubstituted 1,3,5,7-tetramethylpyrromethene-BF(2) complexes: part 1. *Appl Opt* **29**, 3885-3886, doi:10.1364/AO.29.003885 (1990).

134 Boyer, J. H. *et al.* Pyrromethene-Bf2 Complexes as Laser-Dyes .2. *Heteroatom Chem* **4**, 39-49, doi:DOI 10.1002/hc.520040107 (1993).

135 Sathyamoorthi, G., Boyer, J. H., Allik, T. H. & Chandra, S. Laser Active Cyanopyrromethene-Bf2 Complexes. *Heteroatom Chem* **5**, 403-407, doi:DOI 10.1002/hc.520050413 (1994).

136 Guggenheimer, S. C. *et al.* Efficient Laser Action from 2 Cw Laser-Pumped Pyrromethene-Bf(2) Complexes. *Appl Optics* **32**, 3942-3943 (1993).

137 Hermes, R. E., Allik, T. H., Chandra, S. & Hutchinson, J. A. High-Efficiency Pyrromethene Doped Solid-State Dye-Lasers. *Appl Phys Lett* **63**, 877-879, doi:Doi 10.1063/1.109887 (1993).

138 Kamkaew, A. *et al.* BODIPY dyes in photodynamic therapy. *Chem Soc Rev* **42**, 77-88, doi:10.1039/c2cs35216h (2013).

139 Jiao, L. *et al.* Long wavelength red fluorescent dyes from 3,5-diiodo-BODIPYs. *Org Biomol Chem* **8**, 2517-2519, doi:10.1039/c001068e (2010).

140 Ni, Y. & Wu, J. Far-red and near infrared BODIPY dyes: synthesis and applications for fluorescent pH probes and bio-imaging. *Org Biomol Chem* **12**, 3774-3791, doi:10.1039/c3ob42554a (2014).

141 Awuah, S. G., Das, S. K., D'Souza, F. & You, Y. Thieno-pyrrole-fused BODIPY intermediate as a platform to multifunctional NIR agents. *Chem Asian J* **8**, 3123-3132, doi:10.1002/asia.201300855 (2013).

142 Cheng, B. *et al.* The Mechanisms and Biomedical Applications of an NIR BODIPY-Based Switchable Fluorescent Probe. *Int J Mol Sci* **18**, doi:10.3390/ijms18020384 (2017).

143 Watley, R. L. *et al.* Dual Functioning Thieno-Pyrrole Fused BODIPY Dyes for NIR Optical Imaging and Photodynamic Therapy: Singlet Oxygen Generation without Heavy Halogen Atom Assistance. *Chem Asian J* **10**, 1335-1343, doi:10.1002/asia.201500140 (2015).

144 Kowada, T., Maeda, H. & Kikuchi, K. BODIPY-based probes for the fluorescence imaging of biomolecules in living cells. *Chem Soc Rev* **44**, 4953-4972, doi:10.1039/c5cs00030k (2015).

145 Bura, T. & Ziessel, R. Water-soluble phosphonate-substituted BODIPY derivatives with tunable emission channels. *Organic letters* **13**, 3072-3075 (2011).

146 Niu, S. L. *et al.* Water-soluble BODIPY derivatives. *Org Lett* **11**, 2049-2052, doi:10.1021/ol900302n (2009).

147 Li, L., Han, J., Nguyen, B. & Burgess, K. Syntheses and spectral properties of functionalized, water-soluble BODIPY derivatives. *J Org Chem* **73**, 1963-1970, doi:10.1021/jo702463f (2008).

148 Moriarty, R. D. *et al.* The application of water soluble, mega-Stokes-shifted BODIPY fluorophores to cell and tissue imaging. *J Microsc* **253**, 204-218, doi:10.1111/jmi.12111 (2014).

149 Zhu, S. *et al.* Highly water-soluble neutral BODIPY dyes with controllable fluorescence quantum yields. *Org Lett* **13**, 438-441, doi:10.1021/ol102758z (2011).

150 Hendricks, J. A. *et al.* Synthesis of [18F]BODIPY: bifunctional reporter for hybrid optical/positron emission tomography imaging. *Angew Chem Int Ed Engl* **51**, 4603-4606, doi:10.1002/anie.201107957 (2012).

151 Courtis, A. M. *et al.* Monoalkoxy BODIPYs--a fluorophore class for bioimaging. *Bioconjug Chem* **25**, 1043-1051, doi:10.1021/bc400575w (2014).

152 Hapuarachchige, S. *et al.* Design and synthesis of a new class of membrane-permeable triazaborolopyridinium fluorescent probes. *J Am Chem Soc* **133**, 6780-6790, doi:10.1021/ja2005175 (2011).

153 Zheng, Q., Xu, G. & Prasad, P. N. Conformationally restricted dipyrromethene boron difluoride (BODIPY) dyes: highly fluorescent, multicolored probes for cellular imaging. *Chemistry* **14**, 5812-5819, doi:10.1002/chem.200800309 (2008).

154 Zhu, S. *et al.* Highly water-soluble neutral BODIPY dyes with controllable fluorescence quantum yields. *Organic letters* **13**, 438-441 (2010).

155 Santos, S. A. *Medicinal Chemistry Approaches To Malaria Drug Discovery* PhD thesis, University of Lisbon, (2016).

156 Ueki, M. & Amemiya, M. Removal of 9-Fluorenylmethyloxycarbonyl (Fmoc) Group with Tetrabutylammonium Fluoride. *Tetrahedron Lett* **28**, 6617-6620, doi:Doi 10.1016/S0040-4039(00)96928-4 (1987).

157 Chen, C. C. *et al.* A mild removal of Fmoc group using sodium azide. *Amino Acids* **46**, 367-374, doi:10.1007/s00726-013-1625-7 (2014).

158 Prasher, D. C., Eckenrode, V. K., Ward, W. W., Prendergast, F. G. & Cormier, M. J. Primary structure of the Aequorea victoria green-fluorescent protein. *Gene* **111**, 229-233 (1992).

159 Cubitt, A. B. *et al.* Understanding, improving and using green fluorescent proteins. *Trends Biochem Sci* **20**, 448-455 (1995).

160 Keppler, A. *et al.* A general method for the covalent labeling of fusion proteins with small molecules in vivo. *Nat Biotechnol* **21**, 86-89, doi:10.1038/nbt765 (2003).

161 Gautier, A. *et al.* An engineered protein tag for multiprotein labeling in living cells. *Chem Biol* **15**, 128-136, doi:10.1016/j.chembiol.2008.01.007 (2008).

162 Los, G. V. *et al.* HaloTag: a novel protein labeling technology for cell imaging and protein analysis. *Acs Chem Biol* **3**, 373-382, doi:10.1021/cb800025k (2008).

163 Stagge, F., Mitronova, G. Y., Belov, V. N., Wurm, C. A. & Jakobs, S. SNAP-, CLIP- and Halo-tag labelling of budding yeast cells. *PLoS One* **8**, e78745, doi:10.1371/journal.pone.0078745 (2013).

164 S, N. P. & Kwon, K. The HaloTag: Improving Soluble Expression and Applications in Protein Functional Analysis. *Curr Chem Genomics* **6**, 8-17, doi:10.2174/1875397301206010008 (2012).

165 Coste, J., Lenguyen, D. & Castro, B. Pybop - a New Peptide Coupling Reagent Devoid of Toxic by-Product. *Tetrahedron Lett* **31**, 205-208, doi:Doi 10.1016/S0040-4039(00)94371-5 (1990).

166 Chang, P. V. & Bertozzi, C. R. Imaging beyond the proteome. *Chem Commun (Camb)* **48**, 8864-8879, doi:10.1039/c2cc31845h (2012).

167 Tsien, R. Y. Constructing and exploiting the fluorescent protein paintbox (Nobel Lecture). *Angew Chem Int Ed Engl* **48**, 5612-5626, doi:10.1002/anie.200901916 (2009).

168 Iyer, A. K., Duan, Z. & Amiji, M. M. Nanodelivery systems for nucleic acid therapeutics in drug resistant tumors. *Mol Pharm* **11**, 2511-2526, doi:10.1021/mp500024p (2014).

169 Santosh, B. & Yadava, P. K. Nucleic acid aptamers: research tools in disease diagnostics and therapeutics. *Biomed Res Int* **2014**, 540451, doi:10.1155/2014/540451 (2014).

170 Joshi, B. H. & Pachchigar, K. P. siRNA: novel therapeutics from functional genomics. *Biotechnol Genet Eng Rev* **30**, 1-30, doi:10.1080/02648725.2014.921495 (2014).

171 Hannon, G. J. & Rossi, J. J. Unlocking the potential of the human genome with RNA interference. *Nature* **431**, 371-378, doi:10.1038/nature02870 (2004).

172 Burnett, J. C. & Rossi, J. J. RNA-based therapeutics: current progress and future prospects. *Chem Biol* **19**, 60-71, doi:10.1016/j.chembiol.2011.12.008 (2012).

173 Chakraborty, C., Sharma, A. R., Sharma, G., Doss, C. G. P. & Lee, S. S. Therapeutic miRNA and siRNA: Moving from Bench to Clinic as Next Generation Medicine. *Mol Ther Nucleic Acids* **8**, 132-143, doi:10.1016/j.omtn.2017.06.005 (2017).

174 Schwechheimer, C., Merkel, M., Bohländer, P. R. & Wagenknecht, H.-A. in *Modified Nucleic Acids* (eds Kazuhiko Nakatani & Yitzhak Tor) 83-100 (Springer International Publishing, 2016).

175 Holzhauser, C. & Wagenknecht, H. A. In-stem-labeled molecular beacons for distinct fluorescent color readout. *Angew Chem Int Ed Engl* **50**, 7268-7272, doi:10.1002/anie.201101968 (2011).

176 Bohlander, P. R., Abba, M. L., Bestvater, F., Allgayer, H. & Wagenknecht, H. A. Two wavelength-shifting molecular beacons for simultaneous and selective imaging of vesicular miRNA-21 and miRNA-31 in living cancer cells. *Org Biomol Chem* **14**, 5001-5006, doi:10.1039/c6ob00691d (2016).

177 Holzhauser, C. & Wagenknecht, H. A. DNA and RNA "traffic lights": synthetic wavelength-shifting fluorescent probes based on nucleic acid base substitutes for molecular imaging. *J Org Chem* **78**, 7373-7379, doi:10.1021/jo4010102 (2013).

178 Hovelmann, F., Gaspar, I., Ephrussi, A. & Seitz, O. Brightness enhanced DNA FIT-probes for wash-free RNA imaging in tissue. *J Am Chem Soc* **135**, 19025-19032, doi:10.1021/ja410674h (2013).

179 Holzhauser, C., Liebl, R., Goepferich, A., Wagenknecht, H. A. & Breunig, M. RNA "traffic lights": an analytical tool to monitor siRNA integrity. *Acs Chem Biol* **8**, 890-894, doi:10.1021/cb3006616 (2013).

180 Bohlander, P. R. & Wagenknecht, H. A. Synthesis and evaluation of cyanine-styryl dyes with enhanced photostability for fluorescent DNA staining. *Org Biomol Chem* **11**, 7458-7462, doi:10.1039/c3ob41717d (2013).

181 Walter, H. K., Olshausen, B., Schepers, U. & Wagenknecht, H. A. A postsynthetically 2'-"clickable" uridine with arabino configuration and its application for fluorescent labeling and imaging of DNA. *Beilstein J Org Chem* **13**, 127-137, doi:10.3762/bjoc.13.16 (2017).

182 Berndl, S. *et al.* Comparison of a nucleosidic vs non-nucleosidic postsynthetic "click" modification of DNA with base-labile fluorescent probes. *Bioconjug Chem* **20**, 558-564, doi:10.1021/bc8004864 (2009).

183 Gramlich, P. M., Wirges, C. T., Manetto, A. & Carell, T. Postsynthetic DNA modification through the copper-catalyzed azide-alkyne cycloaddition reaction. *Angew Chem Int Ed Engl* **47**, 8350-8358, doi:10.1002/anie.200802077 (2008).

184 Meldal, M. & Tornoe, C. W. Cu-catalyzed azide-alkyne cycloaddition. *Chem Rev* **108**, 2952-3015, doi:10.1021/cr0783479 (2008).

185 Wang, Q. *et al.* Bioconjugation by copper(I)-catalyzed azide-alkyne [3 + 2] cycloaddition. *J Am Chem Soc* **125**, 3192-3193, doi:10.1021/ja021381e (2003).

186 Huisgen, R. 1,3-Dipolar Cycloadditions. Past and Future. *Angewandte Chemie International Edition in English* **2**, 565-598, doi:10.1002/anie.196305651 (1963).

187 Lescrinier, E., Froeyen, M. & Herdewijn, P. Difference in conformational diversity between nucleic acids with a six-membered 'sugar' unit and natural 'furanose' nucleic acids. *Nucleic Acids Res* **31**, 2975-2989 (2003).

188 Blackburn, G. M. *Nucleic acids in chemistry and biology*. (Royal Society of Chemistry, 2006).

189 Wahl, M. C. & Sundaralingam, M. Crystal structures of A-DNA duplexes. *Biopolymers* **44**, 45-63, doi:10.1002/(SICI)1097-0282(1997)44:1<45::AID-BIP4>3.0.CO;2-# (1997).

190 Egli, M. & Saenger, W. *Principles of nucleic acid structure*. (Springer Science & Business Media, 2013).

191 Walter, H.-K. *" DNA/RNA Traffic Lights 2.0"-Entwicklung von wellenlängenverschiebenden DNA-und RNA-Sonden unter Verwendung von" Click"-Modifikationen*, Dissertation, Karlsruhe, Karlsruher Institut für Technologie (KIT), 2016, (2016).

192 Steinmeyer, J., Rönicke, F., Schepers, U. & Wagenknecht, H. A. Synthesis of Wavelength-Shifting Fluorescent DNA and RNA with Two Photostable Cyanine–Styryl Dyes as the Base Surrogate Pair. *ChemistryOpen* **6**, 514-518 (2017).

193 Caplen, N. J., Parrish, S., Imani, F., Fire, A. & Morgan, R. A. Specific inhibition of gene expression by small double-stranded RNAs in invertebrate and vertebrate systems. *Proc Natl Acad Sci U S A* **98**, 9742-9747, doi:10.1073/pnas.171251798 (2001).

194 Kaczmarek, J. C., Kowalski, P. S. & Anderson, D. G. Advances in the delivery of RNA therapeutics: from concept to clinical reality. *Genome Med* **9**, 60, doi:10.1186/s13073-017-0450-0 (2017).

195 Stratton, M. R. Exploring the genomes of cancer cells: progress and promise. *Science* **331**, 1553-1558, doi:10.1126/science.1204040 (2011).

196 Lin, M. K. & Farrer, M. J. Genetics and genomics of Parkinson's disease. *Genome Med* **6**, 48, doi:10.1186/gm566 (2014).

197 Bertram, L. & Tanzi, R. E. Thirty years of Alzheimer's disease genetics: the implications of systematic meta-analyses. *Nat Rev Neurosci* **9**, 768-778, doi:10.1038/nrn2494 (2008).

198 Wang, D. & Gao, G. State-of-the-art human gene therapy: part II. Gene therapy strategies and clinical applications. *Discov Med* **18**, 151-161 (2014).

199 Nairne, J., Iveson, P. B. & Meijer, A. Chapter Five-Imaging in Drug Development. *Progress in medicinal chemistry* **54**, 231-280 (2015).

200 Urbanek, M. O., Galka-Marciniak, P., Olejniczak, M. & Krzyzosiak, W. J. RNA imaging in living cells - Methods and applications. *Rna Biol* **11**, 1083-1095, doi:10.4161/rna.35506 (2014).

201 Chen, B., Guan, J. & Huang, B. Imaging Specific Genomic DNA in Living Cells. *Annu Rev Biophys* **45**, 1-23, doi:10.1146/annurev-biophys-062215-010830 (2016).

202 Tsuchiya, K. D. Fluorescence In Situ Hybridization. *Clinics in Laboratory Medicine* **31**, 525-542, doi:https://doi.org/10.1016/j.cll.2011.08.011 (2011).

203 Flors, C. Super-resolution fluorescence imaging of directly labelled DNA: from microscopy standards to living cells. *Journal of Microscopy* **251**, 1-4, doi:10.1111/jmi.12054 (2013).

204 Wood, M., Yin, H. & McClorey, G. Modulating the expression of disease genes with RNA-based therapy. *PLoS Genet* **3**, e109, doi:10.1371/journal.pgen.0030109 (2007).

205 Wang, Y., Jeong, Y., Jhiang, S. M., Yu, L. & Menq, C. H. Quantitative characterization of cell behaviors through cell cycle progression via automated cell tracking. *PLoS One* **9**, e98762, doi:10.1371/journal.pone.0098762 (2014).

206 Atale, N., Gupta, S., Yadav, U. C. & Rani, V. Cell-death assessment by fluorescent and nonfluorescent cytosolic and nuclear staining techniques. *J Microsc* **255**, 7-19, doi:10.1111/jmi.12133 (2014).

207 Tario, J. D., Jr. *et al.* Optimized staining and proliferation modeling methods for cell division monitoring using cell tracking dyes. *J Vis Exp*, e4287, doi:10.3791/4287 (2012).

208 Collings, D. A. Subcellular localization of transiently expressed fluorescent fusion proteins. *Legume Genomics: Methods and Protocols*, 227-258 (2013).

209 Cheng, Y. *et al.* Identification of potential serum biomarkers for rheumatoid arthritis by high-resolution quantitative proteomic analysis. *Inflammation* **37**, 1459-1467 (2014).

210 Yoneyama, K. *et al.* Proteomic identification of autoantibodies in sera from patients with ovarian cancer as possible diagnostic biomarkers. *Anticancer research* **35**, 881-889 (2015).

211 Jiang, J., Liu, H.-L., Liu, Z.-H., Tan, S.-W. & Wu, B. Identification of cystatin SN as a novel biomarker for pancreatic cancer. *Tumor Biology* **36**, 3903-3910 (2015).

212 Lai, X. & Chen, S. Identification of novel biomarker and therapeutic target candidates for diagnosis and treatment of follicular adenoma. *Cancer Genomics-Proteomics* **12**, 271-281 (2015).

213 Liu, M. *et al.* Cell-specific biomarkers and targeted biopharmaceuticals for breast cancer treatment. *Cell Prolif* **49**, 409-420, doi:10.1111/cpr.12266 (2016).

214 Donato, R. *et al.* Functions of S100 proteins. *Curr Mol Med* **13**, 24-57 (2013).

215 Mendoz, E. & Lim, C. T. Collective Migration Behaviors of Human Breast Cancer Cells in 2D. *Cellular and Molecular Bioengineering* **4**, 411, doi:10.1007/s12195-011-0193-8 (2011).

216 Zimmer, C., Labruyere, E., Meas-Yedid, V., Guillen, N. & Olivo-Marin, J.-C. Segmentation and tracking of migrating cells in videomicroscopy with parametric active contours: A tool for cell-based drug testing. *IEEE transactions on medical imaging* **21**, 1212-1221 (2002).

217 Pitsillides, C. M. *et al.* Cell labeling approaches for fluorescence-based in vivo flow cytometry. *Cytometry A* **79**, 758-765, doi:10.1002/cyto.a.21125 (2011).

218 Hong, H., Yang, Y. A., Zhang, Y. & Cai, W. B. Non-Invasive Cell Tracking in Cancer and Cancer Therapy. *Curr Top Med Chem* **10**, 1237-1248 (2010).

219 Swirski, F. K. *et al.* A near-infrared cell tracker reagent for multiscopic in vivo imaging and quantification of leukocyte immune responses. *PLoS One* **2**, e1075, doi:10.1371/journal.pone.0001075 (2007).

220 Foster, A. E. *et al.* In vivo fluorescent optical imaging of cytotoxic T lymphocyte migration using IRDye800CW near-infrared dye. *Appl Opt* **47**, 5944-5952 (2008).

221 Hoffman, R. M. In vivo imaging with fluorescent proteins: the new cell biology. *Acta Histochem* **106**, 77-87, doi:10.1016/j.acthis.2004.02.001 (2004).

222 Hoffman, R. M. Advantages of multi-color fluorescent proteins for whole-body and in vivo cellular imaging. *Journal of biomedical optics* **10**, 041202-041202-041210 (2005).

223 Uddin, M. J. *et al.* Selective Visualization of Cyclooxygenase-2 in Inflammation and Cancer by Targeted Fluorescent Imaging Agents. *Cancer Research* **70**, 3618-3627, doi:10.1158/0008-5472.Can-09-2664 (2010).

224 Uddin, M. J., Crews, B. C., Ghebreselasie, K. & Marnett, L. J. Design, Synthesis, and Structure-Activity Relationship Studies of Fluorescent Inhibitors of Cycloxygenase-2 as Targeted Optical Imaging Agents. *Bioconjugate Chem* **24**, 712-723, doi:10.1021/bc300693w (2013).

225 Jemal, A. *et al.* Annual report to the nation on the status of cancer, 1975–2009, featuring the burden and trends in human papillomavirus (HPV)–associated cancers and HPV vaccination coverage levels. *JNCI: Journal of the National Cancer Institute* **105**, 175-201 (2013).

226 Geller, A. C. *et al.* Melanoma epidemic: an analysis of six decades of data from the Connecticut Tumor Registry. *Journal of clinical oncology* **31**, 4172-4178 (2013).

227 MacKie, R., Hauschild, A. & Eggermont, A. Epidemiology of invasive cutaneous melanoma. *Annals of Oncology* **20**, vi1-vi7 (2009).

228 Garbe, C. & Leiter, U. Melanoma epidemiology and trends. *Clinics in dermatology* **27**, 3-9 (2009).

229 Stern, R. S. Prevalence of a history of skin cancer in 2007: results of an incidence-based model. *Archives of dermatology* **146**, 279-282 (2010).

230 Schadendorf, D. & Hauschild, A. Melanoma in 2013: Melanoma [mdash] the run of success continues. *Nature Reviews Clinical Oncology* **11**, 75-76 (2014).

231 Frinton, E. *et al.* Metastatic melanoma: prognostic factors and survival in patients with brain metastases. *Journal of Neuro-Oncology*, 1-6 (2017).

232 Haake, A., Scott, G. A. & Holbrook, K. A. Structure and function of the skin: overview of the epidermis and dermis. *The biology of the skin* **2001**, 19-45 (2001).

233 Nordlund, J. J. & Boissy, R. E. The biology of melanocytes. *The biology of the skin*, 113-131 (2001).

234 Fitzpatrick, T. B. The biology of pigmentation. *Birth defects original article series* **7**, 5-12 (1971).

235 Uong, A. & Zon, L. I. Melanocytes in development and cancer. *Journal of cellular physiology* **222**, 38-41 (2010).

236 Williams, I. R. & Kupper, T. S. Immunity at the surface: homeostatic mechanisms of the skin immune system. *Life sciences* **58**, 1485-1507 (1996).

237 Balois, T. & Amar, M. B. Morphology of melanocytic lesions in situ. *Scientific reports* **4**, 3622 (2014).

238 Green, A. *et al.* Computer image analysis of pigmented skin lesions. *Melanoma research* **1**, 231-236 (1991).

239 Bandarchi, B., Ma, L., Navab, R., Seth, A. & Rasty, G. From melanocyte to metastatic malignant melanoma. *Dermatology research and practice* **2010** (2010).

240 McGrath, J., Eady, R. & Pope, F. Anatomy and organization of human skin. *Rook's textbook of dermatology*, 45-128 (2004).

241 Korotkov, K. & Garcia, R. Computerized analysis of pigmented skin lesions: a review. *Artificial intelligence in medicine* **56**, 69-90 (2012).

242 Jerant, A. F., Johnson, J. T., Demastes Sheridan, C. & Caffrey, T. J. Early detection and treatment of skin cancer. *American family physician* **62** (2000).

243 Kaufman, H. L. *The melanoma book: a complete guide to prevention and treatment*. (Gotham, 2005).

244 Madan, V., Lear, J. T. & Szeimies, R.-M. Non-melanoma skin cancer. *The Lancet* **375**, 673-685 (2010).

245 Newton Bishop, J. Lentigos, melanocytic naevi and melanoma. *Rook's Textbook of Dermatology, Eighth Edition*, 1-57 (2010).

246 Clark, W. H. *et al.* A study of tumor progression: the precursor lesions of superficial spreading and nodular melanoma. *Human pathology* **15**, 1147-1165 (1984).

247 Guerry, D., Synnestvedt, M., Elder, D. E. & Schultz, D. Lessons from tumor progression: the invasive radial growth phase of melanoma is common, incapable of metastasis, and indolent. *Journal of investigative dermatology* **100**, S342-S345 (1993).

248 Jaworek-Korjakowska, J. & Kłeczek, P. Automatic classification of specific melanocytic lesions using artificial intelligence. *BioMed research international* **2016** (2016).

249 Boyle, P., Maisonneuve, P. & Dore, J. Epidemiology of malignant melanoma. *British medical bulletin* **51**, 523-547 (1995).

250 Elwood, J. M. & Jopson, J. Melanoma and sun exposure: an overview of published studies. *International Journal of Cancer* **73**, 198-203 (1997).

251 Gallagher, R. P., Spinelli, J. J. & Lee, T. K. Tanning beds, sunlamps, and risk of cutaneous malignant melanoma. *Cancer Epidemiology and Prevention Biomarkers* **14**, 562-566 (2005).

252 Shah, C. P., Weis, E., Lajous, M., Shields, J. A. & Shields, C. L. Intermittent and chronic ultraviolet light exposure and uveal melanoma: a meta-analysis. *Ophthalmology* **112**, 1599-1607 (2005).

253 Veierød, M. B. *et al.* A prospective study of pigmentation, sun exposure, and risk of cutaneous malignant melanoma in women. *Journal of the National Cancer Institute* **95**, 1530-1538 (2003).
254 Hammar, N. *et al.* Cancer incidence in airline and military pilots in Sweden 1961-1996. *Aviation, space, and environmental medicine* **73**, 2-7 (2002).
255 Snell, R. & Bischitz, P. A study of the melanocytes and melanin in the skin of the immature, mature and pregnant female guinea-pig. *Cell and Tissue Research* **51**, 225-242 (1960).
256 Snell, R. S. EFFECT OF ALPHA MSH AND ESTROGEN ON MELANIN PIGMENTATION IN THE ALBINO. *The Journal of investigative dermatology* **44**, 17 (1965).
257 Veierod, M. B., Thelle, D. S. & Laake, P. Diet and risk of cutaneous malignant melanoma: a prospective study of 50, 757 Norwegian men and women. *International Journal of Cancer* **71**, 600-604 (1997).
258 Bevona, C., Goggins, W., Quinn, T., Fullerton, J. & Tsao, H. Cutaneous melanomas associated with nevi. *Archives of dermatology* **139**, 1620-1624 (2003).
259 Euvrard, S., Kanitakis, J. & Claudy, A. Skin cancers after organ transplantation. *New England Journal of Medicine* **348**, 1681-1691 (2003).
260 Hollenbeak, C. S. *et al.* Increased incidence of melanoma in renal transplantation recipients. *Cancer* **104**, 1962-1967 (2005).
261 Cho, E., Rosner, B. A., Feskanich, D. & Colditz, G. A. Risk factors and individual probabilities of melanoma for whites. *Journal of clinical oncology* **23**, 2669-2675 (2005).
262 FitzGerald, M. G. *et al.* Prevalence of germ-line mutations in p16, p19ARF, and CDK4 in familial melanoma: analysis of a clinic-based population. *Proceedings of the National Academy of Sciences* **93**, 8541-8545 (1996).
263 Goldstein, A. M. *et al.* High-risk melanoma susceptibility genes and pancreatic cancer, neural system tumors, and uveal melanoma across GenoMEL. *Cancer Research* **66**, 9818-9828 (2006).
264 Chin, L., Garraway, L. A. & Fisher, D. E. Malignant melanoma: genetics and therapeutics in the genomic era. *Genes & development* **20**, 2149-2182 (2006).
265 Schadendorf, D. *et al.* Melanoma. *Nature reviews Disease primers* **1**, 15003 (2015).
266 Hussussian, C. J. *et al.* Germline p16 mutations in familial melanoma. *Nature genetics* **8**, 15-21 (1994).
267 Kamb, A. in *Cold Spring Harbor symposia on quantitative biology.* 39-47 (Cold Spring Harbor Laboratory Press).
268 Kwong, L. N. *et al.* Oncogenic NRAS signaling differentially regulates survival and proliferation in melanoma. *Nature medicine* **18**, 1503-1510 (2012).
269 Herman, C. Emerging technologies for the detection of melanoma: achieving better outcomes. *Clinical, cosmetic and investigational dermatology* **5**, 195 (2012).
270 Jemal, A. *et al.* Cancer statistics, 2009. *CA: a cancer journal for clinicians* **59**, 225-249 (2009).
271 Mayer, J. E., Swetter, S. M., Fu, T. & Geller, A. C. Screening, early detection, education, and trends for melanoma: current status (2007-2013) and future directions: Part I. Epidemiology, high-risk groups, clinical strategies, and diagnostic technology. *Journal of the American Academy of Dermatology* **71**, 599. e591-599. e512 (2014).
272 Wartman, D. & Weinstock, M. Are we overemphasizing sun avoidance in protection from melanoma? *Cancer Epidemiology and Prevention Biomarkers* **17**, 469-470 (2008).

273 Ordóñez, N. G. Value of melanocytic-associated immunohistochemical markers in the diagnosis of malignant melanoma: a review and update. *Human pathology* **45**, 191-205 (2014).

274 Curley, R., Cook, M., Fallowfield, M. & Marsden, R. Accuracy in clinically evaluating pigmented lesions. *BMJ* **299**, 16-18 (1989).

275 Wolf, I., Smolle, J., Soyer, H. & Kerl, H. Sensitivity in the clinical diagnosis of malignant melanoma. *Melanoma research* **8**, 425-429 (1998).

276 Kopf, A. W., Mintzis, M. & Bart, R. S. Diagnostic accuracy in malignant melanoma. *Archives of dermatology* **111**, 1291-1292 (1975).

277 Koh, H. K., Lew, R. A. & Prout, M. N. Screening for melanoma/skin cancer: theoretic and practical considerations. *Journal of the American Academy of Dermatology* **20**, 159-172 (1989).

278 Stolz, W. *et al.* Abcd rule of dermatoscopy-a new practical method for early recognition of malignant-melanoma. *European Journal of Dermatology* **4**, 521-527 (1994).

279 Argenziano, G. *et al.* Epiluminescence microscopy for the diagnosis of doubtful melanocytic skin lesions: comparison of the ABCD rule of dermatoscopy and a new 7-point checklist based on pattern analysis. *Archives of dermatology* **134**, 1563-1570 (1998).

280 Capdehourat, G., Corez, A., Bazzano, A., Alonso, R. & Musé, P. Toward a combined tool to assist dermatologists in melanoma detection from dermoscopic images of pigmented skin lesions. *Pattern Recognition Letters* **32**, 2187-2196 (2011).

281 Ruiz, D., Berenguer, V., Soriano, A. & SáNchez, B. A decision support system for the diagnosis of melanoma: A comparative approach. *Expert Syst Appl* **38**, 15217-15223 (2011).

282 Hauschild, A. *et al.* To excise or not: impact of MelaFind on German dermatologists' decisions to biopsy atypical lesions. *JDDG: Journal der Deutschen Dermatologischen Gesellschaft* **12**, 606-614 (2014).

283 Wells, R., Gutkowicz-Krusin, D., Veledar, E., Toledano, A. & Chen, S. C. Comparison of diagnostic and management sensitivity to melanoma between dermatologists and MelaFind: a pilot study. *Archives of dermatology* **148**, 1083-1084 (2012).

284 Monheit, G. *et al.* The performance of MelaFind: a prospective multicenter study. *Archives of dermatology* **147**, 188-194 (2011).

285 Marghoob, A. A. *et al.* Instruments and new technologies for the in vivo diagnosis of melanoma. *Journal of the American Academy of Dermatology* **49**, 777-797 (2003).

286 Kaufmann, L. *Untersuchung der Glykostrukturtopologie bei Tumor-und Primärzelllinien*. (Cuvillier, 2012).

287 Laughlin, S. T. & Bertozzi, C. R. Metabolic labeling of glycans with azido sugars and subsequent glycan-profiling and visualization via Staudinger ligation. *Nature protocols* **2**, 2930 (2007).

288 Dube, D. H., Prescher, J. A., Quang, C. N. & Bertozzi, C. R. Probing mucin-type O-linked glycosylation in living animals. *Proceedings of the National Academy of Sciences of the United States of America* **103**, 4819-4824 (2006).

289 Agard, N. J., Prescher, J. A. & Bertozzi, C. R. A strain-promoted [3+ 2] azide− alkyne cycloaddition for covalent modification of biomolecules in living systems. *Journal of the American Chemical Society* **126**, 15046-15047 (2004).

290 Olshausen, B. *Neue Fluorophor-Verbindungen als mögliche Werkzeuge zur Detektion von malignen Melanomen*, (2014).

291 Adamczyk, M., Grote, J. & Moore, J. A. Chemoenzymatic Synthesis of 3 '-O-(Carboxyalkyl) fluorescein Labels. *Bioconjugate Chem* **10**, 544-547 (1999).

292 Trost, B. M., Ferreira, E. M. & Gutierrez, A. C. Ruthenium-and palladium-catalyzed enyne cycloisomerizations: differentially stereoselective syntheses of bicyclic structures. *Journal of the American Chemical Society* **130**, 16176-16177 (2008).

293 Itsenko, O., Kihlberg, T. & Långström, B. Photoinitiated carbonylation with [11C] carbon monoxide using amines and alkyl iodides. *The Journal of organic chemistry* **69**, 4356-4360 (2004).

294 Hagendorn, T. *Neue Wege Zu (Hetero-)Cyclooctinen*. (Logos Verlag Berlin, 2014).

295 Baskin, J. M. *et al.* Copper-free click chemistry for dynamic in vivo imaging. *Proceedings of the National Academy of Sciences* **104**, 16793-16797 (2007).

296 Codelli, J. A., Baskin, J. M., Agard, N. J. & Bertozzi, C. R. Second-generation difluorinated cyclooctynes for copper-free click chemistry. *Journal of the American Chemical Society* **130**, 11486-11493 (2008).

297 Sletten, E. M., de Almeida, G. & Bertozzi, C. R. A homologation approach to the synthesis of difluorinated cycloalkynes. *Organic letters* **16**, 1634-1637 (2014).

298 EricáBanks, R. & SankaráLal, G. 1-Alkyl-4-fluoro-1, 4-diazoniabicyclo [2.2. 2] octane salts: a novel family of electrophilic fluorinating agents. *Journal of the Chemical Society, Chemical Communications*, 595-596 (1992).

299 Dodziuk, H. *Strained hydrocarbons*. (Wiley-VCH, 2009).

300 Koeppe, R. E. *et al.* Combined experimental/theoretical refinement of indole ring geometry using deuterium magnetic resonance and ab initio calculations. *Journal of the American Chemical Society* **125**, 12268-12276 (2003).

301 Sugano, K. *et al.* Coexistence of passive and carrier-mediated processes in drug transport. *Nature reviews. Drug discovery* **9**, 597 (2010).

302 Fennema, E., Rivron, N., Rouwkema, J., van Blitterswijk, C. & de Boer, J. Spheroid culture as a tool for creating 3D complex tissues. *Trends in biotechnology* **31**, 108-115 (2013).

303 Ravi, M., Paramesh, V., Kaviya, S., Anuradha, E. & Solomon, F. 3D cell culture systems: advantages and applications. *Journal of cellular physiology* **230**, 16-26 (2015).

304 van Duinen, V., Trietsch, S. J., Joore, J., Vulto, P. & Hankemeier, T. Microfluidic 3D cell culture: from tools to tissue models. *Current opinion in biotechnology* **35**, 118-126 (2015).

305 Worthington, P., Pochan, D. J. & Langhans, S. A. Peptide hydrogels–versatile matrices for 3D cell culture in cancer medicine. *Frontiers in oncology* **5** (2015).

306 Patel, N. R., Aryasomayajula, B., Abouzeid, A. H. & Torchilin, V. P. Cancer cell spheroids for screening of chemotherapeutics and drug-delivery systems. *Therapeutic delivery* **6**, 509-520 (2015).

307 Mathes, S. H., Ruffner, H. & Graf-Hausner, U. The use of skin models in drug development. *Advanced drug delivery reviews* **69**, 81-102 (2014).

308 Fleischli, F. D., Morf, F. & Adlhart, C. Skin concentrations of topically applied substances in reconstructed human epidermis (RHE) compared with human skin using in vivo confocal Raman microscopy. *CHIMIA International Journal for Chemistry* **69**, 147-151 (2015).

309 Pruniéras, M., Régnier, M. & Woodley, D. Methods for cultivation of keratinocytes with an air-liquid interface. *Journal of Investigative Dermatology* **81**, S28-S33 (1983).

310 Rosdy, M. & Clauss, L.-C. Terminal epidermal differentiation of human keratinocytes grown in chemically defined medium on inert filter substrates at the air-liquid interface. *Journal of Investigative Dermatology* **95**, 409-414 (1990).

311 Schmook, F. P., Meingassner, J. G. & Billich, A. Comparison of human skin or epidermis models with human and animal skin in in-vitro percutaneous absorption. *International journal of pharmaceutics* **215**, 51-56 (2001).

312 Reijnders, C. M. *et al.* Development of a full-thickness human skin equivalent in vitro model derived from TERT-immortalized keratinocytes and fibroblasts. *Tissue Engineering Part A* **21**, 2448-2459 (2015).

313 Asbill, C. *et al.* Evaluation of a Human Bio-Engineered Skin Equivalent for Drug Permeation Studies. *Pharmaceutical Research* **17**, 1092-1097, doi:10.1023/a:1026405712870 (2000).

314 Liu, F., Luo, X. S., Shen, H. Y., Dong, J. S. & Yang, J. Using human hair follicle-derived keratinocytes and melanocytes for constructing pigmented tissue-engineered skin. *Skin Research and Technology* **17**, 373-379, doi:10.1111/j.1600-0846.2011.00510.x (2011).

315 Nakazawa, K. *et al.* Pigmented Human Skin Equivalent: New Method of Reconstitution by Grafting an Epithelial Sheet Onto a Non-Contractile Dermal Equivalent. *Pigment Cell Research* **10**, 382-390, doi:10.1111/j.1600-0749.1997.tb00696.x (1997).

316 Fransson, J., Heffler, L., Tengvall Linder, M. & Scheynius, A. Culture of human epidermal Langerhans cells in a skin equivalent. *British Journal of Dermatology* **139**, 598-604 (1998).

317 Gledhill, K. *et al.* Melanin transfer in human 3D skin equivalents generated exclusively from induced pluripotent stem cells. *PloS one* **10**, e0136713 (2015).

318 Laubach, V. *et al.* Integration of Langerhans-like cells into a human skin equivalent. *Archives of dermatological research* **303**, 135-139 (2011).

319 Hill, D. S. *et al.* A novel fully humanized 3D skin equivalent to model early melanoma invasion. *Molecular cancer therapeutics* **14**, 2665-2673 (2015).

320 Vörsmann, H. *et al.* Development of a human three-dimensional organotypic skin-melanoma spheroid model for in vitro drug testing. *Cell death & disease* **4**, e719 (2013).

321 Brohem, C. A. *et al.* Artificial skin in perspective: concepts and applications. *Pigment cell & melanoma research* **24**, 35-50 (2011).

322 Svaasand, L. O. *et al.* Dosimetry model for photodynamic therapy with topically administered photosensitizers. *Lasers in Surgery and Medicine* **18**, 139-149 (1996).

323 de Leeuw, J., van der Beek, N., Neugebauer, W. D., Bjerring, P. & Neumann, H. Fluorescence detection and diagnosis of non-melanoma skin cancer at an early stage. *Lasers in surgery and medicine* **41**, 96-103 (2009).

324 Ackermann, G. *et al.* Simulations on the selectivity of 5-aminolaevulinic acid-induced fluorescence in vivo. *Journal of Photochemistry and Photobiology B: Biology* **47**, 121-128 (1998).

325 Moan, J., Ma, L. W. & Iani, V. On the pharmacokinetics of topically applied 5-aminolevulinic acid and two of its esters. *International journal of cancer* **92**, 139-143 (2001).

326 Ra, H. *et al.* Detection of non-melanoma skin cancer by in vivo fluorescence imaging with fluorocoxib A. *Neoplasia* **17**, 201-207 (2015).

327 Cichorek, M., Wachulska, M., Stasiewicz, A. & Tymińska, A. Skin melanocytes: biology and development. *Advances in Dermatology and Allergology/Postępy Dermatologii I Alergologii* **30**, 30 (2013).

328 Santiago-Walker, A., Li, L., Haass, N. & Herlyn, M. Melanocytes: from morphology to application. *Skin pharmacology and physiology* **22**, 114-121 (2009).
329 Jeong, B., Bae, Y. H., Lee, D. S. & Kim, S. W. Biodegradable block copolymers as injectable drug-delivery systems. *Nature* **388**, 860-862 (1997).
330 Kataoka, K., Harada, A. & Nagasaki, Y. Block copolymer micelles for drug delivery: design, characterization and biological significance. *Advanced drug delivery reviews* **47**, 113-131 (2001).
331 Li, S. *et al.* pH-responsive biocompatible fluorescent polymer nanoparticles based on phenylboronic acid for intracellular imaging and drug delivery. *Nanoscale* **6**, 13701-13709 (2014).
332 Alam, M. A., Ali, R., Al-Jenoobi, F. I. & Al-Mohizea, A. M. Solid dispersions: a strategy for poorly aqueous soluble drugs and technology updates. *Expert opinion on drug delivery* **9**, 1419-1440 (2012).
333 Tirpude, R. N. & Puranik, P. K. Rabeprazole sodium delayed-release multiparticulates: Effect of enteric coating layers on product performance. *Journal of Advanced Pharmaceutical Technology & Research* **2**, 184-191, doi:10.4103/2231-4040.85539 (2011).
334 Wang, C. E., Stayton, P. S., Pun, S. H. & Convertine, A. J. Polymer Nanostructures Synthesized by Controlled Living Polymerization for Tumor-Targeted Drug Delivery. *Journal of controlled release : official journal of the Controlled Release Society* **219**, 345-354, doi:10.1016/j.jconrel.2015.08.054 (2015).
335 Yoshida, T. *et al.* Aminoalkyl methacrylate copolymers for improving the solubility of tacrolimus. I: Evaluation of solid dispersion formulations. *International journal of pharmaceutics* **428**, 18-24 (2012).
336 Liu, S., Maheshwari, R. & Kiick, K. L. Polymer-based therapeutics. *Macromolecules* **42**, 3 (2009).
337 Nicolas, J., Mura, S., Brambilla, D., Mackiewicz, N. & Couvreur, P. Design, functionalization strategies and biomedical applications of targeted biodegradable/biocompatible polymer-based nanocarriers for drug delivery. *Chem Soc Rev* **42**, 1147-1235, doi:10.1039/C2CS35265F (2013).
338 Stebbins, N. D., Ouimet, M. A. & Uhrich, K. E. Antibiotic-containing polymers for localized, sustained drug delivery. *Advanced drug delivery reviews* **78**, 77-87 (2014).
339 Vaupel, P., Kallinowski, F. & Okunieff, P. Blood flow, oxygen and nutrient supply, and metabolic microenvironment of human tumors: a review. *Cancer research* **49**, 6449-6465 (1989).
340 Repasky, E. A., Evans, S. S. & Dewhirst, M. W. Temperature Matters! And Why it Should Matter to Tumor Immunologists. *Cancer immunology research* **1**, 210-216, doi:10.1158/2326-6066.CIR-13-0118 (2013).
341 Zhu, Q., Zhang, A., Liu, P. & Xu, L. X. Study of Tumor Growth under Hyperthermia Condition. *Computational and Mathematical Methods in Medicine* **2012**, 198145, doi:10.1155/2012/198145 (2012).
342 Kirui, D. K. *et al.* Mild Hyperthermia Enhances Transport of Liposomal Gemcitabine and Improves in vivo Therapeutic Response. *Advanced healthcare materials* **4**, 1092-1103, doi:10.1002/adhm.201400738 (2015).
343 Taghizadeh, B. *et al.* Classification of stimuli–responsive polymers as anticancer drug delivery systems. *Drug delivery* **22**, 145-155 (2015).
344 Guo, X., Chang, R. K. & Hussain, M. A. Ion-exchange resins as drug delivery carriers. *Journal of pharmaceutical sciences* **98**, 3886-3902 (2009).

345 Liang, B., Tong, R., Wang, Z., Guo, S. & Xia, H. High intensity focused ultrasound responsive metallo-supramolecular block copolymer micelles. *Langmuir* **30**, 9524-9532 (2014).

346 Phenix, C. P., Togtema, M., Pichardo, S., Zehbe, I. & Curiel, L. High intensity focused ultrasound technology, its scope and applications in therapy and drug delivery. *Journal of Pharmacy & Pharmaceutical Sciences* **17**, 136-153 (2014).

347 Schoellhammer, C. M. *et al.* Ultrasound-mediated gastrointestinal drug delivery. *Science translational medicine* **7**, 310ra168-310ra168, doi:10.1126/scitranslmed.aaa5937 (2015).

348 Demarchi, C. A. *et al.* A magnetic nanogel based on O-carboxymethylchitosan for antitumor drug delivery: synthesis, characterization and in vitro drug release. *Soft Matter* **10**, 3441-3450 (2014).

349 Lee, J.-H., Kim, J.-w. & Cheon, J. Magnetic Nanoparticles for Multi-Imaging and Drug Delivery. *Molecules and Cells* **35**, 274-284, doi:10.1007/s10059-013-0103-0 (2013).

350 Owen, J., Pankhurst, Q. & Stride, E. Magnetic targeting and ultrasound mediated drug delivery: benefits, limitations and combination. *International Journal of Hyperthermia* **28**, 362-373 (2012).

351 Sun, H., Meng, F., Cheng, R., Deng, C. & Zhong, Z. Reduction-responsive polymeric micelles and vesicles for triggered intracellular drug release. *Antioxidants & redox signaling* **21**, 755-767 (2014).

352 Peng, K., Tomatsu, I. & Kros, A. Light controlled protein release from a supramolecular hydrogel. *Chemical communications* **46**, 4094-4096 (2010).

353 Shah, S., Sasmal, P. K. & Lee, K.-B. Photo-triggerable Hydrogel-Nanoparticle Hybrid Scaffolds for Remotely Controlled Drug Delivery. *Journal of materials chemistry. B, Materials for biology and medicine* **2**, 7685-7693, doi:10.1039/C4TB01436G (2014).

354 Shao, Y., Shi, C., Xu, G., Guo, D. & Luo, J. Photo and Redox Dual Responsive Reversibly Cross-Linked Nanocarrier for Efficient Tumor-Targeted Drug Delivery. *ACS Applied Materials & Interfaces* **6**, 10381-10392, doi:10.1021/am501913m (2014).

355 Douroumis, D. Practical approaches of taste masking technologies in oral solid forms. *Expert opinion on drug delivery* **4**, 417-426 (2007).

356 Douroumis, D. Orally disintegrating dosage forms and taste-masking technologies; 2010. *Expert opinion on drug delivery* **8**, 665-675 (2011).

357 Hashimoto, Y. *et al.* Preparation, characterization and taste-masking properties of polyvinylacetal diethylaminoacetate microspheres containing trimebutine. *Journal of pharmacy and pharmacology* **54**, 1323-1328 (2002).

358 Amidon, S., Brown, J. E. & Dave, V. S. Colon-Targeted Oral Drug Delivery Systems: Design Trends and Approaches. *AAPS PharmSciTech* **16**, 731-741, doi:10.1208/s12249-015-0350-9 (2015).

359 Sharma, P. K. Novel prospective in colon specific drug delivery system. *Polim. Med* **44**, 109-118 (2014).

360 Matsumura, Y. & Maeda, H. A new concept for macromolecular therapeutics in cancer chemotherapy: mechanism of tumoritropic accumulation of proteins and the antitumor agent smancs. *Cancer research* **46**, 6387-6392 (1986).

361 Han, L. *et al.* pH-Controlled Delivery of Nanoparticles into Tumor Cells. *Advanced Healthcare Materials* **2**, 1435-1439, doi:10.1002/adhm.201300013 (2013).

362 Tavakol, S. Acidic pH derived from cancer cells may induce failed reprogramming of normal differentiated cells adjacent tumor cells and turn them into cancer cells. *Medical hypotheses* **83**, 668-672 (2014).

363 Adhikari, C., Das, A. & Chakraborty, A. Zeolitic imidazole framework (ZIF) nanospheres for easy encapsulation and controlled release of an anticancer drug doxorubicin under different external stimuli: a way toward smart drug delivery system. *Molecular pharmaceutics* **12**, 3158-3166 (2015).

364 Min, K. H. *et al.* Tumoral acidic pH-responsive MPEG-poly (β-amino ester) polymeric micelles for cancer targeting therapy. *Journal of Controlled Release* **144**, 259-266 (2010).

365 Yoshida, T., Lai, T. C., Kwon, G. S. & Sako, K. pH-and ion-sensitive polymers for drug delivery. *Expert opinion on drug delivery* **10**, 1497-1513 (2013).

366 Prabhu, R. H., Patravale, V. B. & Joshi, M. D. Polymeric nanoparticles for targeted treatment in oncology: current insights. *International journal of nanomedicine* **10**, 1001 (2015).

367 Etrych, T. *et al.* Fluorescence optical imaging in anticancer drug delivery. *Journal of Controlled Release* **226**, 168-181 (2016).

368 Tebben, L. & Studer, A. Nitroxides: applications in synthesis and in polymer chemistry. *Angewandte Chemie International Edition* **50**, 5034-5068 (2011).

369 Aurich, H. G., Breuer, E. & Nielsen, A. *Nitroxides*. (Wiley Online Library, 1989).

370 Gerson, F. & Huber, W. *Electron spin resonance spectroscopy of organic radicals*. (John Wiley & Sons, 2006).

371 Tesch, M., Hepperle, J. A., Klaasen, H., Letzel, M. & Studer, A. Alternating Copolymerization by Nitroxide-Mediated Polymerization and Subsequent Orthogonal Functionalization. *Angewandte Chemie International Edition* **54**, 5054-5059 (2015).

372 Guégain, E., Guillaneuf, Y. & Nicolas, J. Nitroxide-Mediated Polymerization of Methacrylic Esters: Insights and Solutions to a Long-Standing Problem. *Macromolecular rapid communications* **36**, 1227-1247 (2015).

373 Nam, H. *et al.* Highly Sensitive and Selective Fluorescent Probe for Ascorbic Acid with a Broad Detection Range through Dual-Quenching and Bimodal Action of Nitronyl-Nitroxide. *ACS Sensors* **1**, 392-398 (2016).

374 Audran, G. *et al.* Enzymatically Shifting Nitroxides for EPR Spectroscopy and Overhauser-Enhanced Magnetic Resonance Imaging. *Angewandte Chemie International Edition* **54**, 13379-13384 (2015).

375 Krudopp, H., Sönnichsen, F. D. & Steffen-Heins, A. Partitioning of nitroxides in dispersed systems investigated by ultrafiltration, EPR and NMR spectroscopy. *Journal of colloid and interface science* **452**, 15-23 (2015).

376 Emoto, M. *et al.* Brain imaging in methamphetamine-treated mice using a nitroxide contrast agent for EPR imaging of the redox status and a gadolinium contrast agent for MRI observation of blood–brain barrier function. *Free radical research* **49**, 1038-1047 (2015).

377 Emoto, M. C., Sato-Akaba, H., Hirata, H. & Fujii, H. G. Dynamic changes in the distribution and time course of blood–brain barrier-permeative nitroxides in the mouse head with EPR imaging: visualization of blood flow in a mouse model of ischemia. *Free Radical Biology and Medicine* **74**, 222-228 (2014).

378 Lewandowski, M. & Gwoździński, K. Photoprotective and radioprotective properties of nitroxides and their application in magnetic resonance imaging. *Postepy higieny i medycyny doswiadczalnej (Online)* **70**, 1101-1111 (2016).

379 Blinco, J. P., Fairfull-Smith, K. E., Morrow, B. J. & Bottle, S. E. Profluorescent nitroxides as sensitive probes of oxidative change and free radical reactions. *Aust J Chem* **64**, 373-389 (2011).

380 Likhtenstein, G. I., Ishii, K. & Nakatsuji, S. i. Dual Chromophore-Nitroxides: Novel Molecular Probes, Photochemical and Photophysical Models and Magnetic Materials. *Photochemistry and photobiology* **83**, 871-881 (2007).

381 Gijzeman, O., Kaufman, F. & Porter, G. Quenching of aromatic triplet states in solution by nitric oxide and other free radicals. *Journal of the Chemical Society, Faraday Transactions 2: Molecular and Chemical Physics* **69**, 727-737 (1973).

382 Lussini, V. C., Blinco, J. P., Fairfull-Smith, K. E. & Bottle, S. E. Polyaromatic profluorescent nitroxide probes with enhanced photostability. *Chemistry-A European Journal* **21**, 18258-18268 (2015).

383 Morrow, B. J., Keddie, D. J., Gueven, N., Lavin, M. F. & Bottle, S. E. A novel profluorescent nitroxide as a sensitive probe for the cellular redox environment. *Free Radical Biology and Medicine* **49**, 67-76 (2010).

384 Ahn, H.-Y. *et al.* Two-photon fluorescence microscopy imaging of cellular oxidative stress using profluorescent nitroxides. *Journal of the American Chemical Society* **134**, 4721 (2012).

385 Chen, Y., Chen, H. & Shi, J. Drug delivery/imaging multifunctionality of mesoporous silica-based composite nanostructures. *Expert opinion on drug delivery* **11**, 917-930 (2014).

386 Vaijayanthimala, V. *et al.* Nanodiamond-mediated drug delivery and imaging: challenges and opportunities. *Expert opinion on drug delivery* **12**, 735-749 (2015).

387 Kirui, D. K. & Ferrari, M. Intravital Microscopy Imaging Approaches for Image-Guided Drug Delivery Systems. *Current drug targets* **16**, 528-541 (2015).

388 de Lange, J. H. M. *et al.* Quantification by laser scan microscopy of intracellular doxorubicin distribution. *Cytometry* **13**, 571-576, doi:10.1002/cyto.990130604 (1992).

389 Grignard, V. Sur quelques nouvelles combinaisons organometalliques du magnésium et leur application à des synthèses d'alcools et d'hydrocarbures. *Compt. Rend* **130**, 1322 (1900).

390 Lu, B.-L., Lu, J.-M. & Shi, M. Butyl lithium (nBuLi)-mediated carboxylation of vinylidenecyclopropanes with CO 2. *Tetrahedron* **65**, 9328-9335 (2009).

391 Fairbanks, B. D., Gunatillake, P. A. & Meagher, L. Biomedical applications of polymers derived by reversible addition–fragmentation chain-transfer (RAFT). *Advanced drug delivery reviews* **91**, 141-152 (2015).

392 Metri, K., Bhargav, H., Chowdhury, P. & Koka, P. S. Ayurveda for chemo-radiotherapy induced side effects in cancer patients. *Journal of stem cells* **8**, 115 (2013).

393 Tacar, O., Sriamornsak, P. & Dass, C. R. Doxorubicin: an update on anticancer molecular action, toxicity and novel drug delivery systems. *Journal of Pharmacy and Pharmacology* **65**, 157-170, doi:10.1111/j.2042-7158.2012.01567.x (2013).

394 Wang, D., Lin, B. & Ai, H. Theranostic nanoparticles for cancer and cardiovascular applications. *Pharmaceutical research* **31**, 1390-1406 (2014).

395 Gottlieb, H. E., Kotlyar, V. & Nudelman, A. NMR Chemical Shifts of Common Laboratory Solvents as Trace Impurities. *J. Org. Chem.* **62**, 7512-7515, doi:10.1021/JO971176V (1997).